MULTISCALE OPTICAL PATTERNING: USING MICRO AND NANO PERIODIC STRUCTURES TO CREATE NOVEL OPTICAL DEVICES WITH APPLICATIONS TO BIOSENSING

Author:
JOE BAILEY

Primary and Secondary Supervisors:
GABRIEL AEPPLI AND JOSEPH NDIEYIRA

A dissertation submitted in partial fulfilment of the requirements for the degree of Doctor of Philosophy

COMPLEX: CENTRE FOR MATHEMATICS AND PHYSICS IN THE LIFE SCIENCES AND EXPERIMENTAL BIOLOGY

LONDON CENTRE FOR NANOTECHNOLOGY

UNIVERSITY COLLEGE LONDON

JUNE 2016

Joe Bailey: *Multiscale optical patterning: Using micro and nano periodic structures to create novel optical devices with applications to biosensing,* June 2016

DECLARATION

I, Joe Bailey confirm that the work presented in this thesis is my own. Where information has been derived from other sources, I confirm that this has been indicated in the thesis.

London, June 2016

Joe Bailey, October 6, 2016

Dedicated to my friends and family without whose support and love,
starting, let alone finishing this would not have been possible.
In particular to those who didn't get to see it finished.

ABSTRACT

Patterning, the utilisation and manipulation of geometric properties, is important both for the rational design of technological devices and also to the understanding of many natural phenomena. In this thesis I examine the way in which micro and nano patterning can alter optical properties across a large range of wavelength scales and how these novel phenomena can be utilised.

Micro patterned electrodes can tune the geometry of radio frequency electric fields to generate dielectrophoretic microfluidic devices. These devices use the dielectrophoretic force to sort, position and characterise the properties of micro and nano particles.. I develop a new image processing algorithm that radically improves experimental efficiency allowing for real-time supervisor free dielectrophoretic characterisation of nanoparticles.

Metamaterials are composite structures that have repeating units that are much smaller than the wavelength of radiation they are designed to work with. The optical properties of the materials are derived from these units rather than the bulk characteristics of the materials they are composed of. I demonstrate the development of novel THz metamaterial absorber devices. These devices provide a means to design and control the absorption of THz radiation, modulating bandwidth, polarization dependence and frequency in a form that is readily integrable with other standard fabrication processes.

Finally by periodically patterning materials on the nanometer scale I demonstrate the development of novel photonic crystal devices and complementary optical components. In these devices the periodicity of the electromagnetic wave is modulated by the periodicity of the structures themselves resulting in band gaps and resonances analogous to the band gaps and defect states found commonly in semi-conductor physics. I demonstrate the theory, fabrication and measurement of these devices using novel broadband supercontinuum sources and propose a future application for biosensing.

Further topics covered in the appendix include the development of a spin out technology, a $100 open source atomic force microscope developed while spending time in China. Finally I examine the role of patterning for optimising the performance of nanomechanical cantilever biosensors, and show how geometrical effects on the microscopic scale are crucial to understanding the workings of the vancomycin family of antibiotics, as screened using microcantilevers.

Portions of this report are edited extracts from published articles resulting from this work, a full list of which is given in Appendix A.

ACKNOWLEDGEMENTS

I would like to thank Gabriel for both his insight in guiding this work into such interesting territory and the constant and considerable support he has given me and this project. His ability to look on a problem and unravel the fundamental principles at work, see the wider connections and pick out the killer applications has been inspirational.

I would like to thank Joseph for his constant enthusiasm, encouragement and guidance. His perseverance and optimism are an example to all that work with him.

I would also like to thank Rachel McKendry, her belief in me at the start of this work was key to all that came after.

I am hugely indebted to Rodolfo Hermans, his experience, guidance and scrutiny has been invaluable, helping me not only in the day to day experiments but also teaching me to ask more and better questions.

I would also like to thank Guy Matmon, without whose assistance not only would the metamaterial experiments have been impossible, but many other would have gone awry.

I thank Prof Yu Xiaomei and Dr Yongzheng Wen for their generosity and kindness while hosting me in Beijing.

I would like to thank Prof. Francois Grey for involving me in the fascinating world or citizen science and open source hardware and showing such belief in the openAFM project.

I also thank David Holmes for his thoughtful advice and support and in particular for sharing his wisdom concerning microfluidics.

I would like to thank the fantastic technical support team at the LCN, Steve Etienne and VJ in the cleanroom and Fabrizio and Andy in IT. I would also like to thank all the other people who have given up their time to share their expertise and knowledge including but not limited to: David Bakewell, John Hales, Samir Aoudjane, Laura Bovo, Byron Villis, Daniel Engstrom, Samadhan Patil, Richard Thorogate.

This document was typeset using a LaTeX document class adapted from André Miedes typographical work `classicthesis`.

Finally and most importantly of all my partner Zena for her wisdom, support, patience and love.

CONTENTS

1

INTRODUCTION

Over the centuries our societies have been in many ways defined by what we can make and the materials we use, through the stone, bronze and iron ages, to the industrial and then microelectronic revolutions. Current micro and nano fabrication techniques allow the manipulation of matter with unprecedented accuracy[1,2]. This has resulted in new materials and devices intentionally designed to have extraordinary mechanical[3], electrical[4], chemical[5] and optical properties[6]. Frequently these advances have been achieved through the manipulation or patterning of the geometrical forms of otherwise routine materials. That is taking a common material such as silicon or gold and transforming it into structures and patterns at the nanoscale that lead to entirely new properties.

The capability to pattern materials and create features with sizes comparable to and smaller than the wavelength of infrared and even visible light (See Figure 1.1) has provided the opportunity to produce a whole host of materials and devices that interact with and manipulate light in entirely new ways[7]. Such optical devices can and have been employed in a range of technologies, from communication[8] and computing[9] to biosensing[10] and diagnostics[11]. Although often lagging behind their electronic counterparts in terms of commercialisation, the potential benefits of moving to higher frequencies and faster signals are clear. One of the most exciting areas of application for these new devices and materials is in developing new tools for healthcare.

Biosensing, the detection of biological or chemical targets, is a vast and growing field of scientific research, primarily driven by the desire to make cheaper, smaller, more reliable and more sensitive diagnostic devices for healthcare, but also for environmental monitoring, security and life science research applications[12,13]. Aside from the aforementioned desirable features there are essentially two criteria to judge a biosensor by: its specificity and its sensitivity. Both criteria must be satisfied simultaneously for a sensor to be of any use. There are two distinct approaches to gaining specificity, immunoassays rely on an antibody antigen interaction to provide chemical specificity. The

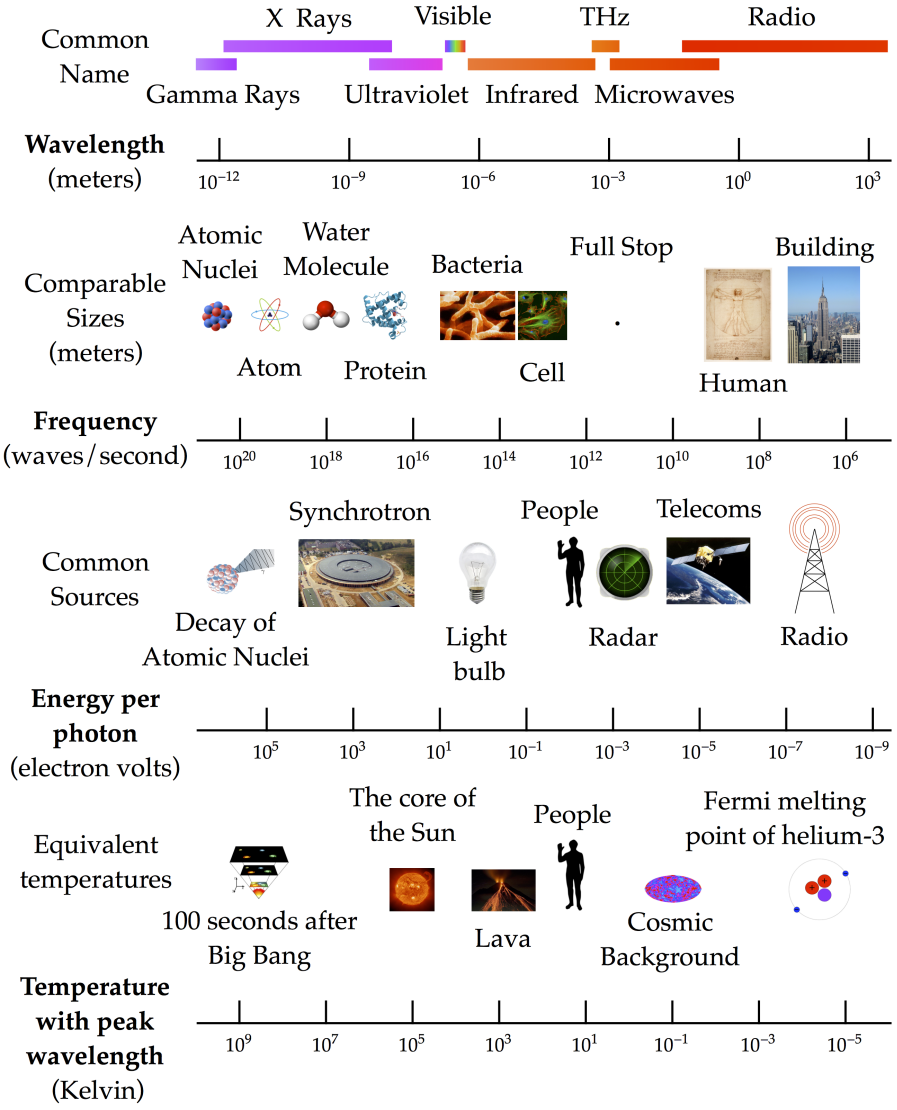

Figure 1.1: Electromagnetic spectrum. Many physical process and properties can be defined by the length scales or energies of photons that they interact with. Modern nanofabrication techniques have allowed the creation of intentionally designed devices that, through the geometric ordering of matter on this scale, make use of these interactions down to the optical and in some cases even x-ray wavelengths. Inset images are taken from Wikipedia under Creative Commons usage.

second approach is to use an interrogative technique that allows for the specific identification of the target. For example a vibrational spectroscopy assay would identify a specific molecule through the presence of a particular set of molecular bond resonances.

Sensitivity is usually determined by the transduction mechanism of the sensor, the change in the system as a response to perturbation, but what should not be ignored are the external factors that contribute to the practical sensitivity of a device, namely the sample delivery and noise in the readout mechanism[14]. While it is true that normally it is the physical limitations of the transduction mechanism that put an ultimate limit on sensitivity these secondary factors can prevent this limit being achieved, they can also have great bearing on the final cost, complexity and practicality of the device.

Optics and optical devices have been used as biological and diagnostic tools since the invention of the microscope. In the last 50 years many more applications have been developed e. g.flow cytometers and microplate readers. In recent years, largely due to the developments in micro and nanofabrication, there has been a huge drive both to miniaturise previously existing tools and develop entirely new ones utilising newly accessible optical properties[15]. Such developments are allowing researchers and clinicians to go beyond qualitative functional descriptions to quantitative analytical studies. Many optical properties have been exploited for biosensing applications, the most common are refractive index changes, fluorescent labelling, Raman scattering, and absorption, with miniaturization, micro and nano patterning and confinement a reoccurring strategy for reducing sample volume and boosting sensitivity[16]. A frequent feature of optical sensors is the use of an optical resonance[17]. Through suitable design, optical resonators can increase the electric field strength, and therefore the light-matter interaction. They can also contain this interaction to extremely small sample volumes and finally they frequently have extremely high quality factors. The combination of these properties can lead to extremely sensitive devices that require only minute quantities of sample.

In this thesis I examine the use of patterning to modify the electromagnetic field on three different scales. At radio frequencies I examine the use of microelectrodes to create dielectrophoretic micro particle characterisation devices, and describe the development of a novel image processing tool for streamlining the use of such devices. At THz frequencies it is possible with standard photolithography

to pattern at the sub wavelength scale to create metamaterials with properties not occurring naturally. I describe work undertaken in collaboration with Peking University to create new broadband and tunable THz metamaterial absorbers. Finally utilising cutting-edge nanofabrication techniques I develop a series of silicon photonic devices based on photonic crystal resonators with optical cavities for near infrared wavelengths. I discuss the computational, nanofabrication and measurement techniques developed for full spectral experimental characterisation of these devices, something surprisingly missing from existing literature in the field.

In the appendix I discuss a number of complimentary projects I have worked on. Firstly I describe an ongoing project to develop low cost scientific instrumentation for use in maker and educator communities, starting with an $100 atomic force microscope . Secondly I describe work investigating microcantilever sensors and their use to study drug action for the vancomycin family of antibiotics.

Before discussing the detail of the devices a general description of the physics involved is provided. Much of the physics is rooted in classical electromagnetism, and the description it provides of electromagnetic waves interacting with matter. I shall briefly summarise this with special attention to the the modifications and particular applications required for materials constructed using the novel micro and nano patterning investigated in this work.

1.1 CLASSICAL ELECTROMAGNETISM

It is hard to overstate the importance of electromagnetism in understanding the world we live in, so many forces and phenomena we experience in our daily lives are due to its effects, from the fact that you do not simply pass through the chair you are sitting on to the process of seeing the paper in front of you. Despite its discovery over 150 years ago many nanotechnological processes and applications, including those in this work, can be readily understood in the purely classical terms of Maxwell's equations, relating the electric field $\overrightarrow{\mathbf{E}}$, the magnetic field $\overrightarrow{\mathbf{B}}$ and their sources, charge and current[18,19,20]. These are given in their differential microscopic form in Table 1.1.

The first of Maxwell's equations is Gauss's Law, which states that all electric field lines start at positive charges and end in negative charges. The third law is Faraday's law of induction, which came

NAME	DIFFERENTIAL FORM
Gauss's law	$\nabla \cdot \mathbf{E} = \frac{\rho}{\epsilon_0}$
Gauss's law for magnetism	$\nabla \cdot \mathbf{B} = 0$
Faraday's law of induction	$\nabla \times \mathbf{E} = -\frac{\partial \mathbf{B}}{\partial t}$
Ampere's law with Maxwell's correction	$\nabla \times \mathbf{B} = \mu_0 \left(\mathbf{J} + \epsilon_0 \frac{\partial \mathbf{E}}{dt} \right)$

Table 1.1: Maxwell's Equations: The modern microscopic formulation of Maxwell's equations from 1864, relating the electric field **E**, the magnetic field **B** to their sources: charge, ρ being equal to charge density, and current, **J** being equal to current density, via the universal constants ϵ_0 and μ_0, the permittivity and permeability of free space respectively.

from observations of currents in circuits perturbed by time varying magnetic fields and states that a time varying magnetic field induces an electric field. The second is Gauss's law for magnetism, which states that there are no magnetic monopoles. The fourth law is Ampere's law with Maxwell's correction, it states that magnetic fields are caused by currents and, this being Maxwell's correction, by time varying electric fields. This symmetry that time varying magnetic fields cause electric fields, and that time varying electric fields cause magnetic fields led to the then ground breaking notion of an electromagnetic wave.

While the ideas and figures presented here are entirely my own interpretations of the subject material, many of the descriptions and examples draw inspiration from Jackson[18] and Griffiths[19], for a more detailed treatment of the subject the reader should consult these sources.

1.1.1 *Electromagnetic waves in vacuum*

In vacuum, where the charge density, ρ and current, **J** are equal to zero we can rewrite Maxwell's equations to get:

$$\begin{aligned} \nabla \cdot \mathbf{E} &= 0 & \nabla \cdot \mathbf{B} &= 0 \\ \nabla \times \mathbf{E} &= -\frac{\partial \mathbf{B}}{\partial t} & \nabla \times \mathbf{B} &= \mu_0 \epsilon_0 \frac{\partial \mathbf{E}}{\partial t} \end{aligned} \tag{1.1}$$

Where ϵ_0 and μ_0 are the permittivity and permeability of free space respectively. These can be decoupled by applying the curl operator to the two lower equations in 1.1, and then using the vector identity:

$$\nabla \times (\nabla \times \mathbf{A}) = \nabla (\nabla \cdot \mathbf{A}) - \nabla^2 \mathbf{A} \tag{1.2}$$

along with the two upper equations to remove the Div terms. This leaves us with:

$$\begin{aligned}\nabla^2\mathbf{E} &= \mu_0\epsilon_0\frac{\partial^2\mathbf{E}}{\partial t^2}\\ \nabla^2\mathbf{B} &= \mu_0\epsilon_0\frac{\partial^2\mathbf{B}}{\partial t^2}\end{aligned} \tag{1.3}$$

Which are three-dimensional wave equations for waves propagating with a velocity equal to:

$$v = \frac{1}{\sqrt{\epsilon_0\mu_0}} = 299\,792\,458\,\mathrm{m\,s^{-1}}$$

Which is the speed of light in a vacuum. One particularly useful solution (plotted in Figure 1.2) to this equation are sinusoidal waves, parametrised by k, the wave vector and ω, the angular frequency, of the form:

$$\begin{aligned}\tilde{\mathbf{E}}(\mathbf{r},t) &= \tilde{E}_0 e^{i(kz-\omega t)}\\ \tilde{\mathbf{B}}(\mathbf{r},t) &= \tilde{B}_0 e^{i(kz-\omega t)}\end{aligned} \tag{1.4}$$

$$B_0 = \frac{1}{c}E_0 \tag{1.5}$$

Where E_0 andB_0 are the electric and magnetic field amplitudes respectively. This allows us to write the general form of a monochromatic plane wave where $\mathbf{k}$ is the wave vector, pointing in the direction of propagation with amplitude k, wave number $2\pi/\lambda$ and $\hat{\mathbf{n}}$ is the polarisation vector, satisfying $\hat{\mathbf{n}}\cdot\hat{\mathbf{k}} = 0$

$$\begin{aligned}\tilde{\mathbf{E}}(\mathbf{r},t) &= \tilde{E}_0 e^{i(\mathbf{k}\cdot\mathbf{r}-\omega t)}\hat{\mathbf{n}}\\ \tilde{\mathbf{B}}(\mathbf{r},t) &= \frac{1}{c}\tilde{E}_0 e^{i(\mathbf{k}\cdot\mathbf{r}-\omega t)}(\hat{\mathbf{k}}\times\hat{\mathbf{n}}) = \frac{1}{c}\mathbf{k}\times\tilde{\mathbf{E}}\end{aligned} \tag{1.6}$$

1.1.2 *Maxwell's macroscopic equations and electromagnetism in matter*

While the microscopic formulation of Maxwell's equations is perfectly correct for the classical case, its notation is such that every source of charge and current must be specified. In reality when dealing with electromagnetism in matter this is rarely possible, nor is it required

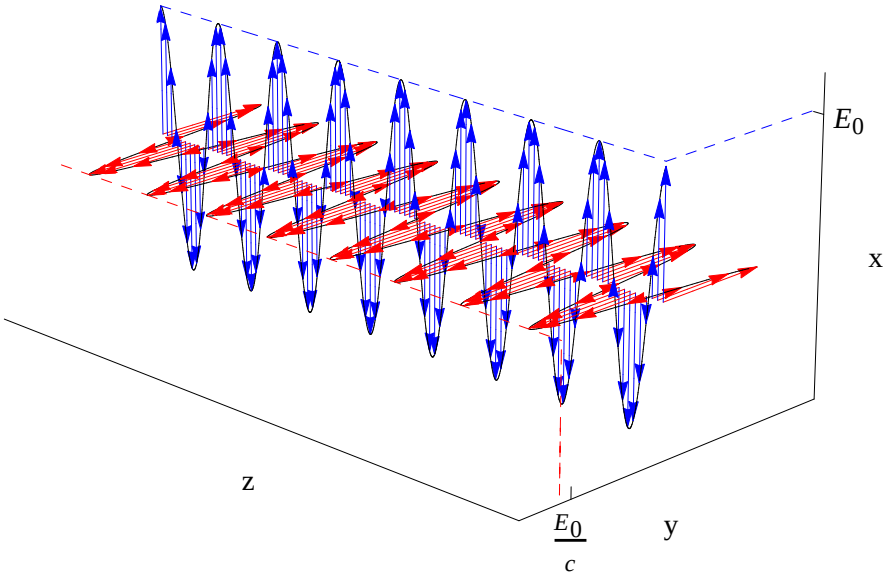

Figure 1.2: Electromagnetic wave in a vacuum showing the electric (blue) and magnetic (red) field oscillations perpendicular to one another and the direction of propogation (z)

to know the field on an atomic level. Instead it is more convenient to take the average of the microscopic quantities over larger length scales to get what is called the macroscopic description. It is this approach, averaging over the fine structure, that indicates that by patterning at the sub wavelength scale one would be able to modify these average material properties.

To arrive at the macroscopic description we first separate the contributions of free current and charge from the bound current and charge, the latter being replaced with an average description of the response of matter when under the influence of an electric or magnetic field. To do this we define the two new fields, the displacement and magnetizing field, $\mathbf{D}$ and $\mathbf{H}$ respectively:

$$\begin{aligned} \mathbf{D}(\mathbf{r},t) &= \epsilon_0 \mathbf{E}(\mathbf{r},t) + \mathbf{P}(\mathbf{r},t) \\ \mathbf{H}(\mathbf{r},t) &= \frac{1}{\mu_0}\mathbf{B}(\mathbf{r},t) - \mathbf{M}(\mathbf{r},t) \end{aligned} \tag{1.7}$$

Where **P** is the polarization and **M** is the magnetization, which are, in terms of bound charges, ρ_b and current J_b, equivalent to:

$$\begin{aligned} \rho_b &= -\nabla \cdot \mathbf{P} \\ \mathbf{J_b} &= \nabla \times \mathbf{M} + \frac{\partial \mathbf{P}}{\partial t} \end{aligned} \tag{1.8}$$

Although they are more commonly described in terms of electric and magnetic susceptibility (χ_e,χ_m), which for isotropic, linear materials is given by:

$$\begin{aligned} \mathbf{P} &= \epsilon_0 \chi_e \mathbf{E} \\ \mathbf{M} &= \mu_0 \chi_m \mathbf{B} \end{aligned} \tag{1.9}$$

Substituting the new definitions gives Maxwell's equations in macroscopic form:

$$\begin{aligned} \nabla \cdot \mathbf{D} &= \rho_f \qquad \nabla \cdot \mathbf{B} = 0 \\ \nabla \times \mathbf{E} &= -\frac{\partial \mathbf{B}}{\partial t} \quad \nabla \times \mathbf{H} = \mathbf{J_f} + \frac{\partial \mathbf{D}}{\partial t} \end{aligned} \tag{1.10}$$

and the accompanying constitutive relations linking **D** to **E**, and **H** to **B**. It will be shown later that it is within these constitutive relations that many complex phenomena and properties arise, but the general form is thus:

$$\begin{aligned} \mathbf{D} &= \epsilon \mathbf{E} \\ \mathbf{H} &= \frac{1}{\mu} \mathbf{B} \end{aligned} \tag{1.11}$$

We should also note the further relationship between the electric and magnetic susceptibilities and the permittivity and permeability:

$$\begin{aligned} \frac{\epsilon}{\epsilon_0} &= \chi_e + 1 \\ \frac{\mu}{\mu_0} &= \chi_m + 1 \end{aligned} \tag{1.12}$$

1.2 ELECTROMAGNETIC WAVES IN MATTER

1.2.1 *Propagation of light in linear non-conducting non-dispersive materials*

To derive the wave equation for the simplest case of a linear, non-conducting, non-dispersive material we consider Maxwell's macroscopic equations setting the unbound charge and current to zero. By using the above constitutive relations for **D** and **H** we rewrite Maxwell's equations as:

$$\begin{aligned} \nabla \cdot \mathbf{E} &= 0 & \nabla \cdot \mathbf{B} &= 0 \\ \nabla \times \mathbf{E} &= -\frac{\partial \mathbf{B}}{\partial t} & \nabla \times \mathbf{B} &= \mu\epsilon \frac{\partial \mathbf{E}}{\partial t} \end{aligned} \tag{1.13}$$

and, following the same route as the vacuum case, end up with the following wave equations:

$$\begin{aligned} \nabla^2 \mathbf{E} &= \mu\epsilon \frac{\partial^2 \mathbf{E}}{\partial t^2} \\ \nabla^2 \mathbf{B} &= \mu\epsilon \frac{\partial^2 \mathbf{B}}{\partial t^2} \end{aligned} \tag{1.14}$$

Which have solutions identical to the vacuum case with the exception that the velocity is now equal to:

$$v = \frac{1}{\sqrt{\epsilon\mu}} = \frac{c}{n}$$

where n, the refractive index of a material, is defined as:

$$n \equiv \sqrt{\frac{\epsilon\mu}{\epsilon_0\mu_0}} \tag{1.15}$$

From this point we could go on to derive Snell's law, the Fresnel equations and many other basic optical principles but it would not be of great use in the context of this work. Of more relevance is to complete the summary of light-material interactions.

1.2.2 *Propagation of light in conducting media*

The above derivations are based on the assumption that both ρ_f and $\mathbf{J_f}$ are zero. In the case of conductors this certainly is not the case. We

may however link the free current density to the electric field through Ohms law:

$$\mathbf{J_f} = \sigma \mathbf{E} \tag{1.16}$$

Where σ is the materials conductivity. Furthermore, we are generally only interested in the steady state behaviour, i.e. after all the free charge has dissipated or ρ_f=0. Substituting equation 1.2.2 into 1.13 and removing the ρ_f term we get:

$$\begin{aligned} \nabla \cdot \mathbf{E} &= 0 \qquad & \nabla \cdot \mathbf{B} &= 0 \\ \nabla \times \mathbf{E} &= -\frac{\partial \mathbf{B}}{\partial t} \qquad & \nabla \times \mathbf{B} &= \mu\sigma\mathbf{E} + \mu\epsilon\frac{\partial \mathbf{E}}{\partial t} \end{aligned} \tag{1.17}$$

We may apply the same method as before to derive the modified wave equation, which admits similar plane wave solutions, except that $\mathbf{k}$ is now complex, resulting in an exponentially decreasing amplitude of the wave and a phase shift in the magnetic component of the wave with respect to the electric:

$$\begin{aligned} \mathbf{E}(z,t) &= E_0 e^{-\kappa z} cos(kz - \omega t + \delta_e)\hat{\mathbf{x}} \\ \mathbf{B}(z,t) &= B_0 e^{-\kappa z} cos(kz - \omega t + \delta_e + \phi)\hat{\mathbf{y}} \end{aligned} \tag{1.18}$$

where κ is the imaginary component of $\mathbf{k}$ and ϕ is the phase of the complex $\mathbf{k}$. This solution also gives us the skin depth of a conducting material, $\frac{1}{\kappa}$ whereby the amplitude of a incident wave will have decreased by a factor of $\frac{1}{e}$. This evanescent wave is depicted in Figure 1.3.

1.2.3 *Propagation of light in dispersive media*

So far it has been shown that the propagation of light in matter is dictated by three parameters, ϵ, μ and σ. What has not been taken into account thus far is the frequency dependence of these parameters. To understand this we must return to the roots of equation 1.9, defining the relationship between the applied electric field and polarization of a substance. The general notion is that the response of a material to an incident wave is not instantaneous; there is inertia in the response that introduces a frequency dependency. The actual mechanisms dictating this response for different materials can be a function of many complicated processes but we can illustrate the prin-

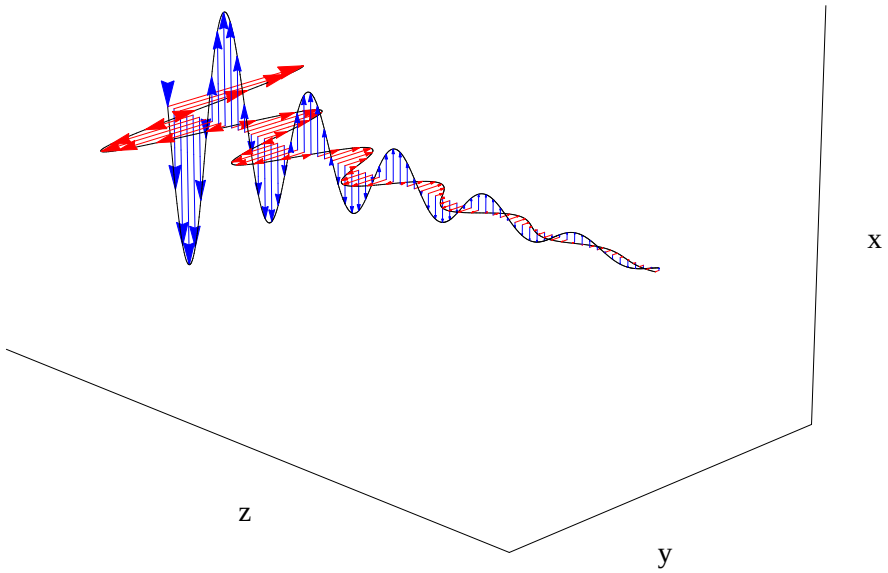

Figure 1.3: Electromagnetic wave in conductor, note the decaying amplitude and phase shift between the electric (blue) and magnetic (red) components

ciple by working though a general case, modelling the bound electron system as a simple damped harmonic oscillator, with the incident wave equated to a driving force. For dense materials it is necessary to also consider the forces from nearby oscillating electrons in the driving force term, nevertheless the resultant formalism of a complex and frequency dependent ϵ holds.

The driven damped oscillator system is described by:

$$\frac{d^2x}{dt^2} + \gamma\frac{dx}{dt} + \omega_0^2 x = \frac{q}{m}E_0 e^{i\omega t} \tag{1.19}$$

where ω is the frequency of the incident wave ω_0 is the natural frequency of the bound electron oscillator model, q is the charge of an electron, m is the mass of an electron and γ is the damping factor. If we solve for the steady state we obtain:

$$x_0 = \frac{q/m}{\omega_0^2 - \omega^2 - i\gamma\omega}E_0 \tag{1.20}$$

Using the fact that the dipole moment is equal to the charge of an electron q times this distance, and the polarisation is just the dipole density we get the complex polarisation as a function of ω for a system of molecules each containing f_j electrons with frequency ω_j and damping γ_j and overall density of N molecules per unit volume:

$$\mathbf{P} = \frac{Nq^2}{m}\left(\sum_j \frac{f_j}{\omega_j^2 - \omega^2 - i\gamma_j\omega}\right)\mathbf{E} \tag{1.21}$$

which in turn via equation 1.12 gives us ϵ:

$$\epsilon_r = 1 + \frac{Nq^2}{m\epsilon_0}\sum_j \frac{f_j}{\omega_j^2 - \omega^2 - i\gamma_j\omega} \tag{1.22}$$

The driven harmonic oscillator system is sensitive to the frequency of the incident wave. This is captured by the complex frequency dependant permittivity:

$$\epsilon(\omega) = \epsilon'(\omega) + i\epsilon''(\omega) \tag{1.23}$$

Although this example used a simple model for diffuse gas, the results are due to the more general property of the inertia in the response of a material. This simple description can be used to encapsulate a huge wealth of the physics of light interacting with many types of

matter. We can calculate absorption coefficients, resonant frequencies, explain the anomalous optical behaviour around those frequencies and the effects of DC conductivity at low frequencies.

The frequency dependence of ϵ has serious consequences for the passage of non-monochromatic light. Up until now we have only looked at solutions of a monochromatic nature, however in real world applications light is never entirely monochromatic. For simplicity, and as a recap on the Fourier representations needed we start with a one dimensional scalar wave $u(x,t)$ without dispersion, this could be considered a polarised electromagnetic wave with the scalar value equating to the electric field along the axis of its polarisation. We can build up a superposition of monochromatic waves to represent $u(x,t)$, in Fourier notation:

$$u(x,t) = \frac{1}{\sqrt{2\pi}} \int_{-\infty}^{\infty} A(k) e^{ikx - i\omega(k)t} \mathrm{d}k \tag{1.24}$$

$A(k)$ is given by the transform of the spatial amplitude of $u(x,0)$:

$$A(k) = \frac{1}{\sqrt{2\pi}} \int_{-\infty}^{\infty} u(x,0) e^{ikx} \mathrm{d}x \tag{1.25}$$

The case where $u(x,0)$ is in fact a harmonic wave of the form e^{ikx}, this of course gives a Dirac delta function $A(k) = \sqrt{2\pi}\delta(k - k_0)$, and results in the familiar travelling wave solution $u(x,t) = e^{ikx - i\omega t}$. If we give our pulse a finite spatial width for $u(x,0)$ then $A(k)$ is a correspondingly peaked function with a width Δk centred around k_0. The function $u(x,0)$, its Fourier transform $A(k)$ and the resultant $u(x,t)$ for these two cases with no dispersion are shown in Figure 1.4.

If we add a dispersive relationship, such that ω is a function of k, we will see spatial separation of the frequency components. This is illustrated in Figure 1.5 which shows the effect of dispersion on two Gaussian pulses of varying widths. A pulse of mixed frequencies will tend to spread out, each frequency component will travel at its ordinary or **phase** velocity:

$$v = \frac{c}{n} = \frac{\omega}{k}$$

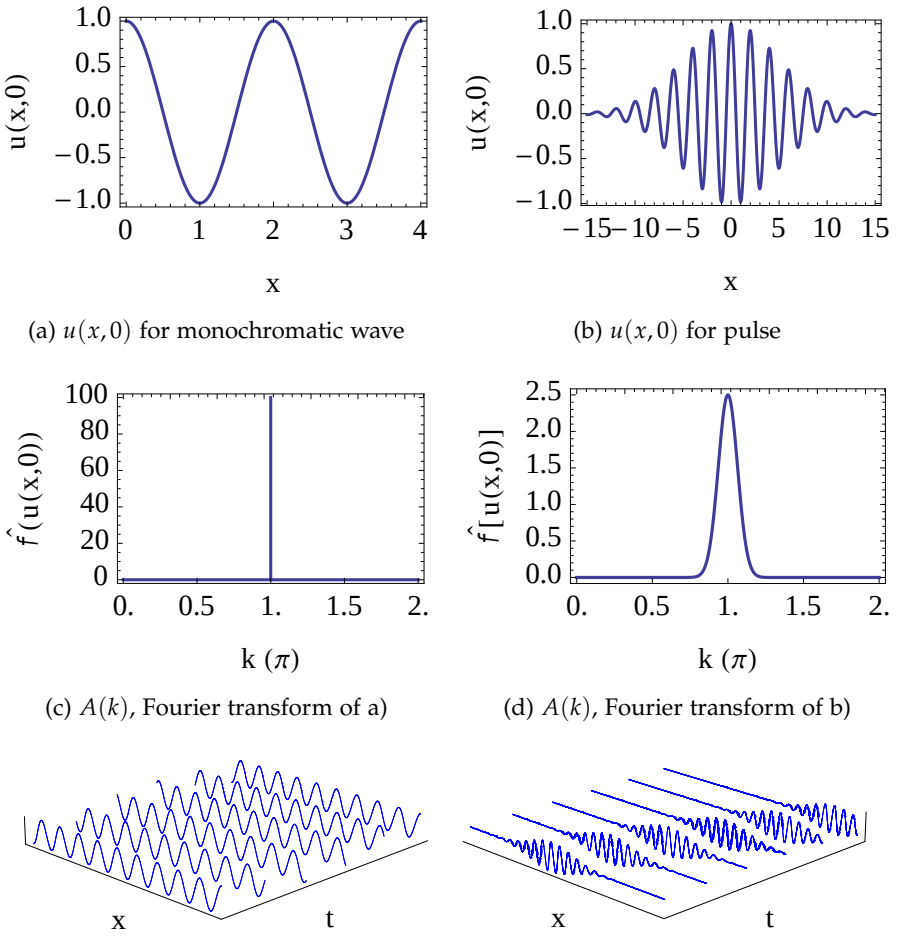

(a) $u(x,0)$ for monochromatic wave

(b) $u(x,0)$ for pulse

(c) $A(k)$, Fourier transform of a)

(d) $A(k)$, Fourier transform of b)

(e) $u(x,t)$ from c)

(f) $u(x,t)$ from d)

Figure 1.4: Fourier treatment of a wave pulse $u(x,t)$. The top plots show the function at time o $u(x,0)$. The left hand plot is a monochromatic wave, the right hand plot is a pulse. The second row shows the Fourier transform of these functions. As the left hand is monochromatic, this corresponds to a single peak, or Dirac-delta function in Fourier space. The right hand function however has a number of frequency components as reflected by the smooth function in Fourier space. Through the Fourier analysis we are able to recover the propagation of the different waveforms in time $u(x,t)$.

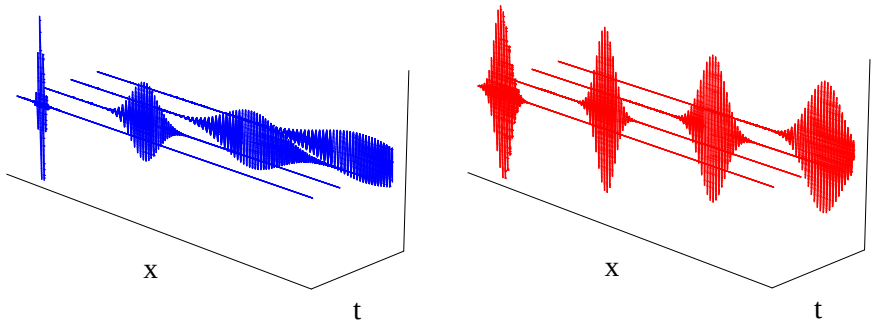

(a) (b)

Figure 1.5: Dispersion of a wave packet is a function of, among other things, the breadth of the original pulse, a narrow pulse consisting of many wave numbers will be subject to a greater spread in phase velocities, as such it will spread quicker.

The pulse itself travels at a shared velocity defined as the **group velocity**:

$$v_g = \frac{d\omega}{dk}$$

A narrow pulse (blue in Figure 1.5), consists of more frequencies, consequentially it spreads out more than the broad (red) pulse.

There are of course further topics of great interest, non-linear materials, for which the response is also a function of intensity, and anisotropic materials, for which the response of the material is dependent on the direction. I will, however, now discuss two topics that are the focus of this work. Firstly, metamaterials, where the atomic charge and current carrying elements are replaced with those we have designed ourselves to create new and intentionally designed values for ϵ and μ. Secondly, photonic band gap materials, for which materials are designed with a periodically varying refractive index such that, in an analogue to the electronic band gaps resulting from atomic lattices, we create photonic band gaps with only certain modes permitted to propagate.

1.3 METAMATERIALS

Metamaterials, as described in this work, are composite structures that have repeating units that are much smaller than the wavelength of the

electromagnetic waves they are designed to work with. Metamaterials work by effectively replacing the charge and current carrying elements of ordinary materials, the atoms, with artificial structures, minute capacitors, induction loops, wires and the like. Of course no atoms are actually replaced, but for the appropriate wavelengths, the same averaging we use to approximate a material by averaging over its atomic components comes to be dominated by the averaging over the artificial components[21]. Furthermore for this averaging to be valid any periodicity in a metamaterial must be sufficiently small in comparison to the wavelength that they *do not* impose a periodic modulation on the incident waves, which, as will be discussed later, is the opposite to photonic band gaps materials .

While not strictly relevant, considering the type of metamaterials developed in the work the most famous application of metamaterials is the generation of negative refractive index, or left handed materials. If one considers the damped oscillator model described in section 1.2.3, then it should be clear that there is no reason why the real parts of ϵ or μ cannot become negative. Having said that, there are constraints placed on dispersive models for permittivity and permeability, for example the system must still obey causality as implicit in the Kramers-Kronig relationship. Figure 1.6 shows the different behaviour of light depending on the value of ϵ and μ. The top left and bottom right quadrants do not permit propagating waves, only exponentially decaying waveforms. The top right quadrant is the realm of normal optical materials. The bottom left quadrant is the realm of negative refractive index left-handed materials. In this quadrant there are propagating solutions to the wave equation, but $\mathbf{k}$ is in the opposite direction to the energy flux, as denoted by $\mathbf{S}$, the Poynting vector. This odd form leads to exotic applications such as cloaking and a super lens.

1.3.1 *Wire mesh structures as low frequency plasmas*

The wire mesh serves as a brief but insightful and historically noteworthy example of a metamaterial with an artificial dispersion relationship for ϵ[22]. By effectively doping the vacuum with metal, a metallic like structure is created with plasma frequencies, not in the UV region as it is for most metals, but in the microwave region. To explain how it works it is first necessary to derive the plasma frequency, for which

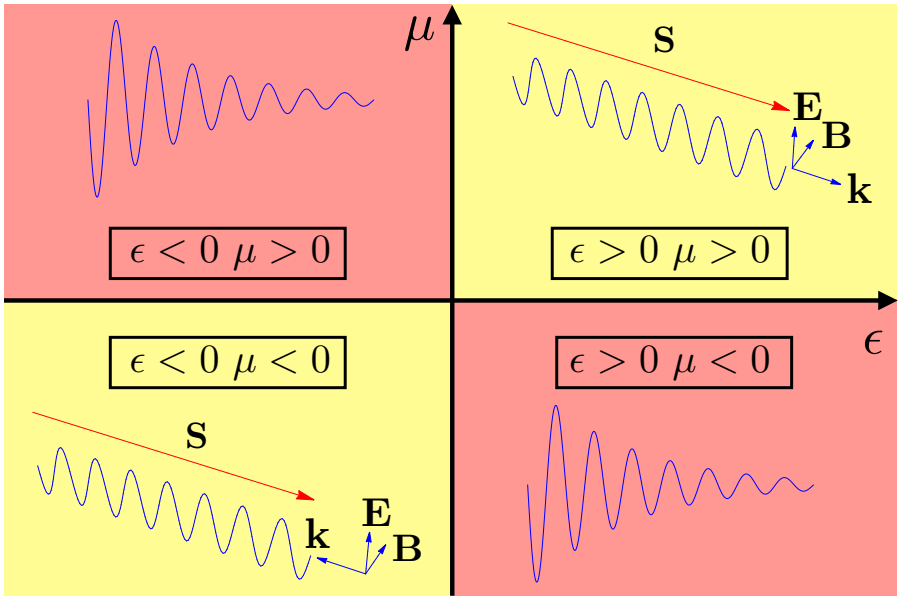

Figure 1.6: The different behaviour of light depending on the real value of ϵ and μ. The top left and bottom right quadrants do not permit propagating waves, only exponentially decaying waveforms, the top right quadrant is the realm of normal optical materials. The bottom left quadrant is the realm of negative refractive index or left handed materials. In this quadrant there are still propagating solutions to the wave equation, but **k** is in the opposite direction to the energy flux, as depicted by **S**, the Poynting vector

we return to the harmonic oscillator model described in section 1.2.3, with the notable difference that there is no restoring force, reflecting that for a good metal or plasma the electrons are free:

$$\frac{d^2x}{dt^2} + \gamma\frac{dx}{dt} = \frac{q}{m}E_0e^{i\omega t} \tag{1.26}$$

Applying the the the same derivations as before (see Eqt 1.9) leads to the following equation for ϵ:

$$\epsilon(\omega) = 1 - \frac{\omega_p^2}{\omega(\omega + i\gamma)}$$

ω_p is the plasma frequency is defined as:

$$\omega_p^2 = \frac{NZq^2}{\epsilon_0 m}$$

where NZ is the electron number density.

Examining this definition there are two mechanisms by which the wire mesh structure shifts the plasma frequency. Firstly averaging over the entire space greatly reduces the the effective electron density, NZ, in comparison to the bulk metal. Secondly the wires have a large self inductance simulating that the electrons have become much more massive, effectively increasing m. More specifically if we recalculate the electron density NZ from the geometric parameters of the wire mesh, and include an effective mass m linked to the magnetic field due to the current in the wires we can derive the following equation for the plasma frequency:

$$\omega_p^2 = \frac{2\pi c^2}{a^2 ln(a/r)}$$

where r is the radius of the wires and a is their separation. By tuning the gaps between the wires one can change the plasma frequency. The wire mesh is paradigmatic of how using macroscopic components in place of the microscopic elements of a dispersion model can result in an effective material with entirely new optical properties that are tunable through the shifting of readily accessible geometric design parameters.

1.3.2 *Split ring resonators as a magnetic metamaterial*

Due to the atomic sources of magnetism the response of most materials for the frequencies and materials relevant for this thesis tends to be extremely low. The split ring resonator structure overcomes this by essentially creating an LC circuit that is driven by the inductance of the oscillating incident magnetic field. The area of the ring equates to the inductance, and the gaps in the ring the capacitance. If can be shown[22] that for this system:

$$\mu_{eff}(\omega) = 1 + \frac{f\omega^2}{\omega_0^2 - \omega^2 - i\Gamma\omega} \tag{1.27}$$

Where f is the filling factor for the material ($f = \pi r^2/a^2$) and ω_0 is the resonant frequency of the LC circuit. Unsurprisingly, the LC result is completely analogous to the damped oscillator electron model that gives us the dispersive relation for ϵ in most natural materials. Furthermore, as $\omega_0 = \frac{1}{\sqrt{LC}}$ with L and C determined from the specific geometry of the device we can tune our magnetic dispersion function by tuning the geometric properties of our split rings.

While we have described analytical methods of deriving a dispersion equation for ϵ and μ based on applying the macroscopic averaging approach to mesoscopic artificial elements, in reality to develop new structures, one may want to introduce complex geometries which are more challenging to treat analytically. In these circumstances it is common to use numerical methods such as finite time and finite frequency domain software to simulate the transmission and reflection properties and deduce from this the dispersion relationships. This method has its hazards, for while it can be applied to any situation and return an answer, this answer may be wildly inaccurate. For example any errors or limitations in the models used to describe the constituent material parameters will lead to unrealistic results, furthermore such approaches may not take account of a periodicity unsuitable for homogenisation. Having said this, if one takes care, these methods can be used to predict the properties of complex metamaterial structures with great success.

1.4 PHOTONIC CRYSTALS

Photonic crystals (PhC), also sometimes referred to as band gap materials (PBGs), are structures featuring periodicities in their dielectric properties over length scales comparable to the wavelength of light they interact with. This is in contrast to metamaterials that tend to have features much smaller than the wavelength of light they work with. As a consequence of these periodicities PhCs modulate the waves they interact with. This modulation can be to the extent that they forbid the propagation of certain wavelengths of light along certain directions, they possess band gaps. The simplest example of a PhC is a Bragg reflectors, which possess one dimensional periodicity leading to the constructive and destructive interference of incident waves[23,24].

Naturally occurring photonic crystals, such as opal and many animals (such as the *Metapocyrtus* Weevil, Figure 1.7) have long been unwittingly appreciated[25]. Scientific study of such structures began as far back as the 19th Century[26], however it wasn't until 100 years later and the seminal papers by Yablonovitch[27] and John[28] in the 1980's, that the term photonic crystal was first coined and it is only recently that it has been possible to manufacture such structures for sub mm wavelengths. Photonic crystals are often touted as central to the future of the optics industry with possible applications in telecommunications, opto-electronics, optical computing and optical sensing. A large part of this excitement is due to the success of the analogous semi-conductor industry, whereby the understanding and engineering of crystalline structures has given us extensive control of the electrical properties of matter. There are many unresolved issues inhibiting the commercial application of photonic crystals but what can be said with confidence is that such structures provide many new approaches to the manipulation and control of light and as such are currently of much interest to engineers and scientists.

1.4.1 *Maxwell's equations in periodic dielectric material*

Photonic crystals and their interaction with light is commonly described using Maxwell's macroscopic equations. The system can be reformulated, as it is by Joannopoulos et al.[29] in their ubiquitous text book *Photonic Crystals: Molding the Flow of Light*[29], as a linear Hermitian eigenvalue problem.

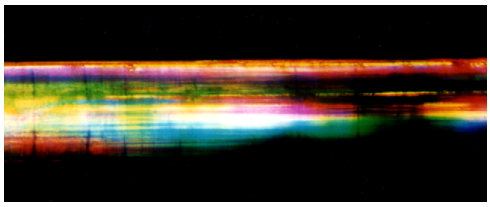

(a) Colour photo of an *Aphrodita sp* sea mouse spine

(b) *Metapocyrtus* weevil with opal analogue markings

Figure 1.7: Naturally occurring photonic crystals. a) Shows the spine of a *Aphrodita sp* sea mouse, it consists of tubes packed hexagonally to form a photonic crystal fibre like structure. b) Shows a *Metapocyrtus* weevil, with scales (blue-green) filled with a naturally occurring opal-analogue. Opal has a 3-D crystal structure of silica spheres 150–300 nm in diameter in a hexagonal or cubic close-packed lattice. Images taken from Parker and Martini [25] (*reproduced with authors permission*).

We begin with the four macroscopic Maxwell equations:

$$\begin{aligned} \nabla \cdot \mathbf{B} &= 0 \quad \nabla \times \mathbf{E} + \frac{\partial \mathbf{B}}{\partial t} = 0 \\ \nabla \cdot \mathbf{D} &= \rho \quad \nabla \times \mathbf{H} - \frac{\partial \mathbf{D}}{\partial t} = \mathbf{J} \end{aligned} \tag{1.28}$$

where $\mathbf{E}$ and $\mathbf{H}$ are the macroscopic electric and magnetic fields respectively. $\mathbf{D}$ and $\mathbf{B}$ are the displacement and magnetic induction fields and ρ and $\mathbf{J}$ are the free charge and current densities. These can be simplified by making the following assumptions:

- Our material is a mixed dielectric medium, that is a material whose dielectric properties vary as a function of position but not time.
- The dielectric response of the material is linear.
- The material is macroscopic and isotropic.
- Our material is non dispersive, we ignore any frequency dependence of the dielectric constant.
- We treat $\epsilon(\mathbf{r})$ as purely real and positive.
- μ_r is taken to be 1 as it is close unity for most dielectric materials.

Which essentially are encapsulated by the following expression of the constituent relations for **D** and **H**:

$$\mathbf{D}(\mathbf{r}) = \epsilon_0 \epsilon(\mathbf{r}) \mathbf{E}(\mathbf{r}) \qquad \mathbf{B}(\mathbf{r}) = \mu_0 \mathbf{H} \tag{1.29}$$

Using these modified constitutive relations Maxwell's equations are reformulated as:

$$\begin{aligned} \nabla \cdot \mathbf{H}(\mathbf{r}, t) = 0 \qquad & \nabla \times \mathbf{E}(\mathbf{r}, t) + \mu_0 \frac{\partial \mathbf{H}(\mathbf{r}, t)}{\partial t} = 0 \\ \nabla \cdot [\epsilon(\mathbf{r}) \mathbf{E}(\mathbf{r}, t)] = 0 \quad & \nabla \times \mathbf{H}(\mathbf{r}, t) - \epsilon_0 \epsilon(\mathbf{r}) \frac{\partial \mathbf{E}(\mathbf{r}, t)}{\partial t} = 0 \end{aligned} \tag{1.30}$$

Due to the linearity of the Maxwell equations we can separate the spatial and temporal dependence, expressing the fields in complex notation:

$$\begin{aligned} \mathbf{H}(\mathbf{r}, t) &= \mathbf{H}(\mathbf{r}) e^{i\omega t} \\ \mathbf{E}(\mathbf{r}, t) &= \mathbf{E}(\mathbf{r}) e^{i\omega t} \end{aligned} \tag{1.31}$$

This results in the following divergence equations:

$$\begin{aligned} \nabla \cdot \mathbf{H}(\mathbf{r}) &= 0 \\ \nabla \cdot [\epsilon(\mathbf{r}) \mathbf{E}(\mathbf{r})] &= 0 \end{aligned} \tag{1.32}$$

and the following single equation for the curl equations:

$$\nabla \times \left(\frac{1}{\epsilon(\mathbf{r})} \nabla \times \mathbf{H(r)} \right) = \left(\frac{\omega}{c} \right)^2 \mathbf{H(r)} \tag{1.33}$$

Which is equivalent to the eigenvalue problem with the operator Θ:

$$\begin{aligned} \Theta \mathbf{H(r)} &= \nabla \times \left(\frac{1}{\epsilon(\mathbf{r})} \nabla \times \mathbf{H(r)} \right) \\ \Theta \mathbf{H(r)} &= \left(\frac{\omega}{c} \right)^2 \mathbf{H(r)} \end{aligned} \tag{1.34}$$

Here the eigenvectors **H(r)** are the spatial patterns of the modes and the eigenvalues $\left(\frac{\omega}{c}\right)^2$ give us the corresponding frequencies.

1.4.2 *The effect of discrete translational symmetry*

Systems with discrete translational symmetry (see Figure 1.8) are invariant under the translation by steps of specific length and direction.

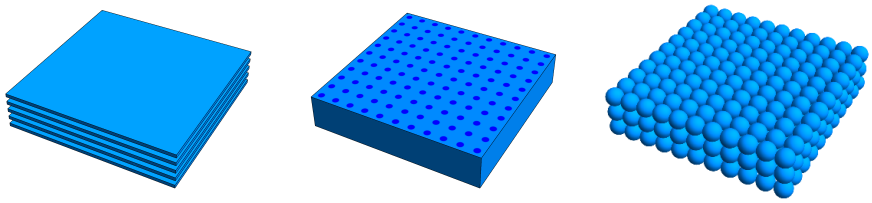

(a) (b) (c)

Figure 1.8: Illustration of one, two and three dimensional photonic crystals. These structures are invariant under discrete translational symmetry in one, two and three dimensions.

These lengths and directions are given by lattice vectors, in our case this can be simply stated as:

$$\epsilon(\mathbf{r}) = \epsilon(\mathbf{r} \pm n\mathbf{a}) \tag{1.35}$$

where $\mathbf{a}$ is the lattice vector and n is an integer. This leads to Bloch's theorem (from quantum mechanics). Bloch's theorem provides us with solutions of the form of a plane wave that is modulated by the periodicity of the lattice:

$$\mathbf{H_{k(r)}} = e^{i\mathbf{k}\cdot\mathbf{r}}\mathbf{u_k}(\mathbf{r}) \tag{1.36}$$

Where $\mathbf{u_k(r)}$ is a function that shares the discrete translational symmetry of the lattice. One of the key facts about Bloch states is that the wave vectors $\mathbf{k}$ and $\mathbf{k} + m\mathbf{b}$ are identical, where m is an integer and $\mathbf{b}$ is known as the reciprocal lattice vector and given by $\frac{2\pi}{\mathbf{a}}$. The lattice vectors, unit cell, reciprocal lattice vectors and Brillouin zone (the reciprocal equivalent of the unit cell) for a simple 2D square lattice are shown in Figure 1.9.

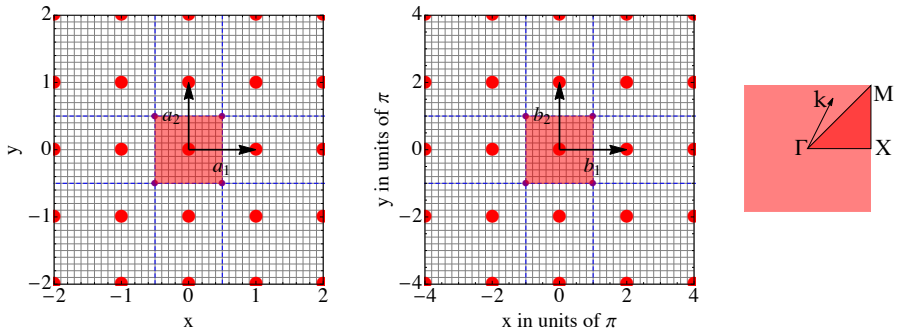

Figure 1.9: The lattice, the reciprocal lattice and the reduced Brillouin zone for a square lattice. The lattice describes the symmetry in normal spatial coordinates. The reciprocal lattice represent this symmetry in wave-vector space, the Brillouin zone is the smallest repeatable unit of the symmetry in wave-vector space.

To find explicit solutions we insert the Bloch state into Equation 1.4.1 for a bloch wave vector $\mathbf{k}$ we get:

$$\begin{aligned}
\Theta\mathbf{H}_\mathbf{k} &= \left(\frac{\omega(\mathbf{k})}{c}\right)^2 \mathbf{H}_\mathbf{k} \\
\nabla \times \left(\frac{1}{\epsilon(\mathbf{r})}\nabla \times e^{i\mathbf{k}\cdot\mathbf{r}}\mathbf{u}_\mathbf{k}(\mathbf{r})\right) &= \left(\frac{\omega(\mathbf{k})}{c}\right)^2 e^{i\mathbf{k}\cdot\mathbf{r}}\mathbf{u}_\mathbf{k}(\mathbf{r}) \\
(i\mathbf{k}+\nabla) \times \frac{1}{\epsilon(\mathbf{r})}(i\mathbf{k}+\nabla) \times \mathbf{u}_\mathbf{k}(\mathbf{r}) &= \left(\frac{\omega(\mathbf{k})}{c}\right)^2 \mathbf{u}_\mathbf{k}(\mathbf{r}) \\
\Theta_k\mathbf{u}_\mathbf{k}(\mathbf{r}) &= \left(\frac{\omega(\mathbf{k})}{c}\right)^2 \mathbf{u}_\mathbf{k}(\mathbf{r})
\end{aligned} \tag{1.37}$$

With a new operator Θ_k defined as:

$$\Theta_k \equiv (i\mathbf{k}+\nabla) \times \frac{1}{\epsilon(\mathbf{r})}(i\mathbf{k}+\nabla)\times \tag{1.38}$$

This description gives us the function $\mathbf{u}$, the mode profiles being determined by the eigenvalue problem with the added conditions coming from the transversality of $\mathbf{k}$ and periodicty of $\mathbf{u}$:

$$\begin{aligned}
0 &= (i\mathbf{k}+\nabla)\cdot\mathbf{u}_\mathbf{k}(\mathbf{r}) \\
\mathbf{u}_\mathbf{k}(\mathbf{r}) &= \mathbf{u}_\mathbf{k}(\mathbf{r}+m\mathbf{b})
\end{aligned} \tag{1.39}$$

For each given $\mathbf{k}$ we expect there to be an infinite number of modes with discretely spaced frequencies, which we can index by band. Conversely as $\mathbf{k}$ enters Θ_k as a continuous parameter for any given band n we expect the frequency $\omega_n(\mathbf{k})$ to vary continuously. This is

the band structure for a given crystal, a set of continuous functions $\omega_n(\mathbf{k})$, indexed in increasing frequency, with accompanying spatial mode profiles $\mathbf{u}(\mathbf{k})$ that are orthogonal to those of lower frequency. To solve these equations a number of computational approaches can be used, plane wave expansion, finite element and finite difference frequency domain calculations being the most common. In this report the solutions were found using two free open source GNU Guile based programs developed at MIT: finite difference time domain software MEEP[30] and finite difference frequency domain software MPB[31].

An important feature of this system is its scale invariance, the only assumption is that it is macroscopic. Indeed although modern work focuses on the near IR and visible regime, early experiments on this area were performed using microwaves[32]. Formulating the problem as a linear hermitian eigenproblem mirrors quantum mechanics in a number of ways and allows us to use some of the mathematical tools and results already well known from this field.

- All eigenvalues and therefore ω's are real.
- Modes with different frequencies are orthogonal.
- The variational theorem.
- Perturbation theory.

More specifically the reformulation of the variational principle can be stated as minimising the energy functional[29]:

$$U_f(\mathbf{H}) = \frac{(\mathbf{H}, \Theta\mathbf{H})}{(\mathbf{H}, \mathbf{H})} = \frac{\int d^3\mathbf{r}\, |\nabla \times \mathbf{E}(\mathbf{r})|^2}{\int d^3\mathbf{r}\, \epsilon(\mathbf{r})|\mathbf{E}(\mathbf{r})|^2} \tag{1.40}$$

This states that modes must concentrate their electric field energy in the higher dielectric regions though they must do this while remaining orthogonal to all the modes of lower frequency and minimizing their spatial oscillations.

1.4.3 *Band Gaps*

To illustrate the physical origins of band gaps we shall consider the 1-D case. As small periodic changes are introduced in the dielectric a band gap begins to appear at the edge of the Brillouin zone, this is when $\mathbf{k}$ is equal to $\pm\frac{\pi}{a}$, i.e the wavelength is equal to twice the lattice

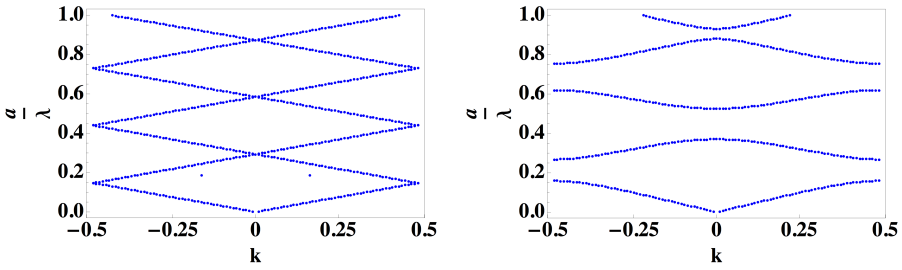

Figure 1.10: The physical origins of the band gap. a) With no periodic modulation, all layers having ϵ =11.68. The band diagram shows no gaps, modes are available at all frequencies b) The band diagram for a one dimensional photonic crystal, a Bragg mirror consisting of layers with varying dielectric properties, in this case $\frac{\epsilon_1}{\epsilon_2} = 0.2$. A gap is present between 0.15 and 0.22, and for higher frequencies. These calculations where performed using MEEP[30]

constant. We know the modes must be symmetrical with regard to the crystal structure so that leaves only two configurations available. The node is either positioned in the region of low or high dielectric.

If we also consider the consequences of the variational theorem, which states that the lower the frequency of the mode the greater the concentration of the electric field energy in regions of high dielectric, then it becomes clear that the higher band, with the energy concentrated in the low-ϵ region must have a higher frequency than the lower band. The difference in this frequency is the band gap, therein exist no modes, and the regions where the energy is concentrated lend their names to the conventional titles of the regions above and below the first gap as 'dielectric band and 'air band' respectively. The calculated band diagrams for a solid dielectric, and a multi-layer dielectric stack along with the density of modes as we vary the dielectric contrast between the two layers is shown in Figures 1.10 and 1.11.

1.4.4 *Defects, cavities and resonators*

When we describe a band gap as having no modes permitted, what we really mean is that no *extended* modes are permitted, if light of a forbidden frequency strikes a photonic crystal its amplitude will decay exponentially, forming an evanescent mode. This leads to the phenomena of defects and localized modes.

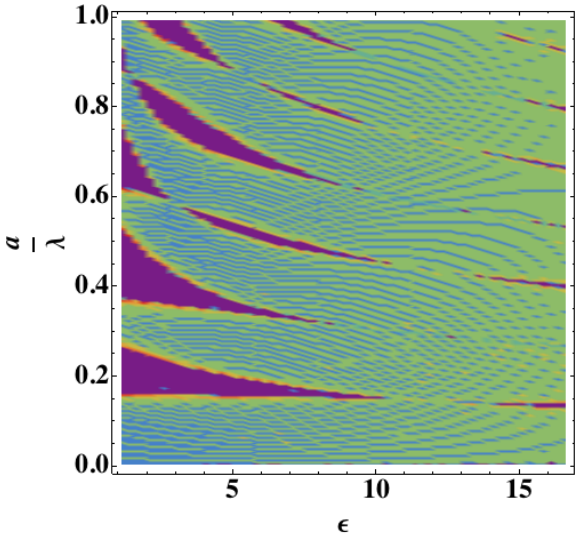

Figure 1.11: The density of modes as we vary the dielectric contrast, the background dielectric is 11.68, i.e. silicon. The dark purple regions correspond to the band gaps, where there are no modes. These calculations where performed using MEEP[30]

If a defect supports a mode that is forbidden by the surrounding material this creates a cavity or localized mode. For an infinite 3-D crystal the Q factor for such a cavity would be infinite, in reality there are losses both due to the finite size of a crystal and coupling to modes that are not contained.

The changing frequency of a defect mode as a function of the dielectric of the defect for a one-dimensional crystal is shown in Figure 1.12. We can see that as the dielectric of the defect is increased a defect mode is pulled down out of the air band into the gap.

The resonances in such defects have been shown experimentally to be capable of having Q factors of up 200,000[33], and even higher theoretically. In addition their perturbation, from the presence of biomolecules and or viruses leads to changes in these resonances, making them suitable for a wide range of biosensing applications[34,35,36,37].

In summary I have briefly described the context, motivation and background of the work included in this thesis. Essentially I have studied the interaction of electromagnetic radiation with materials that, through the utilisation of modern micro and nano patterning techniques, have been intentionally designed to alter and modify this interaction for useful purposes. I will now go through each section, discussing the use of micro electrodes to spatially pattern a radio frequency electric field enhancing and employing the dielecrophoretic

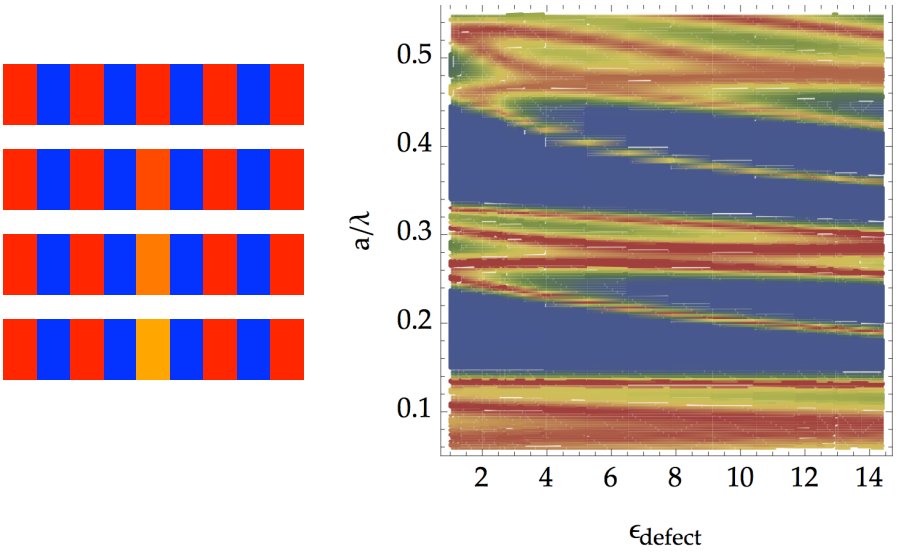

(a) (b)

Figure 1.12: a) We vary the dielectric properties of one segment in the stack b) The mode density as a function of defect dielectric. As we increase the dielectric constant of a single segment we see a defect mode protrude into the band gap

force for nano particle characterisation, the development of metamaterials for the THz frequency and silicon photonic crystal devices for work at optical wavelengths.

2

RADIO FREQUENCY CHARACTERISATION OF MICROPARTICLES

This work was undertaken with Dr Dave Bakewell and Dr David Holmes. My contribution to this work was the electrode simulation and data analysis, in particular the development of novel image and video processing software. Some of the figures and text in this section are edited extracts from the publications resulting from this work[39,40,41]

The term dielectrophoresis (DEP), first used by Pohl[38] in the 1970's refers to the phenomena whereby a force is experienced by a polarizable body in a conducting medium in the presence of a non uniform electric field. This force has been used to manipulate micro particles such as cells, viruses and markers and is a powerful addition to the toolbox of microfluidic total analysis systems (microTAS).

To understand the origins of this force it is useful to consider the general case of a dipole in a non-uniform electric field, as shown in Figure 2.1 a). For this case the net force experienced by the dipole is due to the uneven forces felt by the two poles and can be written as:

$$\overrightarrow{F} = (\overrightarrow{p} \cdot \nabla)\overrightarrow{E}_0 \tag{2.1}$$

Where $\overrightarrow{E}_0$ is the imposed field and $\overrightarrow{p}$ is the dipole moment. To determine the effective dipole moment for a dielectric sphere we compare the potential due to a conventional dipole with that of a dielectric sphere, as shown in Figure 2.1 b). The potential due to the dipole can be written as:

$$\Phi = \frac{(\overrightarrow{p} \cdot \overrightarrow{r})}{4\pi\epsilon_m r^3} \tag{2.2}$$

Where ϵ_m is the permittivity of the surrounding medium, and r is the radial distance form the centre of the dipole. The equivalent statement for a dielectric sphere with permittivity ϵ_p and radius R is[42]:

$$\Phi = \frac{(\epsilon_p - \epsilon_m)R^3\overrightarrow{E}_0 \cdot \overrightarrow{r}}{(\epsilon_p + 2\epsilon_m)r^3} \tag{2.3}$$

Setting these two expressions as equal allows us to define the effective moment as:

$$\overrightarrow{p}_{eff} = 4\pi\epsilon_m K_{CM}(\omega)r^3\overrightarrow{E}_0 \tag{2.4}$$

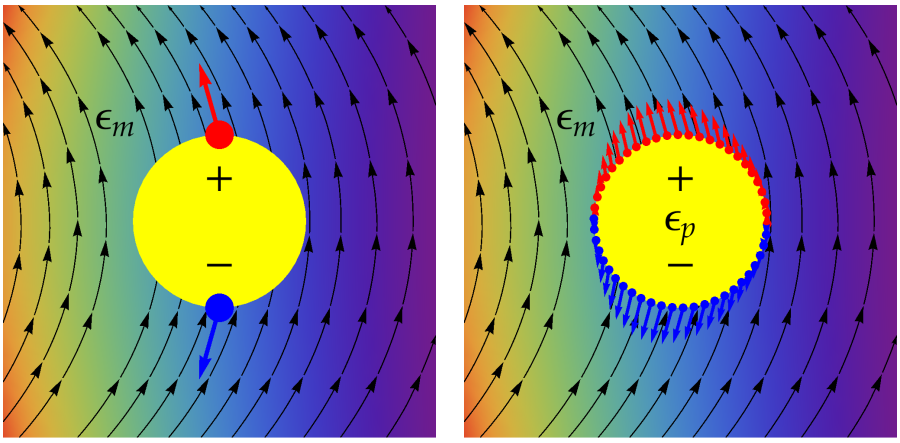

(a) (b)

Figure 2.1: Diagram of the effective dipole moment. a) shows a standard dipole in a non-uniform electric field, the dipole moment is defined by the magnitude and relative positions of the poles (red and blue circles). b) shows the case for a dielectric sphere, in this case an effective moment can be calculated based on the relative permittivity of the sphere and medium.

where $K_{CM}(\omega)$ is the Clausius-Mossotti (CM) factor which describes the complex permittivity of the particle, the medium and their frequency dependence:

$$K_{CM}(\omega) = \frac{\epsilon_p^* - \epsilon_m^*}{\epsilon_p^* + 2\epsilon_m^*} \tag{2.5}$$

For which ϵ_p^* and ϵ_m^* are the complex permittivities of the particle and medium respectively with $\epsilon^* = \epsilon - \frac{j\sigma}{\omega}$ as usual. Substituting this effective moment into Eq.2.1, describing the force on a dipole we get the dielectrophoretic force:

$$\overrightarrow{F}_{DEP}(\underline{x}, t) = 2\pi r^3 \epsilon_m \mathrm{Re}\left[K_{CM}(\omega)\right] \overrightarrow{\nabla} |\overrightarrow{E}(\underline{x})|^2 \tag{2.6}$$

Where $\underline{x}$ is the spatial position, r is the particle radius, ϵ_m is the medium permittivity and $|\overrightarrow{E}(x)|$ is the electric field magnitude rms. This equation is considered to be accurate when electric field gradients are not very large compared with the particle size, because it is based on the dipole approximation[42]. When the electric field gradients are large, such as close to electrode edges, higher order terms become relevant and result in higher forces.

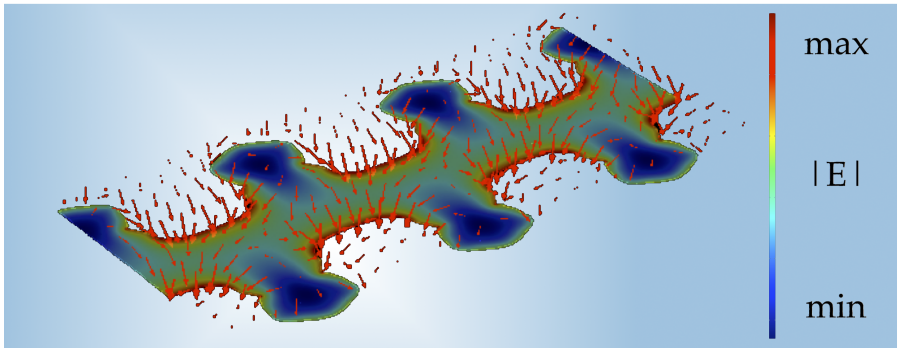

Figure 2.2: Simulations of DEP force in microchannel using experimental electrode geometry (5 µm pitch). The three dimensional plot shows the relative magnitude and direction of DEP force (size and direction of red arrows). The 2D plot shows the E-field magnitude in the plane of electrodes. It is clear that the DEP force directs particles down from the bulk solution towards the regions of high field, and in particular the electrode edges and inter-electrode gap.

The magnitude and direction of the DEP force depends upon the size and polarizability of the particle, the polarizablity of the medium and the frequency dependence of both plus finally the electric field gradient. Using suitable buffers and electrodes it is possible to characterise, manipulate and sort nanoparticles, viruses, and cells based on these properties.[43,44,45] Furthermore DEP is straightforwardly integrated into lab-on-chip (LOC) platforms.[45,46] Figure 2.2 shows the result of COMSOL multiphysics simulations of the pDEP force for a single pair of the interdigitated electrodes used in this work, this design creates repeating regions of high and low electric field magnitude and can be used for electrical characterisation experiments[47].

Microfluidics and more specifically the field of microfluidic DEP devices are of great relevance to the development of biosensing and analytical tools for the life sciences[48]. Electrophoresis and dielectrophoresis are key methods in the microfluidics tool box and are used in diverse applications such as particle speration[43], particle characterisation[49], cell manipulation[50] and droplet sorting[51]. Figure 2.3 reproduces an overview of microfluidic developments and applications.

Image processing, and in particular the tracking, and quantification of florescence signals is of huge significance not only in the field of microfluidics but many other areas of the life sciences[52]. From developmental biology to biochemistry being able to extract quanti-

fied measurements from florescence microscope images is of great importance. Here we present a refined DEP characterisation method using micro fabricated arrays of electrodes. In addition we discuss a previously unrecognised avenue to simple, fast, supervisor free fluorescence image quantification.

2.1 ELECTRICAL CHARACTERISATION WITH DEP

One important application of DEP is the characterisation of particles' electrical properties. These properties can influence their dispersive behaviour and can also be indicative of the state or health of biological entities such as cells, viruses and proteins.[49,53,54] Traditionally to characterise these properties with DEP 'cross-over' measurements have been used.This involves a low voltage radio frequency signal being applied to micro-fabricated electrodes, similar to those shown in Figure 2.2, in or below a microfluidic channel filled with an electrolyte-particle suspension. By varying the frequency of this radio signal and observing the particle behaviour the 'cross-over' frequency at which the DEP behaviour switches from negative to positive, and by implication the particle and medium polarizability are equal, can be determined[55,56]. This cross-over frequency is recorded and the measurement is repeated for a different conductivity medium, the relationship of the cross-over frequency, the point at which the CM factor given in Eq. 2.5 is equal to zero, to the medium conductivity allows us to back out the particles dielectric properties. The problem with the 'cross-over' approach is that it requires the use of multiple mediums, which often have to be prepared manually and it requires the cross-over threshold to be in an experimentally accessible combination of particle and medium conductivity, something that is not always the case.

An alternative approach is to use the initial collection rate of nanoparticles under the action of positive DEP (pDEP) immediately after the force generating signal is switched on. The initial collection rate is approximately proportional to the small-time averaged DEP force[44,49,55] as given in Eq. 2.6. Using this fact we can equate observation of the particle collection rates well away from the cross-over frequency and at a single conductivity medium to the CM factor. To improve measurement accuracy a further step can be taken, that of using pulsed DEP. Pulsed DEP involves the DEP force being switched

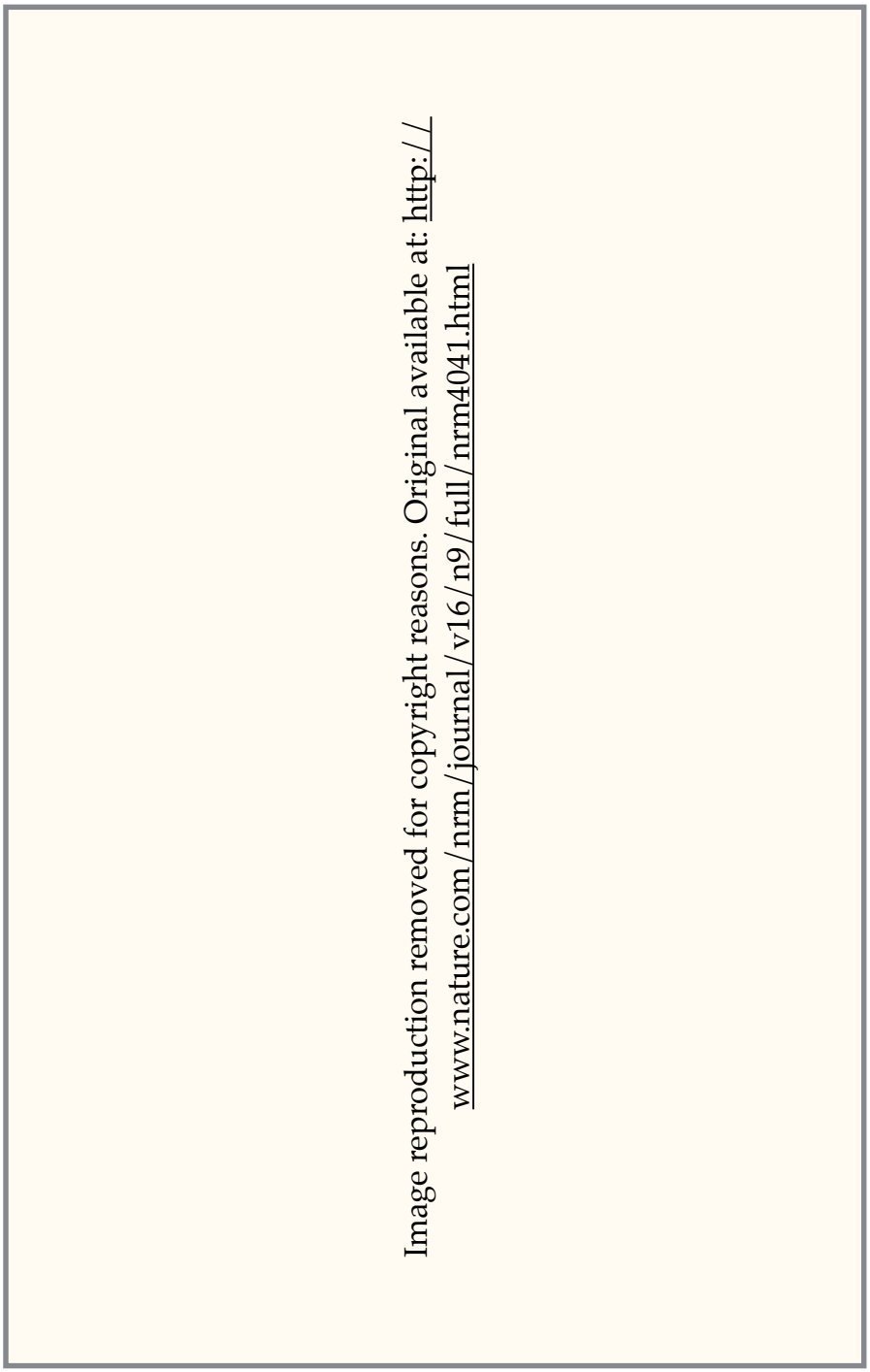

Figure 2.3: Key microfluidic developments and applications in the life science / biosensing area, figure reproduced from Duncombe et al. [48]

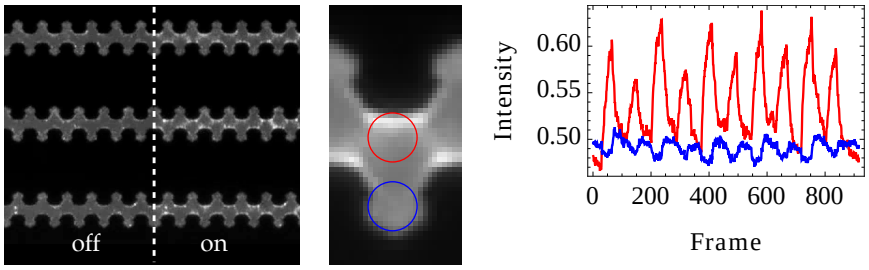

(a) (b) (c)

Figure 2.4: Standard DEP experiment a) shows typical frame images of fluorescent nanoparticles with pDEP off (left) and on (right). The dark regions are the castellated electrodes. During the 'on' state an AC signal is applied causing the fluorescently labelled nanoparticles to collect at the regions of high electric field. b) shows the total unit cell, that is to say a composite image that is the addition of all the repeating unit cells, normalised for observation. The red and blue circles indicate spatially isolated regions of high and low electric field, and the correspondingly coloured traces in c) show the change in mean pixel intensity for these regions as a function of time.

on (i.e the RF signal being applied to the electrodes) for a limited time then switched off, with a continuous repetition of these states. As illustrated in Figure 2.4 a), during DEP 'off', nanoparticles diffuse randomly so that their distribution within a confined chamber volume becomes uniform. When pDEP is switched 'on' (collection phase) the pDEP forces result in nanoparticles moving towards the regions of high electric fields. A single cycle typically comprises a collection phase (pDEP'on') followed by a release phase (pDEP switched 'off'). The collection rate is then estimated by fitting the initial slope of these collection phases to multiple cycles.

Pulsed DEP has been used to characterize the electrical properties of cells and their constituents, e.g. DNA, RNA, viruses, and colloidal bioparticles[38,49,43], whereby initial collection rates were measured and fitted to the real part of CM. A newly developed improvement on traditional pulsed DEP is is dual-cycle continuously pulsed DEP[47]. In this scheme two frequencies are used, the first collection phase frequency acts as a reference, while the second collection phase frequency acts as a probe. By maintaining a constant reference frequency, and varying the probe frequency one can measure the collection rate ratio as a function of frequency. By fitting these collection ratios to the

CM function and using the values for medium conductivity one can extract the values for the nanoparticle conductivity.

Cross-over experiments typically rely on the user to judge the frequency at which the cross-over occurs, collection rate measurements however require a quantitative measure of the collection rate of target particles. To do this collection rate measurements typically involve using fluorescently labelled particles and post-processing videos recorded with a fluorescence microscope. Post-processing the videos to extract quantitative information is not always trivial, here I describe and compare conventional methods and a novel approach I have developed.

2.2 IMAGE PROCESSING FOR DEP EXPERIMENTS

To calculate the collection rates it is necessary to estimate the concentration of the target particles in the regions close to the electrodes as a function of time. To do this it is common to fluorescently label the target particles and record or observe the activity using a fluorescence microscope. The fluorescence intensity at a given point is assumed to be proportional to the concentration of target particles. While at particularly high concentrations this assumption may not hold, such concentrations are not used in this work. There may also be erroneous contributions from particles above and below the focal plane of the image, but ultimately as we are interested in collection rates, that is the change in concentration with respect to time, rather than absolute concentrations these effects should not be problematic.

The simplest measure of nanoparticle collection is the evaluation of the mean intensity of the entire frame, this quantifies the total flux of particles into the focal plane of the image. Above the plane of the electrodes the pDEP force is predominantly down into their plane, as can be seen in Figure 2.2, so this could a be a feasible approach. What is found though is that the results of this approach are often noisy and unsatisfactory so instead it is desirable to restrict the measurement of collection rates to a region of interest (ROI), typically the regions of high electric field, where the collection signal is clearest (for example the red circle in Figure 2.4). Previous work has used a combination of electric field simulations and feature recognition to spatially extract these regions[49]. The definition, and automatic extraction of these

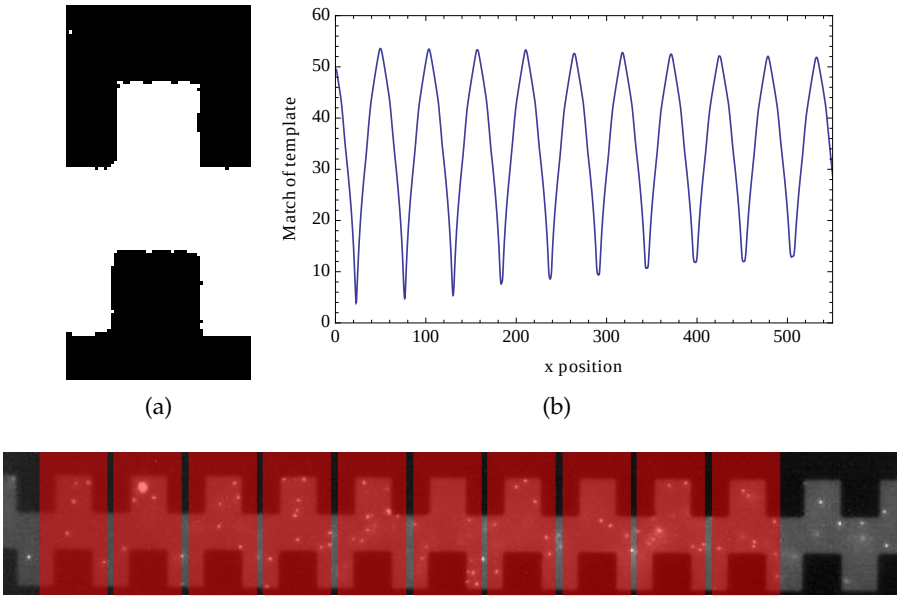

(a) (b)

(c)

Figure 2.5: Traditional spatial filtering implemented in Mathematica. a) A single unit cell is isolated and filtered to produce a template. b-c) Template matching, the measurement of distance (in this case Euclidean) between the template and image location, provides the location of all other unit cells, seen as the minima in c), and red overlays in c). This is a simple approach to identifying the unit cells of the electrodes across the image frame, more complex approaches can include extracting the spatial frequency of the features using Fourier methods, edge detection and morphological analysis.

regions, referred to here as spatial filtering, from recorded or live videos can however be a challenging.

2.2.1 *Spatial Filtering*

While the manual selection of the regions of interest (ROI) can be straight forward for single electrode pairs, the frequently used periodic arrays of repeating electrode geometries demand automated processing. Typically this processing involves two steps, first the repeated unit cell of the electrodes must be identified and located across the entire image. There are a various approaches to this image partitioning, including but not restricted to edge detection, feature recognition, template matching and Fourier analysis. In our case we used template matching, using a euclidean distance measure from a template (unit

cell filtered to remove fine detail) to the different locations in the main image (also filtered to remove fine detail).. Once the image has been partitioned it can then be spatially averaged over the periodically repeating (10's - 100's) unit cell of the electrode array. The approach employed here is a combination of manual selection and template matching. Figure 2.5 shows a unit cell (a) manually selected by the user, followed by the automated partitioning and localisation of each unit cell in the image (b-c), giving us pixel intensity, which is proportional to particle concentration, as a function of position over the entire unit cell, averaged across every unit cell repetition, as shown in Figure 2.6 a) and b).

The second step uses the information from the first step and involves defining a ROI, typically covering the region where particle collection is greatest, in the averaged unit cell. The mean pixel intensity for the ROI is evaluated for each frame of the video, providing a measure of the concentration within the ROI as a function of time.

Spatial filtering offers a direct and intuitive approach to the measurement of collection rates. The drawbacks of spatial filtering are the complexity of the image processing quantification, the introduction of uncertainties due to the specific choice of ROI and lack of robustness to changes in the experimental configuration. For example the movement of the microfluidic chip or camera may require a new round of processing, limiting ones ability to compare one video to the next and taking up valuable time. The algorithms used may also not work if the electrode geometry is changed, furthermore the complexity of the algorithms required often scale with the complexity of electrode geometry. Most significantly even with highly efficient algorithms live processing can be problematic delaying the feedback loop to the experimentalists by minutes if not hours.

2.2.2 *Statistical Filtering*

An alternative to separating each image into its spatial components is to consider the distribution of pixel intensities. Under DEP action regions of low electric field are depleted of particles, lowering their fluorescent intensity, and regions of high electric field collect particles therefore increasing their fluorescent intensity. The population of pixels with a given intensity should therefore be a measure of the state of the sample. Typical pixel intensity distributions (normalized frequency

histograms, made continuous by interpolation) for two frames, a frame during the collection period, 'on' state (blue) and during the off state (red) are plotted in Figure 2.6 c). Both distributions exhibit two modes, the left mode for intensities less than 0.15 represent the dark regions above the electrodes, and the right mode of moderately low intensities represents the fluorescence from the nanoparticle suspension. The high intensity tail corresponds to regions of high concentration, such as aggregations of particles. Comparing DEP 'on' (blue line) distribution in Figure 2.6 c) with the DEP 'off' (red) distribution distinguishes two important features. First, pixel populations near the right mode peak that indicate moderately low nanoparticle concentration decrease with the onset of pDEP. Second, pixel populations in the distribution tail, indicating high concentration, increase markedly with pDEP. These changes correlate to the depletion, and accumulation of particles in the regions of low and high electric field during pDEP. A statistical measure of this distribution sensitive to these changes should denote DEP activity. One such measure is the standard deviation of the pixel intensity distribution. This can be computed rapidly, in real time from acquired video data and requires no input from the user regarding electrode geometry.

2.3 EXPERIMENTAL METHODS

An arbitrary function generator (Tektronix AFG 3022B, OR, USA) was used to provide low voltage, square wave enveloped, sinusoidal signals applied to the electrodes with fixed control frequency (0.7 MHz) and variable probe frequency (100 kHz to 10 MHz). Equal dual-cycle periods, comprising 7 s signal on, 10 s signal off were applied and the ground-to-peak voltage, during the DEP collection phase, was 1 V for all experiments. Each experiment was video recorded with frame rate 10 frames/s. Collections for the first cycle were transient whereas the four remaining cycles exhibited cyclic steady state. Pulse duration, amplitude and applied frequencies were controlled by custom software written in LabVIEW 2011. Castellated geometry interdigitated microelectrode arrays with edge sizes of 5 µm were fabricated using lift-off techniques. A 100 nm thick layer of platinum was patterned on 500 µm pyrex wafers and the arrays were cut from the wafer and mounted on a PCB to allow robust electrical connection to the signal generator. A 3 mm internal diameter sample reservoir was fabricated

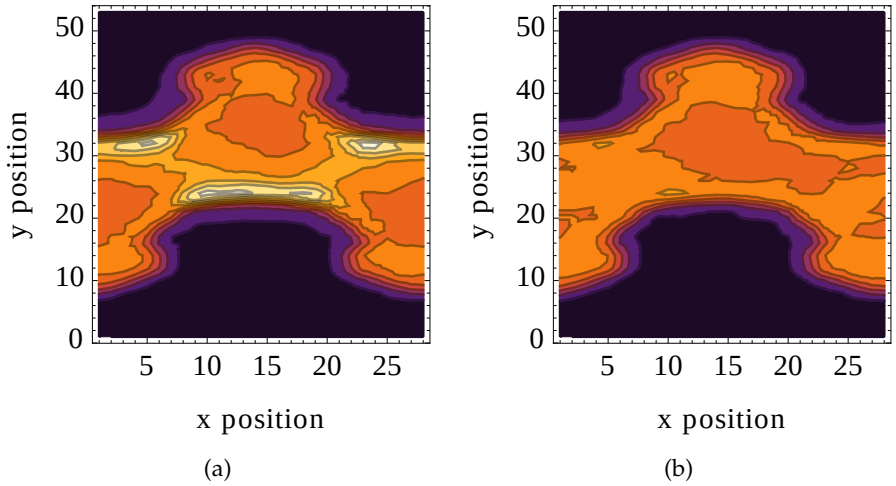

(a) (b)

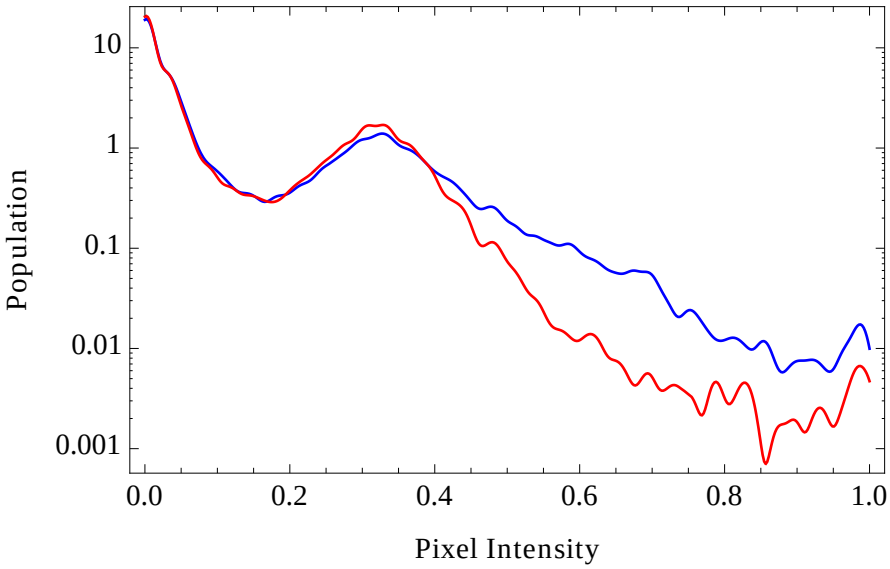

(c)

Figure 2.6: Spatial and statistical processing. a) and b) show spatial intensity distributions across the unit cell (averaged across the whole image). a) shows the distribution while the pDEP signal is applied, b) while it is not. c) shows the normalised pixel intensity distribution for on (blue) and off (red) states. Both approaches show clear differences between the off and on states, the pixel intensity distribution in c) however requires very little processing to extract from the image.

in poly-dimethylsiloxane (PDMS); the reservoir was bonded to the glass/electrodes using O2 plasma exposure. In each experiment a 50 µL aliquot of nanosphere suspension was pipetted into the PDMS reservoir on top of the device. A glass cover-slip was then used to prevent sample evaporation.

Carboxylate modified 200 nm diameter latex spheres (InvitrogenTM Molecular Probes, Eugene, OR) with yellow-green fluorescence (505/515 nm wavelength) were washed three times in KCl buffer ($2 \times 10^{-4}\,\mathrm{S\,m^{-1}}$) and suspended in the same buffer at a concentration of 5×10^{10} spheres/ml (diluted 1:100 from 2% w/v stock solution). The motion of the nanospheres was observed using an inverted microscope (Axiovert 200M, Zeiss, Germany) with epi-fluorescent illumination (HBO100, Zeiss), imaged with x40 objective and recorded with a digital camera (Thorlabs USB 2.0, Newton, NJ). Videos were analyzed using software written in Mathematica 8 (Wolfram Research, Champaign, IL) and Matlab 7.14 (Mathworks Inc., Natick, MA).

2.4 RESULTS

A comparison of the standard deviation frame intensity (statistical method), and mean of the ROI inter-electrode gap intensity (spatial method), for dual-cycle continuously pulsed DEP is shown in 2.7 a) and b) respectively. The control and probe frequencies were 0.7 MHz and 3 MHz, respectively; all other parameters are as described in the Experimental Methods section. The profiles show excellent correlation, i.e. notwithstanding differences in their scale and baseline, their time profiles closely agree, the correlation between the two traces being equal to 0.965 and the frequency spectrums overlapping as can be seen in Figure 2.8.

A further investigation used continuously pulsed dual-cycle DEP frequency collections with an 'on' control pulse set at 0.7 MHz and the probe frequencies spanning the range, 1–4 MHz. Time dependent collection profiles for each of the control and probe cycles were quantified by linear fitting of the first fourteen data points at the onset of each collection cycle. The initial collection rate ratio of the dual-cycle control and probe, for each experiment, was evaluated by dividing the probe rate by the control rate. Representative data involving quadruple replicates for each of the seven applied frequencies, was fitted to the real part of CM, with a curve shown in Figure 2.9 giving estimates of

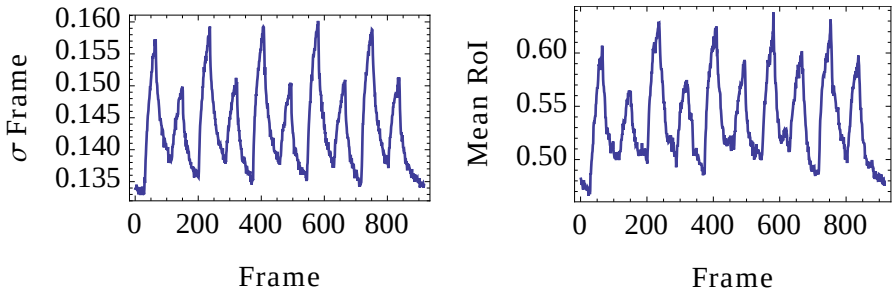

(a) (b)

Figure 2.7: Comparison of spatial results (a) and statistical results (b). Both traces clearly show a reference and probe collection cycle.

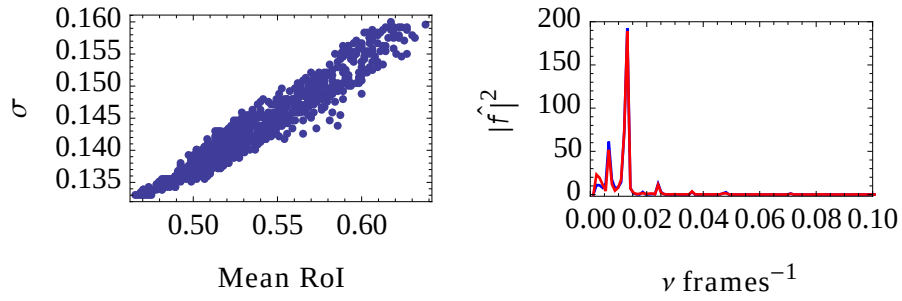

(a) (b)

Figure 2.8: Comparison of spatial results vs statistical results. a) shows the frame standard deviation vs the RoI mean. b) shows the Fourier transform of the standard deviation (blue) and the RoI mean (red). Both plots show the clear consistency between the two measures

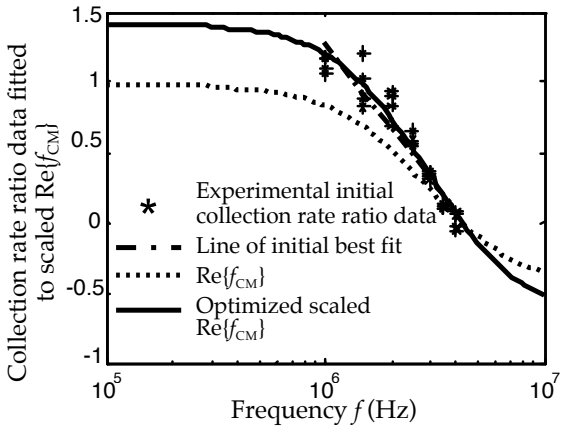

Figure 2.9: Fit of the real part of the Clausius-Mossotti factor which leads to estimates of nanoparticle conductivity and surface conductance.

the nanoparticle real part of CM magnitude scaling factor and conductivity σ_p . The CM values used in the calculation were $\sigma_m = 0.2\,\mathrm{mS\,m^{-1}}$ for the medium conductivity, and $\epsilon_m = 78.4$ and $\epsilon_p = 2.55$ for the medium and particle relative permittivity, respectively. The final estimate for the nanoparticle conductivity, was $\sigma_p = 25.8\,\mathrm{mS\,m^{-1}}$. Using the relation between the nanoparticle conductivity, its radius, bulk and surface conductivity, $\sigma_p = \sigma_b + 2\kappa_s/r$, and assuming $\sigma_b = 0$ and $r = 100\,\mathrm{nm}$, the estimate for the surface conductance was $\kappa_s = 1.29\,\mathrm{nS}$. The values for the nanoparticle conductivity and surface conductance concur closely with earlier work[47].

2.5 CONCLUSIONS AND FURTHER WORK

A novel, robust and easy-to-implement statistical filtering method is demonstrated for quantifying pDEP behaviour using video images of nanoparticles. The method does not require any input about electrode array geometry and allows accurate quantification of nanoparticle dynamics. The algorithmic and computational simplicity of method enables rapid, real-time, supervisor-free data processing; features that are useful to the experimentalist. The method is suitable for a range of investigations involving intricate and extensive electrode designs that would be much more difficult with conventional geometric filtering. Statistical filtering, using the standard deviation, is demonstrated to yield reliable and accurate differential collection rate measurements

that can be used for evaluating dielectric properties, such as, the nanoparticle conductivity and surface conductance. Statistical measures, such as the standard deviation are easy to implement, using software such as Matlab, Mathematica, or LabVIEW for live video processing, and require little programming experience.

We are pursuing further investigations into the application of statistic-based methods for quantifying and analysing nanoparticle dynamics. Figure 2.10 a) shows the pixel intensity populations as a function of frame normalised for each pixel intensity value, we can observe the pixel values that are insensitive to the DEP signal, those that are in phase and those that are out of phase with the DEP signal. These in and out of phase pixel values are correlate to the spatial regions that are have high and low electric fields, the regions that are populated or depopulated by the DEP signal, as can be seen in Figure 2.10 b). With the knowledge that certain processes correspond to certain pixel intensities, or range of intensities one can select the spatial areas and signals that correspond to these processes in a purely statistical way. This potentially opens the door to quantification of many different processes in a single image without the need for spatial identification, something that could be of great use in DEP experiments where rapid collection, diffusion and convective flux all seem to play a role, furthermore this approach may be useful for other techniques that rely on the observations of fluorescence signals.

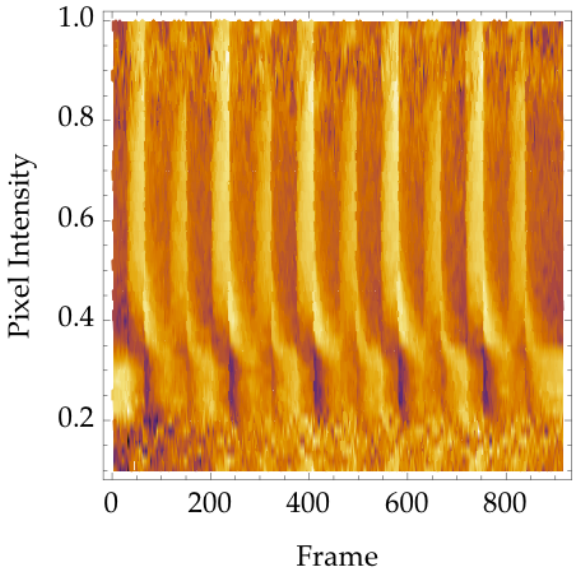

(a)

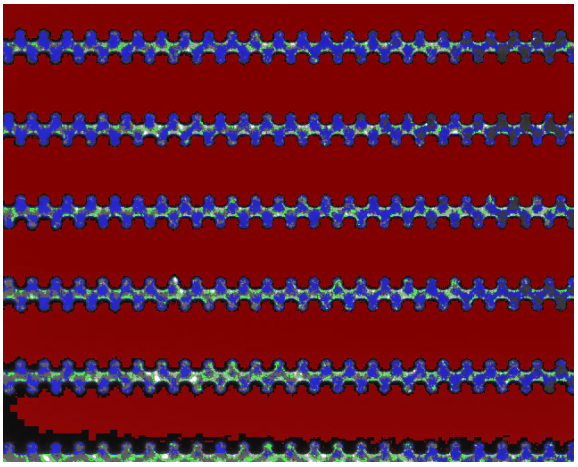

(b)

Figure 2.10: A plot of pixel values and populations as a function of frame, with each row (pixel value slice) normalised. b) Is an typical 'on' state image with regions highlighted by pixel value. Red equates to those pixels with intensity values equal to zero, blue 0.3 and green 0.5. It is clear that selecting regions by pixel value can accurately select the regions of interest.

3

TERAHERTZ METAMATERIALS

3.1 INTRODUCTION

Terahertz (THz) metamaterials consist of sub wavelength features that can be tuned to generate novel electrical and magnetic responses to THz electromagnetic radiation. While the precise definition varies from field to field, THz refers to electro-magnetic radiation with wavelengths roughly in the range of 0.1–1 mm, equivalent to 3–0.3 THz, and can be considered as the part of the electro-magnetic spectrum lying between the infrared and microwaves (see Figure 1.1), and thus between the traditional domains of optics and electronics. This location, with frequencies too high for conventional electronics and photon energies too low for conventional optics, makes it difficult to apply traditional electronic or optical techniques to the production and detection of THz radiation, something that has led to THz technology being comparatively underdeveloped. Despite this lack of exploitation there are many interesting physical processes involving or sensitive to THz photons and/or occurring on the time scale of the THz period leading to many exciting applications[61].

THz radiation probes the large amplitude vibrational, configurational and inter-molecular transitions of organic and biological molecules, this can provide information about configuration, hydration, structure and behaviour along with the possibility to identify molecules from their spectral features. In solid state physics there are also many physical processes that correlate to the low energies of the THz regime such as transitions among impurity states in semiconductors and intra-band transitions. More generally there is a high contrast between metallic, polar and non-polar materials in the THz range. Metals are extremely reflective while polar materials such as water are extremely absorptive and non polar materials such as fabrics and plastics largely transparent.[62]. These properties in combination with the fact that THz radiation is non-ionizing, and as such causes little or no damage to most tissues[63], has lead to many imaging applications[64]. THz imaging can be used to inspect goods and people

The work presented here was performed in collaboration with Yongzheng Wen and Xiaomei Yu of Peking University, and made possible due to a CoMPLEX study abroad grant which allowed me to spend 3 months visiting PKU. Wen designed and fabricated the devices. My own contribution was performing the measurements of the devices and assisting with the simulation and fabrication. Some of the figures and text in this section are edited extracts from the publications resulting from this work[57,58,59,60]

PROPERTY	RELATION	VALUE
Frequency	ν	1 THz = 1000 GHz
Angular Frequency	$\omega = 2\pi\nu$	6.28 rad / sec
Period	$\tau = 1/\nu$	1 ps
Wavelength	$\lambda = c/\nu$	0.3 mm = 300 µm
Wavenumber	$\bar{k} = k/2\pi = 1/\lambda = \nu/c$	33.3 cm^{-1}
Photon Energy	$E = h\nu = \hbar\omega$	4.14 meV
Temperature	$T = h\nu/k_B$	48 K

Table 3.1: Comparable measures of THz frequency

for concealed weapons as well as specific explosives from their spectral features.[65,66] Imaging has also been shown to detect cancerous tissue.[67] A significant hurdle to such applications is however the availability of cheap detectors.

3.1.1 *THz technology in the life sciences*

Although traditionally THz science and technology has been the preserve of space sciences, molecular spectroscopy and solid state physics the recent interest in THz, and accompanying developments that have increased accessibility have lead to many applications beyond these fields. One area rapidly growing is in biology and medicine. This broadly falls into two categories, imaging and sensing.

Due to the non-ionizing nature of THz radiation it can probe tissue without damaging it. The exceptionally high absorption of at THz frequencies of polar liquids like water make imaging at any substantial (>1 mm) thickness impossible. This high absorption can, however, also be utilised however to examine the water take up or density in tissue[64]. This has lead to studies of tissue burns and commercial applications for detecting epithelial cancer (TeraView Ltd. Cambridge UK).

Sensing with THz technology is exciting due to the ability to sense not only presence of a target but properties such as hydration, configuration, and binding process through spectroscopic fingerprints. This has been applied to detect DNA, along with single base muta-

tions. Approaches have included fee-space, waveguide and on-chip resonator techniques[68,69,61]. Other applications have included observing the label-free observation of biotin with avidin binding events using time domain measurements[70]. What should be said however is much of this work is at a very exploratory phase, and the ability to differentiate the broad resonances due to biological processes that occur at these wavelengths from instrumentation and sample errors make it challenging.

The work here will present a number of novel absorbers that will aid in the development of effective THz detectors, a key capability for THz imaging. The development of detectors with tunable wavelength sensitivity will help lead to devices with improved signal to noise for key spectroscopic signals, such as those outlined above.

3.1.2 *THz Detectors*

THz detectors can be broadly classified into coherent and incoherent types, the difference being that the former measures the phase and amplitude of the field whereas the latter simply measures intensity. Coherent detectors use a host of devices and techniques, nonlinear crystals, photoconductive antennas and diodes to perform optical probe sampling, photomixing and heterodyne detection. The focus of this work is however absorbers for incoherent detectors. Incoherent detectors also work in a variety of ways but almost universally rely on a change in temperature due to absorbed radiation causing a measurable pertubation to the readout system. Two common approaches are microbolometers[71] and bi-material micro-cantilever technology[72]. Both of these methods sense the THz wave by transforming the radiation energy to heat within the sensing element, changing the resistance of the microbolometer or deforming the cantilevers bi-material structure. The main limitation of these approaches is the combination of low radiation energy absorbed by the detectors and relatively low output power of most THz sources. In this work we develop metamaterials primarily for enhancing and tuning THz absorption, in particular for use with bimaterial cantilever focal plane array (FPA) detectors.

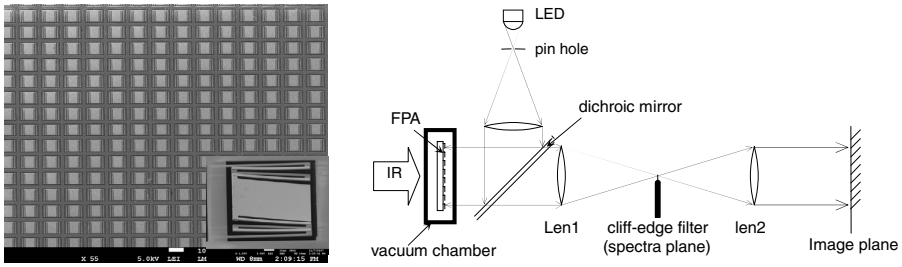

(a) (b)

Figure 3.1: IR Focal plane array detectors a) SEM image of array and individual MEMS detector pixel. Each pixel contains a bimaterial cantilever which heats up as it absorbs the incident radiation. This heating causes a deformation of the element. b) optical measurement of the detector, the backside of the FPA can imaged thus transforming the infrared image in to an optical one. Images from Yu et al. [73] at the Institue of Microelectronics, Peking University

3.1.3 *Metamaterial THz absorbers*

To improve the performance of detectors, materials with high THz absorption coefficient must be developed and incorporated into the existing platforms. It is difficult, however, to find naturally existing materials with strong absorption coefficients that are also compatible with standard micro-fabrication techniques. Recently, artificial metamaterials have attracted a great deal of research interest due to their ability to provide an enhanced and tunable electromagnetic response to THz radiation while also being readily integrable with existing detection platforms. Metamaterials (MMs) are materials designed and constructed to have properties not exhibited in naturally occurring materials. They are commonly made by using repeating cells, their bulk properties are a result of the geometry, composition and interaction of these sub-elements rather than the bulk characteristic of the materials they are composed of, for optical MMs this means having features smaller than the wavelength of light they are designed to operate at[74]. Due to the comparatively long wavelength of THz radiation, MMs for the THz range can be made relatively easily with standard photolithography.

The devices discussed here are often referred to as frequency selective surfaces (FSS), they are in effect two dimensional MMs in that they consist of repeating unit cells across a plane. While not in the exotic category of left-handed materials they are an important

application of MM theory, namely to create structures with large imaginary components of ϵ for the THz region, a property lacking in many machinable natural materials. In addition to being absorptive in regions uncommon in natural materials further properties can be intentionally designed to match the intended applications. This section will discuss the design, fabrication and measurement of a number of devices. The devices examined are polarisation independent absorbers with dual band absorption resonances, broadband absorbers that use nested structures, broadband absorbers that use asymmetries and finally mechanisms for tuning the absorption. The overall strategy and material choices for our devices are discussed first, this is followed by FDTD simulations to design optimal structures, the experimental methods, results and outcomes.

3.2 DEVICE OVERVIEW

All the devices share a metal/dielectric spacer/metal (MDM) sandwich structure, this is an extremely common approach due the ease with which it can be fabricated and incorporated with existing THz detector devices. The top layer is a periodically patterned metallic sub-wavelength structure that serves as an electric resonator. The bottom layer is generally a thick metal ground plane that significantly reduces transmittance. The coupling between these two metallic layers results in magnetic resonance depending on the thickness and dielectric constant of the dielectric layer[75]. The desired properties, such as absorption, acceptance angle, bandwidth and polarization-dependence, can be achieved by modifying the size and shape of the sub-wavelength structure in combination with the the ground plane and spacer properties. Along with the standard gold layer ground plane, ground planes made of metal silicide, such as cobalt silicide (Co-Si), have been investigated. Co-Si has a high conductivity and melting point and is also commonly used in complementary metal oxide semiconductor (CMOS) processes.

A common limiting factor on the performance of THz MM's are the dielectric spacers, which are often polyimide or silicon dioxide (SiO_2). Due to the spin coating process of polyimide, it is difficult to control the thickness precisely, something vital to device performance. Although SiO_2 can be deposited for well-controlled thicknesses, it is mainly used in thin or ultrathin MM absorbers because of the

difficulty of depositing a thicker film. In addition to this limitation the Young's Modulus of SiO_2 is much higher than that of a polymer, making it impossible for SiO_2 to be used for flexible structures[76]. To address the requirements of both accurate control of layer thickness and a highly flexible structure, parylene-C is used as the dielectric spacer. Parylene-C is a widely used polymer with great flexibility and biocompatibility and its thickness can be precisely controlled in the course of chemical vapour deposition (CVD), its dielectric properties ($\epsilon = 3.15$) are comparable to that of silicon dioxide ($\epsilon = 3.9$).

3.2.1 *Polarization-independent dual-band absorber*

A dual-band THz metamaterial absorber (MMA) was developed. The top periodic metal pattern in the MMA structure was designed with a cross resonator surrounded by a square ring resonator, the schematic view and microscope image of which are shown in Figure 3.2. The structure exhibits two distinct absorption bands due to the strong resonances, which can be configured separately. Moreover, due to the symmetrical structure in the unit cell the resonances are insensitive to the polarization of the incident THz wave[77,78]. In order to verify the independence of the two absorption peaks, single square ring and cross structures with the same dimensions as the dual-band absorber were also designed and processed at the same time.

3.2.2 *Broadband absorber using nested resonators*

Most MMAs exhibit a narrowband EM response due to the resonant nature of the metamaterial response. Although dual-band and triple-band MMAs have been demonstrated with distinct narrow absorption frequencies[79,80], the development of broadband MMAs with high absorption remains challenging. A vertically stacked multilayer MMA proposed by Grant et al. [81] achieved more than 0.6 absorptivity with a bandwidth of 1.86 THz, where the central resonant frequency is 5 THz. Vertical stacking structures are, however, complicated to fabricate, which limit their applications. Instead a broadband MMA with nested back-to-back split ring resonators (BSRRs) was designed in one unit cell using cobalt silicide (CoSi) film as the ground plane and parylene-C as the dielectric spacer. The single resonator exhibits three strong inductance-capacitance (LC) resonances with two of them

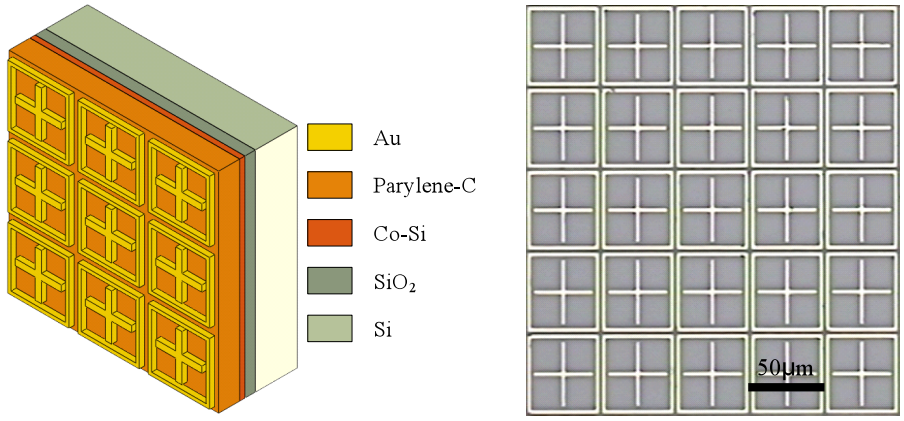

Figure 3.2: Device schematic for dual band polarization independent absorber. A cross-square resonator provides the dual band polarization insensitive resonances, the dielectric spacer and ground plane contribute to the magnetic component of resonances and prevent transmission. a) shows the structure of the devices b) is an optical microscope image of the fabricated device

close enough to realize a broad absorption band at THz regime. The schematic diagram of the broadband MMA is shown in Figure 3.3. The resonator comprises two BSRRs sharing the same center bar, and the inner BSRR is symmetrically nested in the outer one.

3.2.3 *Broadband absorber using asymmetric resonators*

Although the nested approach can produce multiple resonances, the extent to which structures of different sizes can be combined or nested is restricted by the frequencies one wishes to work with and the ability to fabricate fine structures. An alternative to using separate or nested resonators is to use asymmetric resonators. By breaking the symmetry of a split ring resonator, two asymmetric resonances are excited. The effect of breaking the symmetry of a split ring resonator (schematic shown in Figure 3.4) and nesting different asymmetric resonators (ASR) was investigated to combine both the nesting and symmetry breaking effects to achieve a near perfect absorption over a wide frequency range.

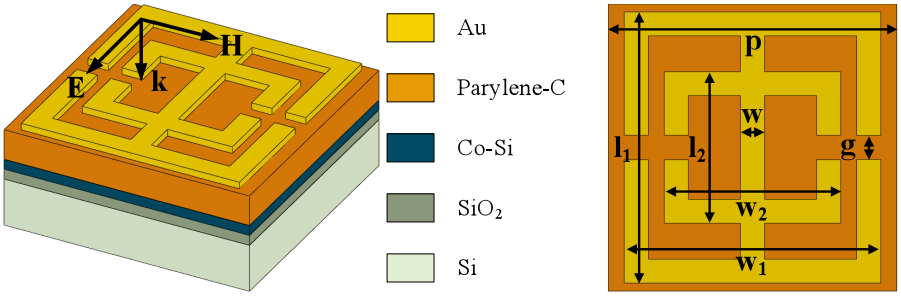

(a) (b)

Figure 3.3: Device schematic for nested resonators. Two backside split ring resonators (BSRR) share a central bar, the geometric parameters are optimised through FDTD simulations to provide a high absorption broadband response.

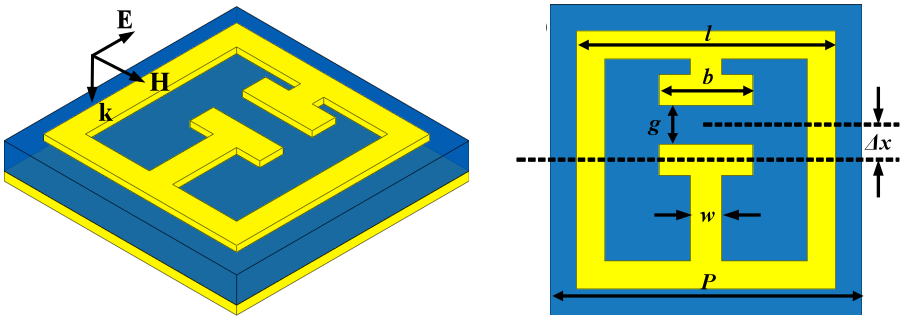

(a) (b)

Figure 3.4: Device schematic for asymmetric resonators. The gap between the two bars acts like a capacitor with the square comparable to an induction loop generating an LC like resonance. The higher order dipole like resonances are perturbed by introducing an asymmetry in the gap position determined by Δx.

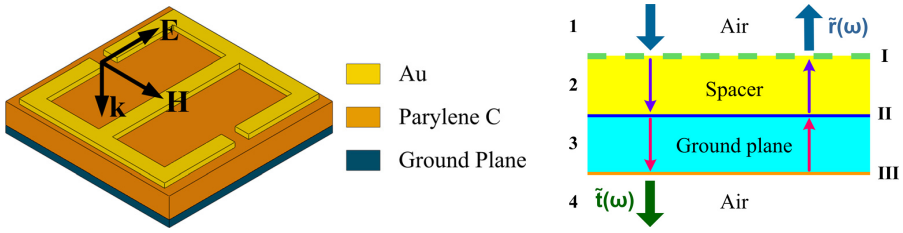

(a) (b)

Figure 3.5: Device schematic for varying the ground plane to tune absorptions. A single back side split ring resonator (BSRR) with a ground plane of varying conductivity. A multiple layer reflectance/transmission model has been used to calculate the absorption.

3.2.4 *Tunable Metamaterial Structures*

Aside from the geometrical properties of the resonator and thickness of the dielectric spacer another property which can modify MMA performance is the conductivity of the ground plane, the normally metallic film that lays below the resonator and dielectric plane. The conductivity can be tuned by using different materials for the ground plane, such as the silicides employed, but also by changing the temperature of the MMA. Investigating the effect of changing the conductivity of the ground plane potentially opens up a new mechanism to adapt MMA devices and also actively tune them post-fabrication. Simple back to back split ring resonators (BSRR) with cobalt-silicide ground planes (see Figure 3.5) were compared to those with gold ground planes.

In addition to tuning the performance of the the devices the modelling of the MMA was decoupled into two parts: the metamaterial, composed of metal resonator and dielectric spacer,which responds to the incident EM wave, and the metal ground plane functions as a reflector[82,83].

3.3 SIMULATIONS

The absorbers were modelled using commercially available finite-difference time-domain (FDTD) software (CST Microwave Studio). This was done to optimise the geometric parameters of the structures, explore the mechanisms of resonance and compare with the experimental results. The simulation parameters where as follows: the

ground plane is 100 nm thick with a conductivity of $8.3 \times 10^5\,\mathrm{S\,m^{-1}}$ for the Co-Si case and $4.09 \times 10^7\,\mathrm{S\,m^{-1}}$ for Au, the parylene-C spacer were modelled with thickness of 2 , 6 and 10 µm depending on device with a dielectric permittivity of 2.62 , and loss tangent of 0.005 The resonator motifs are gold with a conductivity of $4.09 \times 10^7\,\mathrm{S\,m^{-1}}$ and a thickness of 100 nm. The incident source is assumed to be normal to the surface and the transmission of the ground plane to be zero, simplifying the equation for the absorption to $A = 1 - R$. The simulation results for each type of device are discussed below.

3.3.1 *Polarization-independent dual-band absorber*

Figure 3.6 shows the simulated spectrum for the polarization independent dual band absorber, revealing two distinct peaks at 0.84 THz and 2.26 THz for the 6 µm parylene-C spacer. Using the same lattice constant (50 µm) and parylene-C thickness 6 µm the single resonator components, the square ring and cross absorbers, were also simulated individually. Both the square ring and cross absorbers have a single absorption peak, located at 0.84 for the square and 2.35 THz for the cross, as indicated in Figure 3.6. The peak strengths and positions for the single resonance frequency structures are almost the same as those for the dual-band structure, demonstrating that the two absorption peaks in the dual-band absorber are contributed by the square rings and crosses largely independently. There is a 0.09 THz difference in the second peak, likely due to the loading effect when both resonators are combined together[84]. The magnitude of absorption is tuned by modifying the thickness of the parylene-C spacer, as shown in Figure 3.6. Both peaks achieve near unity absorption for the structure with a thickness of 6 µm. The simulations demonstrate the device to be a dual band absorber with nearly independent absorption peaks deriving from the cross and square motifs.

3.3.2 *Broadband absorber using nested resonators*

The simulated transmission spectrum of the nested BSRR MMA for light polarized with the electric field lines crossing the gaps (as shown in Figure 3.3) with dielectric layer thickness of 9.3 µm is plotted in Figure 3.7. The simulation show that the transmittance is less than 0.01 from 0–4 THz when using 100 nm Co-Si film as the ground plane,

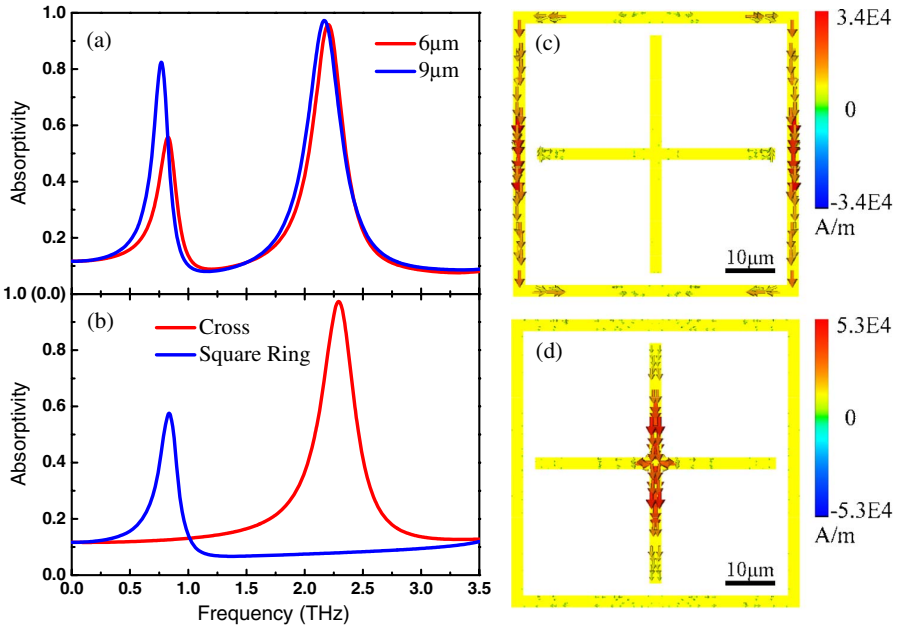

Figure 3.6: Simulated absorption spectra of dual-band absorbers with 6 µm and 9 µm of the parylene-C spacer, (b) Simulated absorption spectra of two single band absorbers for 6 µm parylene-C spacer, (c) Simulated surface current density at 0.84 THz, (d) Simulated surface current density at 2.26 THz.

justifying the simplification of the absorption calculation to A =1-R. In the absorption spectra three resonance peaks at 0.89 THz, 2.45 THz and 2.87 THz are observed with the absorptivity of 0.90 , 0.99 and 0.98 respectively. Due to their close proximity and relatively low Q factors, the resonant peaks at 2.45 THz and 2.87 THz overlap considerably to form a single broad absorption band. For the merged absorption band, the bandwidth is 1.23 THz for absorptivity beyond 0.6 , and it is 0.89 THz for absorptivity higher than 0.8 Taking the central frequency of the broadband resonance as 2.66 THz, the full width at half-maximum (FWHM) of the broadband absorption is 55%, and the Q factor is 1.82

For comparison, the single BSRR MMA were simulated for identical geometric parameters as the outer BSRR of the nested resonator MMA, including the thickness of the dielectric layer and the lattice constant. As shown in Figure 3.7, there are two resonance peaks in the absorption spectrum of the single BSRR MMA with the absorptivity of 0.82 at 0.89 THz and 0.73 at 2.60 THz. The FWHM of the two peaks are 24% and 38%, and their Q factors are 4.2 and 2.63 respectively. It can be seen that there is no absorption above 0.8 and the bandwidth is

0.46 THz for absorptivity beyond 0.6 at the dipole resonance which is only 37% of that of the combined band in the nested BSRR MMA.

The simulated surface currents distributions of the nested resonator at three resonance peaks are also shown in Figure 3.7. It can be seen that the surface currents at the 0.89 THz resonance, which is common to both the single and nested resonators, occur mainly along the central bar and outer ring. The 2.45 THz resonance has currents in both the inner and outer rings, suggesting it comes from the interplay of the two elements, the 2.87 THz resonance is mainly confined to the inner BSRR. The single nested resonator realizes three BSRRs in total which produces three resonances with the overlapping resonant peaks of 2.45 THz and 2.87 THz leading to broadband absorption in that region.

3.3.3 *Broadband absorber using asymmetric resonators*

As for the other structures, numerical simulations were performed to ascertain optimal geometric parameters and aid the understanding of the nature of the resonances. The simulations were performed under normal incidence with the polarization aligned across the gap, as shown in Figure 3.4 a). These devices were fabricated using SiO_2 for the dielectric spacer and as such the simulations employed a relative dielectric constant of $\epsilon = 3.9$ and loss tangent $\delta = 0.025$, the layer has thickness of 3 µm. The other components (Au resonator and ground plane) share the same material parameters as the other devices and simulations. The offset of the gap from the centre of the outer ring (shown in Figure 3.4 b), Δx is the parameter that measures the asymmetry, it is varied from 0 , at which point the device is symmetric, to 1.2 µm.

The simulated absorption spectrum of the symmetric SRR MMA with $\Delta x = 0$ µm is shown in Figure 3.8. Two resonances are found, with an absorptivity of 0.96 at 2.30 THz and 0.72 at 4.90 THz, the full width at half maximum (FWHM) for the two peaks are 8.5% and 19.3% corresponding to the Q factors of 11.76 and 5.18 respectively. The ASR MMAs are simulated for $\Delta x = 0.2$ µm, 0.5 µm, 0.9 µm and 1.2 µm, the simulated absorption spectra are also plotted in Figure 3.8. Although the resonators are asymmetric, the absorptivity and resonant frequency of low frequency peak are unaffected by the asymmetry. The higher frequency dipole resonance however increases in height

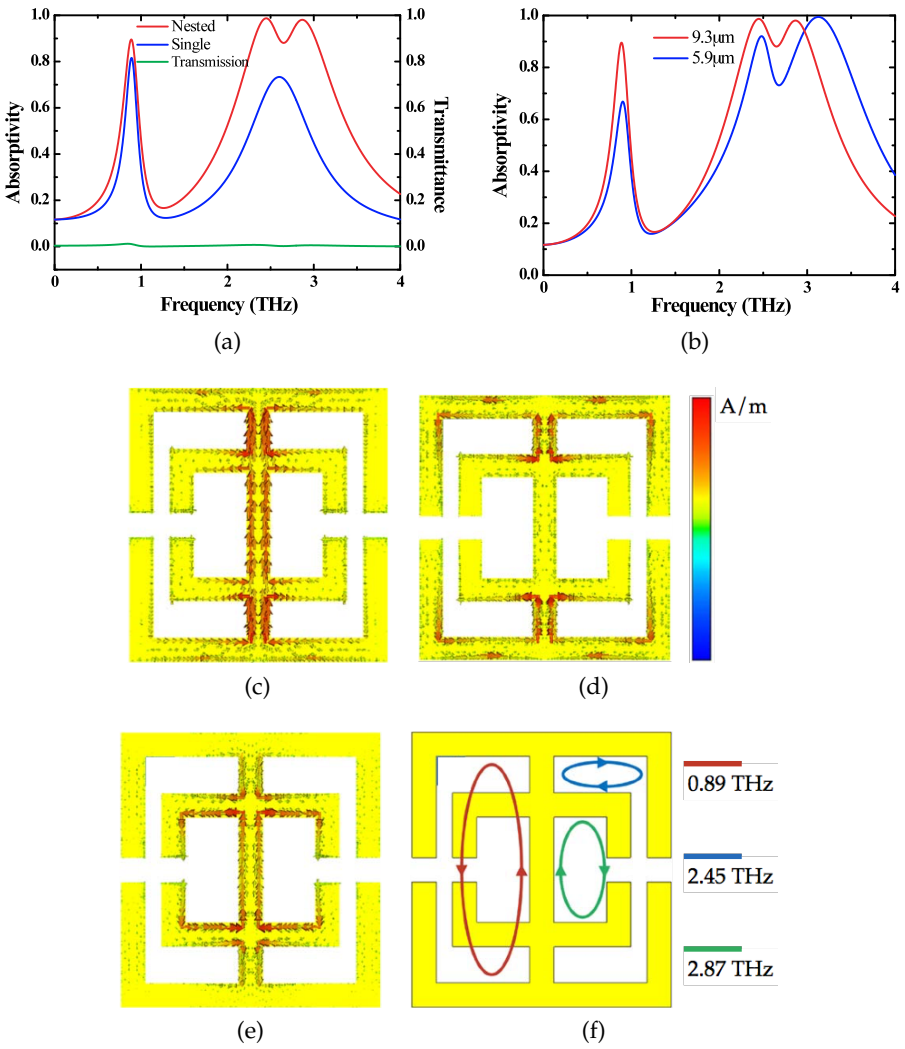

Figure 3.7: Simulations of nested resonators a) Shows the Transmission (green) and absorption of a single and nested resonator (blue and red respectively). b) shows the absorption for nested resonators with dielectric space thickness 9.3 µm and 5.9 µm. c),d) and e) show the surface currents in the resonator motifs for the 0.89 THz, 2.45 THz and 2.87 THz resonances respectively. f) schematics of the the current loops for all three resonances.

and width from 0–0.5 µm and then splits into two peaks for the larger Δx. For the maximum simulated Δx of 1.2µm, two obvious peaks at 4.42 THz and at 5.30 THz are shown with the absorptivity of 0.97 and 0.94 respectively. The resonances are also narrower with the Q factor of 8.47 and 7.35 respectively.

In order to understand the nature of resonances the surface currents for the symmetric SRR and the ASR of Δx=1.2µm were simulated. The surface currents density distributions at 2.30 THz, 4.90 THz for the symmetric device are shown in Figure 3.8 c) and d). The split dipole resonance for the asymmetric case at 4.42 THz and 5.30 THz in Figure 3.8 e) and f). We identify the resonance at 2.30 THz as the LC mode from the circulating surface currents and the fact it doesn't change as the symmetry is broken. Which is consistent with the fact that the effective the inductance paths and capacitance also remain unchanged as the asymmetry is introduced. The resonance at 4.90 THz is generated by the symmetric in-phase currents in the both short bars at the center, which is the dipole mode resonance[76]. By breaking the symmetry of the SRR, however, the asymmetric resonances at 4.42 THz and 5.30 THz are trapped in the longer and shorter central bars, as shown by the surface currents plotted in Figure 3.8 e) and f). Although the in-phase currents show that the two asymmetric peaks are also dipole-like resonances, the surface currents densities are both larger than that of the dipole resonance at 4.90 THz. The two bars with different lengths produce the two divided peaks at lower and higher frequencies. More importantly, due to the asymmetry, trapped mode responses are excited. This mode is normally suppressed in symmetric SRR, but can be excited if the resonator has asymmetry. At the trapped mode resonance, the structure is coupled to free space weakly and the strength of the induced currents reaches high values. As a consequence, both the sharpness and the absorptivity of the peaks increases[85].

To incorporate the advantages of both the asymmetric resonance splitting and enhancement with the broadband performance observed for the nested structures described in the previous section the ASRs with $\Delta x = 0.2\,\mu m$, $0.5\,\mu m$, $0.9\,\mu m$ and $1.2\,\mu m$ were combined into one unit cell. The other geometric parameters are kept the same, including the gap and line length, and the lattice constant of the wideband unit cell is 40 µm. The simulated absorption spectrum plotted in Figure 3.8 b) possesses two peaks: one narrow band peak at 2.30 THz with an

absorptivity of 0.96 , and second wideband peak at the central frequency of 4.82 THz with a maximum absorptivity of 0.99 Compared with the dipole resonance at 4.90 THz of the MMA with the symmetric SRR, the absorptivity of the wideband sample has increased 37.5% from 0.72 to 0.99 In fact, even if with a very strict criterion of the absorptivity being greater than 0.9 , the bandwidth of the wideband MMA achieves 0.85 THz. The wideband resonance approaches a flat band absorption with only three small dips at the absorption band, and a lowest absorptivity of more than 0.93 Although the bandwidth with high absorption is wide, the FWHM of wideband peak is only 26.7%, which is comparable to that of the of dipole resonance and shows high steepness at the edges of the band, resulting in sharp rejection of out-of-band power. The steepness of the wideband peak edges results from the sharpness of the trapped mode resonances that it is formed of.

3.3.4 *Tunable Metamaterial Structures*

The simulations for the tunable metamaterial devices employed a different approach to the previous structures. Instead of using FDTD techniques for the entire structure, this technique was combined with a multi-layer reflection and transmission model. The typical metal resonator/dielectric spacer/ground plane structure of MMAs is modelled by considering the EM wave propagation as depicted in Figure 3.5. Including the air on both sides of the structure, there are four numbered zones and three interfaces in the decoupled model of MA. The normally incident EM wave from the front air region (zone 1) will propagate through the dielectric spacer (zone 2) and the ground plane (zone 3) successively until it reaches the back air region (zone 4). Transmission and reflection occurs at each interface. The reflection and transmission coefficients at interfaces II and III can be calculated from the permittivities of the dielectric layers and ground plane. At the interface I, the normally incident THz wave is partially reflected back to the air and transmitted into the spacer with the transmission and reflection coefficients for this case obtained from simulations.

The top row in Figure 3.9 shows the calculated reflection, transmission, and absorption spectra when decreasing the conductivities of the ground plane from 1.8×10^7–3×10^5 S/m. An electric resonance around 0.89 THz and a dipole resonance around 2.62 THz are pre-

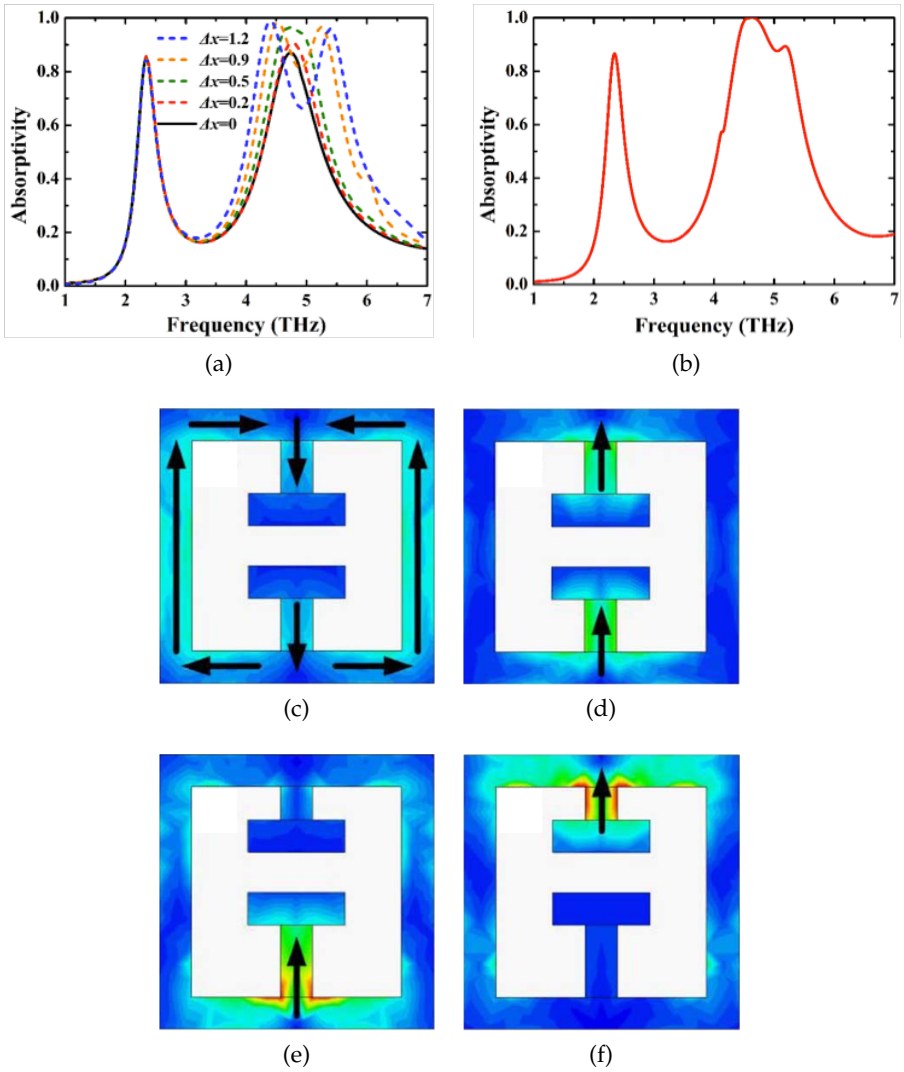

Figure 3.8: Simulations of asymmetric resonators. a) shows the simulated absorption spectrum of devices with varying Δx. The low frequency resonance at 2.30 THz is largely unaffected by the introduced asymmetry. For the higher frequency resonance, however, both a broadening and an increase in magnitude as Δx increases can be observed, until two clear resonance peaks are formed. b) shows the simulate absorption spectrum for the 'wideband cell', consisting of 4 asymmetric resonators with $\Delta x = 0.2\,\mu m$, $0.5\,\mu m$, $0.9\,\mu m$ and $1.2\,\mu m$ in a single unit. c) and d) show the simulated surface current density for the symmetric devices at the 2.30 THz and 4.90 THz resonances respectively. e) and f) show the higher frequency split resonances at 4.42 THz and 5.30 THz for the asymmetry device with Δx =1.2 µm

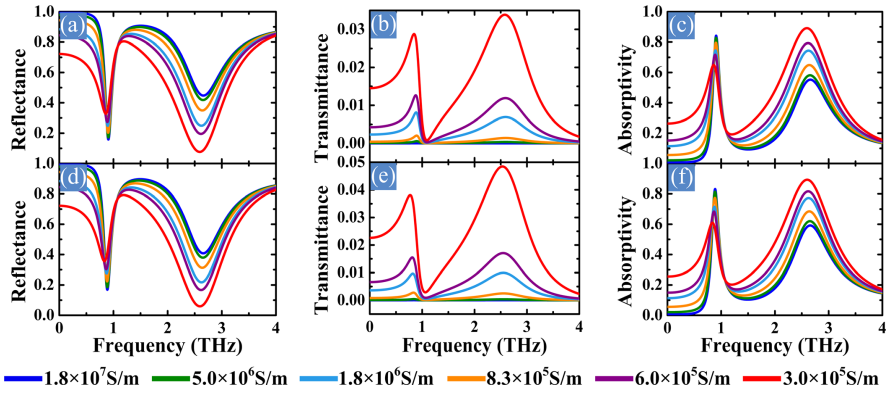

Figure 3.9: Calculation sand simulations of device performance for varying ground plane conductivity. Top row (a-c) calculated using the multi-layer model. Bottom row: (d-f) from full device FDTD simulations. Left a) and d) show reflectance, middle b) and e) show transmittance and right c) and f) show absorption spectra for varying ground lane conductivities.

sented in all spectra. It can be seen that as the conductivity decreases, the transmittance increases from 0 to 0.034 , and the absorptivity of the electric resonance decreases by 23% from 0.84 to 0.65 , while that of the dipole resonance increases by 62% from 0.55 to 0.89 In addition, the Q factors of the dipole peaks decrease from 2.7 to 2.1 , which means that the bandwidths of the absorption peaks increase by 22%. It is also noted from Figure 3.9 that both resonances shift slightly to lower frequency with the decrease of the conductivity. The same structure was also simulated with the FDTD software with the same parameters, and the simulated spectra are plotted in the bottom row of Figure 3.9. It can be seen that the simulated and calculated results are in excellent agreement.

3.4 FABRICATION

The samples where fabricated at Peking University using standard micro-fabrication techniques. The Co-Si ground planes were fabricated as follows: First a 200 nm thick SiO_2 film, which was used as the isolator for the Co-Si alloying process, was deposited on the 400 µm double polished Si substrate by low pressure chemical vapour deposition (LPCVD) processing. This was followed by a 100 nm LPCVD poly-Si film. For better Co-Si conductivity phosphorus ions were implanted into the poly-Si film and activated at 1000 °C for 30 minutes. After that,

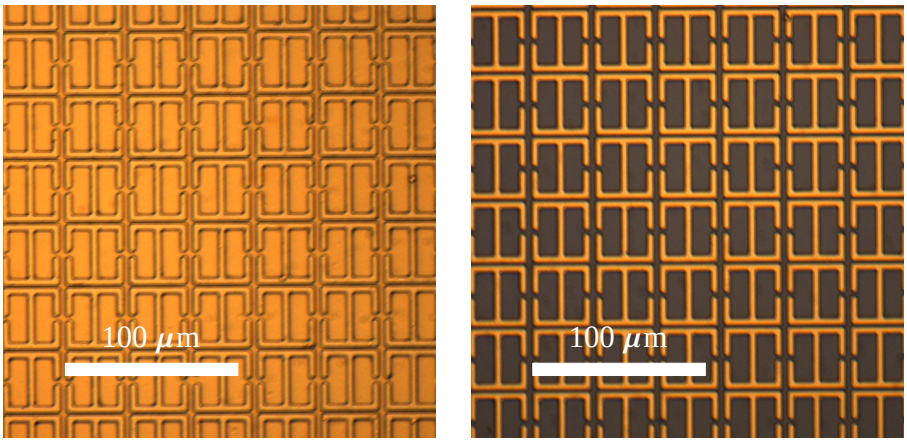

(a) (b)

Figure 3.10: Optical micrsocpe images of single BSSR with gold groundplane (left) and CoSi (right)

40 nm cobalt was deposited using sputtering. To form high quality Co-Si, a two-step rapid thermal process (RTP) was applied[86]. The first step was carried out at 600 °C for 1 minute, CoSi is formed at this step. After removing the unalloyed Co by a wet etch, the second RTP was at 850 °C for 1 minute. The final thickness of $CoSi_2$ was 100 nm. For the Au ground planes similar techniques were employed, after depositing the SiO_2 a 20 nm Cr adhesion layer followed by a 100 nm Au were sputtered. The parylene-C dielectric spacer layers were deposited on the ground planes using chemical vapour deposition (CVD) with vapour phase parylene-C monomer at room temperature and pressure of 22 mTorr. Finally for the resonator top layer, a 20 nm/100 nm Cr/Au pattern is produced by standard optical lithography and lift-off process. The thickness of the parylene C spacers were verified using a thin film reflectometry system with the conductivity of the Au and Co-Si layers measured using a four-probe meter, reading $1.8 \times 10^7\,\mathrm{S\,m^{-1}}$ and $8.3 \times 10^5\,\mathrm{S\,m^{-1}}$.

The polarisation insensitive dual band device was previously shown in Figure 3.2. The single and nested backside split ring resonators are shown in Shown in Figure 3.10 and 3.11 respectively, with both Au and Co-Si ground planes. The asymmetric resonators are shown in Figure 3.12.

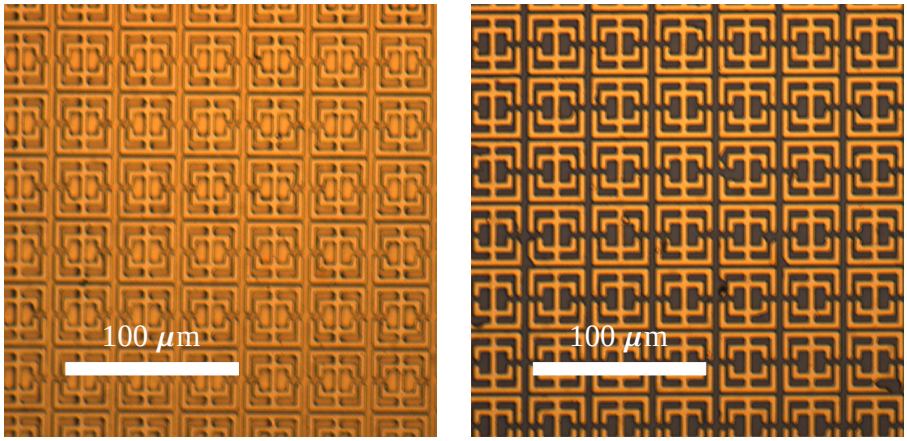

(a) (b)

Figure 3.11: Optical micrscope images of nested BSSR with gold groundplane (left) and CoSi (right)

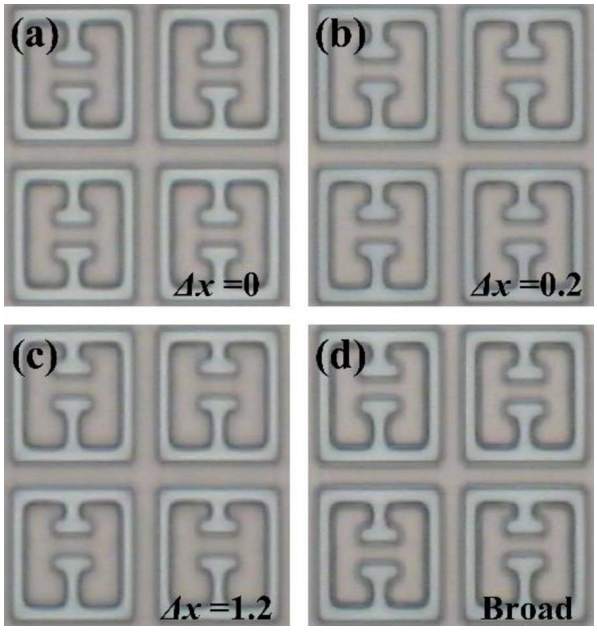

Figure 3.12: Fabricated asymmetric resonators with Δx equal to a) 0 µm, b) 0.2 µm, c) 1.2 µm. d) shows the 'broadband' device combing $\Delta x = 0.2$ µm, 0.5 µm, 0.9 µm and 1.2 µm resonators.

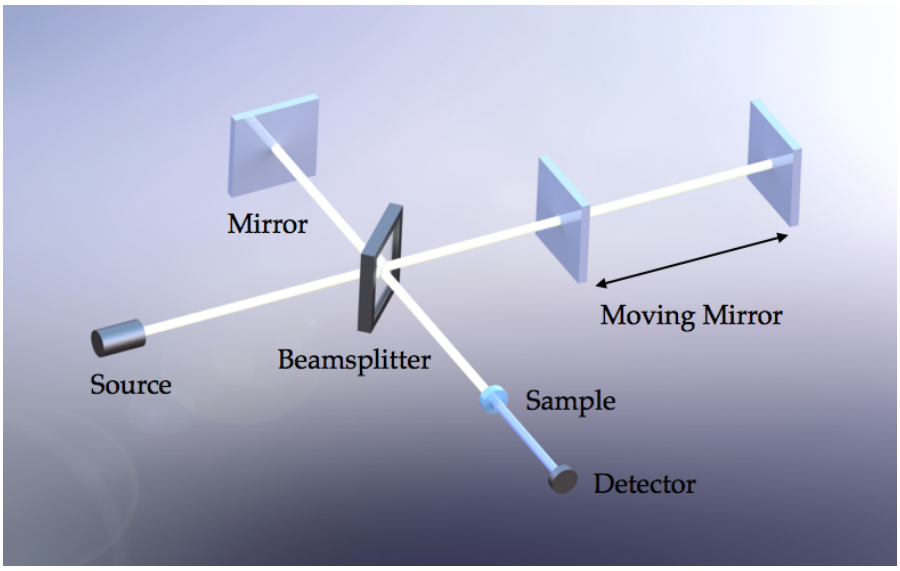

Figure 3.13: Schematic of standard Michelson interferometer type FTIR instrument. A broad band source is split into two paths by a beam splitter, one goes to a fixed mirror, the other to a scanning mirror, the difference in path length introduces a phase shift in the recombined beam which is then directed through or of a sample and into a detector. The intensity as a function of path difference is an interferogram which when Fourier transformed gives the spectrum.

3.5 MEASUREMENT

The fabricated absorbers were characterized using Fourier-transform infrared (FTIR) spectroscopy. FTIR spectroscopy uses a broad band source and detector, simultaneously collecting data over a broad spectral range. The spectral resolution is recovered by splitting the source and introducing a path difference into one of the paths. The measured intensity is then correlated to a path difference, this being the interferogram, which when Fourier transformed gives a spectrum. This is different to other spectroscopy techniques that use either a tunable source or collection window to obtain spectral resolution. The key components of the instrument are the source, the beam splitter and moving mirror which introduce the path difference, the sample holder and finally detector, a typical instrument schematic is shown in Figure 3.13.

The FTIR used was a Bruker IFS125HR which provides high spectral resolution due the long travel distance of its moving mirror, in this case a cube retro-reflecting mirror (Figure 3.14 c) which eliminates

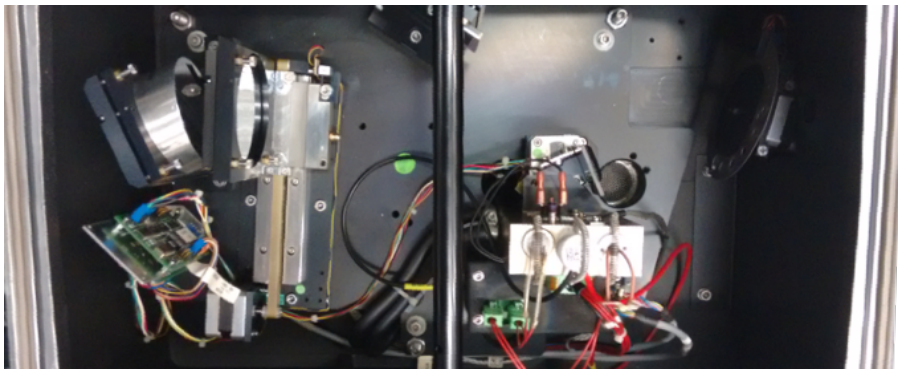

(a) Sources and apertures

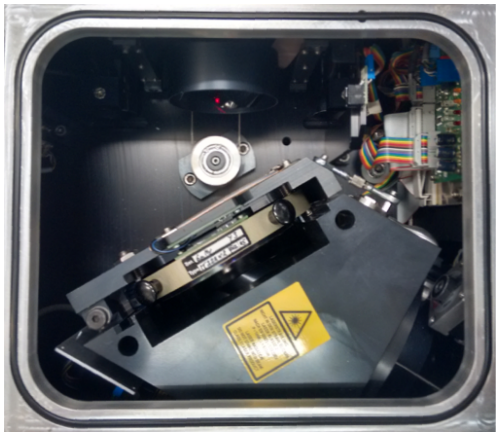

(b) 50 µm Mylar beam splitterr

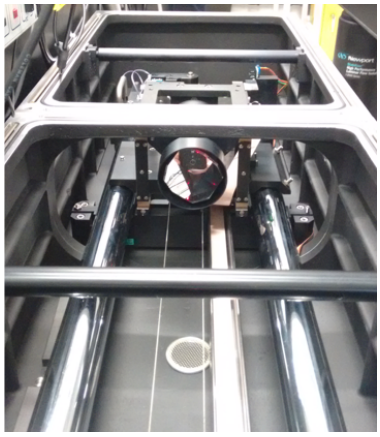

(c) Travelling mirror

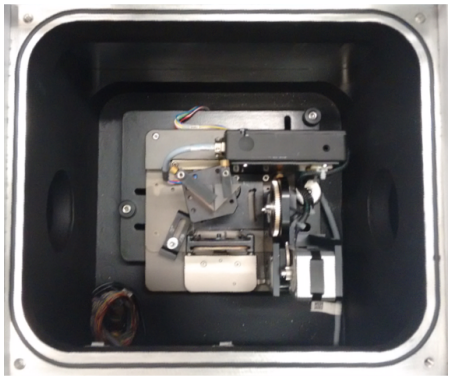

(d) Sample holder for reflection measurements

(e) Liquid helium cooled detector

Figure 3.14: Experimental arrangement for THz metamaterial absorber measurements. A Bruker IFS125HR was extended to the low Thz range through the use of a mercury vapour source (a) and a 50 µm mylar beam splitter (b). 7.6 GHz of resolution is achieved through the large range of the scanning mirror (c). Reflection measurements were made using a custom built sample holder (d). The detector, e) is a liquid helium cooled bolometer, HDL Series Infrared Laboratories

errors due to misalignment in this arm and the movement of which is tracked with a HeNe laser. To measure at 0.5–4 THz a mercury vapour source (Figure 3.14 a) was used, along with a 50 µm mylar beam splitter (Figure 3.14 b). The spectrometer was able to sample radiation from 0.5–4 THz with a resolution of 7.6 GHz. To perform reflection measurements a custom built adaptor piece was made (Figure 3.14 d) this included a motorized linear polarising filter (wire grid) and held two gold coated prisms in the beams path, directing it onto the sample at at $\approx 5°$ from the normal, and then back to the usual path into the detector. Detection was performed using a helium cooled bolometer (HDL Series Infrared Laboratories, Figure 3.14 e). The bolometer was first cooled using liquid nitrogen, then a transfer pipe was used to fill it with liquid helium, which would keep it functional for approx 8hrs. Measurements were performed under vacuum using 20 scans per spectrum and an 8 mm aperture.

3.6 RESULTS

For the vast majority of cases studied transmission has been found to be negligible, as is predicted by the simulations and shown here experimentally in Figures, 3.15 a), 3.17 a) and 3.19. As such the formula A=1-R was used to calculate the experimental absorptivity of the designed MM absorbers. Polarization was either varied, to determine polarisation sensitivity or kept constant as indicated in the relevant sections below.

3.6.1 *Polarization-independent dual-band absorber*

The measured absorption spectra for the dual band absorbers are demonstrated in Figure 3.15, in which two distinct resonance peaks were observed at 0.83 THz and 2.38 THz, which are slightly different peak frequencies than predicted by the simulations (0.84 THz and 2.26 THz respectively). The two peaks have 0.54 and 0.94 absorptivity at 0.83 THz and 2.38 THz respectively, which show similar absorption compared with the conventional dual-band THz MM absorbers using gold as ground plane and polyimide as dielectric space[84,87]. Absorbers with only the cross or square components were measured and found to have resonances that match the paired resonators, demonstrating their largely independent contribution to the resonator behaviour.

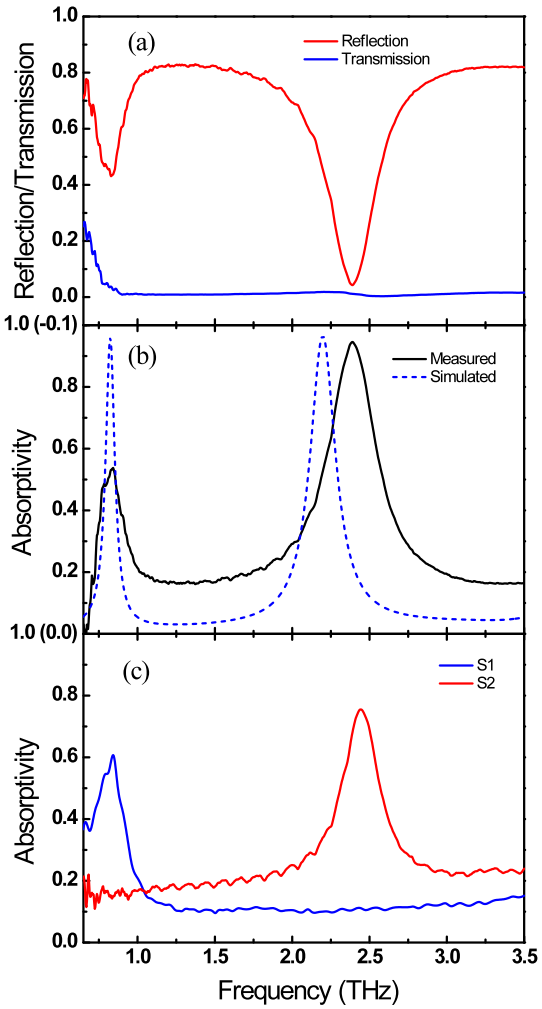

Figure 3.15: (a) Measured reflection and transmission spectra of dual band sample, (b) Measured and simulated absorption spectra of dual band sample, (c) measured absorption spectra of two single band samples, one with cross and one with square mode.

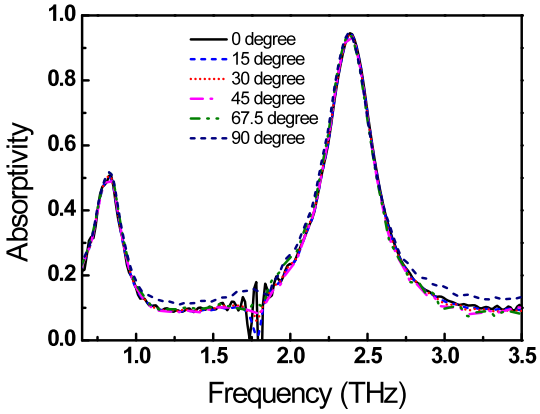

Figure 3.16: (a) Measured reflection of dual band sample for varying polarisations

The polarization dependence of our samples was also studied by changing the polarization angle of the incident beam (using a wire-mesh polarizer) from 0 degree to 90 degree. As shown in Figure 3.16, the absorption response is insensitive to the incident polarization due to the 90 degree rotational symmetry of the resonator.

3.6.2 *Broadband absorber using nested resonators*

The MA's where measured with the incident THz radiation polarized with the electric field perpendicular to the BSRR gap, a necessary condition for coupling to the capacitive action of the gaps. The measured transmission spectrum of the broadband with dielectric layer thickness of 9.3 µm is shown in Figure 3.17. The transmittance less than 0.01 in the range from 0.8 THz to 4.0 THz indicates that the Co-Si ground plane blocks the THz transmission.

For the nested BSRR , three absorption peaks can be observed from the measured absorption spectrum as shown in Figure 3.17, with absorptivity of 0.79 at 0.91 THz, 0.97 at 2.54 THz and 0.90 at 2.88 THz. As predicted by the simulation, the two high frequency peaks merge to form a broadband peak. The bandwidth is 0.98 THz with the absorptivity more than 0.6 Even under the strict criterion of the absorptivity beyond 0.8 , the bandwidth is as 0.66 THz. For comparison the measured absorption spectrum of the single BSRR with 9.3 µm thick dielectric layer is also shown in 3.17. It is clear that the nested resonator exhibits both larger bandwidth and absorptivity compared with the single BSRR . The measured absorption spectrum of the nested BSRR

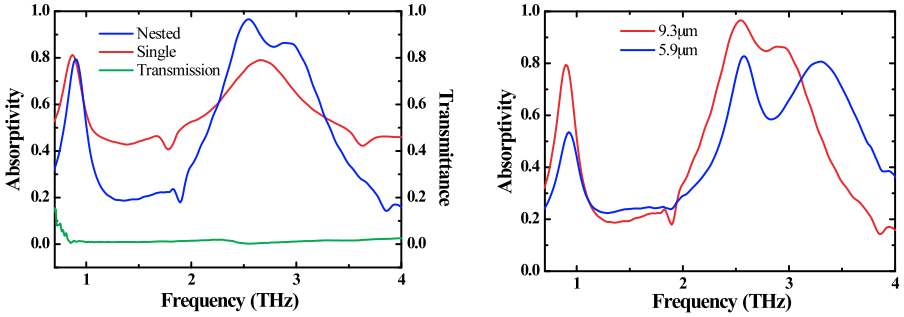

(a) (b)

Figure 3.17: Measured Absorption spectrum of nested resonators. a) compares the nested and single resonator devices, both with a dielectric thickness of 9.3 μm. The nested resonator displays an additional high frequency resonance. Transmission is also noted to be negligible in the range measured. b) shows nested devices with thickness's of 9.3 μm (red) and 5.9 μm (blue). The thinner device has lower absorption and its higher frequency resonances are more distinct from one another, demonstrating for our application of a broadband absorber the thicker device is better.

with 5.9 μm thick dielectric layer is demonstrated in Figure 3.17 b). As observed in the simulation, in comparison with the thicker dielectric devices the resonance frequency shifts to higher frequency with a decrease of the absorptivity, and greater definition between the two high frequency resonances. Although the response is clearly less uniform the bandwidth for absorption above 0.6 increases to 1.2 THz.

It is noted that the measured resonance frequencies and absorptions of both samples are slightly different from the simulations. The variations are likely caused by process errors during the fabrication. The round corners of the resonator patterns, as shown in Figure 3.11, along with deviations of the simulation parameters for the parylene-C and Co-Si film from the actual material parameters, pinholes and roughness in the parylene-C film all contribute to the deviation between the simulation and the measured results.

3.6.3 *Broadband absorber using asymmetric resonators*

Reflection spectra were measured with the FTIR beam polarized across the gaps, as shown in Figure 3.4. The measured absorption spectrum of the symmetric SRR with $\Delta x = 0$ μm is plotted in Figure 3.18. Two

peaks at 2.23 THz and 4.83 THz can be seen in the acquired spectrum with absorptivity of 0.76 and 0.93 respectively. The Q factor of the lower resonance is 5.02, and that of the higher resonance is 4.06, corresponding to the FWHM of 20% and 25%, respectively.

The measured absorption spectra of the ASR MMAs with $\Delta x =$ 0.2 µm, 0.5 µm, 0.9 µm and 1.2 µm are also shown in Figure 3.18. It can be seen that the introduction of the asymmetry has no impact on the lower frequency peak with both the resonant frequency and the absorptivity largely unchanged, confirming the simulations predictions and the interpretation of it as LC in nature. On the other hand, with the increase of the asymmetry, the dipole resonance peak splits to two trapped mode peaks which show higher absorptivity and sharper peak than the dipole one. For the ASR with $\Delta x = 1.2$ µm, two obvious peaks are shown with the absorptivity of 0.96 at 4.44 THz and 0.94 at 5.31 THz. The Q factors of the two peaks are 5 and 4.5 , which are 23% and 11% higher than that of the symmetric dipole resonance, respectively. Note that for the sample with $\Delta x = 0.5$ µm, a relatively flat band absorption is obtained with the highest absorptivity of 0.99 The bandwidth with the absorptivity above 0.93 is 0.55 THz, and the Q factor is 3.31 corresponding to the FWHM of 30%.

As can be seen in Figure 3.18 b), the measured absorption spectrum of the combined resonator 'wideband' device presents two absorption bands. As expected, the LC resonance at 2.23 THz with the absorptivity of 0.79 is the same as the MMAs with ASRs and symmetric SRR. The wideband absorption band composed of the trapped mode resonances is located at a central frequency of 4.80 THz with the highest measured absorptivity of 0.98 at 4.54 THz and 5.03 THz, and a lowest in-band absorptivity of 0.93 Under criterion of the absorptivity more than 0.9 , the measured bandwidth of the wideband peak is 0.82 THz, which is 3.4 times as wide as the 0.24 THz bandwidth of the symmetric dipole peak. Due to the steepness of the trapped mode resonance, the measured FWHM is 32%, corresponding to a Q factor of 3.10 , which is only 7% wider than that of the dipole resonance. The low FWHM provides high reflection of out-of-band radiation.

3.6.4 *Tunable Metamaterial Structures*

The reflection and transmission spectra were measured with the polarization shown in Figure 3.5. The measured transmission and absorp-

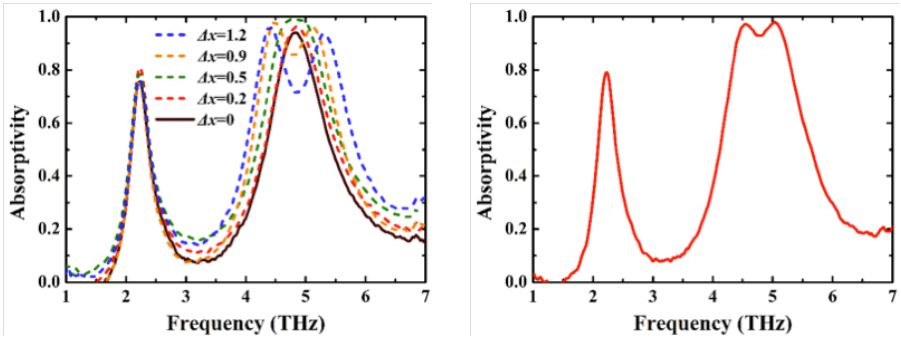

(a) (b)

Figure 3.18: Measured Absorption spectrum of asymmetric resonators. a) Shows the measured absorption spectra for devices with varying levels of asymmetry, ranging from the symmetric case, black $\Delta x = 0\,\mu m$, to blue dashed $\Delta x = 1.2\,\mu m$. The introduction of asymmetry has little to no affect on the lower frequency LC resonance, the higher frequency dipole like modes however split into two trapped mode resonances with increased absorption and sharpness. b) Shows the combined resonator 'wideband' device. By combining the different asymmetries a relatively flat response broadband absorber is achieved, furthermore it has sharp edges leading to a high reflection out-of-band radiation.

tion spectra of the gold and Co-Si ground plane MAs are plotted in Figure 3.19. The transmittance of the Co-Si sample is below 0.02 in the entire experimental range and only a little higher than the zero transmittance of the gold sample in the entire experimental range, which agrees well with the calculated and simulated results. In both absorption spectra, there are two clear absorption peaks at 0.89 THz and 2.67 THz, which originate from electric resonance and dipole resonance, respectively. The absorptivities of the gold and Co-Si sample are 0.84 and 0.81, respectively, at the low frequency peak, and 0.55 and 0.79, respectively, at the high frequency peak. The absorptivity of the Co-Si ground plane increases 44% compared with that of the gold sample at the dipole resonance. At the same time, the absorptivity decreases only 4% for the electric resonance. The shapes of the two absorption curves and especially the variation of the two peaks in the measured results are the same as the calculations and simulations.

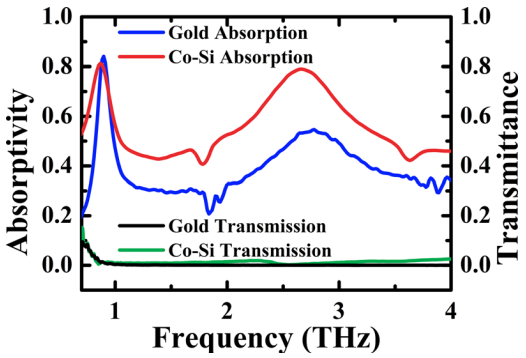

Figure 3.19: Results for devices with varying ground plane conductivities. The lower resonance is equal for both the Au and CoSi ground planes, whereas the higher frequency resonance is significantly reduced for the Au case.

DEVICE TYPE	RESONANCES (THZ)	ABSORPTION
Polarization-independent dual-band absorber	0.83, 2.38	0.54, 0.94
Broadband absorber using nested resonators	0.91, 2.54, 2.88	0.79, 0.97, 0.90
Broadband absorber using asymmetric resonators	2.23, 4.8	0.8, 0.98
Tunable Metamaterial Structures - Au	0.89, 2.67	0.84, 0.55
Tunable Metamaterial Structures - CoSi	0.89, 2.67	0.81, 0.79

Table 3.2: A comparison of the different devices and their performance. The broadband nested asymmetric resonators is the best performer, with the highest absorption along with bandwidth, and out of band acceptance (not shown in table).

3.7 CONCLUSIONS AND FURTHER WORK

3.7.1 *Polarization-independant dual-band absorber*

We have designed and fabricated a polarization-independent THz MM absorber with two distinct absorption bands based on MDS structure. Co-Si film and parylene-C film were applied as the ground plane and dielectric spacer respectively. We have investigated, both theoretically and experimentally the characteristics and adsorption mechanism of these new THz metamaterials. Two peaks at 0.83 THz and 2.38 THz could be tuned individually by optimizing the corresponding single resonator's geometrical parameters. The measured absorption spectra show a good agreement with those of the simulations, and up to 0.98 absorption has been achieved experimentally. Compared with conventional materials, using a silicide film provides good process compatibility, and the application of parylene-C film as the dielectric spacer provides better thickness control, biocompatibility and flexibility, furthermore it is a low-cost material that is amenable to standard fabrication processes. All the advantages of the designed MDS absorber make it a promising candidate for further application in THz detectors and biosensors.

3.7.2 *Broadband absorber using nested resonators*

We investigated a planar THz broadband with single nested BSRR as the resonator both theoretically and experimentally. The Co-Si film and parylene-C were applied as ground plane and dielectric layer during the fabrication, which bring great thermal process compatibility and thickness controllability. The measured FWHM of the fabricated nested BSRR is 47% for the sample with 9.3 µm thick dielectric layer. The bandwidths of 0.66 THz with the absorptivity greater than 0.8 and 1.2 THz with the absorptivity greater than 0.6 were experimentally obtained for the samples with 9.3 µm and 5.9 µm thick dielectric layer respectively. However, for the single BSRR , the absorptivity is below 0.8 and the bandwidth with the absorptivity beyond 0.6 is 0.84 at the same frequency regime of the nested BSRR. The excellent performance of the planar nested BSRR with simple structure brings it great application potentials on microwave, THz and infrared detections.

Compared with the reported broadband MAs in which stacked resonators have been integrated into a unit cell to give multiple close resonances, the two-dimensional nested resonator proposed by us presents broadband and high absorptivity performances with great simplicity to design and fabricate. The measured FWHM of our sample is 47%, which is almost the same as the FWHM of 48% of the previously reported vertical stacked broadband absorber[81], and a significant improvement on other planar broadband absorbers. By modifying the geometric parameters of the nested resonator, the absorption band can be broadened further.

3.7.3 *Broadband absorber using asymmetric resonators*

We numerically and experimentally studied a wideband THz absorber using ASR as resonator. By breaking the symmetry of SRR, the trapped mode resonance was excited, which shows higher absorption and sharpness compared with the dipole resonance of the symmetric SRR. By combining four ASR with different asymmetry into one unit cell, a wideband resonator was realized with a bandwidth of 0.82 THz and absorptivity more than 0.9 , which is 3.4 times as wide as the 0.24 THz bandwidth of the symmetric dipole peak at the same frequency regime. Meanwhile, due to the steepness of the trapped mode resonance, the measured FWHM of wideband peak is only 7% wider than that of the dipole resonance, which makes it effective at rejecting the out-of-band radiation. The simulated and measured results show that by using trapped mode resonances of the ASR, MMAs with both near unity absorption high Q factor can be realized. Furthermore by combing this approach with a nested style structure combining the different ASRs a wideband MMA's with high absorption and sharp band edges can be realized in THz regime. In practical applications, especially in THz sensing, the near unity absorption would greatly improve the sensitivity of the detectors, and the steep wideband would benefit the selectivity and signal to noise ratio (SNR).

3.7.4 *Tunable Metamaterial Structures*

We have modulated the absorption of THz radiation by varying the conductivity of the ground plane. Both the decoupled model of the absorber with EM wave propagation theory and numerical simulations

have been used to analyse the performance. Both approaches show that as the conductivity of ground plane decreases from 1.8×10^7–8.3×10^5 S/m, the theoretical absorptivity of the dipole resonance increases by 62%, while that of the electric resonance decreases by 23%. The measured absorptivity of the Co-Si ground plane decreases by 4% for the electric resonance and increases by 44% for the dipole resonance compared with the gold sample.

In practical applications, by utilizing phase-change materials, such as vanadium oxide (VOx), with high temperature coefficient of resistance (TCR), for the ground planes, the conductivity can be thermally modulated in a wide range. In addition, the ground planes could also be replaced with doped semiconductor films, whose conductivity can be tuned with optical lasers which can be switched at ultrafast speed. Therefore the approach of varying the conductivity of the ground plane opens the door to many exciting applications. Conversely the approach presented also provides a practical method to measure, e.g., as a function of temperature, external magnetic field, optical excitation, or gate voltage, the THz rather than DC conductivity of the ground plane, and this could be helpful both for the development of THz devices as well as materials physics and chemistry.

In summary we have designed, fabricated and theoretically and experimentally tested a range of THz absorber devices, revealing a number of strategies available to the design of wideband high absorption MDM type structures. Through the implementation and combination of these approaches we have expanded the capability of MDM style metamaterial absorbers, something important to the design of THz detectors and optical elements. Our work also demonstrates a new avenue for tunable THz devices, through the modulation of ground plane conductivity, and furthermore suggested a novel way of measuring THz conductivities of thin films.

4

PHOTONIC CRYSTAL DEVICES FOR BIOSENSING

4.1 INTRODUCTION

Photonic crystals (PhCs) provide an elegant method to produce many novel optical devices, including optical biosensors. PhCs are utilised as sensors in numerous ways. The fundamental feature common to all the different approaches is that a geometric or dielectric perturbation induces a change in the wavelengths of electromagnetic radiation that are either blocked, propagate, or resonate within a structure. One of the key features of this approach is it is label free, this is in contrast to fluorescence based methods, and such has a number of advantages, reducing the dependence on expensive reagents and laborious labelling steps. Furthermore labels can interfere with the biological function of a sample and quantification of fluorescence signals can be hard as it is often impossible to control the number of fluorophores on a specific molecule[16].

This work was carried out independently of any collaborators. I would, however, like to thank Rodolfo Hermans for his advice and assistance, Daniel Engstrom for his help getting me started in the cleanroom and the LCN IT support team for assisting with cluster computing.

Of course photonic crystals are only one of a number of label-free optical biosensing techniques. Most rely on the local changes in refractive index due to the binding of sample molecules on the active surfaces of the sensors. Surface plasmon resonance (SPR) is the most widely known optical biosensing technology[88,89] and has had widespread success with commercial instruments such as the Biacore becoming a gold standard in immunoassay technology. SPR does have inherent limitations however, due to its reliance on evanescent fields with exponentially decaying amplitudes, sensing is restricted to the immediate vicinity of the surface, making it unsuitable for sensing of larger targets such as cells and bacteria. Most devices also use macroscopic optical components making it hard to massively parallelise and increasing reagent costs. Optical waveguide sensors get over this restriction by using lithographically patterned waveguides, often also using resonant coupling conditions, and their dependence on the local refractive index as a sensing mechanism[90]. Optical ring resonators are a technology that has shown great promise. By utilising the extremely high-Q whispering gallery mode resonances in micro-

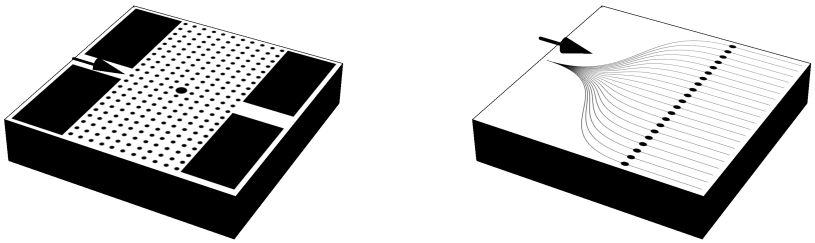

(a) (b)

Figure 4.1: Schematic of a multiplexed photonic crystal cavity sensor. a) shows a single cavity with waveguides for measurement, b) shows a multiplexed system with many cavities on a single chip.

patterned discs or spheres single viruses are detectable[91]. Another promising field of optical biosensing is that of fiber based sensors. This is particularly appealing due to the inbuilt ease of using fiber systems, and the extensive commercial support and availability of fiber optics through the telecommunications industry. Frequently Bragg gratings, one-dimensional photonic crystals, are introduced to the fiber core, these act as band stop filters for which transmission depends on the local refractive index[92]. There has also been considerable success in developing one-dimensional photonic crystals as free space reflection mode sensing surfaces[93]. Despite this they lack the natural application to highly parallelised integrated on-chip devices. This is due to the fact that they must be addressed by macroscopic optical components, scaling the number of devices thus requires scaling the number of macroscopic optical components or building automated alignment processes to scan serially through the devices. Planar or slab quasi-2D photonic crystal waveguides and cavities however naturally fit in with standard fabrication techniques and other on-chip components.

Photonic band gap cavities and waveguides have been adopted for many different biosensing applications, both molecular and viral[94,95]. Generally all share a similar motif, a structure either waveguide, cavity or a combination of the two possessing either narrow pass or narrow

stop characteristics is functionalised with an antibody. After exposure to a sample, the target binds to these antibodies. The increased concentration of the target in the vicinity of the optical structure alters the refractive index and changes the band pass characteristics. The change in transmitted intensity or the shift of a resonant peak is correlated to the concentration of sample providing a measurable output. In this work I will address the development of photonic crystal cavities, which incorporate many of the beneficial features of the different techniques outlined above. The major benefits of photonic crystal cavities are their high-Q resonances which provide great sensitivity. Their minute volume means they also have extremely high total sample volume sensitivities[17]. They are also massively parallelisable, and readily integrated with other on chip devices[96,97] (See Figure 4.1). As opposed to SPR where these changes must occur at the surface of the device, PhC devices can be designed such that they are sensitive to changes in the refractive index within predefined regions of the device, meaning the detection of larger objects such as viruses and cells can also be done effectively. One of the major challenges is the accurate functionalisation and sample delivery to make full use of such minute sensing areas. One approach to help tackle these challenges is to make membrane structures so that the sample is forced to flow through the gaps in the structure, which normally are also the sensing areas[34].

As will be shown below there are many challenges involved in the successful development and implementation of such sensors. Prior to describing my work in more detail I briefly summarise the current literature on photonic crystals with particular attention to the measurement of the slab structures I am concerned with.

4.1.1 *Brief summary of published work*

While a great deal of work has been published on photonic crystals, reports including experimental data for their broadband spectral properties is surprisingly sparse. This is particularly true for slab structures. Here I present the results of a brief literature survey on the experimental study of photonic crystals. Table 4.1 is a list of the 20 most cited papers with the words 'Photonic Crystal' in their title, abstract or keywords (along with a further 7 papers which were found in the top 150 to have measured spectra of photonic crystal devices). These papers

have been surveyed for their inclusion of experimental measurement of band-gaps and is noted in the Data and Type columns.

Table 4.1: Publications with 'Photonic Crystal' in their title, abstract or keywords ranked by number of citations (as matched by Scopus academic database). The publications have been surveyed for their inclusion of experimental spectra of photonic crystal devices. Starred entries have figures reproduced for discussion in the following section

Rank	Title	Year	Data	Type
1	Photonic crystals: Molding the flow of light[29]	2011	No	
2	Magnetism from conductors and enhanced nonlinear phenomena[98]	1999	n/a	
3	Revival of the magnetoelectric effect[99]	2005	n/a	
4	All-silica single-mode optical fiber with photonic crystal cladding[100]	1996	Yes	Mode image
5	Photonic crystal fibers[101]	2003	Yes	Mode image
6	Endlessly single-mode photonic crystal fiber[102]	1997	No	
7	Nanoengineering of particle surfaces[103]	2001	No	
8	Photonic crystals: Putting a new twist on light[104]	1997	No	
9	Supercontinuum generation in photonic crystal fiber[105]	2006	Yes	Solitons
10	Optical Solitons: From Fibers to Photonic Crystals[106]	2003	n/a	

11	Two-dimensional photonic band-gap defect mode laser[107]	1999	Yes	Resonance
12*	High-Q photonic nanocavity in a two-dimensional photonic crystal[108]	2003	Yes	Resonance
13	Monodispersed colloidal spheres: Old materials with new applications[109]	2000	Yes	Spectra
14	Preparation of photonic crystals made of air spheres in titania[110]	1998	Yes	Spectra
15	Epitaxial core-shell and core-multishell nanowire heterostructures[111]	2002	No	
16	Poly(aryleneethynylene)s: Syntheses, properties, structures, and applications[112]	2000	No	
17	High transmission through sharp bends in photonic crystal waveguides[113]	1996	No	
18	Vacuum Rabi splitting with a single quantum dot in a photonic crystal nanocavity[114]	2004	Yes	Resonance
19	Fabrication of photonic crystals for the visible spectrum by holographic lithography[115]	2000	Yes	Image of scatter
20	Single-mode photonic band gap guidance of light in air[116]	1999	Yes	Spectra

22	Large-scale synthesis of a silicon photonic crystal with a complete three-dimensional bandgap near 1.5 micrometres[117]	2000	Yes	Spectra
23*	On-chip natural assembly of silicon photonic bandgap crystals[118]	2001	Yes	Spectra
33*	Photonic band-gap structures[119]	1993	Yes	Spectra
51	Guided modes in photonic crystal slabs[120]	1999	No	
81*	Two-dimensional photonic-bandgap structures operating at near-infrared wavelengths[121]	1996	Yes	Spectra
83	Experimental demonstration of guiding and bending of electromagnetic waves in a photonic crystal[122]	1998	Yes	Spectra
147	Defect modes of a two-dimensional photonic crystal in an optically thin dielectric slab[123]	1999	No	

Of the 20 most cited papers with the words 'Photonic Crystal' in the title, abstract or keywords three are actually not concerned with photonic crystals[98,99,111], of the remaining seventeen:

- Eight contained experimental measurements of structures, of which five contained actual spectral measurements of photonic crystal transmission or reflection (not including photonic crystal fiber). Only two of these attempt to measure entire band-gaps or even edges.

- Five focus on the fabrication of three-dimensional photonic crystal structures, including two that contain measurements of the optical properties.
- Seven are reviews, including two books.
- Three were exclusively concerned with theoretical or simulated results

Inspecting lower ranked articles revealed five further papers in the top 150 that had spectral measurements. It is difficult to carry out a exhaustive study for a field such as photonic crystals, many of the applications of which have grown into large areas of research themselves, for example photonic crystal optical fibers[100] , supercontinuum generation in photonic crystal fibers[105] and quantum dynamics in photonic crystal cavity structures[114,124]. Nevertheless the publications shown here do to the best of my knowledge represent the extent to which photonic crystal structures have been experimentally characterised in terms of the broad spectrum of optical states they transmit, absorb and reflect.

Publications of particular note for their optical characterisation across relatively large wavelength ranges are reproduced here. Figure 4.2 includes data from Yablonovitch's seminal paper 'Photonic band-gap strcutures'[125]. This article is the first experimental demonstration of photonic crystals. The authors used macroscopic three-dimensional structures for the microwave regime. They do not explicitly compare their transmission spectra was theoretical results but show a clear band gap from 13–15 GHz.

Vlasov et al. perform broad band measurements (data shown in Figure 4.2) of the reflectance of three-dimensional structures for the near infrared using bottom-up fabrication techniques. The measured and simulated spectra have many differences but do largely agree on the position of band gaps, visible due to the near 100% reflectivity at 1.1–1.3 µm for the inverted opal structure.

Figure 4.3 shows measured spectra of slab-like photonic devices. Published broad spectra for these type of devices is extremely sparse, with the work of Krauss et al. being the only published data found which attempted to show an entire band-gap, although even in this work the authors state that they did not measure an entire gap due to fabrication errors. Akahane et al. do not show band-gap behaviour but their work shows the manual tuning of both the resonant frequency

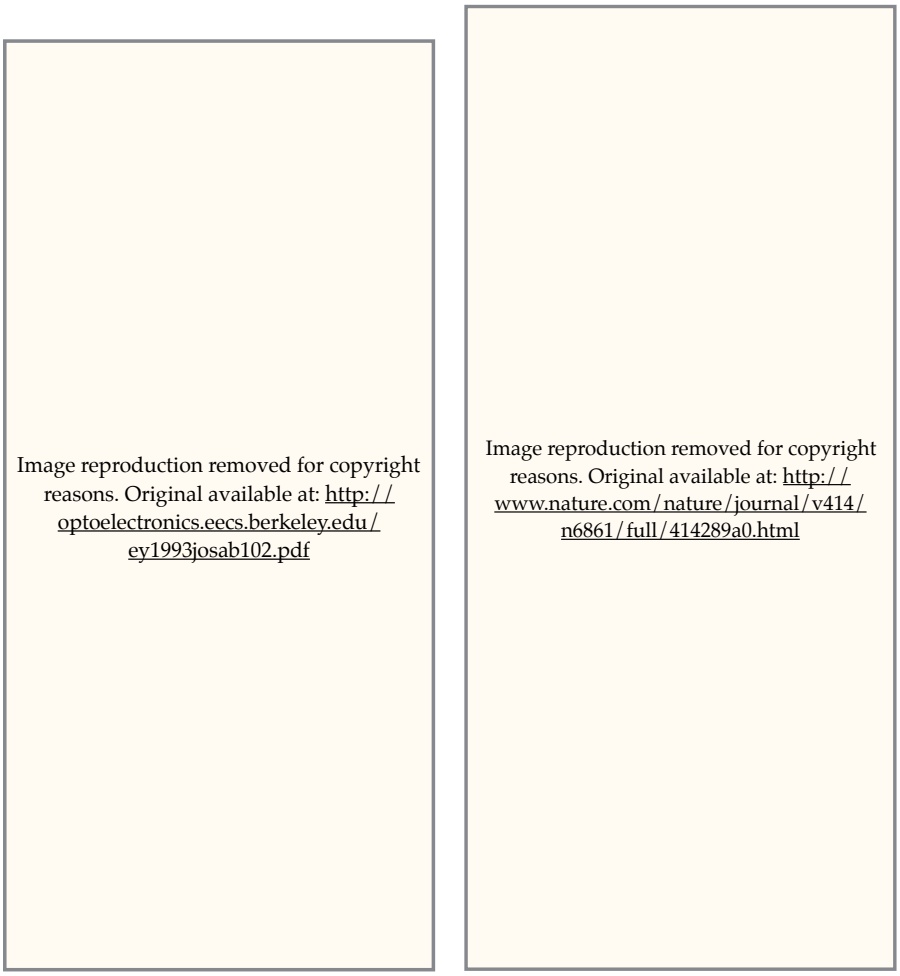

Figure 4.2: Published band gap data showing broad spectral response. a) Shows the attenuation spectra for three-dimensional macroscopic structures fabricated for the microwave regime. A clear band-gap is visible from 13–15 GHz. b) Shows the reflectance spectra fora three-dimensional microscopic structures for the near infrared. Simulated and measured data diverges frequently but does agree well for the bandgap from 1.1–1.3 µm. Images taken from a) Yablonovitch, E. (1993). Photonic band-gap structures. Josa B.[125] and b) Vlasov, Y. A., Bo, X. Z., Sturm, J. C., & Norris, D. J. (2001). On-chip natural assembly of silicon photonic bandgap crystals. Nature, 414(6861), 289293[118]

and quality factor of a defect through the fabrication of a series of devices with a hole shift. In addition to to the impressive Q factors, their work notable in that it does not just show a single device with simulations tuned to match but a series of devices for which there is clear intentional control of the optical properties through the precise manipulation of the geometric parameters.

Motivated both by the successful implementation of a high-Q photonic crystal biosensor but also to address what I posit are some shortcomings in the field I have attempted to produce a series of photonic crystal slab devices, and will now expand on the theory underpinning such structures.

4.1.2 *Slab photonic crystals*

The discussion of one and two dimensional photonic crystals in the introduction deals with structures that do not control the propagation of light in all directions. Waves with an off-axis wave vector, that is not in the direction or plane of symmetry, are free to propagate. To contain light in these directions it is common to introduce low refractive index regions above and below the photonic crystal structure, which contain the light by the means of index guiding[126]. Such structures, which have a periodicity in two dimensions, are called slab photonic crystals. There are important qualitative differences between the hypothetical two-dimensional structures described previously and the slab devices described here. Before going into further details for the more complex structures a brief description of index guiding is given.

Index guiding is a generalisation of the more familiarly termed total internal reflection, which is governed by Snell's law:

$$n_1 \sin\theta_1 = n_2 \sin\theta_2 \tag{4.1}$$

Where n_1 and θ_1 refer to the refractive index and angle for the incident ray and the material it is travelling in and n_2 and θ_2 refer to the angle of refraction and refractive index for the medium on the other side of the boundary, see Figure 4.4. For the case where $\theta_1 > \sin^{-1}(n_2/n_1)$ there are no real solutions to Snell's law. The physical interpretation of this is the incident ray undergoes total internal reflection, with θ_c, the critical angle defined as $\sin^{-1}(n_2/n_1)$. Snell's law, despite being based on ray optics, holds for structures with dimensions much smaller than

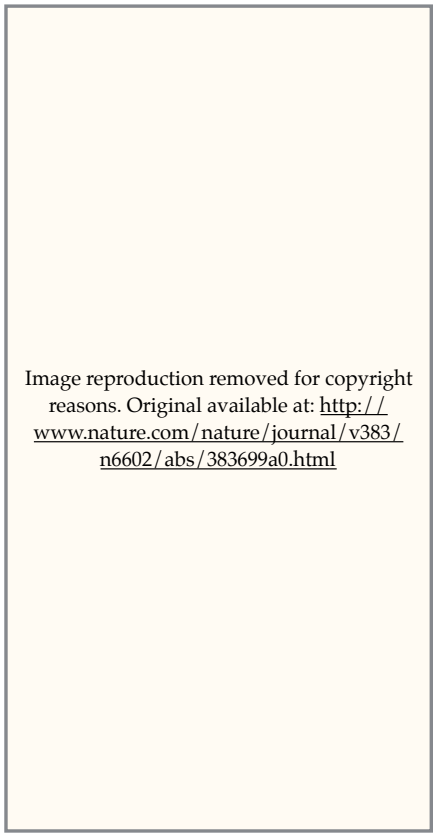

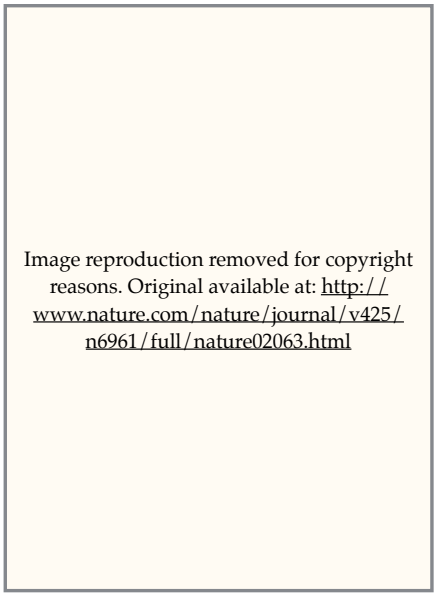

(a) (b)

Figure 4.3: Published band gap data for slab structures a) is one of the only found measurements of a full band-gap for a slab photonic crystal structure. b) Shows the manual tuning of both the resonant frequency and quality factor of a defect through the the precise manipulation of the geometric parameters. Images taken from a) Krauss, T. F., Richard, M., & Brand, S. (1996). Two-dimensional photonic-bandgap structures operating at near-infrared wavelengths. Nature.[121] and b) Akahane, Y., Asano, T., Song, B.-S., & Noda, S. (2003). High-Q photonic nanocavity in a two-dimensional photonic crystal. Nature, 425(6961), 944947[108]

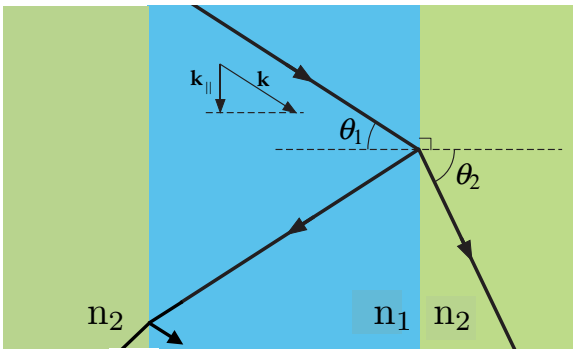

Figure 4.4: Light propagates in a piece of glass, for certain angles light may pass across the boundary and into the space surrounding, for other angles it undergoes total internal reflection. This system can be recast in the terminology of index guiding, where $\omega = c|\mathbf{k}| = c\sqrt{k_{||}^2 + k_{\perp}^2}$ For a given value of $k_{||}$ there will be modes with every frequency greater than $ck_{||}$. These solutions are a continuum of modes, as $k_{\perp}$ can take any value, this region is termed the light cone and contains all the solutions to Snell's law for which θ_1 is less than the critical angle. For modes with a frequency lower than this $k_{\perp}$ must be imaginary, i.e. evanescent modes that decay exponentially into the air. These second modes are the totally internally reflect modes, or guided modes. This figure was adapted from Joannopoulos et al.[29]

the wavelength of light. To show this, and also to explain how it holds for non-continuous boundaries such as those in a photonic crystal, it is useful to reframe the question. Snell's law can be reframed in terms of the conservation of $\mathbf{k}_{||}$, the wave vector component parallel to the interface, which follows from the continuous symmetry along this interface. From the geometry it is known that $\mathbf{k}_{||} = |\mathbf{k}| \sin\theta$, and from the dispersion relation $|\mathbf{k}| = n\omega/c$.

Consider the situation for light in a piece of glass surrounded by air (Figure 4.4), $\omega = c|\mathbf{k}| = c\sqrt{k_{||}^2 + k_{\perp}^2}$. For a given value of $k_{||}$ there will be modes with every frequency greater than $ck_{||}$. These solutions are a continuum of modes, as $k_{\perp}$ can take any value, this region is termed the light cone and contains all the solutions to Snell's law for which θ_1 is less than the critical angle. For modes with a frequency lower than this, $k_{\perp}$ must be imaginary, i.e. evanescent modes that decay exponentially into the air. These second modes are the totally internally reflected modes, or guided modes. Due to the spatial confinement, and the constraint of orthogonality, these modes form a discrete set of modes, as the frequency increases each mode is orthogonal to the one before. Another way of describing this is that to ensure the phase matching of

wave fronts along the direction of the confinement, the off-axis values of k must be such that in effect a standing wave is generated in the off axis direction.

This description, based on conservation of $\mathbf{k}$, gives a better understanding of how index guiding can be used to confine light in non-continuous structures such as photonic crystals. The solid and periodically structured situations are much the same, except that in the structured case the conservation of $\mathbf{k}_{||}$, the in plane component of the wave vector, is due to discrete rather than continuous translational symmetry along the interface.

Figure 4.5 shows the band structure calculated for a slab photonic crystal with air holes on a triangular lattice. The black line marks the light cone, for frequencies higher than this there exists a continuum of modes. Due to the symmetry through the $z = 0$ plane the modes can be split into TE-like (red) and TM-like (blue).

There are a number of advantages to working with two dimensional slab structures. Firstly they are far easier to fabricate (when one considers top down approaches), and integrate with other on chip components than three-dimensional structures. They also provide a higher level of control of light than the one dimensional case. In addition their structure is open to perturbation, lending themselves to sensing applications. Here I describe the theoretical tools I have developed for the designing of photonic band gap structures, the processes and process optimisation I have undertaken to fabricate them, the measurement techniques employed and results obtained.

4.2 SIMULATIONS

4.2.1 *Two-dimensional Simulation of device*

I first implemented two-dimensional simulations. Although there are important differences between two-dimensional and quasi-2d slab configurations, the relative simplicity and speed at which two-dimensional simulations can be run make them a useful first step, giving insight and boundaries for the expected behaviour of more complex three-dimensional simulations and indeed measurements. The devices are targeted at detecting the presence of nanoparticles like viruses. As such they have been designed with defect that consists of an enlarged hole in a hexagonal air hole configuration addressed by a pair of

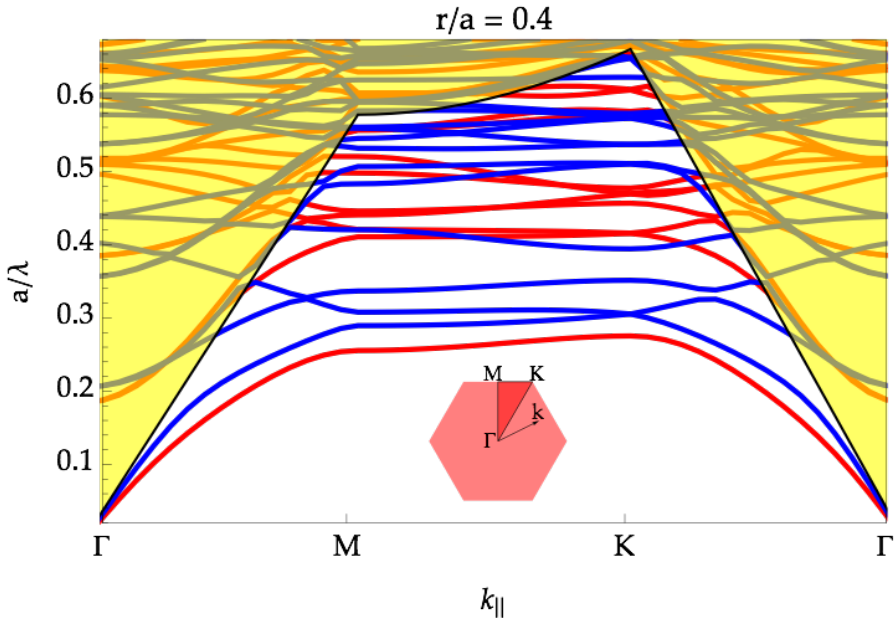

Figure 4.5: Plot shows TE (red) and TM (blue) modes for a slab photonic crystal membrane with air holes on a hexagonal lattice calculated using MEEP[30]. The yellow shaded region is the light cone determined by $\omega = ck$. Above this frequency there is a continuum of modes escaping the slab. Below this cone are the guided modes that decay exponentially from the slab - free space interface. In the plot there are discrete modes below, above and along the edge of the light cone. These can be described respectively as guided modes, leaky and extended modes. Leaky modes are those that are in the slab but couple to the radiating states in the light cone. Extended modes are not coupled to the slab at all but due to the low $k_\perp$ are not absorbed by the PML layers on the z boundary of the simulation

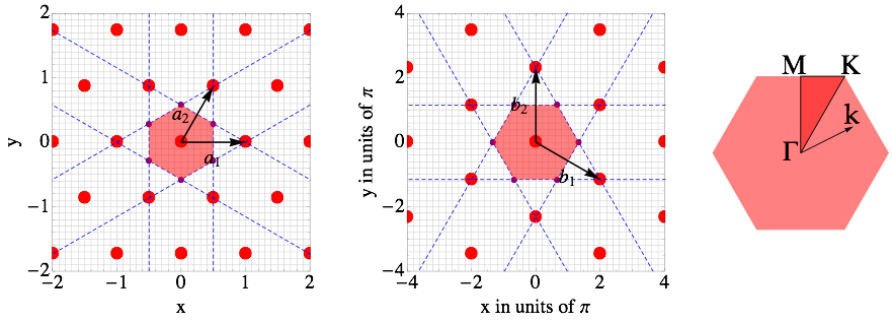

Figure 4.6: Hexagonal lattice, showing the standard lattice, the reciprocal lattice and the Brillouin zone

standard ridge waveguides, a structure inspired by the work of Lee and Fauchet[127].

4.2.1.1 *Band structure determination using MPB*

The first step in the simulations uses the MIT Photonic Bands Package (MPB)[31] to calculate the band structure and its dependence on the hole radius. The simulation is used to calculate the first 12 modes (in increasing frequency) for k values that trace the edge of the reduced Brillouin zone.

k is swept from the Γ point (origin) to M, K then back to Γ. The simulation calculates 12 values for k in between each of these symmetry points. The bulk of the geometry is modelled as silicon with a dielectric constant of 11.86, the holes are modelled as air with a dielectric constant of 1. The simulation was run for values of r/a running between to 0.03 and 0.71 in increments of 0.01. To determine the mode density further analysis was performed. First for each mode the number of k values was increased using an interpolating function. The resulting data was then processed by a histogram binning function to extract the density of modes for a given parameter set and frequency.

The band structure (Figure 4.7) and band gap maps (Figure 4.8) show that band gaps exist for both the TE and TM case, with the largest gap being for the TE case and a r/a value of roughly 0.4. The gap is also large in terms of the range of radii it is present for extending all the way down to 0.2 and up to 0.5. The gap at r/a = 0.3 runs from f=0.21 to f=0.275 giving a a gap-mid-gap ratio of 0.27 (all frequencies are given in the normalised frequency units of a/λ). The size of the gap at this value makes it a promising candidate for isolating a high-Q defect state, as any frequencies in the middle of this gap will be highly

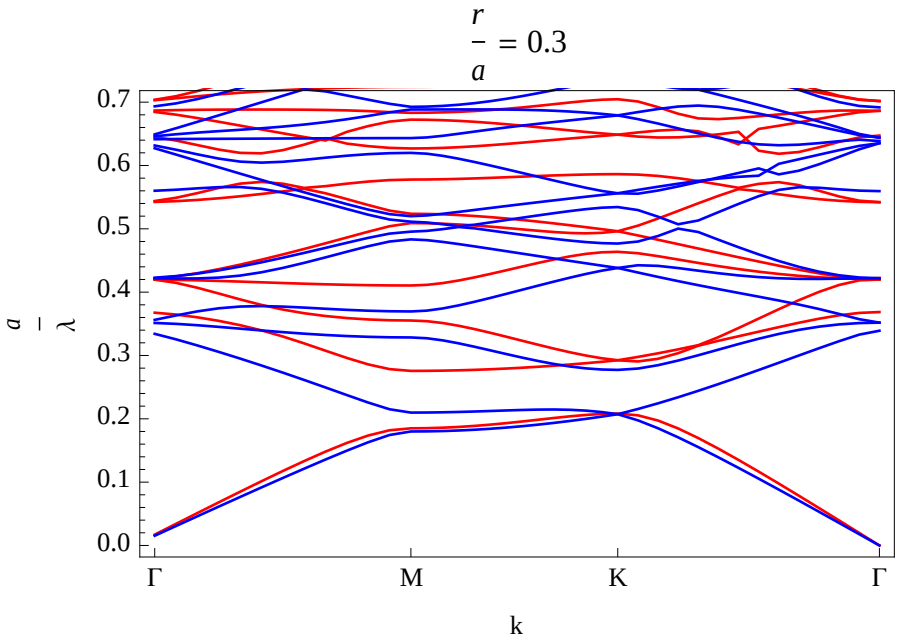

Figure 4.7: Band structure for two-dimensional triangular lattice of air hole. In this case $r/a = 0.3$. The red lines show TE modes and the blue show TM modes. A gap in the TE modes can be seen between the first (dielectric) and second (air) modes, spanning the normalised frequencies of 0.21 - 0.3 a/λ

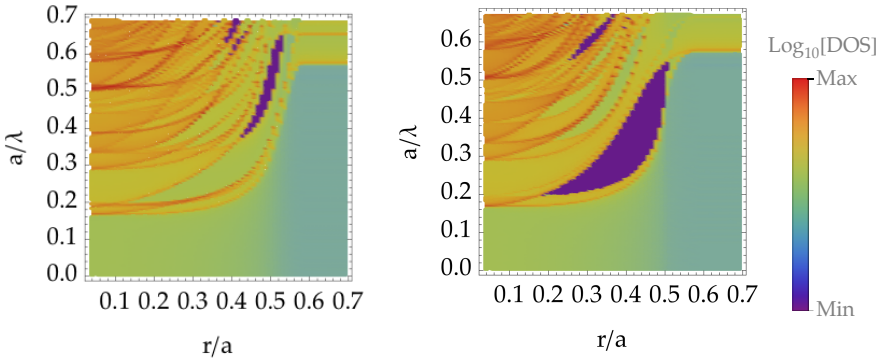

(a) TM Mode densities for air-holes on a triangular lattice

(b) TE Mode densities for air-holes on a triangular lattice

Figure 4.8: Band gap map for two-dimensional triangular lattice of air holes. Mode density (DOS) is plotted on a log scale (red maximum, purple minimum) as a function of hole radius (r/a). a) shows TM, b) shows TE. The veins trace the location of the higher density regions at the corners of the reduced Brillouin zone (Γ, M, K)

localized. This effect could be made stronger by increasing *r/a* but fabricating the devices would become challenging due to the thin walls between holes.

4.2.1.2 *Defect mode determination by MPB*

Following on from the band gap calculations MPB can also be used to study the introduction of a point defect. As mentioned previously in this work I was interested in making devices that can detect the presence of a virus like particle. To do this it is important to make the defect open to the environment such that it can be perturbed by a binding event. As such I examined enlarging a single hole, to make it capable of capturing relatively large particles. Furthermore so as to ease fabrication and not make the wall surrounding the enlarged hole too thin I also removed some of the surrounding holes. This lead to the structure shown in Figure 4.9.

To calculate the defect modes I used MPB. To calculate a defect mode a super-cell must be used, that is the defect surrounded with a photonic crystal structure that is large enough to confine the modes to the defect. This increases the computational time for a simulation considerably. Firstly the geometry being simulated is much larger and secondly due to the fact it is a super-cell lower modes loop round so that to get the full band structure many more more bands had to be simulated. The defects states are situated in the first gap, this means that we must calculate n^2 bands where n is the number of unit cells repeated in each lattice direction to reach the first gap. To verify the reliability of the simulations I tested both the effect of resolution and the size of the super-cell on the simulation results, the results of which can be seen in Figure 4.9.

Having determined a suitable resolution and super-cell size the simulation is repeated for varying radii of the defect hole. Each simulation gives the frequency of the found modes and the Hz fields. A program was written to track the modes from one value of defect radius to the next. The program extrapolates from previous modes, selecting those that are within an acceptable frequency range (0.01 a/λ) of the extrapolated frequency. The correct mode out of the remaining was then selected based on an image analysis of the *Hz* fields. By comparing the Fourier transform of the image the correct mode was matched so that a smooth transition of modes could be observed as the defect radius was changed.

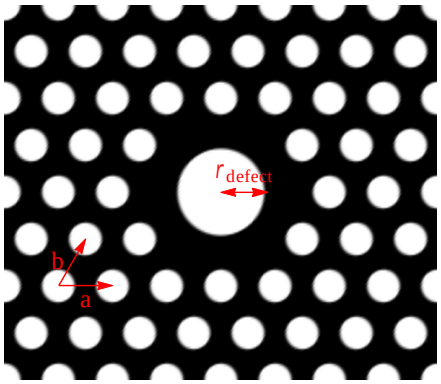

(a) Schematic of point defect

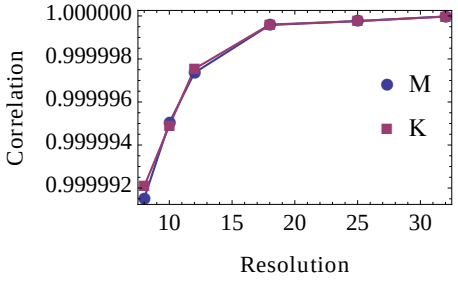

(b) Convergence for resolution

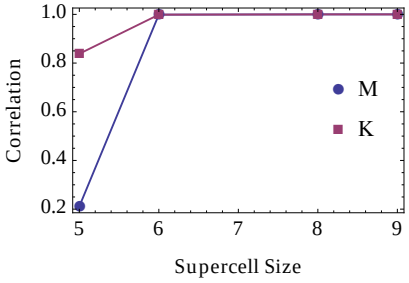

(c) Convergence for super-cell size parameters

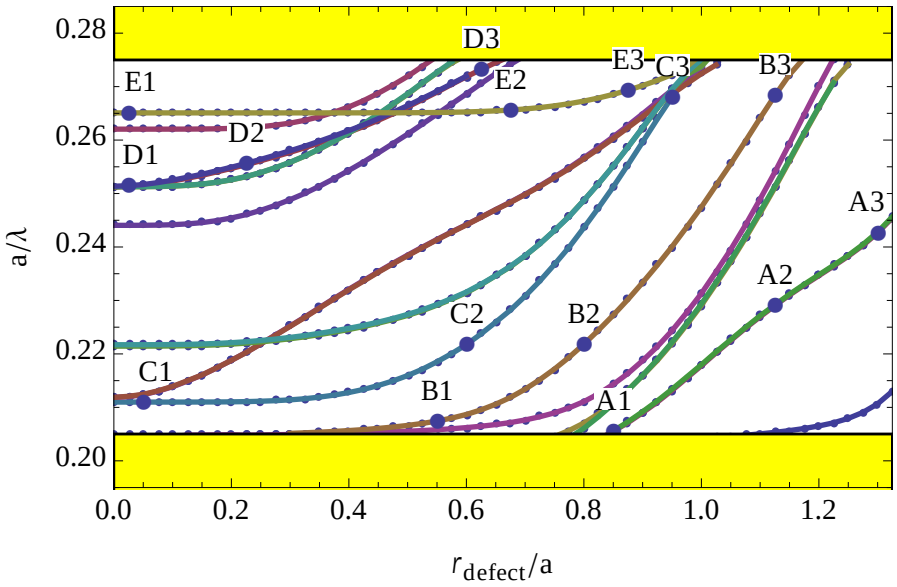

(d) Defect band structure

Figure 4.9: a) Schematic of simulation with 8x8 unit cell super-cell, two-dimensional triangular lattice with enlarged central hole and removed surrounding holes. b) and c) Convergence plots for the resolution and super-cell size. d) Two-dimensional triangular lattice point defect simulation results showing the resultant defect modes for varying defect radius. The yellow regions show the position of the air and dielectric bands with the region in between corresponding to the TE gap. The labels (A-E, 1-3) show the progression (by number) of a selection of modes (letters), their corresponding Hz field patterns are shown in Figure 4.10.

Figure 4.9 shows the band structure as the defect radius r_{defect} is varied from 0 to 1.3. Because the defect is actually a combination of the central hole and the removed surrounding holes quite a complex structure is observed. The labels show the progression of a number of modes, their corresponding Hz field patterns are shown in Figure 4.10. The results show that as r_{defect} is increased modes are pulled up out of the continuum below the gap, then isolation as defect states and finally absorbed into the modes above the gap.

4.2.1.3 *Transmission through a two-dimensional device using MEEP*

The two previous sections have examined the mode structure and defect modes using MPB, an eigensolver, to analyse the modes supported by a theoretically infinite structure. A complimentary method of analysis is to use a finite difference time domain method such as MEEP to determine the transmission spectrum through a device. This approach has the advantage of incorporating some of the properties of 'real-life' devices such as finite in-plane crystal size and the coupling to and from waveguides addressing the device. The output of this method is a transmission spectrum for the simulated device. This can provide information on the position and nature of band gaps (regions of zero or near zero transmission) and defect mode resonances (peaks within these stop bands) without solving explicitly for every mode, making it computationally quicker in many cases.

MEEP simulates the propagation of a pulse through a user defined structure, with the source pulse having a finite width in terms of time and therefore frequency. The power transmitted through the structure is then calculated at a user specified location in the geometery e. g. at the adjacent end of the waveguide to where the source is defined. The Fourier transform of this power gives the frequency spectrum. To get a result that is independent of the input pulse the transmission should be compared to that of a reference, typically a straight waveguide.

The three structures simulated are shown in Figure 4.11, they consist of the waveguides, central PhC housing and structure with resonator, the waveguides and PhC housing only and a reference waveguide. The number of time steps for which a simulation should be run is determined by a number of factors. First the length of time for which the source pulse lasts, which is inversely proportional to the range of frequencies specified. Secondly a period of time so that the pulse may propagate through the structure to reach the region

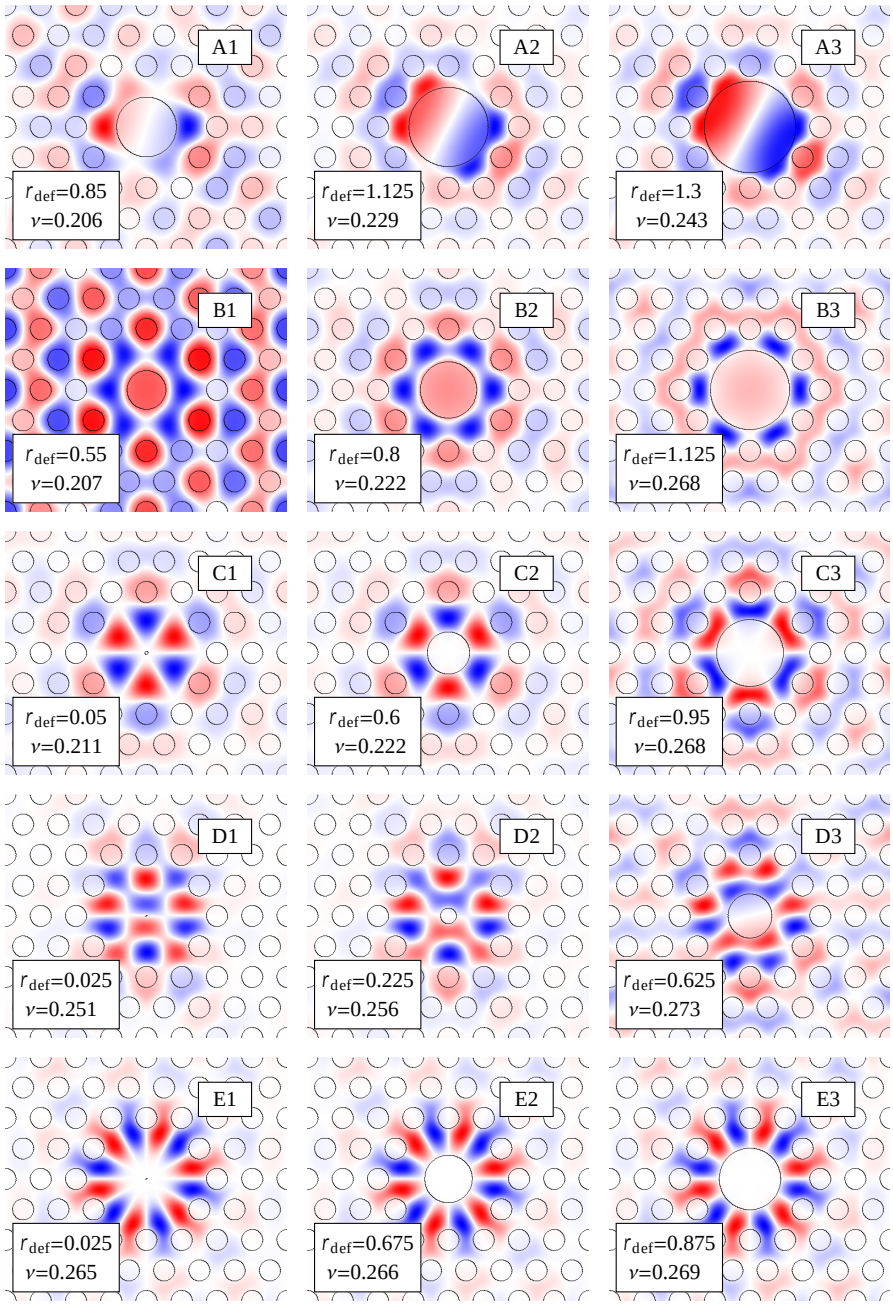

Figure 4.10: Two-dimensional triangular lattice point defect simulation results showing the defect modes Hz fields. Labels correspond to the band structure plotted in Figure 4.9

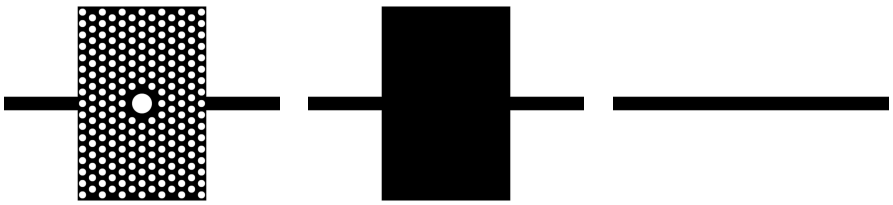

(a) (b) (c)

Figure 4.11: Structures simulated using MEEP. A geometry is defined by the shape and dielectric of the structure. A pulse is then specified and the time evolution of its propagation is simulated. A probe point in the simulation allows you to collect the transmission spectrum of the device. a) the full device, b) the device devoid of photonic crystal structure and c) the straight waveguide.

where transmission is calculated. Finally, time for the pulse to finish propagating which is given by a set ratio of decay in the fields at a specified point in the structure. As with the MPB simulations the dielectric is modelled as silicon with an permittivity of 11.86. The hole radius is simulated to be 0.3 a and the defect radius to be 0.856 a. The resultant transmission spectra are tested to be independent of resolution but also the length of simulation as determined by the factor by which the E_y field has decayed at the point of measurement . The convergence of these two parameters is shown in Figure 4.12.

To compare the MEEP simulation results to those from MPB the full device was simulated with a range of photonic crystal air hole radii. A TE pulsed line source that covers the width of the waveguide is injected into the device, the transmitted power is then calculated as a fraction of the transmitted power in the straight waveguide case. Figure 4.13 shows the resultant spectra overlaid above the band gap map found using MPB. The resultant band gap can be seen to match with that found in the MPB simulations. Furthermore to compare the MEEP simulation to the MPB defect mode simulation the transmission spectrum alongside the defect band structure is shown for $r_{defect} = 0.856\ a$ in Figure 4.14. As expected, we observe good agreement between the two sets of simulations, suggesting that numerical errors are being minimized and the results are not artefacts of the simulation technique

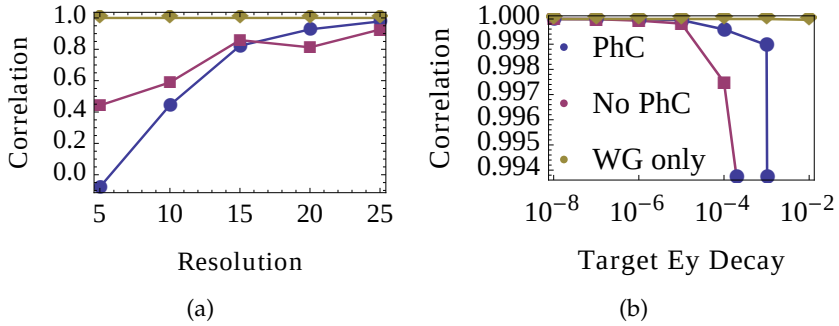

(a) (b)

Figure 4.12: a) the full simulation resolution, b) the decay of fields at the transmission point. The blue line corresponds to the full device, the red line to the device without the photonic crystal features and the yellow line is for the waveguide only simulation.

and that MEEP provides an effective and efficient way of simulating the device performance.

4.2.2 *Three-dimensional simulation of device*

As discussed in the introduction there are important differences between two and thee-dimensional slab structures, the index guiding of the light in the out of plane direction means that light is only contained in that direction for certain k values. Furthermore the finite thickness in the out of plane direction means nodes in this direction can alter the band structure. To investigate these differences I implemented a three-dimensional MEEP model of the devices. This model takes into account the finite thickness of the device layer, along with a substrate. The x-y, x-z and y-z slices of the model (sliced though the origin at the centre of the device) are shown in Figure 4.15.

The simulations examined the role of the hole radius, the defect radius, the device thickness and the refractive index of the substrate. The simulation has been run using the parallel implementation of MEEP using cluster computing facilities. As for the two-dimensional case the device layer is modelled as silicon, with dielectric constant 11.86, in the cases for which they are not being varied the device thickness h is 0.6, the holes radius r is 0.3, the defect radius r_{defect} is 0.856 and the substrate refractive index is 1 (equivalent to a bridge type device with air on either sides).

We can see from the simulations varying r (see Figure 4.16) that there is a large region of low transmission that corresponds to the gap

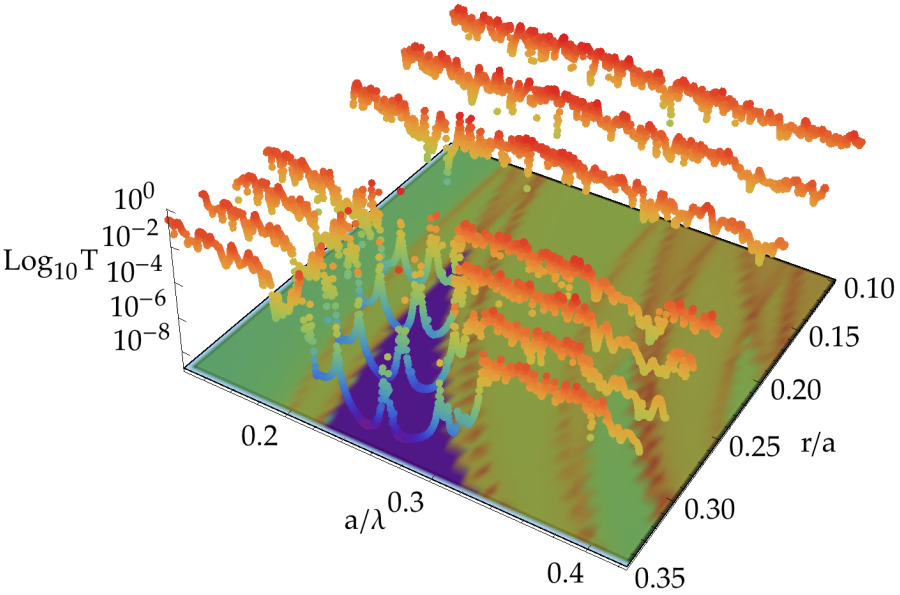

Figure 4.13: Two-dimensional MEEP transmission spectra overlaid on top of the MPB TE band gap map. It is clear that the band gap matches that of the MPB case, with the low frequency edge remaining relatively flat, the higher frequency edge widening the gap as r is increased. The peaks within the band gap correspond to the defect modes.

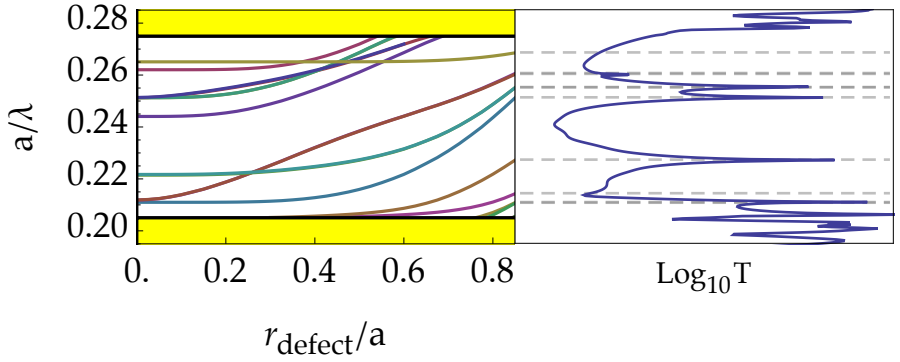

Figure 4.14: Two-dimensional MPB defect mode structure shown with corresponding two-dimensional MEEP transmission spectra for $r_{defect} = 0.85625a$

.

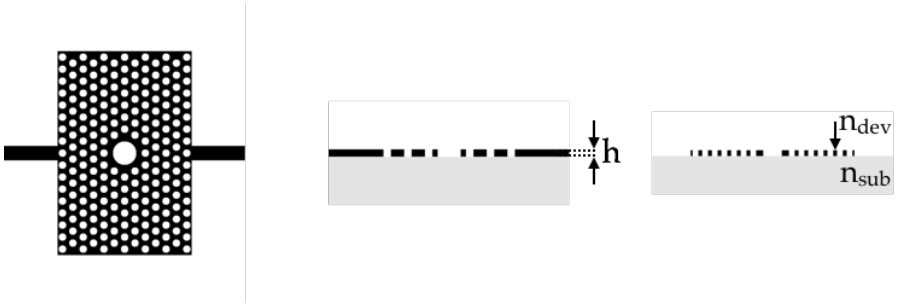

Figure 4.15: The structure simulated for three-dimensional transmission studies. The parameters explored are the height of the device layer h, the refractive index of the substrate n_{sub}, along with the hole radius and defect radius.

.

found in the two-dimensional simulations. Although the transmission over this region is not zero, and there is a smaller subsection for which the transmission is minimized corresponding to the true complete band gap.

For the simulations with varying r_{defect} (see Figure 4.16) we also see features shared with the two-dimensional case, the defect modes are pushed out of the lower band, cross the gap and are absorbed into the higher band as r_{defect} increases, and the isolation of a mode near the centre of the gap for $r_{defect} = 0.7 - 0.9$.

The effect of varying the device layer thickness is shown in Figure 4.17. The band gap region both reduces in size and frequency as the layer thickness increases . In the region of thickness from 0.5-1 the defect modes essentially track this scaling of the band gap, retaining their relative position, for the thicker devices this no longer holds as the top frequency band edge contracts rapidly.

Varying the substrate refractive index (see Figure 4.17) has a pronounced effect as one would expect due to the breaking of the systems symmetry. The band gap essentially disappears as the refractive index increases, although the transmission in these frequencies is still lower than those outside the gap region. There is also a slight red shift of the features, such as band edges and defect modes.

The simulations carried out have identified a promising design including a defect made from an enlarged central hole. Simulations of the transmission spectra through the three dimensional slab structure show a band gap clear with a resonance for which the electric field energies are mainly in free space, and as such open to perturbation

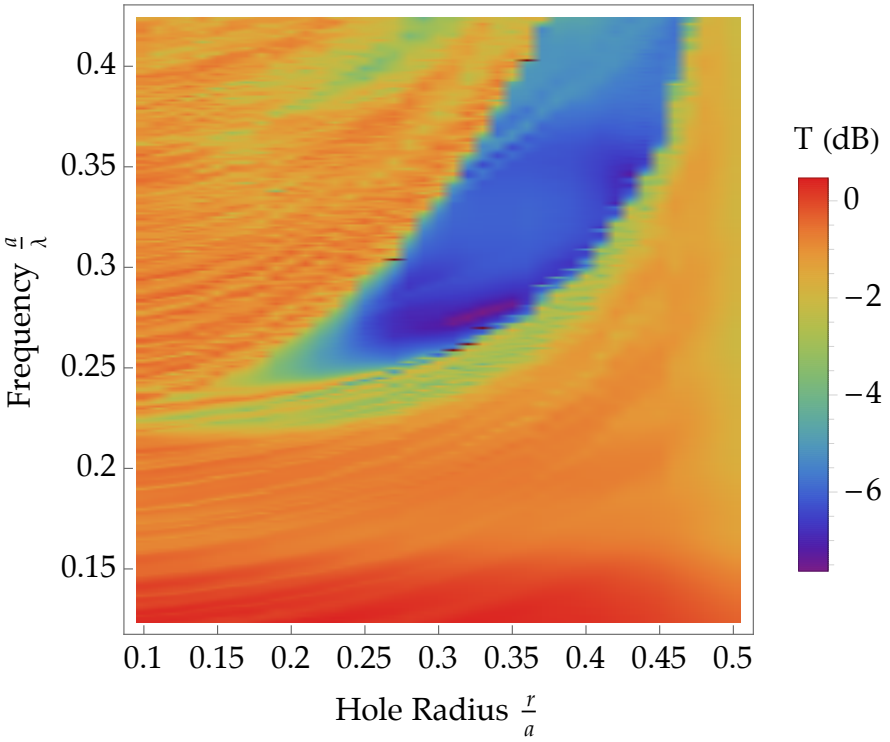

(a)

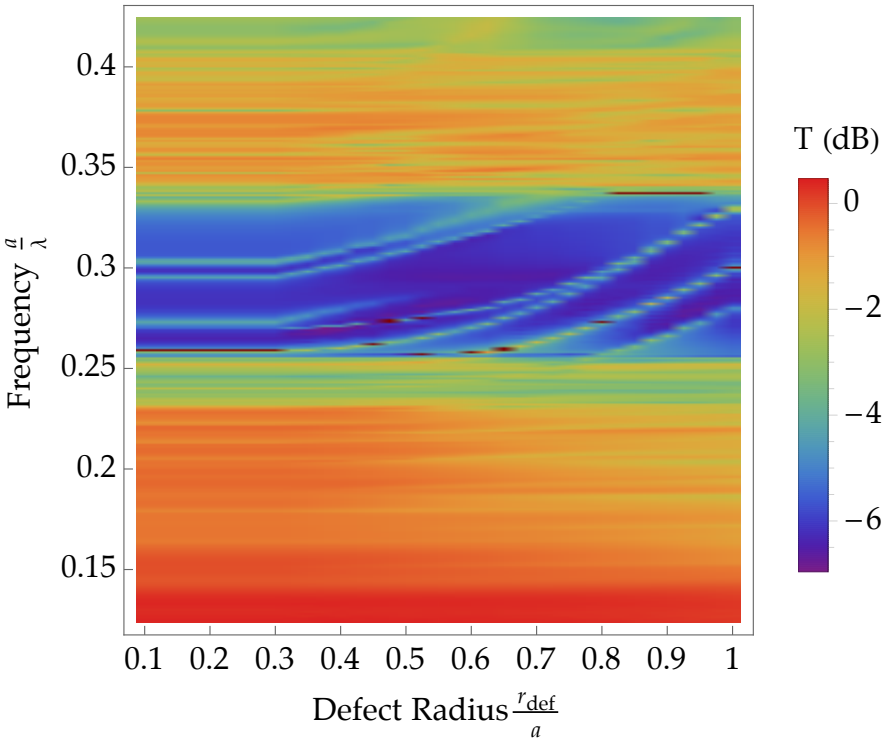

(b)

Figure 4.16: a) Simulated transmission spectra for a three-dimensional defect free device with varying hole radius. The colour scale reflects $Log_{10}T$ in comparison to a straight waveguide with equivalent thickness and substrate refractive index. There is a large region of low transmission which equates to the two-dimensional band gap, however the true guided mode gap is much smaller. b) Simulated transmission spectra for three-dimensional device with varying defect hole radius ($r = 0.3$).

.

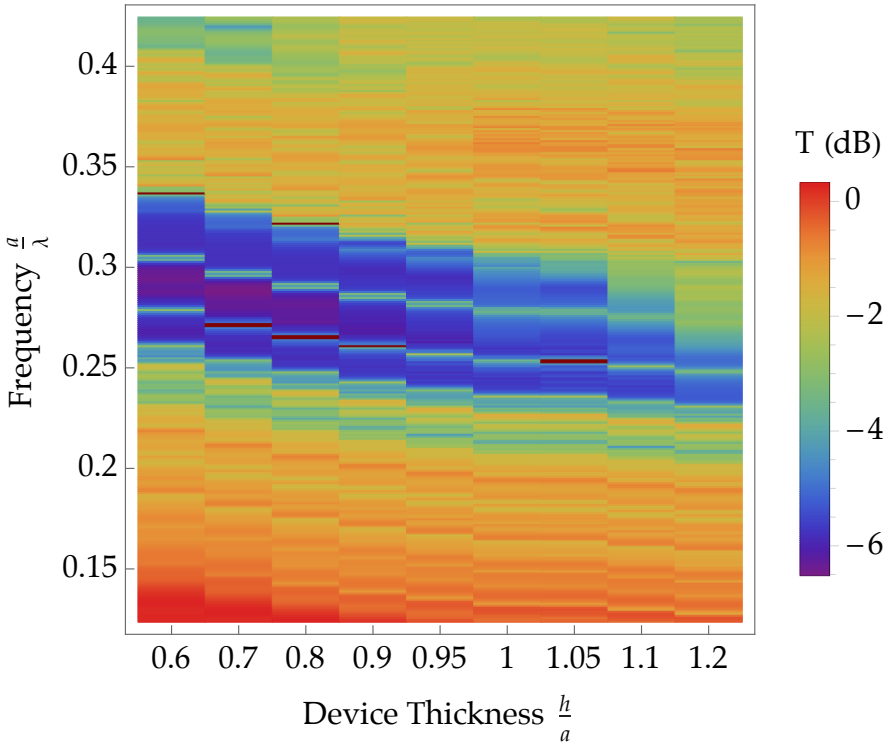

(a)

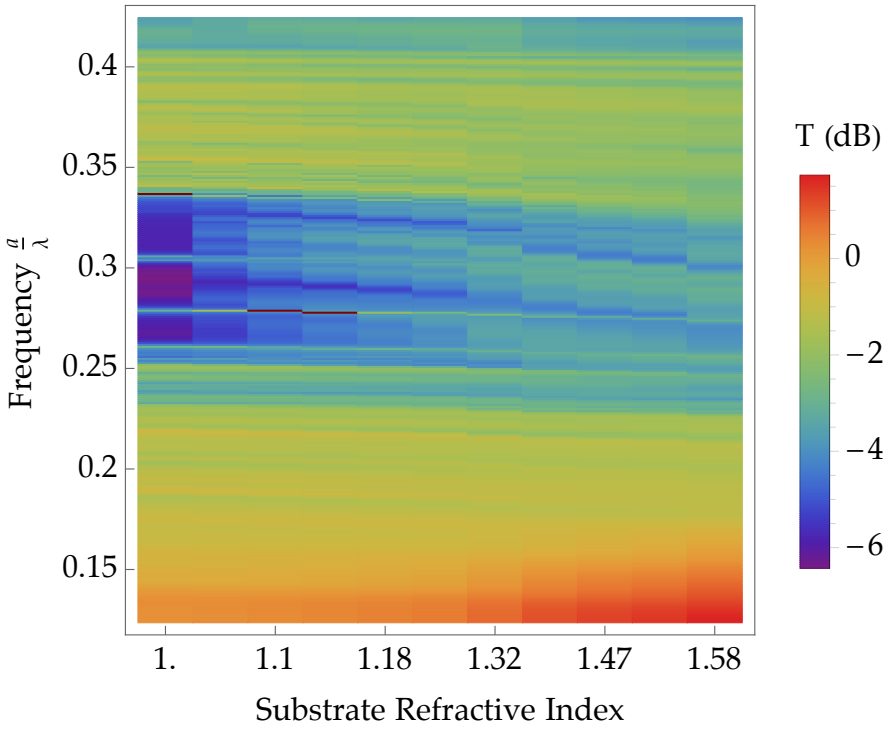

(b)

Figure 4.17: a) Simulated transmission spectra for three-dimensional device with varying thickness ($r = 0.3$, $r_{def} = 0.856$ and $n = n_{SiO2}$) b) Simulated transmission spectra for three-dimensional device with varying substrate refractive index ($r = 0.3$, $r_{def} = 0.856$ and $h = 0.6$)

.

from the binding of outside agents. Ideally further analysis and optimisation would have been carried out but as a proof of concept device this deign was taken forward to the fabrication stage.

4.3 FABRICATION

The complexity involved in fabricating photonic crystals increases with the dimensionality of the photonic crystal. One-dimensional photonic crystals can be made by simply depositing different layers of material. Three-dimensional photonic crystals in the visible regime are still a considerable challenge, although there has been some progress with both top down, multi beam interference lithography techniques[128] and bottom up techniques such as using nanospheres.[129] The structures discussed here are all two dimensional slab photonic crystals. That is to say they consist of periodic patterns in the x-y plane and of finite depth in the z plane.

In this section I will discuss the methods employed to fabricate structures along with grating coupler elements that couple the light into and out of the waveguides addressing the devices. Figure 4.18 shows scanning electron microscope (SEM) images of some of the final devices, consisting of photonic crystal resonator connected by waveguides to grating couplers for input and output optical fibres to our source and detector. Figure 4.19 shows an optical microscope image of a test PhC resonator, the red colouration is due to the patterning.

The basic methodology (see Figure 4.20) makes use of a silicon on insulator substrate to determine the z structure of the slab (a silicon device layer with a silicon dioxide layer below followed by a silicon handle). This substrate is then coated with an e-beam sensitive polymer. Next a pattern is formed in this polymer using electron beam lithography (EBL). This pattern is then transferred into the silicon substrate using reactive ion etching (RIE). All of these steps must be optimised, and are frequently interdependent, for example changing the device layer thickness may affect the etching process, which may in turn affect the polymer masking requirements, which would then in turn effect the electron beam lithography process.

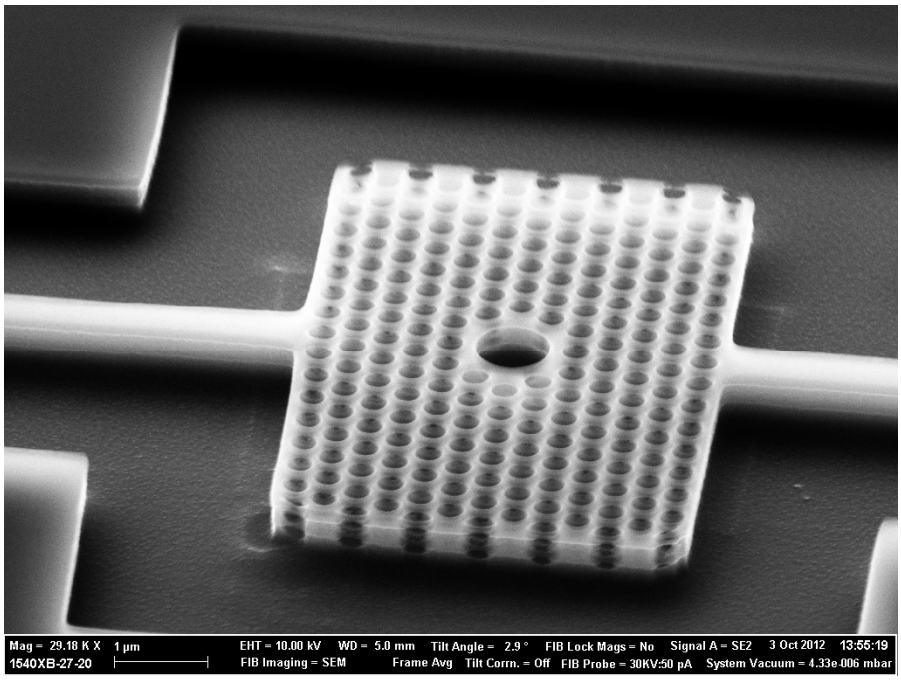

(a)

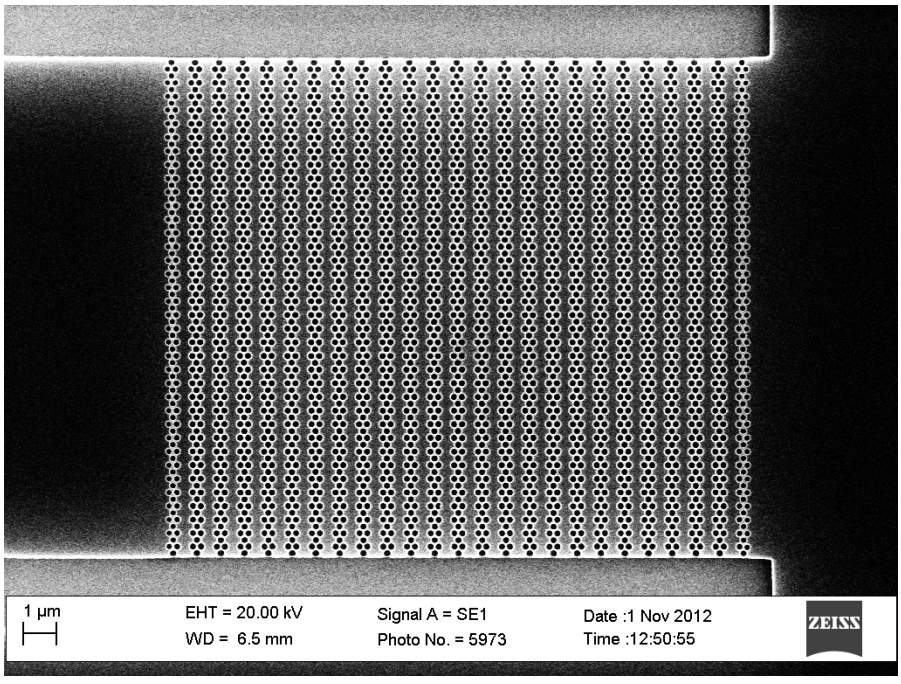

(b)

Figure 4.18: Scanning electron microscope images of completed devices: a) The central device, consisting of input and output waveguides and a photonic crystal cavity. b) A grating coupler.

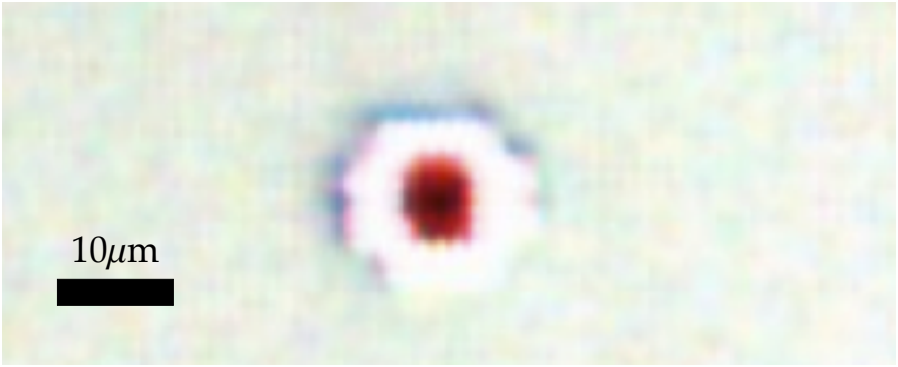

Figure 4.19: A real colour optical microscope (100x) image of a test PhC without waveguides.

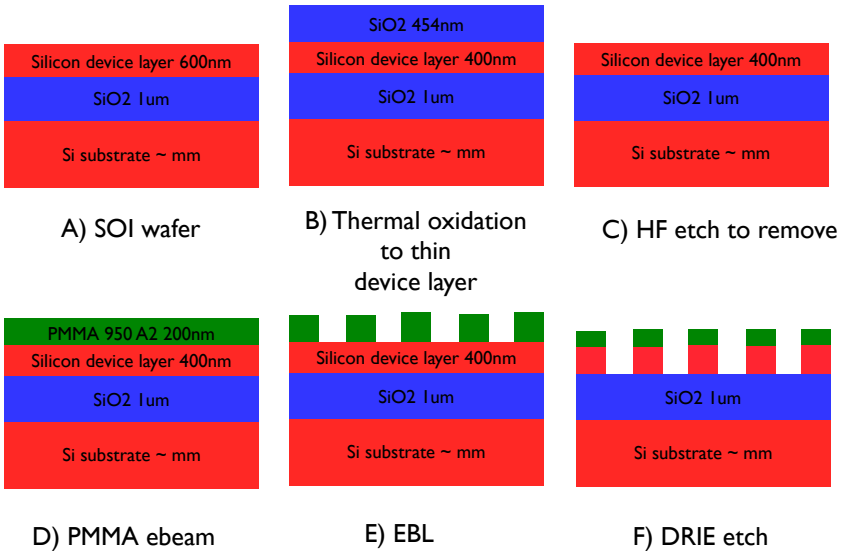

Figure 4.20: Fabrication of slab photonic crystals. The method is to first thin the device layer using a thermal oxidisation followed by a hydrofluoric acid etch (A - C). The second step is to pattern the device layer using electron beam lithography (D-E). Finally a RIE or DRIE etching process is used to transfer this pattern into the silicon device layer, using the SiO_2 as a stop layer.

4.3.1 *Substrate preparation*

The thickness of the device layer is an important factor in creating effective two-dimensional slab photonic crystals. To fine tune the thickness of the device layer in the SOI wafers a preliminary oxidisation step is taken. The thermal oxidisation consumes oxygen from the environment and silicon from the substrate. For every nanometre of silicon consumed 2.17 nm of oxide is grown. The oxide is then removed with a hydrofluoric acid etch. The oxidation rate is sensitive to fluctuations in the furnaces performance and sample location within the furnace. The general procedure is to gradually ramp the temperature up to the oxidisation temperature while flowing an inert gas such as nitrogen into the chamber. Once the ramping process is complete, oxygen is flowed into the chamber and the temperature is held constant. Once the desired time has passed the oxygen is switched off and the temperature is ramped down again. The recipe used was adapted from other users and follows the following set points:

1. Ramp up to 600°C over 20min
2. Ramp up to 1080°C over 20min
3. Hold at 1080°C for oxidisation
4. Ramp down to 600°C over 20min
5. Ramp down to 250°C over 20min

Although the results so far have been somewhat inconsistent, as can be seen in Figure 4.21, they are all within an acceptable thickness for the application. The oxidisation was followed by a hydrofluoric acid etch. This consumes the SiO_2 but does not attack the Si, or at least the relative rate of consumption is so low that it can be treated as such.

4.3.2 *Electron Beam Lithography*

Electron beam lithography (EBL) is a lithography technique that makes use of the very short wavelengths of electrons to pattern down to the nanometer scale. A substrate is coated in a polymer resist that changes its properties when exposed to a beam of electrons. EBL is, in contrast to photolithography, a raster technique that can become prohibitively slow for large patterns. As such it is primarily used for research and

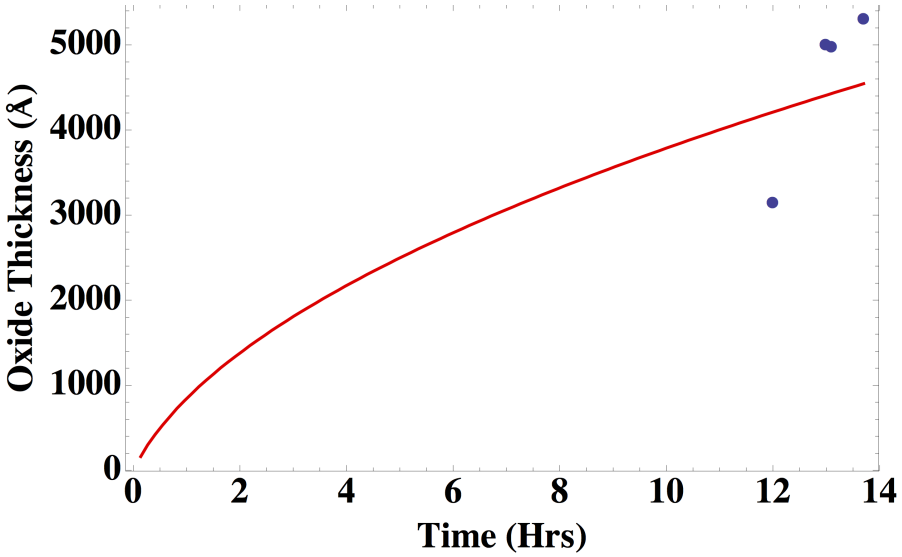

Figure 4.21: Graph shows expected growth of silicon dioxide, blue points show actual measured thickness, the deviations are probably due to variation in the position of the sample relative to the furnace and equipment inconsistencies.

prototyping applications. For our devices we used a positive resist, that is a resist that when exposed to a beam of electrons the bonds holding the polymer together are broken so that when developed in the appropriate chemicals the exposed areas dissolve, leaving the substrate exposed to further fabrication steps.

There are many factors to consider when performing electron beam lithography, but essentially it is a case of tuning the dose received by the photo resist to achieve an accurate a recreation of the designed pattern. As shown in Figure 4.22, electrons do not travel in a straight path through the resist, instead scattering in the polymer and substrate. Furthermore they can excite secondary electrons which may travel up to 30 nm. Calculating the correct dose can often depend on a number of factors:

- Electron energy, increasing the accelerating voltage of your beam leads to higher electron energies and may reduce forward scattering, but increase back scattering.
- Electron beam aperture
- Electron beam exposure time
- Type of photo resist, different photo resists have different response curves.

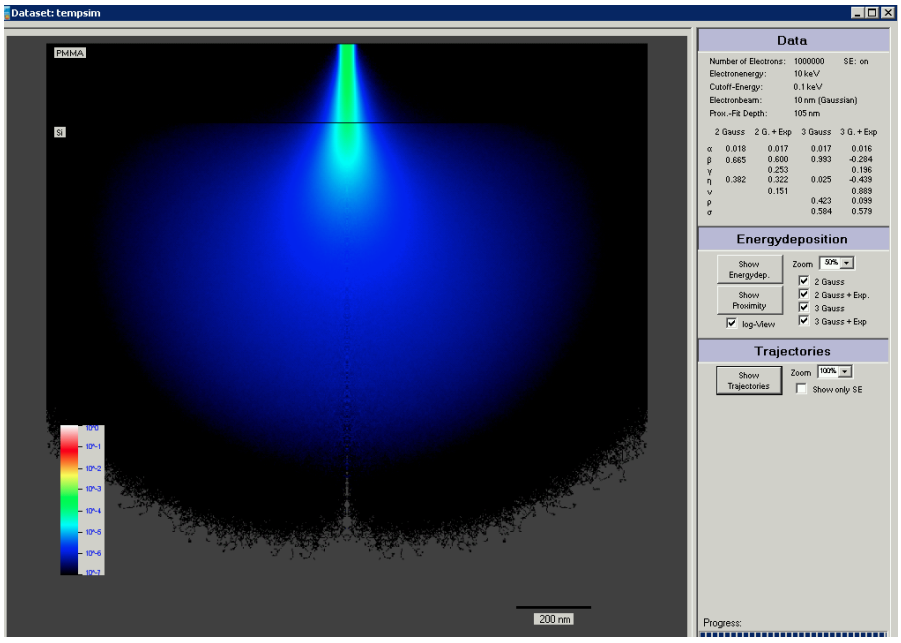

Figure 4.22: A screen shot from Raith software used to calculate the dosage as a function of position from the beam. The beam passes through the PMMA resist into the silicon substrate, with collisions leading to a scattering of the beam

- Thickness of photo resist, as electrons strike the photo resist they undergo forward and in some cases backward scattering, the forward scattering results in a spreading of the exposure area. Backscattered electrons can travel much further and are more destructive to adjacent features than the exposed point itself.
- Substrate material, this can affect scatter and charging.
- Proximity effects, the leakage of does from one part of an exposure to another.

These parameters can be varied using the exposure software (Raith eLine), processing steps and device design.

4.3.2.1 *Dose and pattern size optimisation*

When creating two-dimensional photonic crystal patterns there are essentially two parameters we wish to control: the pitch and the radius of the elements, be they pillars or holes. In terms of our design this can be achieved in two ways, exposing dots, or circles. To expose dots the beam is held on one spot and the dose controls the radius. Alternatively the design can include circles where the EBL software

tries to draw a circle using the beam, for this case we can change both the dose and circle radius. There are pros and cons with both approaches though dots should usually be used for smaller features.

As my devices incorporate both smaller and larger holes, for the grating coupler and cavity respectively, I use both. To optimise the design and dose parameters I fabricated test arrays and analysed the resulting structures using SEM images and a purpose built program. Figure 4.23 shows tests for dose and radius of the PhC holes while Figure 4.24 shows the effects of varying the pitch. The results of the automated analysis for the circle designs are plotted in Figure 4.25. The results of the automated analysis for the dot designs are plotted in Figure 4.26.

The optimum parameters found were 200 nm thick resist, achieved using A4 950 K MicroChem PMMA spun with the following settings:

1. 1000 rpm, with a ramp of 0.5 rpm/min dwell for 1s.

2. 4000 rpm, with a ramp of 0.5 rpm/min, dwell for 30sec.

The exposure uses an accelerating voltage of 10 kV, with an aperture of 20 µm. The beam can normally be focussed to a spot size of approx 15 nm. Automated height control using a laser scanning system is also used to maintain focus over the large distances between samples and along the waveguides. Rigorous write-field alignment steps must be taken to avoid stitching errors along the edges of the waveguides.

4.3.2.2 *Proximity Correction*

The back scattering of electrons in the resist and also off the substrate can lead to exposure as far as 100 nm from the intended location. This can result in a varying 'baseline' dose depending on the surrounding pattern. For photonic crystal devices this can be a problem for maintaining a constant feature size, particularly at the edge of devices. To correct for this, the dose 'spillage' from one feature to the next should be considered. While there are commercial programs that claim to estimate this, the variation between operating conditions means their accuracy is not always adequate. As this was found to be the case I instead created my own software to calculate a correction factor based on non-proximity corrected devices. This custom software calculated the unwanted variation in feature size across the structure and produced new EBL designs with corrected doses for the different

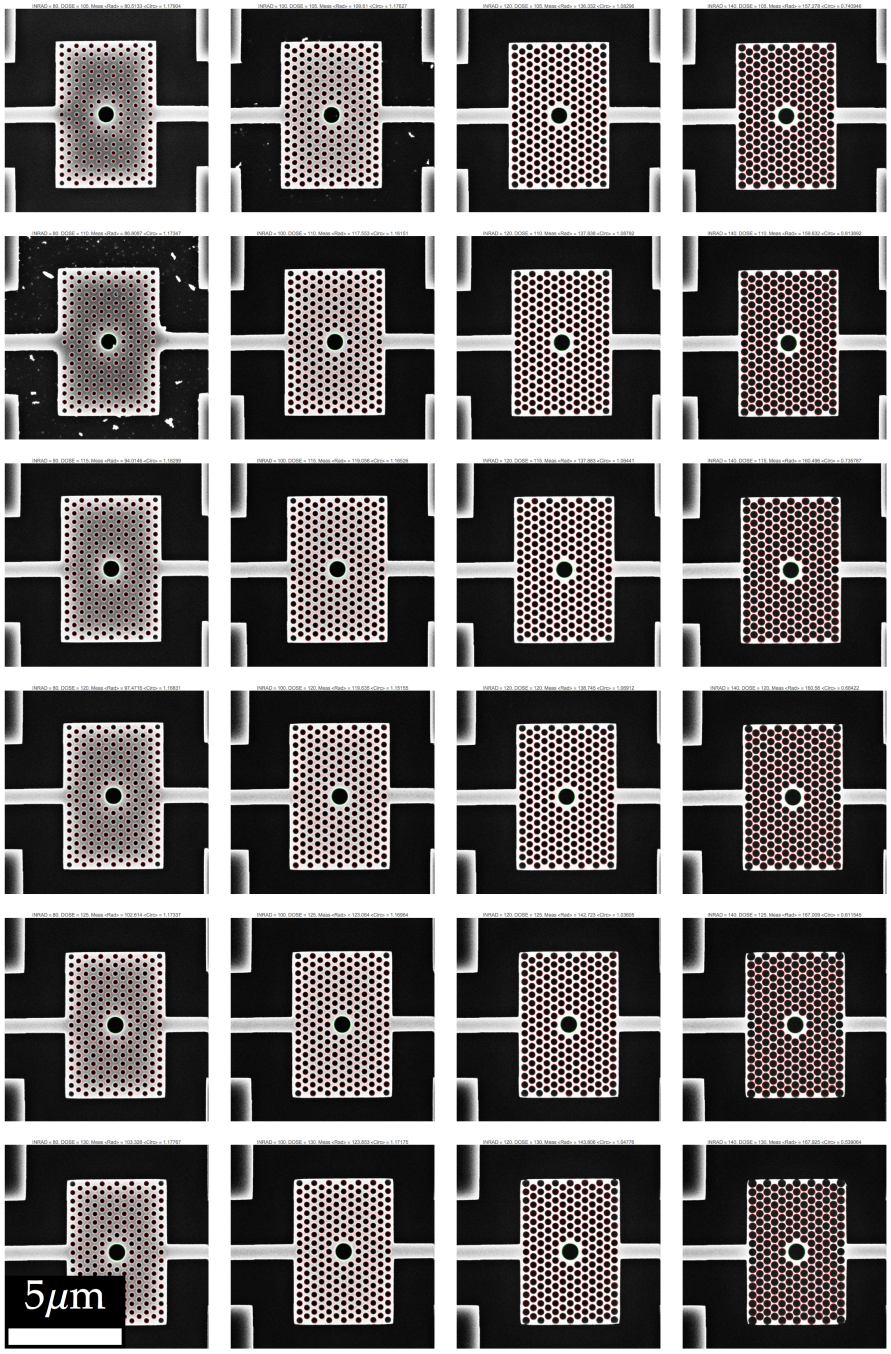

Figure 4.23: SEM images of a selection of devices with varying dose and radius design parameters along with the automated measurement analysis. The combination of altering the design radius and dose can generate varying holes in the fabricated devices, with some combinations offering better uniformity or performance for differing radii. The automated measurements software written in Mathematica has allowed for identifying these combinations over a large range of test devices. All images have the same magnification.

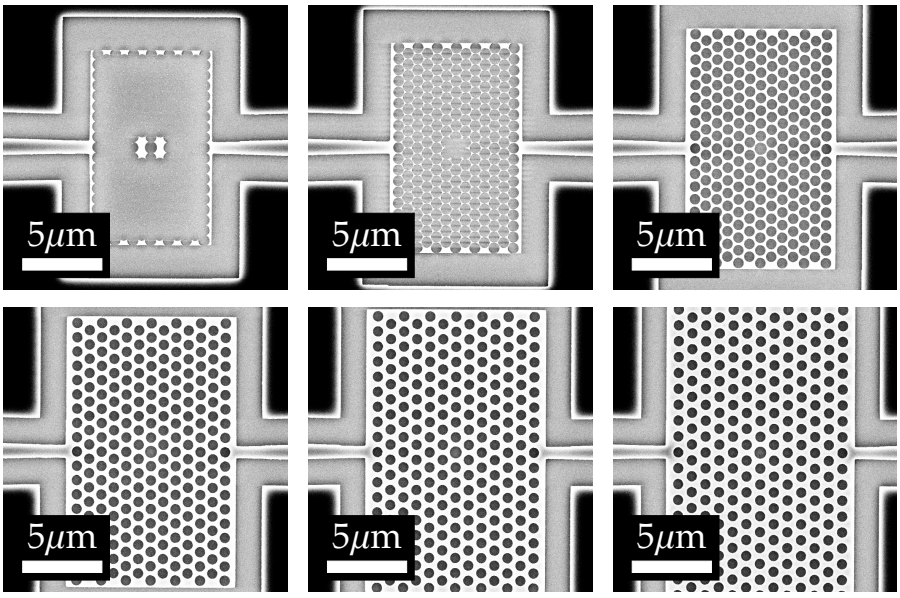

Figure 4.24: SEM images of a selection of devices with varying pitch design parameter. Varying the pitch between holes has, as would be expected, a drastic effect on the effective dose for each hole. As the pitch is reduced the proximity effects increase leading to overexposure of the PhC elements.

elements. Figure 4.27 shows a grating coupler without proximity correction, the new design with the colour scale reflecting the corrected dose and the resulting proximity corrected devices. The oversize holes seen at the edges of the first device are no longer visible in the final devices.

4.3.2.3 *Single step lithography of pillar devices*

Although the focus of this work is the air-hole type of photonic crystal, dielectric pillars are also extremely promising candidates for biosensing and developing a single step process to reliably fabricate them along with the other peripheral components such as waveguides and grating couplers would be desirable. A somewhat serendipitous discovery has highlighted a possible way to achieve this. The method shown here makes use of the fact that as one approaches extremely high doses the behaviour of the resist undergoes an inversion, and the resist begins to behave like a negative resist[130,131]. This was observed while fabricating the standard air hole configurations, and explained the randomly orientated 'notches' on the side of the hole shown in Figure 4.28 b). The notches can be attributed to pillars, which resulted

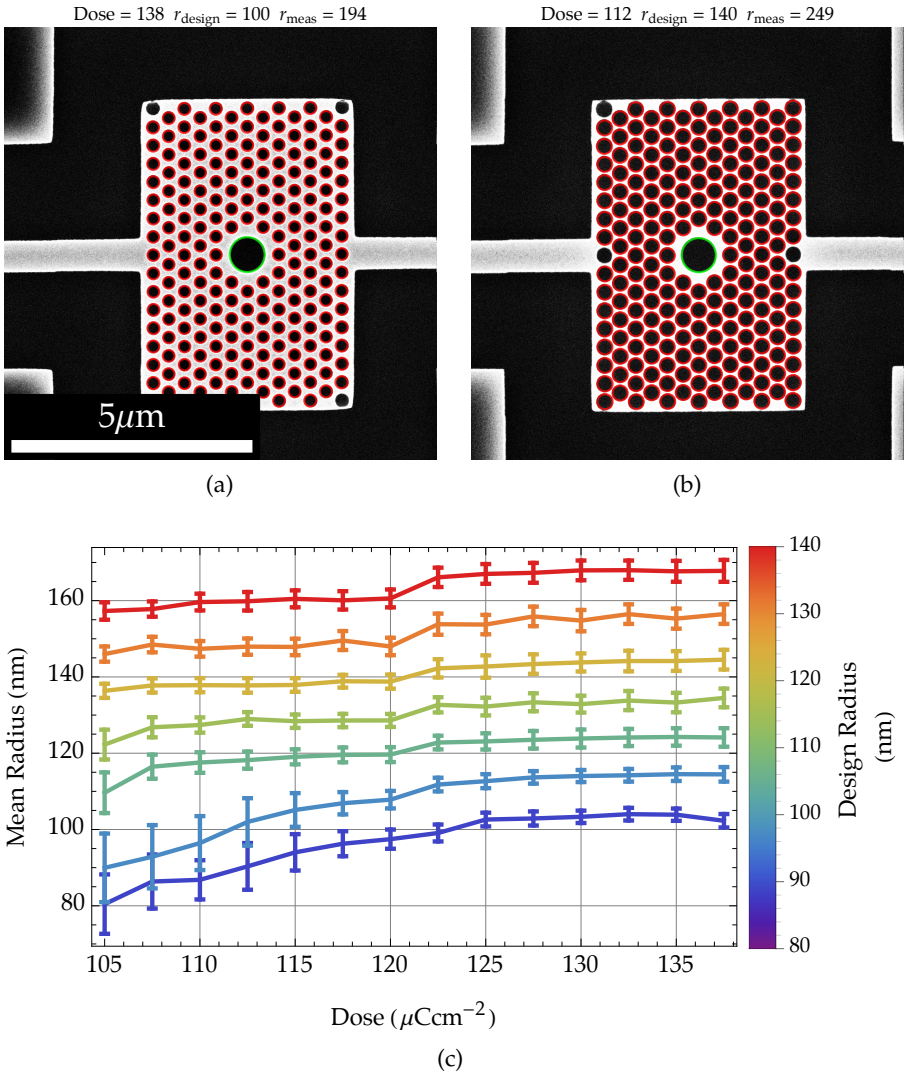

Figure 4.25: Device hole radius optimisation a) Shows a SEM image of a fabricated device, the red circles show the holes identified by the image processing software. b) Shows how the circle radius varies as we increase the dose for varying design radii.

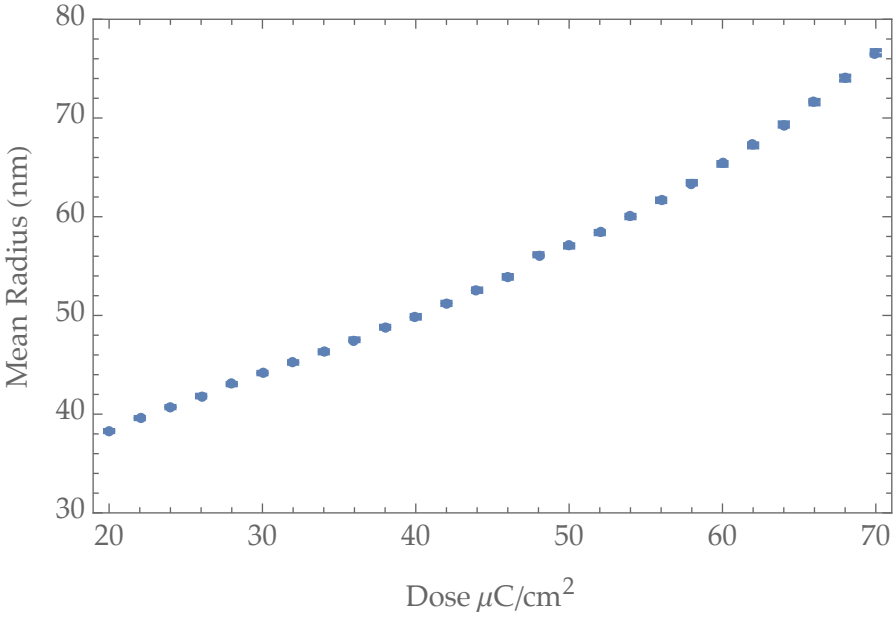

(a)

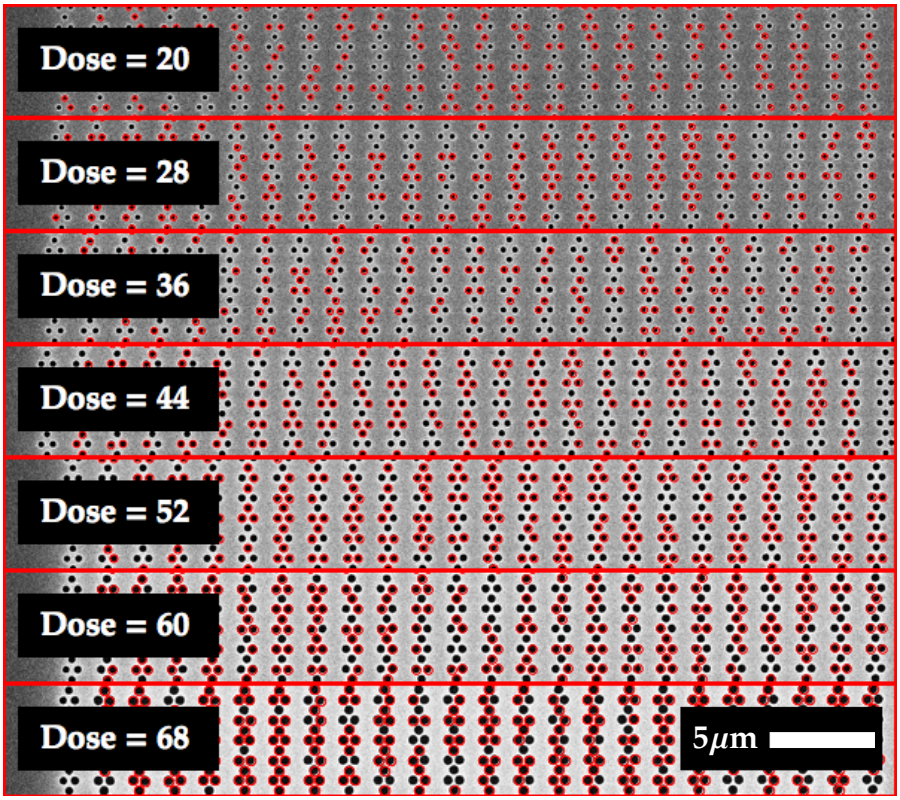

(b)

Figure 4.26: Grating coupler hole radius optimisation a) Shows how the circle radius varies as we increase the dose for dot exposures on the grating couplers b) Shows SEM images of a grating couplers fabricated with the dot method of exposure.

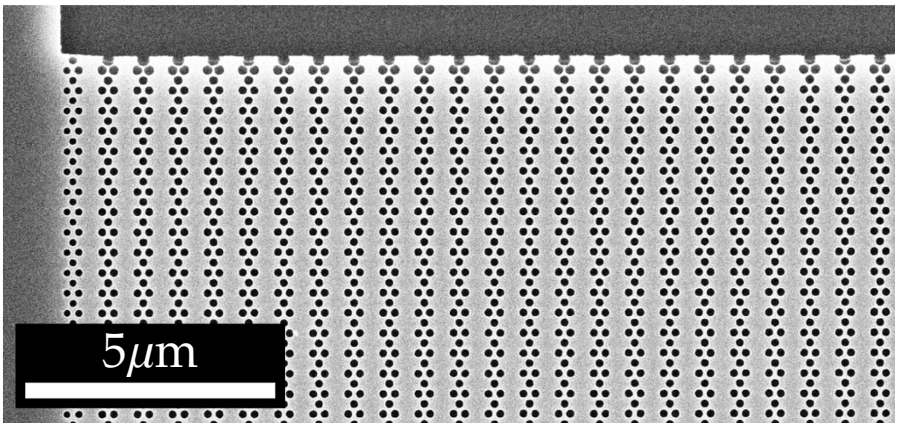

(a)

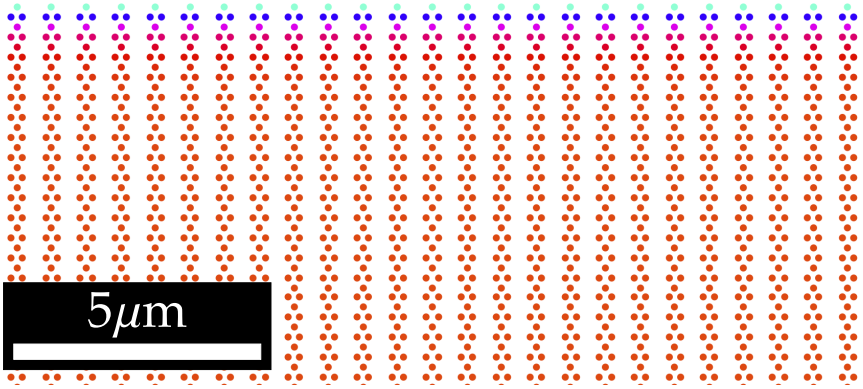

(b)

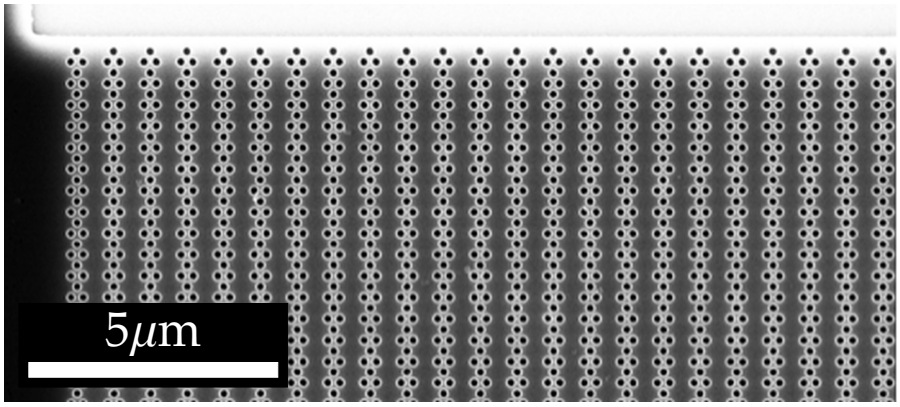

(c)

Figure 4.27: Proximity correction a) Shows a grating coupler fabricated without any proximity correction, the holes at the edge of the coupler are significantly larger than those in the middle due to the extra dose from the isolating edges of the waveguide. b) Shows a dose adjustment based on a custom made Mathematica program that analyses the over exposure of uncorrected devices. c) A grating coupler fabricated with the adjusted dose shows the uniformity of hole size is greatly improved.

from overexposure in the centre of the holes, and then had fallen randomly to one side in post processing.

I have shown it is possible to harness this unwanted behaviour to produce grating couplers and waveguides, which require positive resist, and pillar devices which require negative resist in a single exposure. These results are shown in Figures 4.28 and 4.29. Although this method needs further optimisation these preliminary results are very promising. Optimisation must be undertaken in particular regarding the post processing, both etching and wash steps need to be performed with great care due to the fragility of the structures.

4.3.3 *Reactive Ion Etching*

To transfer the EBL patterns into silicon I used reactive ion etching, a standard microfabrication technique that uses a chemically reactive plasma to etch in an anisotropic manner. A chemically reactive ion is accelerated onto the sample (see Figure 4.30). This approach uses a combination of physical and chemical processes to remove the target material. The direction of the electric field and the resulting acceleration of the ions results in a highly directional etch.

The main process outcomes to control are etch depth and, side wall angle and smoothness. This is done by tuning flow rates, forward powers and also establishing good practice in terms of coil matching and chamber preparation to ensure stability and repeatability of results. The optimised recipe for this etch used a flow rate of 90 sccm for SF_6, 80 sccm for C_4F_8. An oxygen flow was experimented with but ultimately abandoned as too aggressive.

The fabrication of devices on this scale is not a trivial endeavour. The design and dose optimisation for accurately recreating both the grating coupler and photonic crystal devices has been thoroughly investigated and optimised. The etching protocols have also been refined such that the pattern transfer into SOI is accurate and robust. Through the use of self made software this process optimisation has been carried out for a large range of devices and parameters. Ideally further characterisation of side wall roughness and SOI device layer thickness would be undertaken. Another process step not yet carried out is a backside etch to isolate the PhC structures from the SiO_2 substrate, although this could be introduced to future devices. In summary, by establishing robust preparation, exposure and etching

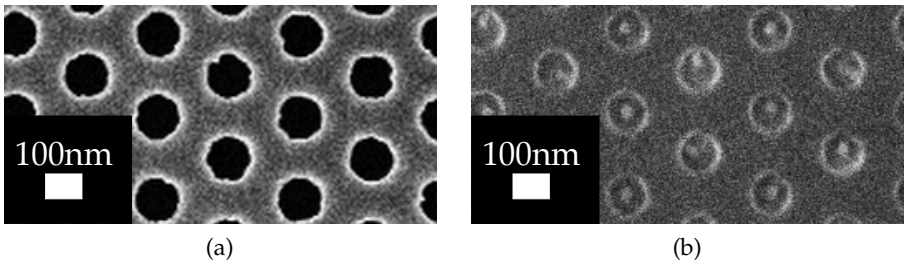

(a) (b)

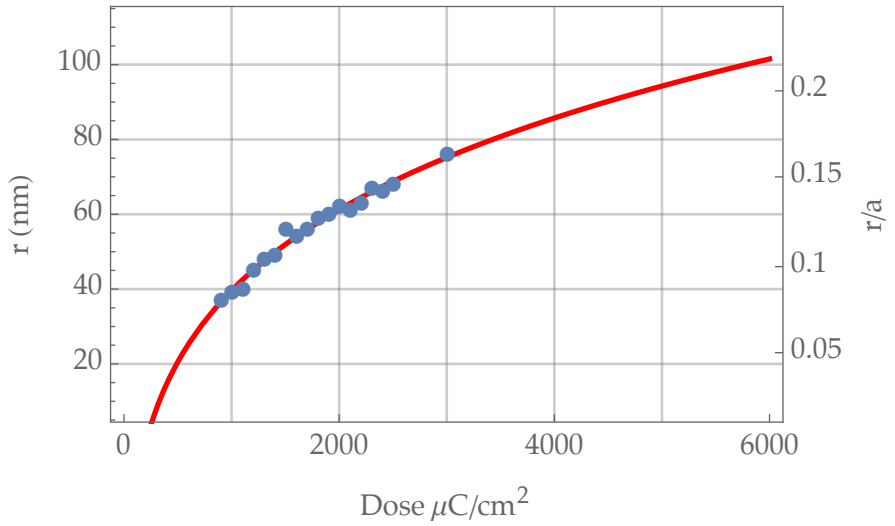

(c)

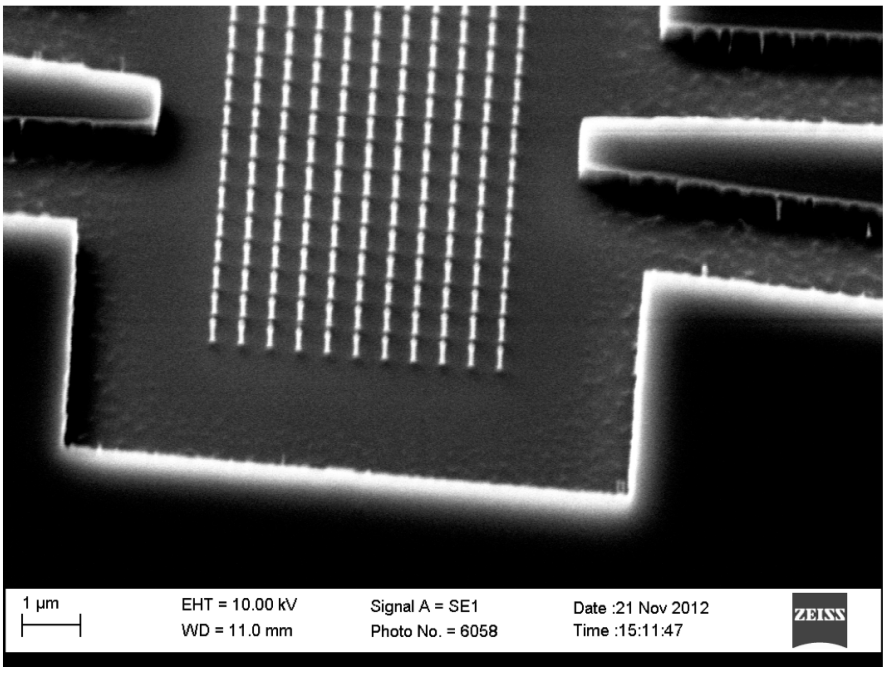

(d)

Figure 4.28: a) SEM image showing fabrication errors for of an etched air-hole device. The errors are the randomly orientated notches b) SEM image of the resist after an over exposure shows the cause of the notches, resist inversion has created very fine pillars n the centre of the holes which collapse in a random direction c) Shows the pillar radius as a function of dose d) A SEM of a pillar device

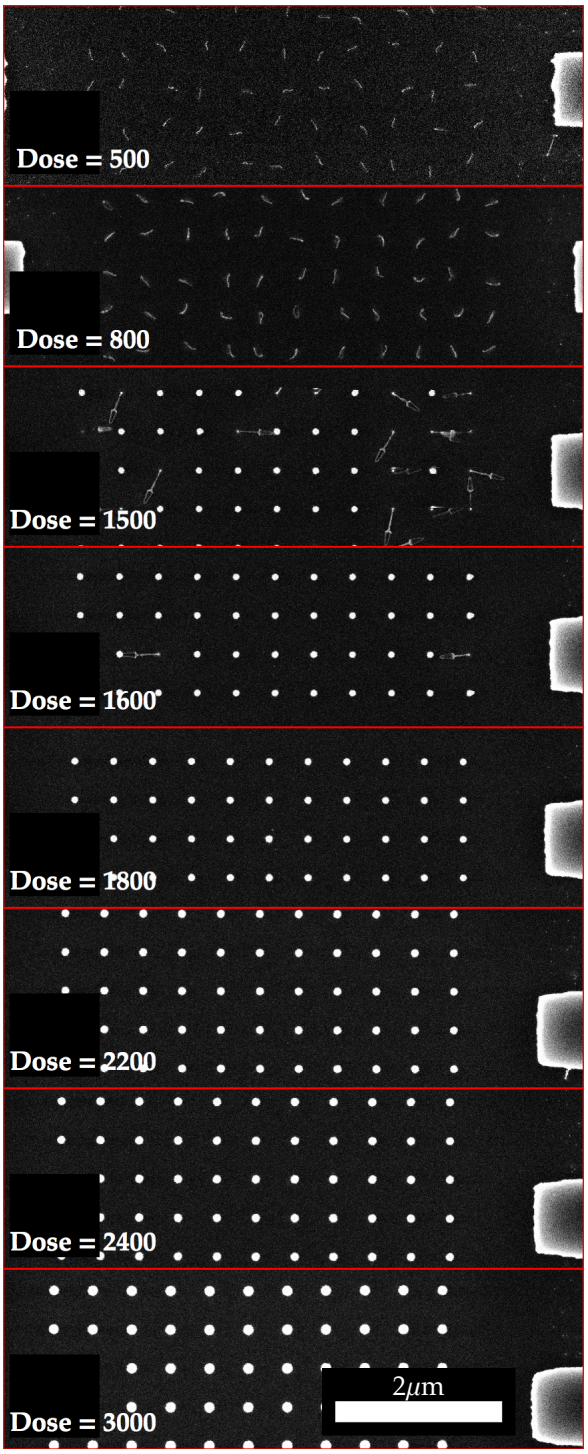

Figure 4.29: Pillar devices with varying dose. For the lowest doses the structures have completely collapsed. For 1500 μC cm^{-2} some pillars have collapsed and it is visible that resist pattern is under-etched such that the the silicon pillars are actually much narrower. For higher doses the structures remain intact although the resist removal and washing steps remain to be optimised.

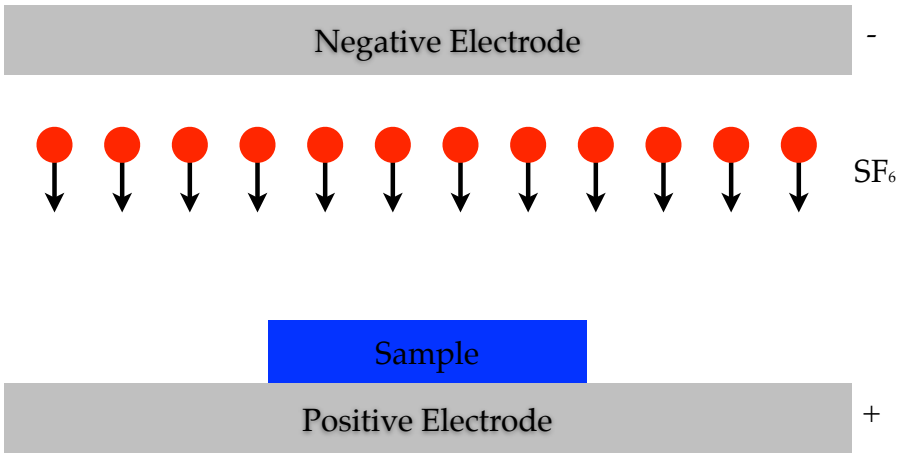

(a)

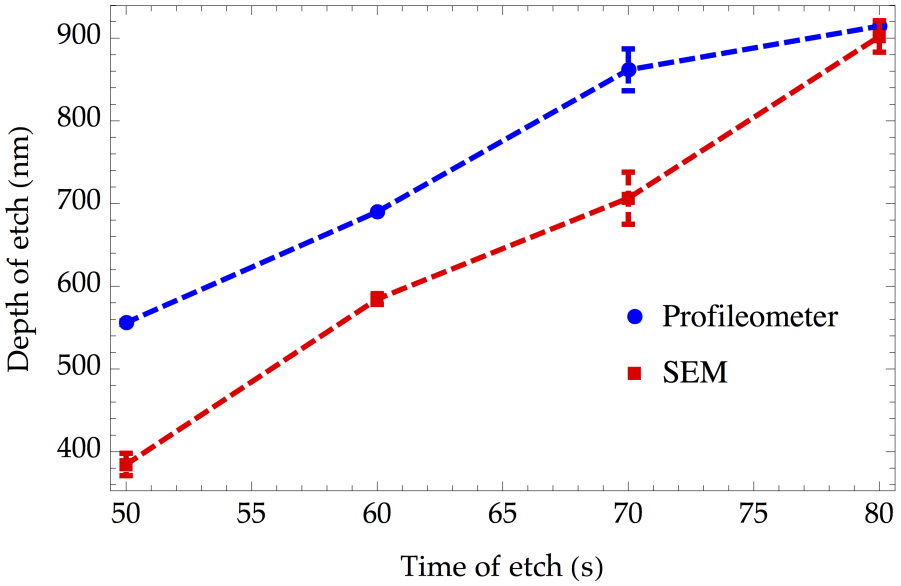

(b)

Figure 4.30: a) is a diagram of the RIE process, whereby a chemically reactive ion is accelerated onto the sample. b) shows the measured etch rates measured using the Dektak profileometer and SEM

processes a number of devices have been successfully fabricated, these devices include input and output grating couplers along with a variety of PhC cavities, the next section details the measurement methods used to characterise these devices.

4.4 MEASUREMENTS

To characterise the broadest possible optical properties of the devices they have been measured using a broadband super-continuum source and spectrum analyser. To deliver light to and from the devices, optical fibers, grating couplers and waveguides were used.

The source used a was supercontiniuum laser (NKT SuperK EXTREME EXR-15), which emits from the visible to the infrared (476–2400 nm) paired with a NKT SPLIT module that coupled the infra red portion (1100–2400 nm) into a polarisation maintaining fiber. To measure the ouptut from the devices an optical spectrum analyser (OSA) was used (Yokogawa AQ6370D, courtesy of the EPSRC engineering instrumentation pool). This OSA is capable of measuring from 600–1700 nm, giving a workable overlap between the source and detector of 1100–1700 nm.

To couple light into the devices a bare polarisation maintaining fiber was aligned with grating couplers fabricated into waveguides addressing the devices. Light was then captured from the output grating coupler using a bare single mode fiber. The output light was divided in a 90:10 splitter with 10% going to a standard IR photo diode (918D-IR Newport) as quick feedback for alignment purposes, 90% was sent to the OSA for spectrum measurement. Figures 4.31 and 4.32 show the experimental configuration.

The super continuum source was sufficiently bright in the near infrared that the coupling of light into and out of the devices could in be observed with a regular USB microscope (see Figure 4.32). This allowed us to perform a coarse alignment based on the scattered light viewed in this way. Once light was observed to be coupled into the device further automated processes were used to optimise the alignment. LabVIEW software (see Figure 4.33) was created to control the experimental apparatus and automate alignment and measurement of multiple devices based on the following steps:

- Remove output fiber from field of view (large step of output motor) for image acquisition.

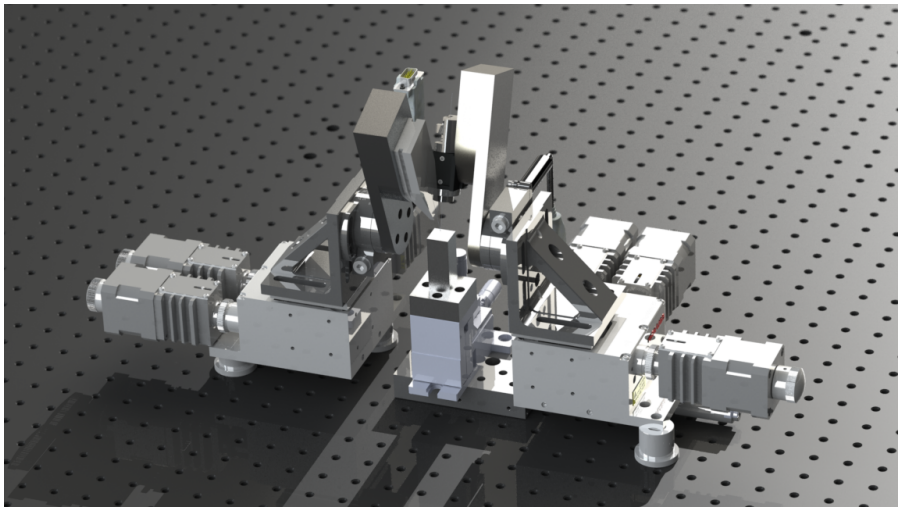

Figure 4.31: Experimental configuration. Two stepper motor micropositioners are used to align the fiber with the grating couplers. Further motorised rotational stages are used to adjust the angle. Custom made pieces are used to mount the fiber launchers. A coarse stage is used to move the sample from one device to the next.

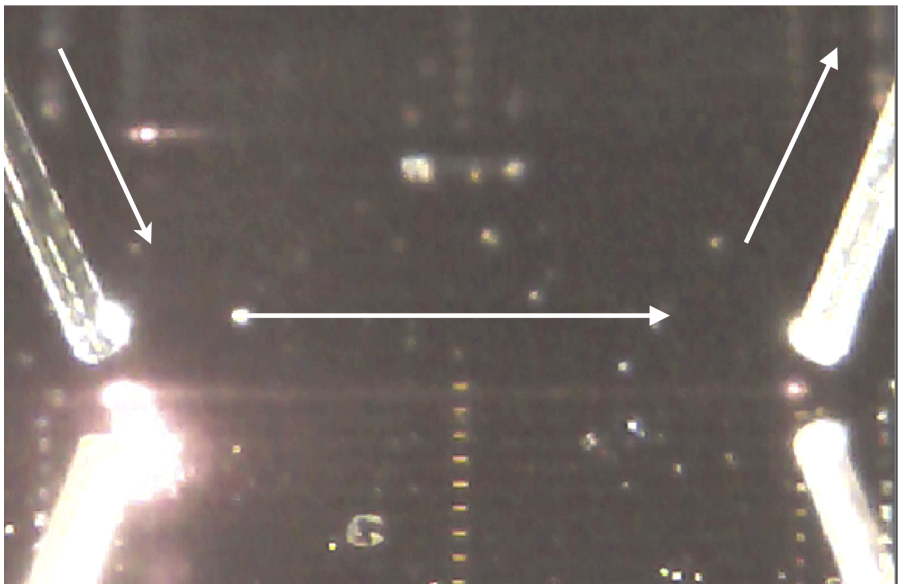

Figure 4.32: Grating coupler configuration. By observing the scattered light it is possible to obverse the light coupling into a waveguide device and out of the adjacent grating coupler

- Maximise input fiber coupling by scanning input fiber while measuring intensity of scattered light at output grating coupler using image processing.
- Return output fiber to original position and maximise output alignment by scanning position of output fiber while measuring transmitted power using photodiode.
- Fine scan (typically 20 µm in 0.1 um steps) of both input and output fibers with measured transmitted power. Data from a typical scan measurement is shown in Figure 4.4.
- Measure spectrum with OSA.
- Move sample with coarse motor such that next device is beneath fibers.
- Repeat.

By combining this functionality with the fabrication of large arrays of devices relatively high throughput and automated measurement of devices was made possible.

The precise coupling configuration was a standard angled FC/APC connector from the NKT source to a PM fiber. This fiber was then spliced to a longer segment of bare fiber which was cleaved to give a clean end. This was coupled into a device and then out into a bare single mode fiber, itself spliced onto a standard FC connector. This was fed into 90:10 splitter and onto the photodiode and spectrum analyser. A single mode fiber was used for collection so it could be coupled efficiently into the 90:10 splitter available, the losses due to the insertion of the separate fibers and components were measured and are shown in Figure 4.35.

To determine the angle of the polarisation maintaining fiber a Glan-Calcite laser polariser (ThorLabs GL10-A) was fixed while the fiber is rotated using a rotational fiber launcher. The transmitted power (see Figure 4.36) was then fitted with a two part function accounting for the changes due to polarisation which occurs with 180° periodicity but also the small variations in alignment with 360° periodicity.

4.4.1 *Supercontinuum Source*

A relatively unique aspect of the measurement technique employed is the use of a supercontinuum source. This source provides both

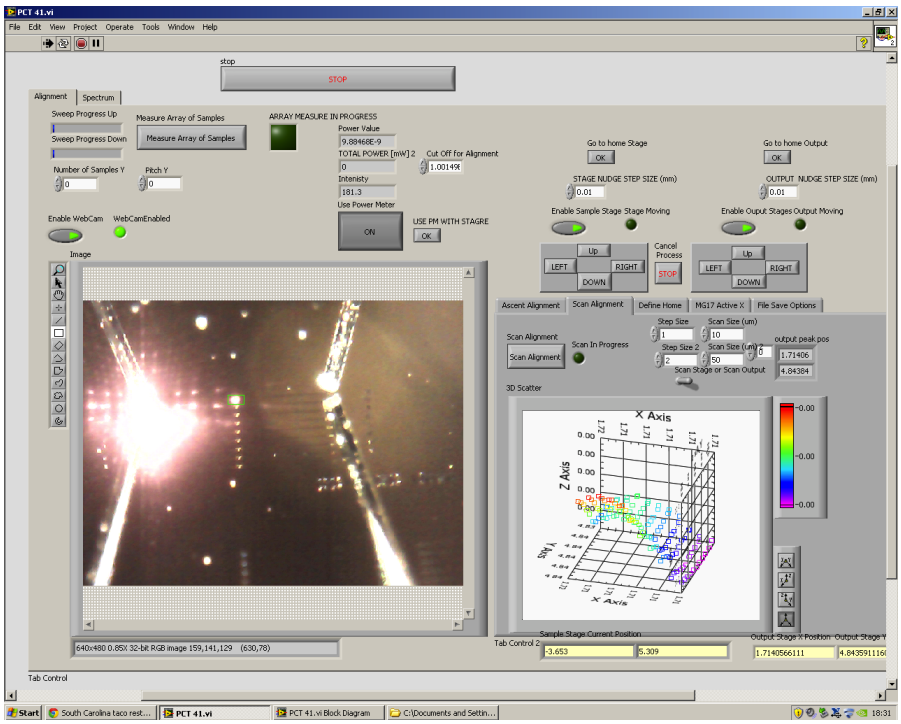

Figure 4.33: Experimental control software written in LabVIEW. The software automates the process of alignment, and allows for unsupervised measurement of multiple devices.

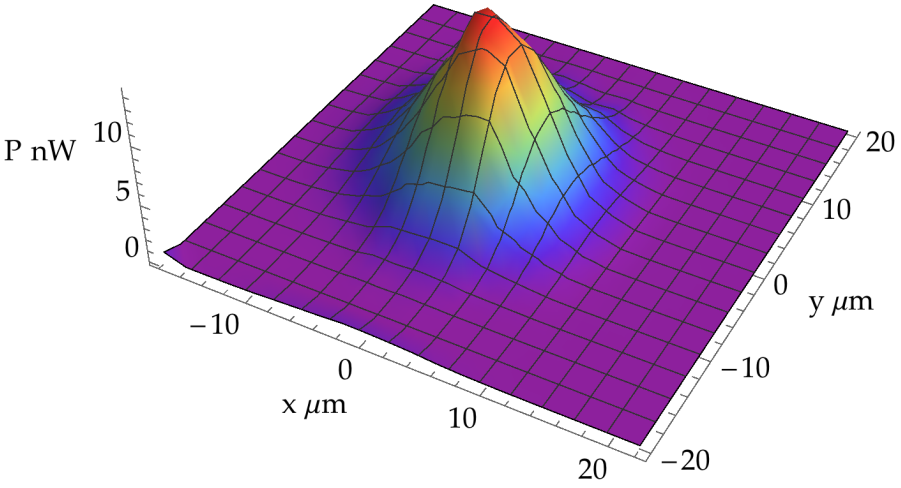

Figure 4.34: Alignment scan showing the area in the x-y plane where coupling through the grating coupler is achieved

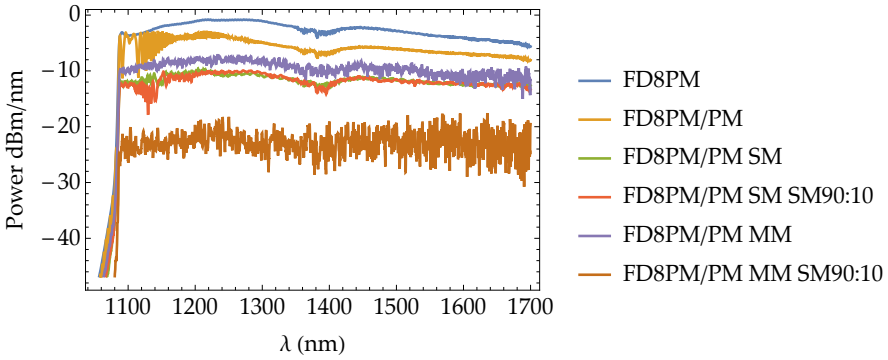

Figure 4.35: Measurement of coupling with different components, The NKT supplied PM maintaining fiber output (FD8PM), this connected using standard FC/APC connectors onto a similar similar PM fiber (FD8PM/PM), this then butt coupled into SM and MM (FD8PM/PM SM and FD8PM/PM MM) with and without a 90:10 SM splitter (FD8PM/PM SM SM90:10 and FD8PM/PM MM SM90:10). The experimental configuration used with devices was FD8PM/PM SM SM90:10.

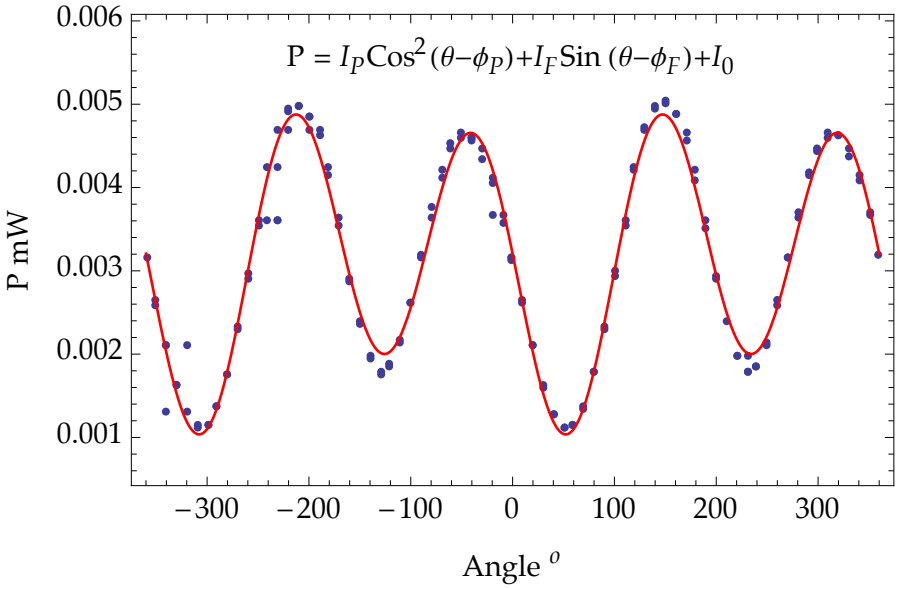

Figure 4.36: Measurement of the transmission through a fixed polarisation filter as the PM-fiber is rotated. There are two contributions to the change in transmission, primarily the polarisation which occurs with 180° periodicity but also the small variations in alignment with 360° periodicity, fitting a suitable function allows for a more accurate measurement of the polarisation and allows for extrapolation to the precise values required. $I_P = 0.0032$,$\phi_P = -36.9^o$,$I_F = 0.0015$,$\phi_F = -49.8^o$,$I_0 = 0.0015$

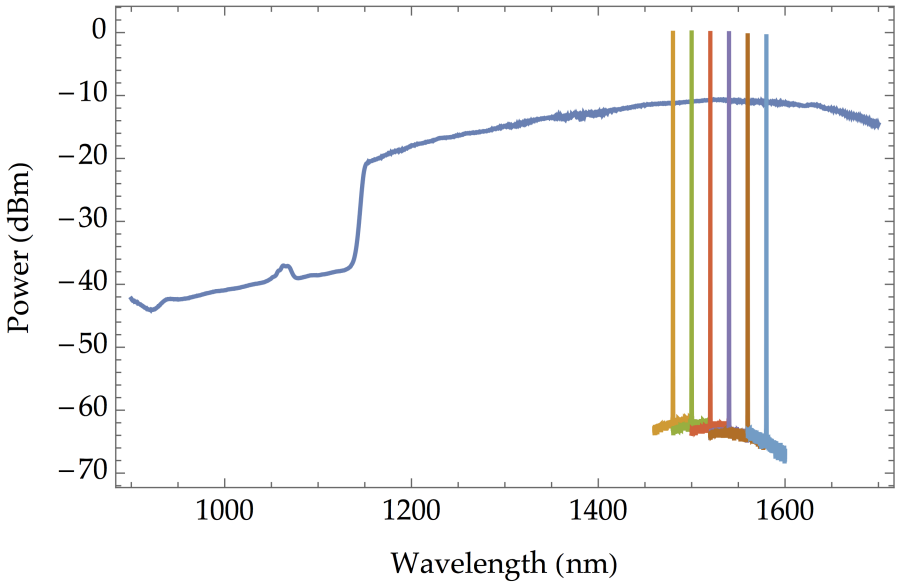

Figure 4.37: Measured spectra of our supercontinuum source compared to a tunable laser source (Hewlett Packard, 8168F).

the laser like intensity and coherence along with an extremely broad spectral response. This meant we were able to probe the devices response across a broad range of wavelengths.

The NKT supercontinuum source uses a photonic crystal fibre as a nonlinear material for transforming a sharp pulse into an extremely broad source (see Figure 4.37) while maintaining the spatial collimation of the original laser input[132].

Supercontinuum generation, first observed by Alfano and Shapiro in the 1970's[133,134], does not refer to a specific process but instead a combination of processes that can combine to lead to the extreme pulse broadening the name implies. There is an interplay between the dispersion in the fibre, the spectral broadening of the input pulse, and the self phase modulation, the non linear response of the fibre to a high energy pulse that results in a frequency chirp across the temporal profile of the pulse[135]. These two processes can lead to periodic soliton generation and soliton fission, which result in new frequencies being generated both at the high and low frequency edges of the pulse bandwidth. The combination of a broad but well collimated and extremely bright light source makes it ideal for our experiments.

4.5 GRATING COUPLER RESULTS

One of the challenges of measuring on-chip devices is coupling them to macroscopic optical elements such as light sources and detectors. A common approach is to use fibre coupling and waveguides to deliver the light directly to and from the device. Coupling into the waveguide can be achieved in a a number of ways. The narrow device layer available to us (approx 0.5 µm) makes fiber butt coupling, which involves bringing the tip of a fibre as close as possible to the cleaved edge of a waveguide, quite challenging[136] and inefficient without the use of specialist lensed fibres. To avoid this problem we opted to use grating couplers. Prior to discussing the photonic crystal devices I will summarise the work done on optimising the grating couplers required to measure them.

Grating couplers are periodic modulations in a waveguide's refractive index that allow for the coupling of diffractive modes into and out of the waveguide. This can be considered as matching the diffractive behaviour of the grating to the supported modes of the waveguide.

The waveguide uses index guiding to trap the light. Due to the requirements of continuous translation symmetry these guided modes are discrete. The out of plane component of the wavevector must take a discrete set of values such that the wavefronts are in phase, this can be described in terms of the propagation constant:

$$\beta = k_0 n_{eff} = k_0 n_2 \sin\theta_m \tag{4.2}$$

Where β is the propagation constant of the waveguide mode, and takes the value $-\beta$ for reverse propagation, n_2 is the refractive index of the waveguide slab, k_0 is the wavevector of the waveguide mode, n_{eff} the effective refractive index of the waveguide mode and finally θ_m is the angle of the waveguide mode. Secondly there is the equation describing the transmitted modes of the diffraction grating:

$$n_2 \sin\theta_t^m = n_1 \sin\theta_i - m\frac{\lambda}{\Lambda} \tag{4.3}$$

Where n_1 is the refractive index of the material on the incident side of the grating, θ_i is the angle of incidence, Λ is the period of the grating, n_2 is the refractive index on the transmission side of the grating and θ_t^m is the angle of transmission relative to the grating normal, where m indicates mode number and is an integer.

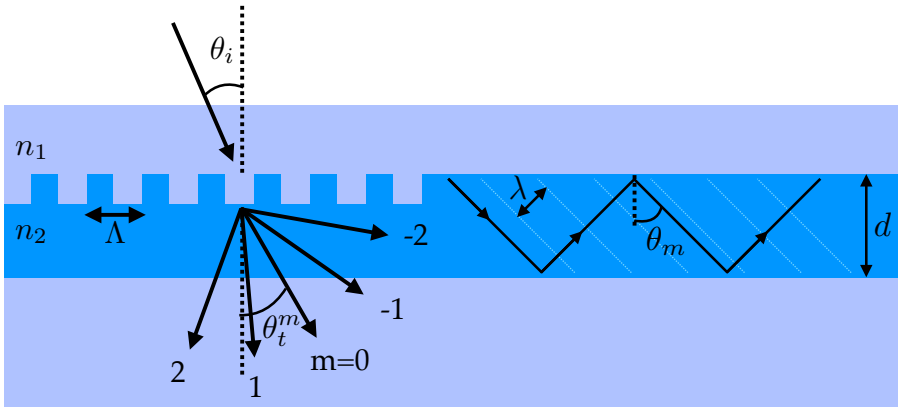

Figure 4.38: Grating coupler schematic. n_1 is the refractive index of the material on the incident side of the grating, θ_i is the angle of incidence, Λ is the period of the grating, n_2 is the refractive index on the transmission side of the grating and θ_t^m is the angle of transmission relative to the grating normal, where m indicates mode number and is an integer. For waveguide coupling the diffraction mode must match a guided mode in the waveguide. This will occur at a discrete set of angles that the ensure phase matching between wavefronts required by the continuous translational symmetry of the waveguide.

To excite modes within the waveguide the modes of the diffraction grating θ_t^m must match the waveguide mode θ_m. Using this resonance condition we can combine these two equations to get a simple phase matching equation:[137]

$$n_{eff} = n_1 \sin\theta_i - m\frac{\lambda}{\Lambda} \tag{4.4}$$

or in terms of λ

$$\lambda = \frac{\Lambda}{m}\left(n_1 \sin\theta_i - n_{eff}\right) \tag{4.5}$$

Where θ is the angle of coupling, n_1 is the refractive index of the cladding, n_{eff} is the effective refractive calculated based on the materials and geometry of the grating along with the mode (n_{eff} is essentially a function of the filling factor due to the grating coupler geometry. This is plotted for silicon in the experimental range in Figure 4.39.) Λ is the pitch of the grating and m is an integer denoting mode number. Using this equation one can begin to design suitable grating couplers to work at the wavelengths of interest.

A further issue for consideration was the fabrication of the grating couplers. Many methods have been implemented to fabricate grating

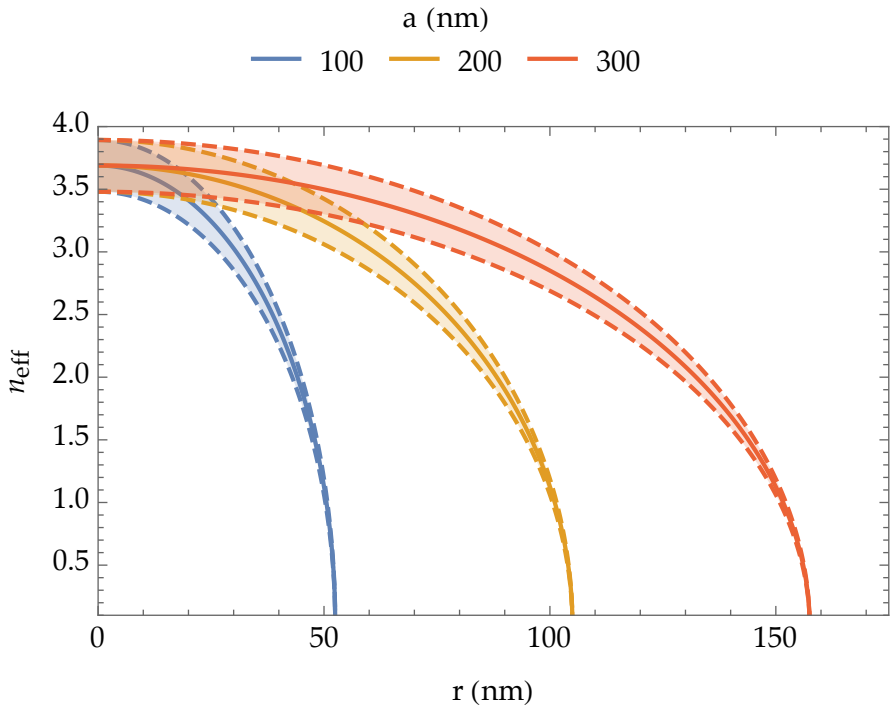

Figure 4.39: Effective refractive index plotted as a function of grating coupler geometry. Varying the pitch and radius result in varying filling factors, which are weighted to estimate the effective refractive index. The solid lines show the values for 1400 nm, the dashed lines and shaded regions show the variation due to the dispersive nature of silicon in the experimental range 1100–1700 nm.

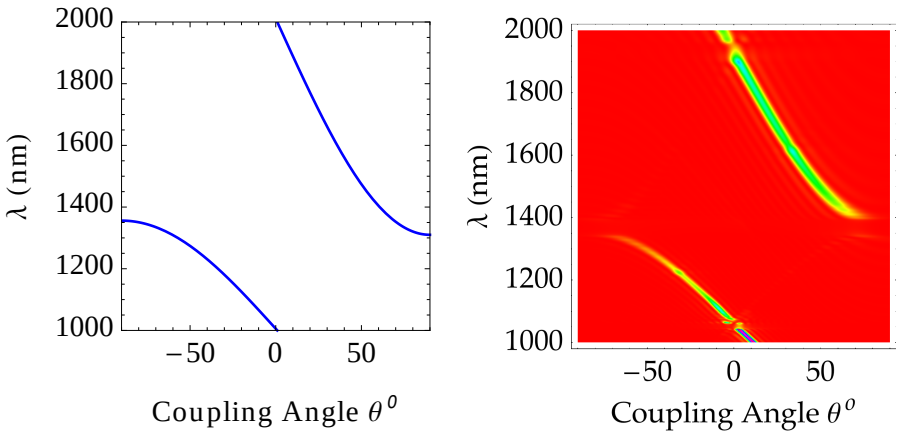

Figure 4.40: a) and b) show the phase matching and FDTD results for a grating coupler with hole radius 69 nm. The deviations between the two results can be attributed to the finite depth of the devices in the simulations, and back reflections from the silicon dioxide box layer

couplers, but the most common way of modulating the refractive index is to shallow-etch strips part way into the wave-guide.[138] A through-etch normally would result in the refractive index contrast being too high and unacceptable losses.[138] As the PhC devices require a full through etch and so as to avoid a two step fabrication process, an alternative approach developed by Liu et al.[139] was followed. By etching strips of holes on a hexagonal lattice a reduced effective refractive index (the averaged refractive index of silicon and air weighted in accordance to the filling factor of the etched patterns) is created for efficient coupling (see Figure 4.41). Calculations based on this design and the above simple phase matching condition and specific FDTD simulations match well, as can be seen in Figure 4.40. The differences can be ascribed to the finite depth (less than 1 µm) of the grating couplers and back reflections from the bottom of the silicon dioxide box layer below the grating coupler.

To test the performance of the grating couplers and experimentally verify the theoretical predictions I fabricated and measured a number of grating coupler devices consisting of a ridge waveguide in with a grating coupler at either end. The devices covered a range of geometrical parameters, such as the hole radius, inter row pitch and intra row pitch. We also tested the basic size and shape of grating couplers (see Figure 4.41).

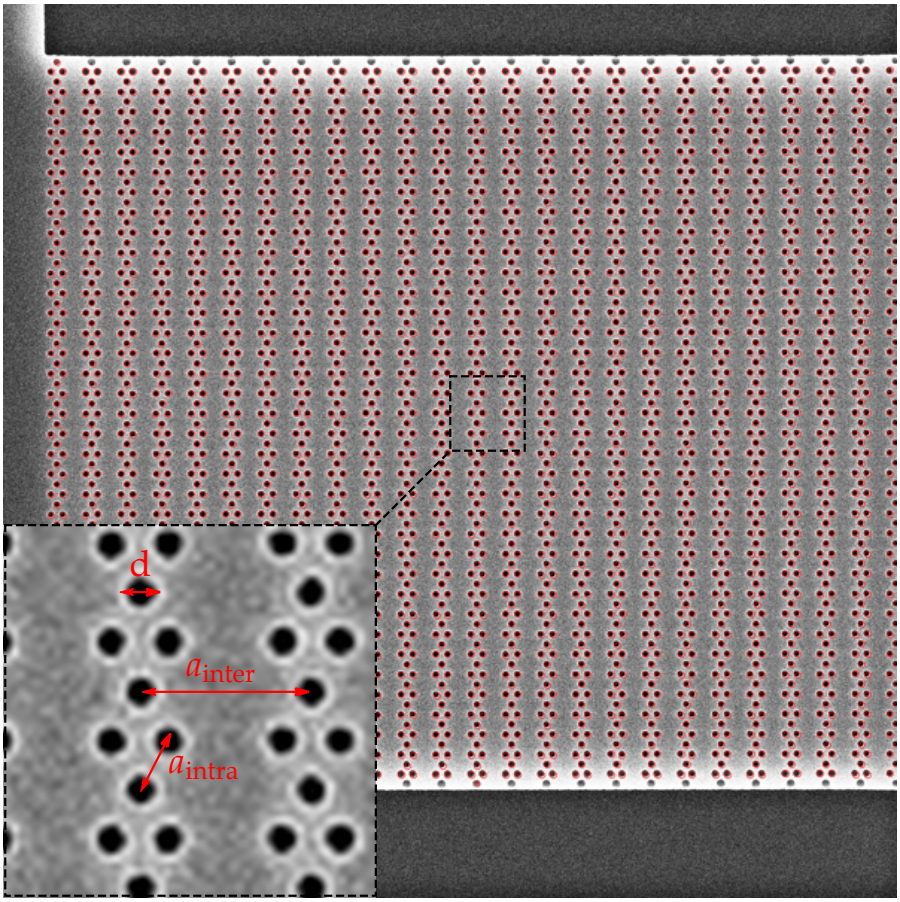

Figure 4.41: Grating coupler have been fabricated for a range of geometries, the key parameters that were varied are the hole diameter d, the pitch of the holes that make up the rows a_{intra} and the pitch between rows a_{inter}

4.5.1 *Grating coupler fabrication*

I fabricated a series of devices with varying hole radius by varying the dose used on point exposures. The dose was varied from 36–72 $\mu C\,cm^{-2}$ in steps of 4 $\mu C\,cm^{-2}$. This achieved a spread of hole radius from 65–95 nm. Cropped sections of these devices and the measured radius are shown in Figure 4.42.

A series of devices with varying hole to hole pitch, a_{intra} were fabricated. The pitch was varied from 220–300 nm in steps of 20 nm. Devices with a varying row to row pitch a_{inter} were also fabricated with pitches ranging from 0.6–5 µm. Cropped sections of these devices are shown in Figure 4.43.In addition to this devices were made that had varying grating coupler length and width.

4.5.2 *Grating coupler results*

Using the automated alignment system we were able to measure a large variety of devices. We studied how the grating couplers performed as a function of coupling angle θ, polarisation ϕ ((Figure 4.44), radius of the holes r, the intra row pitch a_{intra}, the inter row pitch a_{inter}, the width and the length.

To study the polarisation dependence we varied the polarisation angle of the input fiber. The resulting transmission spectrum through the wave guide-grating coupler system is shown in Figure 4.45. We observe a number of things, first of all the TE polarisation is indeed transmitted strongly with a broad peak centred around 1600 nm. This is shifted slightly from the design of 1550 nm. Secondly there is still significant transmission in the TM case with an alternative transmission band at 1500 nm for the TM input. Finally we also observe a secondary transmission band for both the TE and TM case, this is much less clean than the longer wavelength band but still delivers significant power, and is likely due to a higher order diffractive mode.

The overall coupling efficiency is low ($< 5\%$) suggesting the grating couplers and waveguides are not performing optimally, likely sources of these losses are the roughness of the etched side walls, and variations in the device layer thickness. The transmission does follow the expected behaviour however with a clear band of transmission for the TE case in the expected window. The lower wavelength transmission peak is a higher order mode. This lower wavelength mode has not

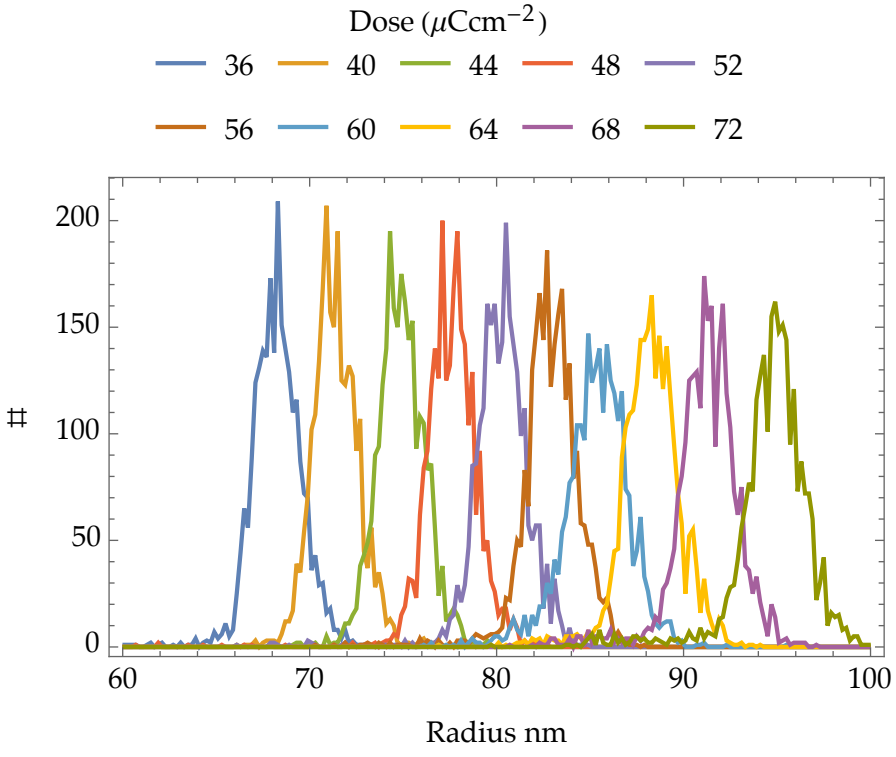

(a)

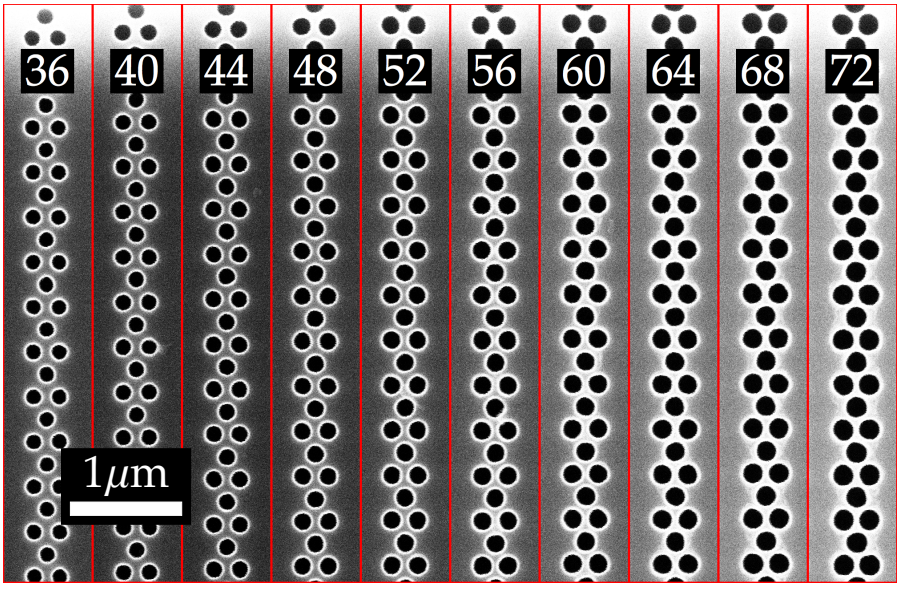

(b)

Figure 4.42: a) the measured distributions of hole size for each of the grating coupler devices, b) crops of the actual devices (inset numbers correlate to dose).

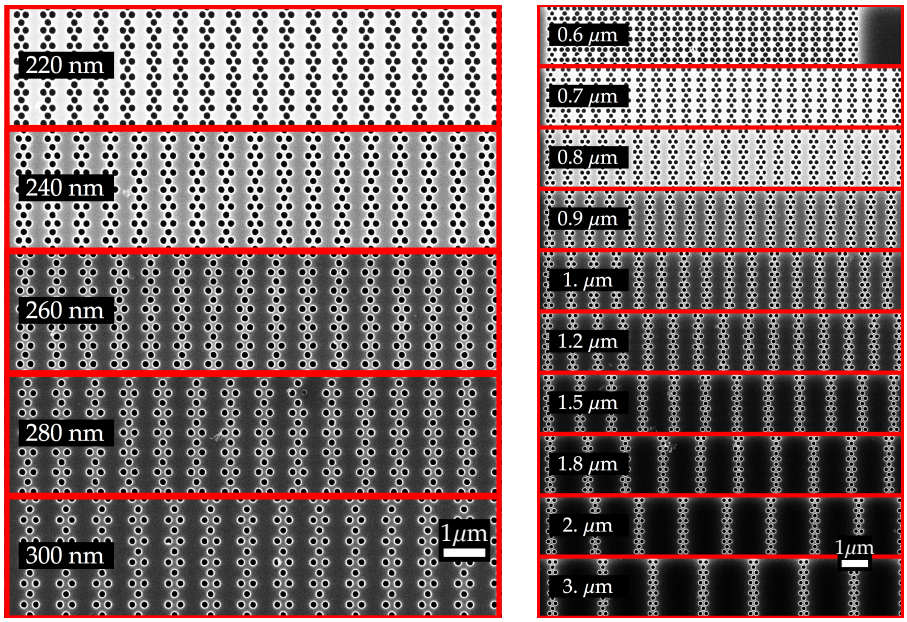

(a) (b)

Figure 4.43: a) The devices with varying pitch a_{intra} b) The devices for varying pitch a_{inter}. Automated image analysis measured the hole size for the varying devices for further analysis / fitting of experimental data.

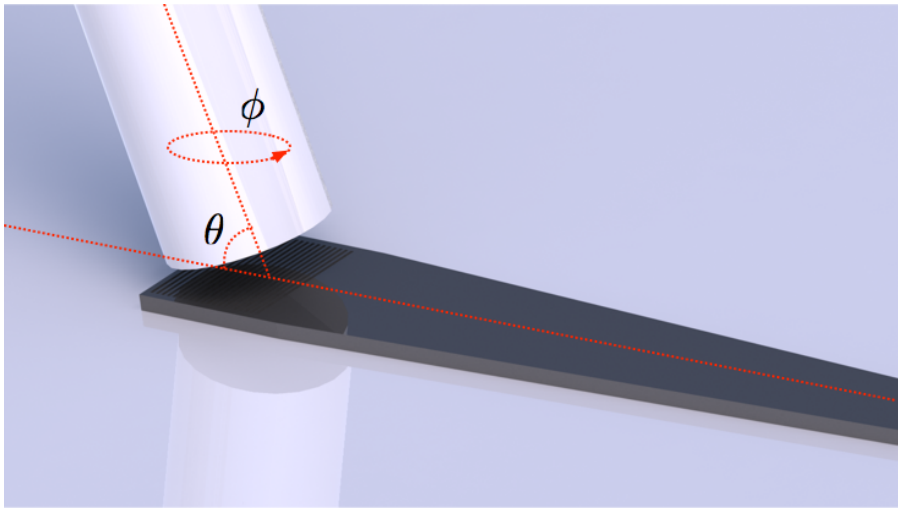

(a)

Figure 4.44: a) shows a diagram of the fiber coupling system, by varying the angle ϕ of the PM fiber we selectivly couple TE or TM light, changing θ will shift the peak coupling wavelength.

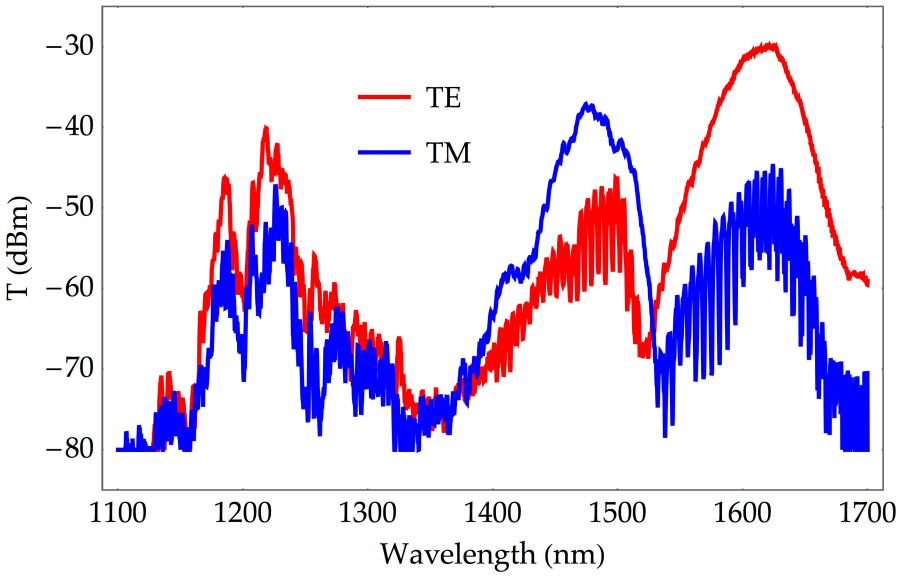

(a)

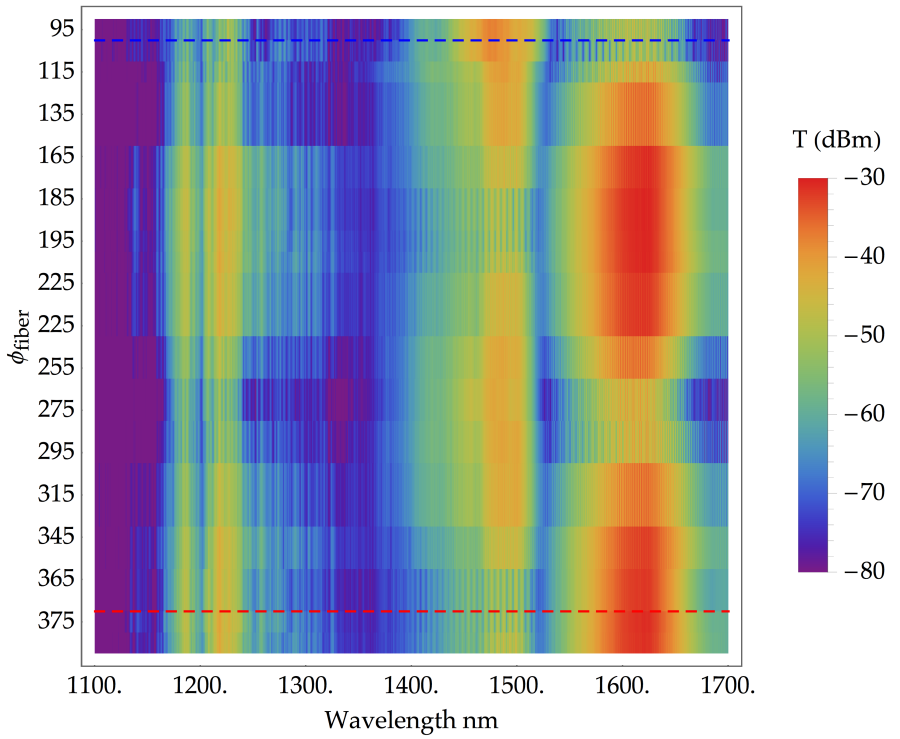

(b)

Figure 4.45: TE and TM transmission through the wave guide - grating coupler system. a) shows the transmission spectrum at TE (red) and TM (blue) polarisations. b) shows the the transmission as a function of polarisation angle, with the dotted lines showing the slices taken for a)

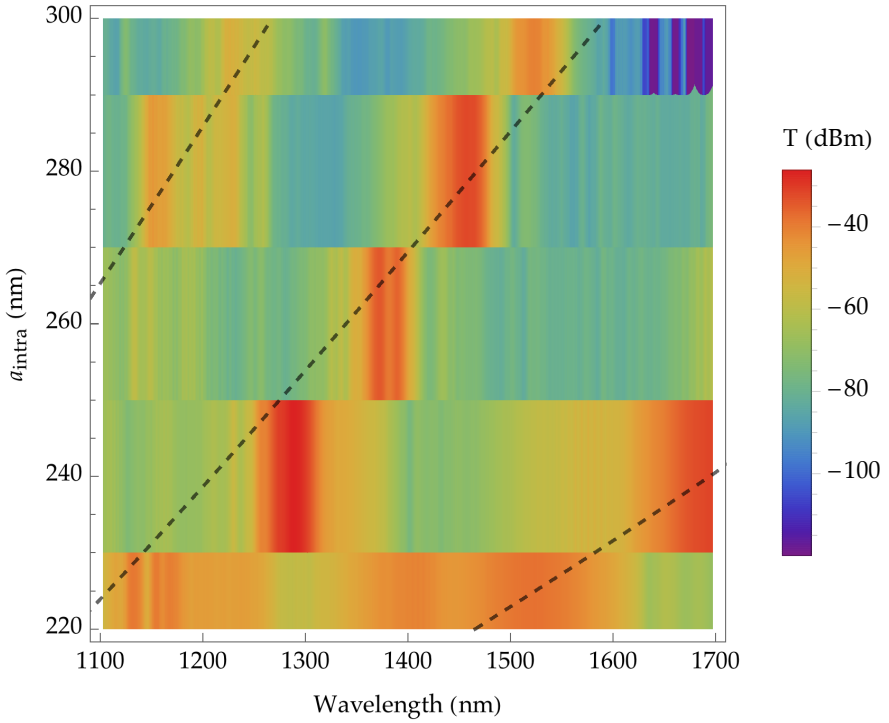

Figure 4.46: TE transmission through grating coupler as a function of a_{intra}. Dashed lines correspond to phase matching equation.

been reported in previous works due to the narrow sources that tend to be used.

The change in width and length have, as one would expect, very little effect on the coupling efficiency or wavelength dependence, except for the cases where the length or width becomes less than the 10 µm that would match a single mode fibre core.

Changing the radius and the pitch have a pronounced effect on the wavelength dependency of the coupling as predicted by the phase matching condition. As we increase both a_{intra} and a_{inter} we see the modes shift to longer wavelengths (Figure 4.46 and 4.47) , as predicted by the phase matching equation. We also see the appearance of higher order and back reflected modes with surprisingly high coupling efficiencies. This suggests that the devices can be used to couple efficiently across significantly different wavelength ranges using this non-standard mechanism.

Changing r also has a pronounced effect as shown in Figure 4.48. By changing the radius of the holes that form the low n part of the grating the effective refractive index in the grating coupler is altered. Indeed as we increase the radius, this effective refractive index of the grating

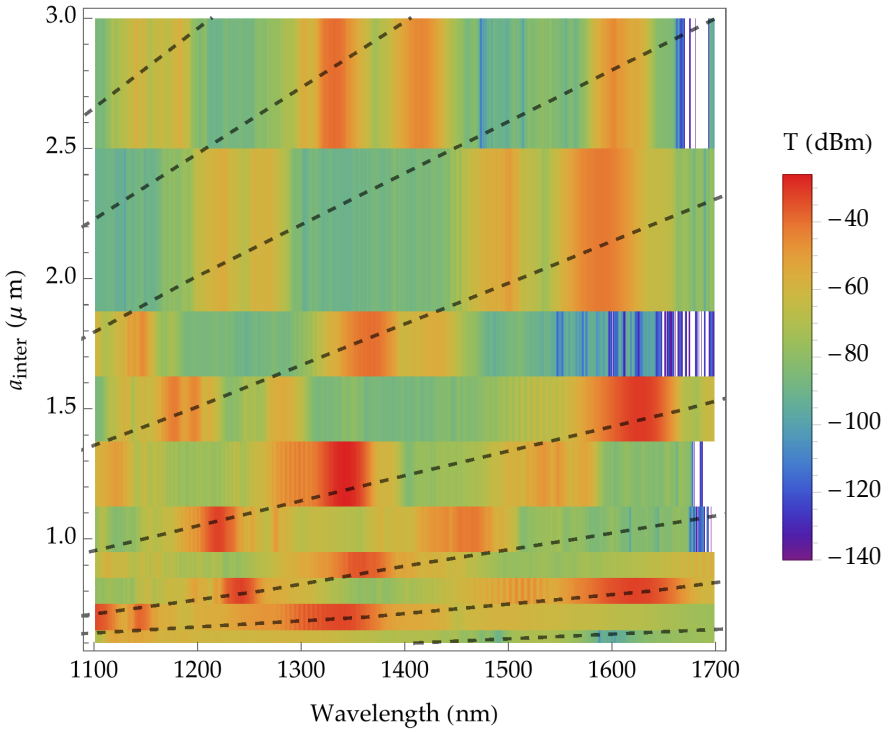

Figure 4.47: TE transmission through grating coupler as a function of a_{inter}. Dashed lines correspond to phase matching equation.

coupler is lowered, leading to a shorter peak coupling wavelength as predicted by the phase matching condition. We also see a shift in bandwidth and peak coupling efficiency with the largest coupling efficiency being found for the smaller radii, this is in keeping with the notion that if the index contrast is too high we see inefficient coupling.

Changing the fiber angle alters the grating modes, and thus the phase matching condition. This leads to a decrease in the peak coupling wavelength for both the high and low wavelength modes as shown in Figure 4.49.

The phase matching equation (Equation 4.5) provides a relatively good fit for the data, although to achieve the fits shown the parameters did require tweaking, implying that there are some small systematic errors in the automated feature measurement, and angle of fiber. A more serious issue with the fit of the data was that the phase matching equation had to be modified to account for the non-uniform refractive index of silicon over the wavelength ranges measured. Figure 4.50 shows this variation along with the power series expansion that was used to solve the phase matching equation for an $n_{Si}(\lambda)$ and $n_{SiO_2}(\lambda)$.

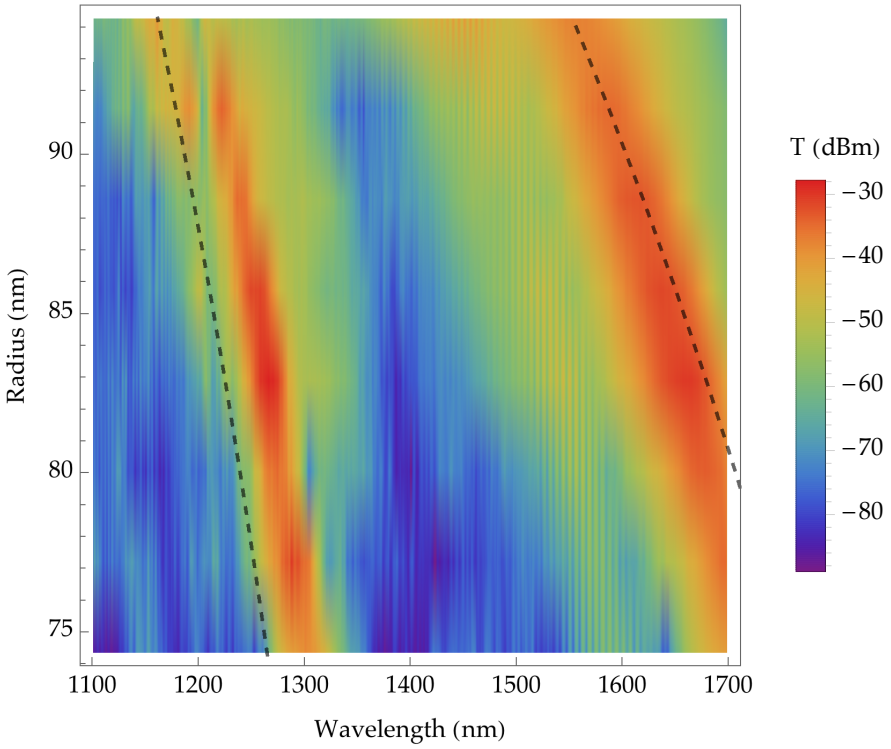

Figure 4.48: TE transmission through grating coupler as a function of r. Dashed lines correspond to phase matching equation.

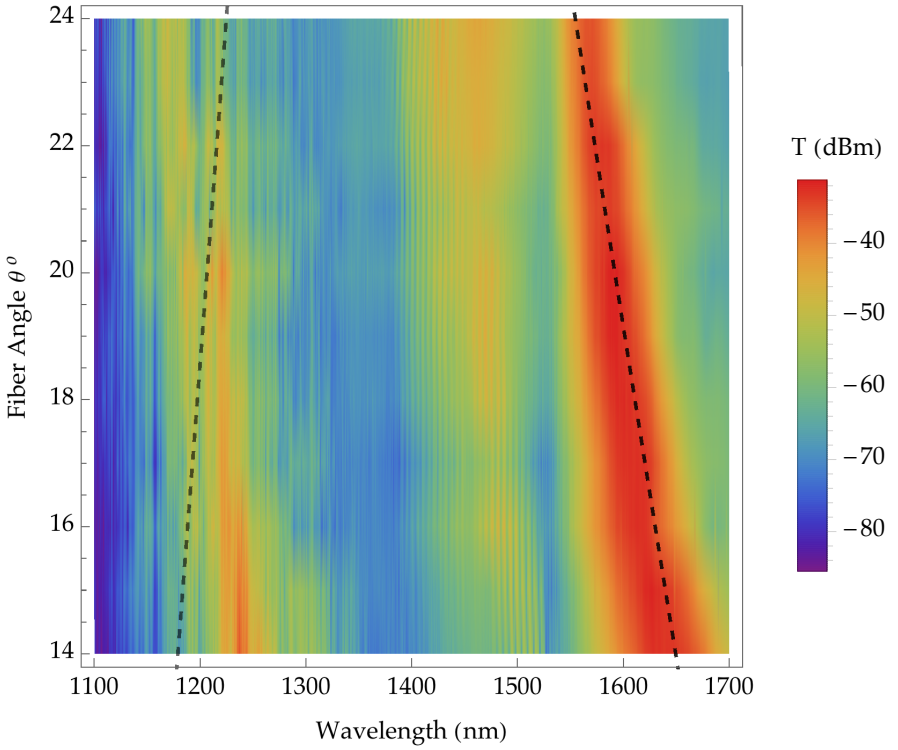

Figure 4.49: TE transmission through grating coupler as a function of fiber angle θ. Dashed lines correspond to phase matching equation.

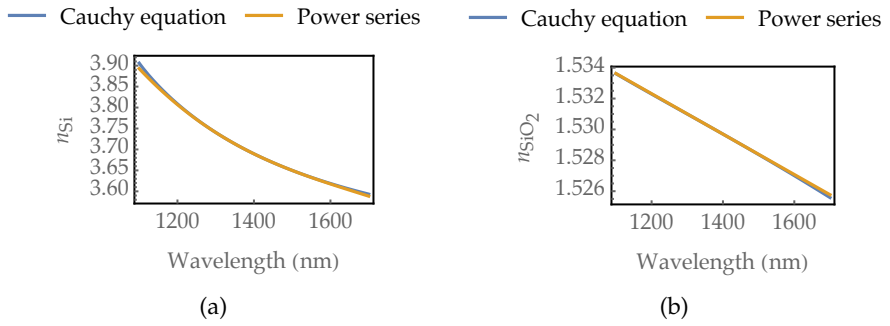

Figure 4.50: Refractive index of silicon a) and silicon dioxide b). To modify the phase matching grating coupler equation to account for the non-uniformity of the refractive indices a 3rd order power series expansion around the mid-wavelength of 1400 nm of the Cauchy dispersion formulae was used.

The grating coupler results show that by implementing a variety of strategies it is possible to tune grating coupler performance over a wide range of wavelengths, not only shifting peak coupling wavelength for the 1st order diffraction mode but also higher and back reflected modes, coupling efficiency and bandwidth. They also show that the slightly low transmission efficiency of the grating couplers are not due to the geometrical, or experimental parameters tested, leaving variations in device layer thickness or edge wall roughness as possible candidates. The relatively low transmission efficiency should however not prevent further measurement of PhC devices as although lower than expected there is still clearly measurable signals across a wide range of wavelengths. In the next section I will discuss the results of the PhC measurements.

4.6 PHOTONIC CRYSTAL RESULTS

A number of devices testing the photonic crystal resonator behaviour have been measured. The overall strategy was to gradually introduce complexity to the system and try and ensure full understanding of each new aspect. The ultimate goal was to classify the broadband behaviour of the cavity devices so to inform a strategy for biosensing with them. Furthermore a thorough investigation, utilising the broadband nature of the supercontiuum source would be a valuable academic contribution, as mentioned before there is surprisingly little work of this type. Unless otherwise stated 'relative transmission' refers to transmission relative to a straight waveguide with identical grating coupler, polarisation and coupling angle.

4.6.1 *In-line devices*

The first set of PhC resonator devices are a series of waveguides with identical grating couplers at each end and a varying taper in the middle. The wave guides were fabricated in two configurations, one simply the waveguide and a second with an 'in-line' device, a photonic crystal resonator patterned across the full width of the waveguide. The taper varies from a straight waveguide with a width equal to the grating coupler (15 µm) down to 2.14 µm. SEM images of these devices are shown in Figure 4.51.

The resonator consists of a photonic crystal lattice with a pitch a of 400 nm and a radius r of 100 nm equal to 0.25 a. The defect consists of an enlarged central hole (r_{defect} = 385.8 nm = 0.964 a), with the surrounding holes removed (as discussed in the simulations Section 4.2.1.2). This set of devices was designed to provide like-for-like comparison of the grating coupler - waveguide system with and without the PhC resonators and assess the impact of the taper on device performance. Further measurements investigated the effect of changing the polarisation of the input and the coupling angle of the fiber.

The measured spectra for an 'in-line' type device with and without PhC resonator for TE input at 15° coupling is shown in Figure 4.52. This is typical of the data, showing attenuation across the measured spectrum but most notably between 1500 nm and 1700 nm for the devices including the resonator. The complete datasets with the transmission relative to the relevant waveguide under a range of device parameters and coupling conditions are now discussed.

4.6.1.1 *Waveguide Taper*

For effective mode matching to a single mode fiber core, the grating couplers are 15 µm in length and width, the PhC resonator devices can however be much smaller, and in fact the coupling of modes into them should depend on the modes supported by the waveguide at the point it meets them. As such one of the aspects of device design we want to investigate is the effect of varying the width of the waveguide at the point it meets the PhC device . A series of waveguides with and without PhC resonator devices but with varying taper have been measured. The effect of varying the taper was found to be minimal (see Figure 4.53). The taper occurs over the course of 2 mm, and at its greatest is equivalent to to less than 0.5° with a narrowest width equal to 1.2 µm . The changes we do see are attributable to variations in the fabrication of the grating couplers, along with some variations in alignment.

4.6.1.2 *Polarisation Measurements*

The next set of measurements investigated the devices dependence on polarisation, as we expect only the TE modes to be coupled effectively by the grating coupler and the PhC resonator to have a band gap for the TE modes. Figure 4.54 shows the relative transmission through

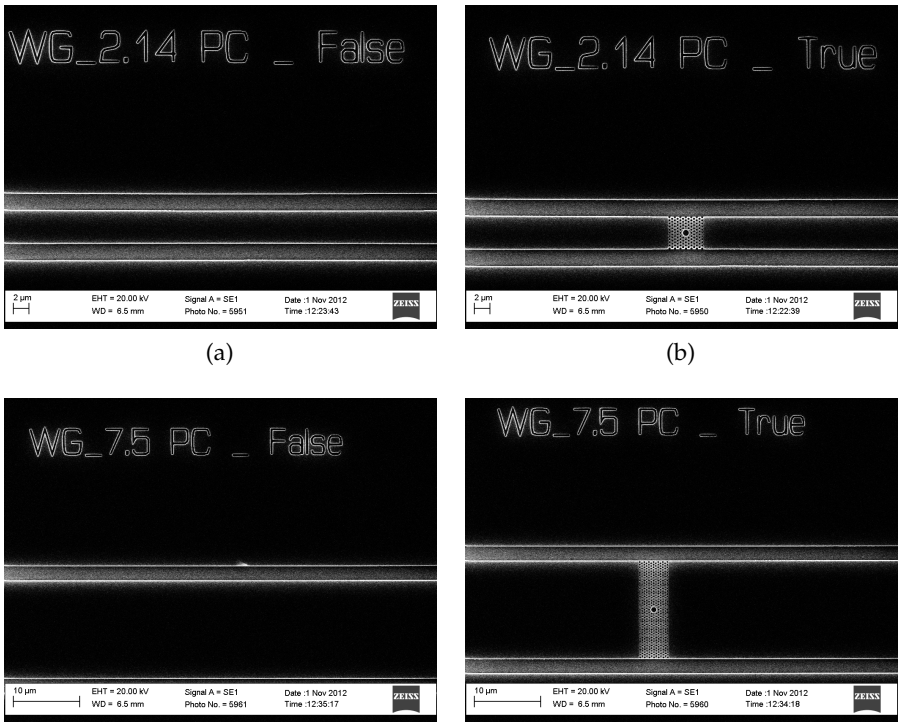

(a) (b)

(c) (d)

Figure 4.51: SEM images of in-line devices. The first set of devices are a series of waveguides with identical grating couplers that taper in the center, each taper is replicated with two configurations, one with a PhC resonator, one without. The widths taper from (15 µm a straight device) down to 1.2 µm. The resonator has an air hole photonic crystal lattice with a pitch a of 400 nm and a radius r of 120 nm equal to 0.3 a, with a enlarged central hole with radius $r_{defect} = 385.8\,\text{nm} = 0.964\,a$

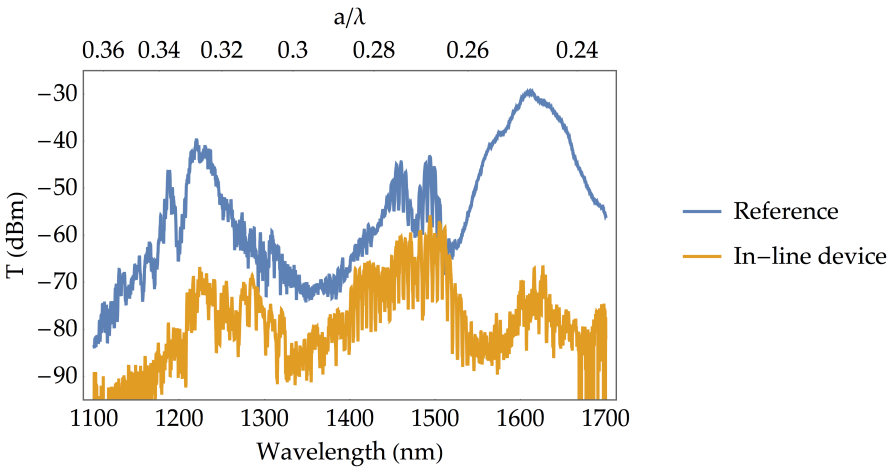

Figure 4.52: TE transmission for in-line device. Showing the reference spectra of a waveguide, and an in-line device (width = 2.14 µm). In this case the fiber angle is 15°.

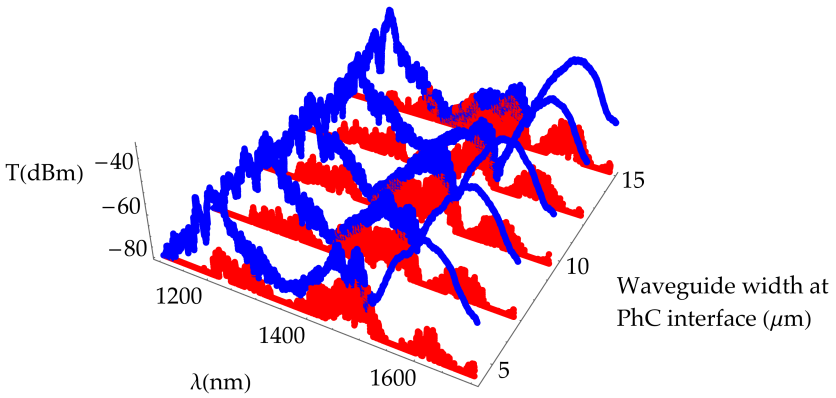

Figure 4.53: Transmission through in-line devices with varying tapers. Blue traces show the measured spectrum through devices without a resonator. Red traces show the transmission through equivalent devices with a resonator. In both cases the fiber angle is 15° and the polarisation is TE. There are no obvious effects of tapering, and the attenuation of the transmission for wavelengths greater than 1500 nm is consistently observed for all the devices.

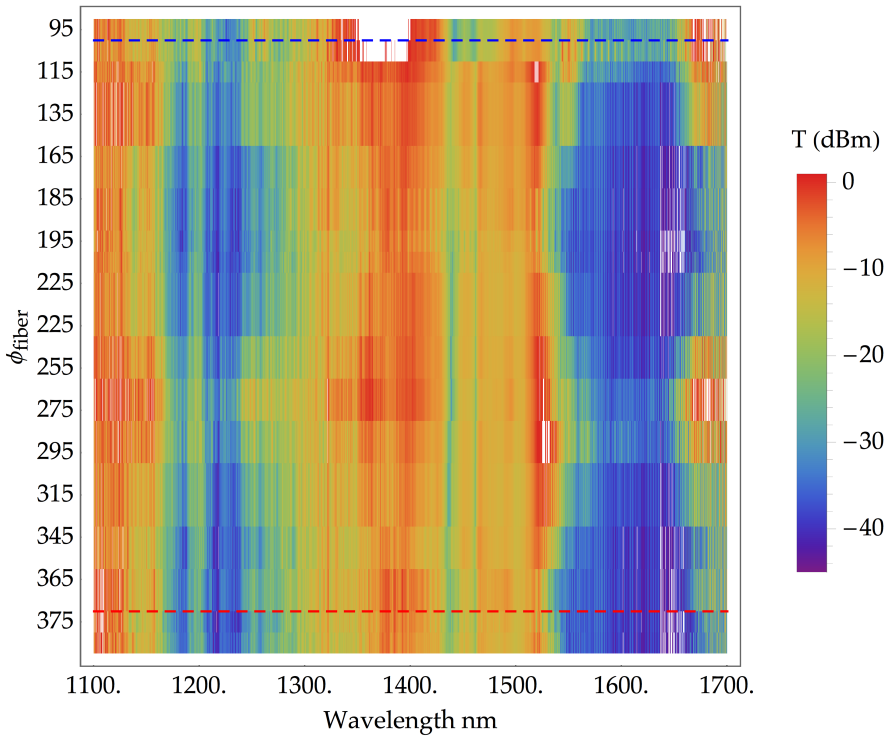

Figure 4.54: Relative transmission (to identical waveguides without PhC device) through the in-line PhC device for varying polarisation. The dotted lines showing the slices plotted in Figure 4.55.

PhC resonator devices as a function of the rotation ϕ of the PM fiber. Figure 4.54 w shows the measured traces at the TE and TM angles. These plots are for an input coupling angle θ of 15° and a taper/thickness of 15 um. We observe a steep drop off around 1500 nm, with the start of a slope back up around 1650nm. We also observe some sharp features in between 1400 nm and the drop off at 1500 nm. Finally the drop off in the TM case occurs around 20 nm longer wavelength than the TE case.

4.6.1.3 *Fiber Angle Measurements*

The third set of measurements for the in-line devices varied the coupling angle of the fiber to the grating coupler, this results in a change in the peak coupling wavelength as the effective path length between grating elements changes. The results for two devices are shown in Figure 4.56, the top plot corresponds to the narrowest device (width 2.14 µm), the bottom plot to the widest (width 15 µm). There are a number of features of note. There is a clear drop or edge close to

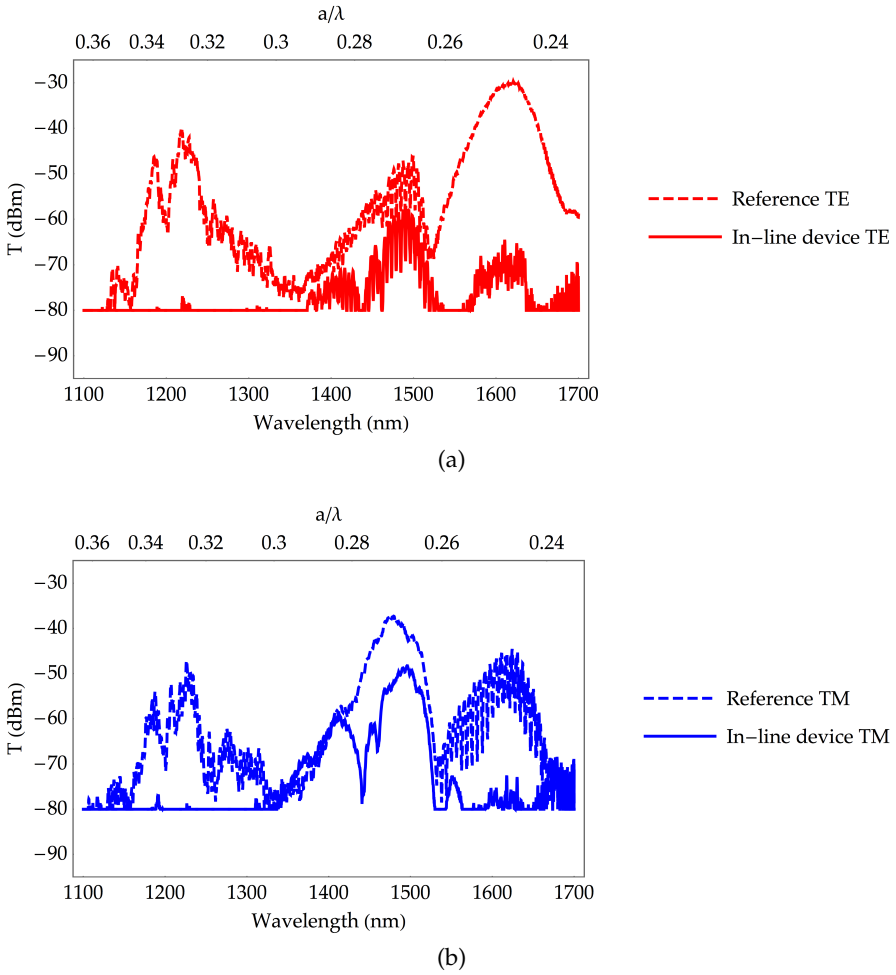

Figure 4.55: TE and TM transmission through the in-line devices without (dashed) and with (solid) PhC devices. The angles correspond to the dashed lines in Figure 4.54

1400 nm and a second at 1500 nm, and peak around 1550 nm. These plots show that the device width does not affect the performance of the resonator significantly but show that there are features the depend strongly on the coupling conditions, most notably the peak at 1550 nm. These features will be investigated further by simulations shown in the proceeding section.

4.6.2 *Boxed Devices*

The second set of devices measured have identical grating couplers to the first set, but in their case the tapered waveguide leads to a boxed resonator device. To study the effects of the PhC structure the boxed device was fabricated with four different forms, an empty box, a box with the defect hole but no surrounding PhC array, a box filled with the PhC array and a box filled with PhC and defect. SEM images of the devices are shown in Figure 4.57. The measured spectra of the different devices and the reference spectrum of a straight waveguide with identical coupling conditions is shown in Figure 4.58. These show once again the clear attenuation of the signal between 1500 nm and 1600 nm for the devices including the PhC, the other boxed devices do not show this attenuation. There are some sharp resonances visible, both for the PhC cases and the no PhC cases, this is to be expected as the empty box will also form a cavity of sorts. The results are similar to the in-line case, the boxed device with and without the defect hole both give broadly flat responses, although there are some clear resonances for the case with the defect hole, with noticeable features at 1500 nm and at 1620 nm. The presence of the PhC structure, both for the cases with a defect and without clearly attenuate the signal strongly in the region 1500–1600 nm, and there are noticeable resonances in this region, although they are not clearly identifiable with any of the theoretically predicted features.

4.6.2.1 *Fiber Angle Measurements*

As for the in-line devices a number of measurements were taken. Each device was measured with varying input fiber angle to test which features were independent of the grating coupler and therefore due to the devices themselves. These results show that the stop band between 1500 nm and 1600 nm is independent of coupling angle, as is the resonance at the 1600 nm upper stop band edge for the non-

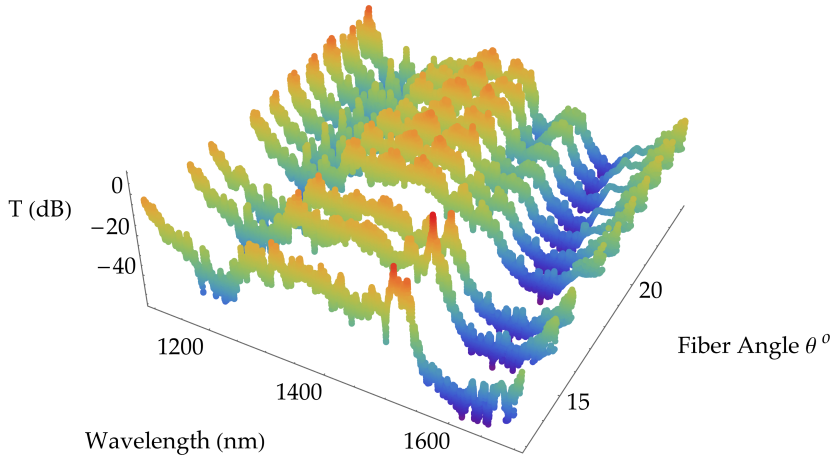

(a)

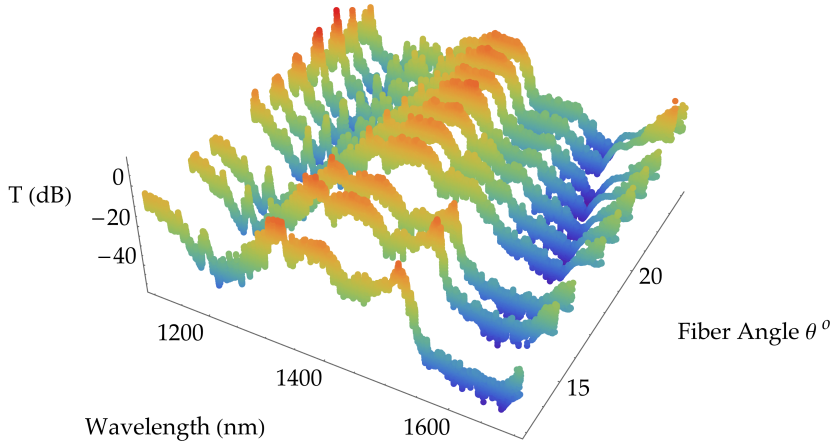

(b)

Figure 4.56: Relative TE transmission (to straight waveguide) through in-line resonator for varying the fiber angle for two different device widths. Top is for the narrowest device 2.14 µm and the bottom is for the widest 15 µm. The varying angle changes the peak coupling wavelength, however we expect the key features of the resonator to be independent of this

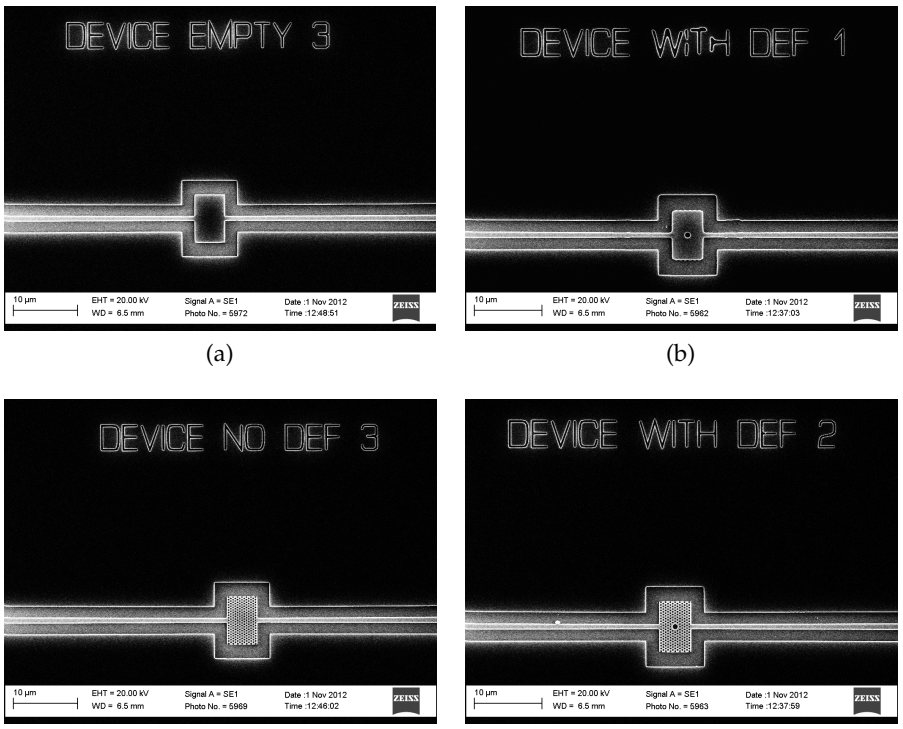

Figure 4.57: Boxed devices with a) cavity holder, b) cavity holder with defect hole, d) photonic crystal and e) photonic crystal with defect

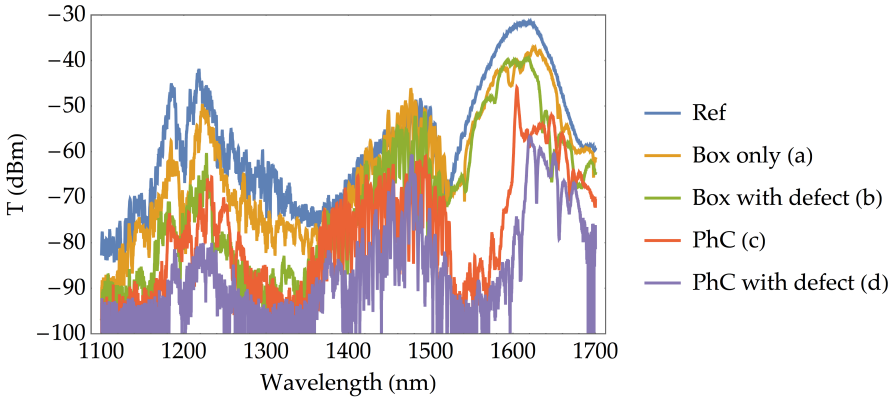

Figure 4.58: TE transmission for boxed devices. Showing the reference spectra of a waveguide, and the various boxed devices. In this case the fiber angle is 15°.

defect case. For the both cases there is a resonance at the lower band edge that does seem to depend on the coupling, it is visible only for the smaller angle coupling conditions. For the higher coupling angle conditions this peak transforms into a more shelf like feature with a lower band edge of 1400 nm and further drop off at the higher wavelength of 1500 nm.

4.6.2.2 *Increasing the size of the PhC*

Measurements were also performed that investigated the size of the photonic crystal by varying the number of rows in the device, that is the size of it in the direction of the propagation of light. These results are plotted in Figure 4.60. These results show the attenuation between 1500–1600 nm is dependant on the number of rows, with the transmission in this window decreasing as the number of rows increase to 12 after which it remains constant. This is not the case for the rest of the spectrum which remains almost entirely unchanged as the number of rows varies. This is further evidence that it is indeed the PhC structure that is attenuating the light in this wavelength range.

4.6.3 *Device Specific Simulations*

It is clear the devices in both the in-line case and the boxed case have a pronounced effect of the transmission. There is significant attenuation from 1500–1600 nm, with other preserved features such as peaks at 1500 nm and 1600 nm along with the shelf like feature at 1400 nm. However it is difficult to say with great certainty the precise source of these features. To try and understand these results further I have implemented a further set of simulations designed to match the studied geometries precisely.

4.6.3.1 *Boxed device simulation*

The simulations use the design geometry of the boxed devices. The simulated geometries are shown in Figure 4.61, which match the devices shown in Figure 4.57. The simulations assuming a device layer thickness of 400 nm as measured with profileometery and a SiO_2 box layer.

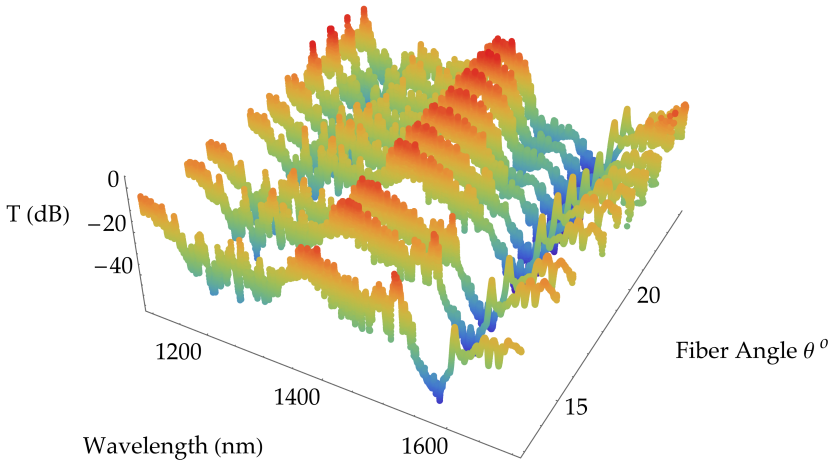

(a) Boxed PhC

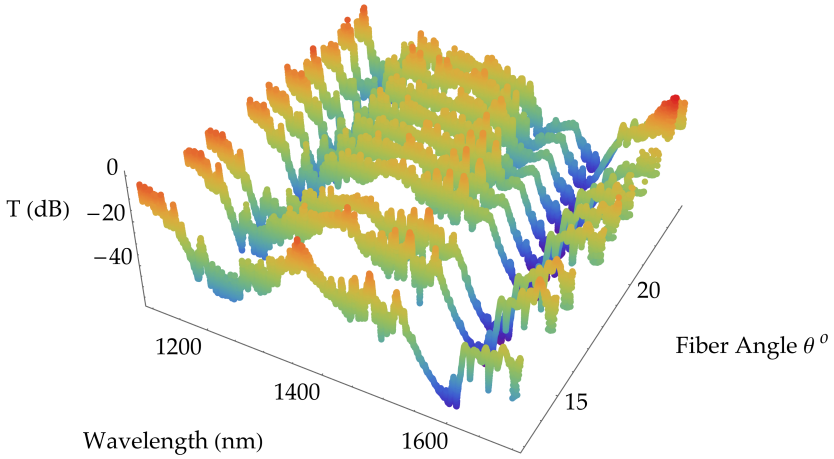

(b) Boxed PhC with defect

Figure 4.59:
Relative (to straight waveguide) TE transmission through boxed devices. Top is for the boxed PhC device (Figure (c) in 4.57), bottom is the PhC device with defect (Figure (d) in 4.57). It is clear that the stop band between 1500 nm and 1600 nm is independent of coupling angle, as is the resonance at the 1600 nm upper stop band edge for the non-defect case. For the both cases there is a resonance at the lower band edge that does seem to depend on the coupling, it is visible only for the smaller angle coupling conditions. For the higher coupling angle conditions this peak transforms into a more shelf like feature with a lower band edge of 1400 nm and further drop off at the higher wavelength of 1500 nm.

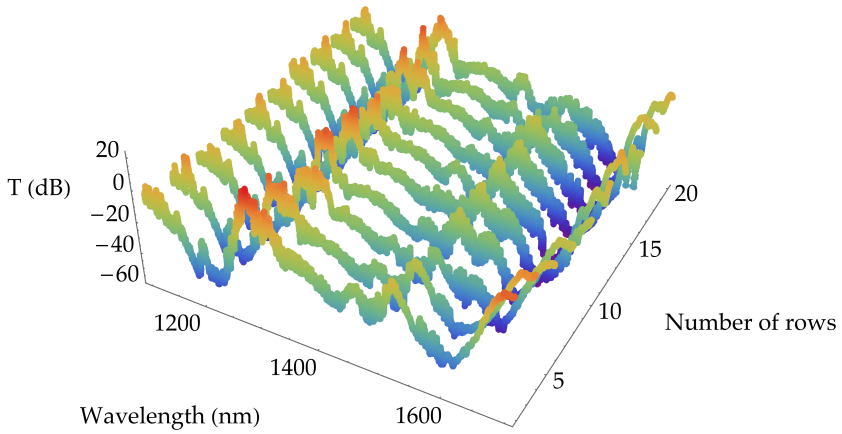

Figure 4.60: Measured relative TE Transmission for increasing size of PhC, size refers to the number of rows of the PhC, varying the 'depth' of the PhC in the direction of the propagation of light

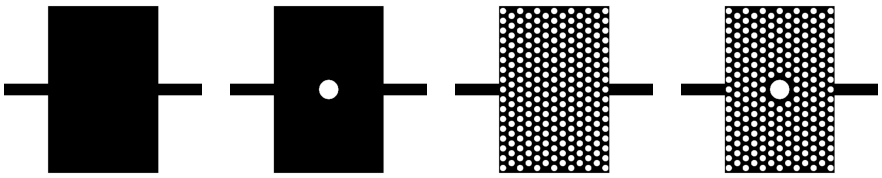

Figure 4.61: Simulation structures for TE transmission through boxed devices a) empty box, b) empty box with a defect hole, c) boxed PhC device and d) PhC device with defect.

Figures 4.61 and 4.62 show the results, along with the relative (to a straight waveguide device) transmission measured experimentally. The non-PhC simulations (Figure 4.61) do not precisely overlap with the experimental data, however their are some common features. Both sets of data and simulations show a small dip around 1200 nm and a broader flatter transmission from 1400–1500 nm. Furthermore for device b), the box with a defect hole but no PhC structure, both the simulations and measurements show smoother, longer wavelength oscillations with some sharp drops in transmission around 1500–1700 nm.

It is a similar case for the devices with the PhC structure (Figure 4.62). While the fine structure does not really match there are some common broader features. Most noticeably the drop in transmission that appears to be a band edge around 1500 nm is clearly visible in both measured and simulated results. Less encouragingly the simulations show this band gap like feature extending to wavelengths well beyond the range of our measurement set up, whereas in our measured spectra we see a more window like feature with transmission recovering for wavelengths above 1650 nm. The simulation plotted in Figure 4.63 b) demonstrates that the presence of the defect when not functioning optimally to produce a sharp resonance can instead populate the band-gap to the extent that it is no longer clearly visible. Although these results are far from definitive, they are comparable in the extent to which they match the simulations, to those shown in the literature review (Figures 4.2). Recreating the fine structure of such broad spectral response on a log scale is challenging to achieve with so many variables unaccounted for.

4.6.3.2 *Custom 'tailored' simulations*

To extend this study and account for potential variations in our devices from the design parameters a custom program was developed. This program uses EBL images of the devices measured to generate MEEP geometries accurately representing them.

The MEEP geometry file consists of a list of rectangles of specified size location and dielectric constant. Because the bulk of our structure consists of high epsilon features we can speed up the analysis and reduce geometry file size by generating MEEP code corresponding to the low epsilon features (air). The first step was sweeping a template box across a binarized EBL image, if no pixels corresponding to silicon are present in the box a MEEP rectangle is created at that

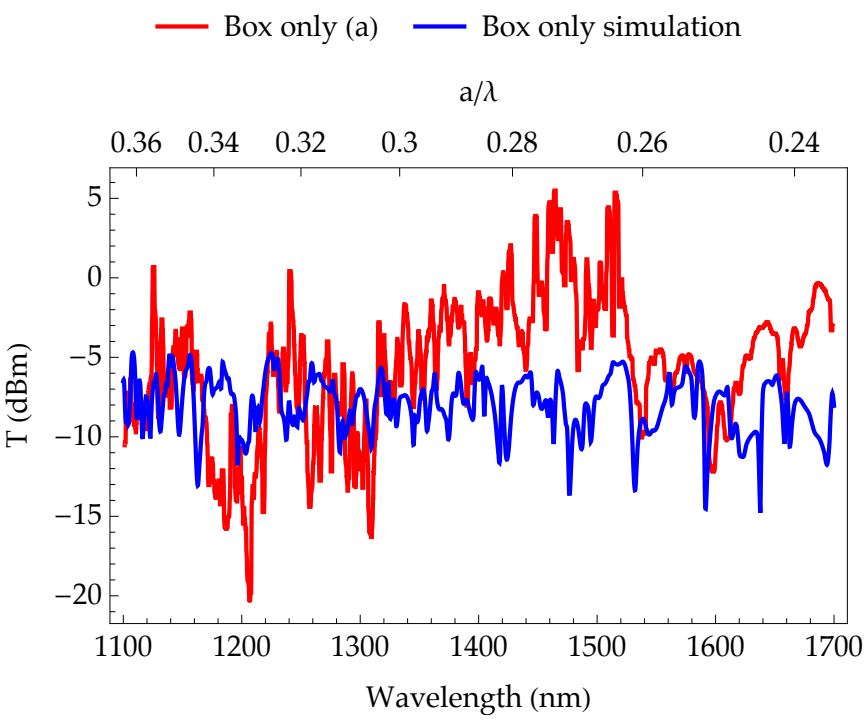

(a)

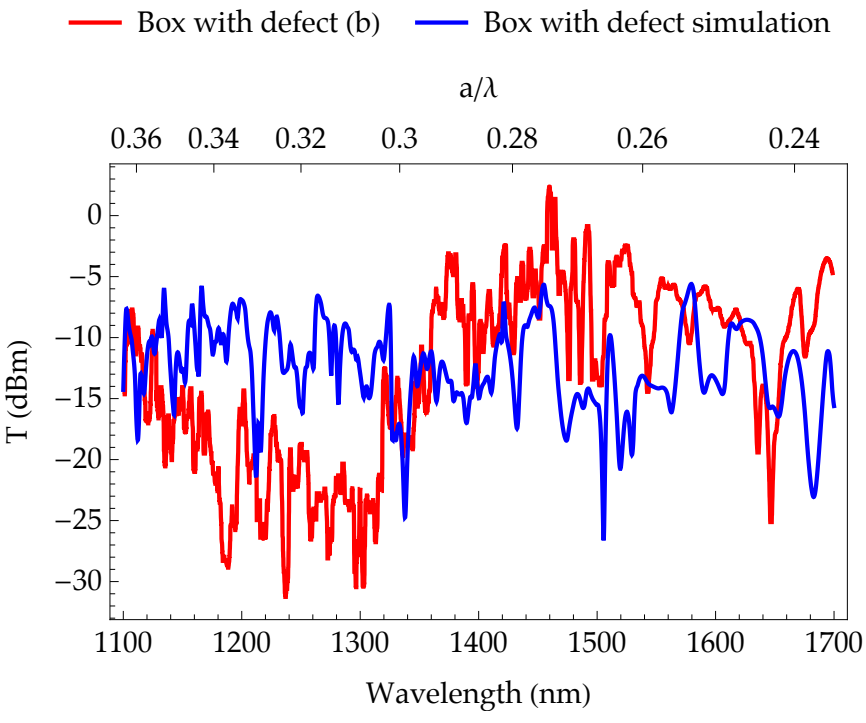

(b)

Figure 4.62: Comparison of simulated and experimental results for boxed devices without PhC structure. a) the empty box, b) the empty box with a defect hole. Letters in legend refer to structures as shown in Figures 4.57 and 4.61.

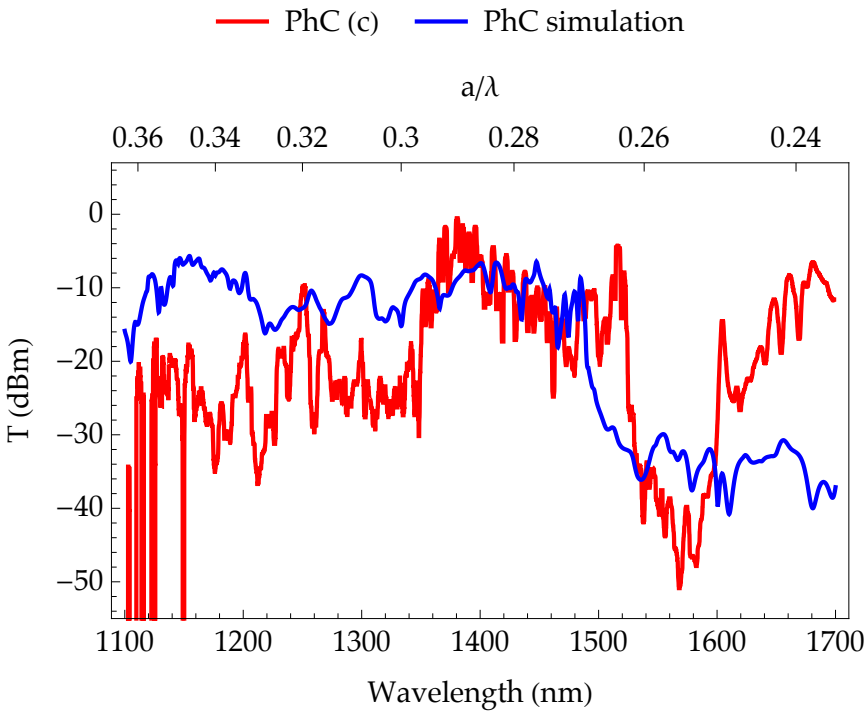

(a)

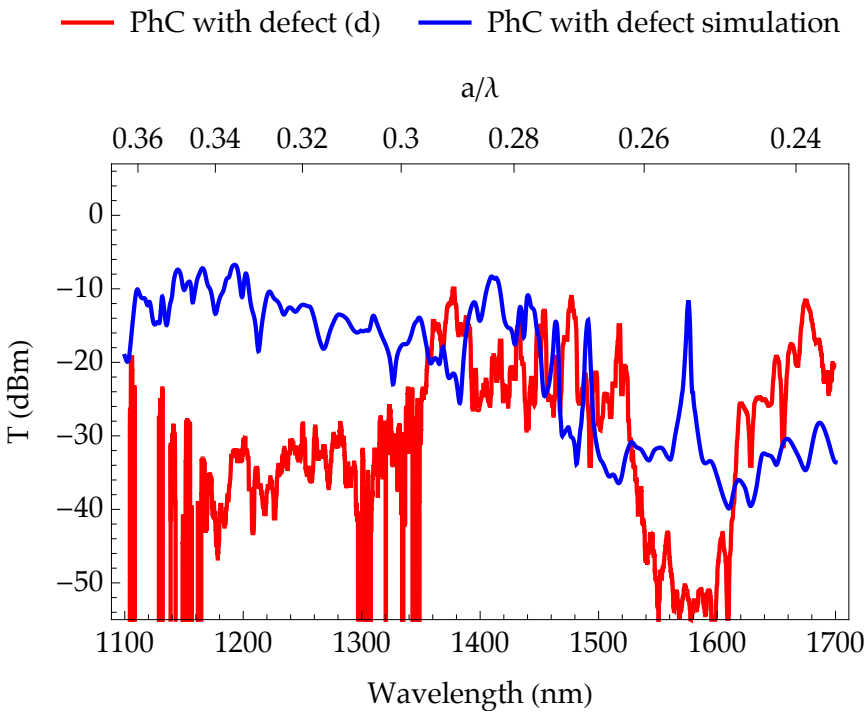

(b)

Figure 4.63: Comparison of simulated and experimental results for boxed devices with PhC structure. c) the boxed PhC device and d) PhC device with defect. Letters in legend refer to structures as shown in Figures 4.57 and 4.61.

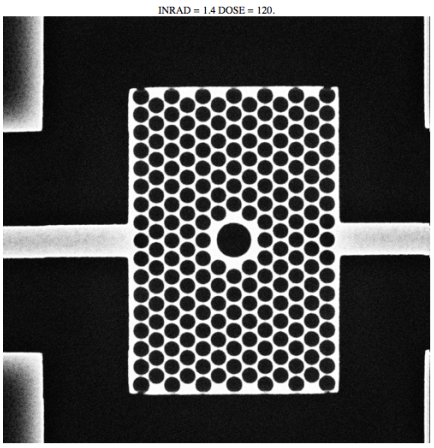

(a) Original SEM image of device

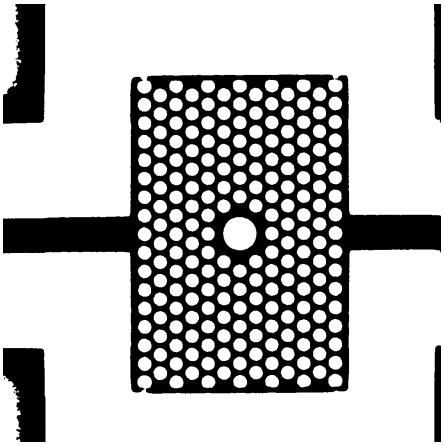

(b) Filtered SEM image

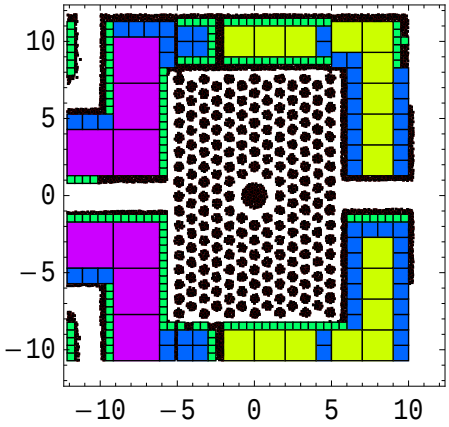

(c) Regions of image identified as air by algorithm

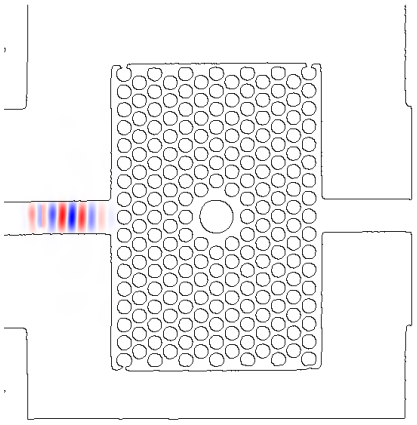

(d) Ouput MEEP simulation geometry

Figure 4.64: Meep geometry generation from SEM images. To generate simulation geometries that capture all the details of a physical devices fabrication a program was written that takes SEM images of devices and generates matching meep simulations. a) The original SEM image of a device to be simulated. b) This image is processed such that it may binarized into silicon and air regions. c) This image is processed such that all the regions representing air parts of the device are covered by a series of rectangles.This list of rectangles is then translated into a meep geometry file. d) The meep geometry can then be used for simulating the transmission spectra of the original device.

location corresponding to air. This is repeated across the image for rectangles of decreasing size. At a certain point searching the image regularly becomes inefficient and instead we randomly select from the remaining points of the image that have not been represented in the MEEP geometry forming rectangles to cover these sections. Figure 4.64 demonstrates this process showing and EBL image of a device, the binarized version, the rectangles found to match the air regions of this image and finally the MEEP geometry with input pulse.

The simulations were performed with varying device layer thickness. This was to test whether inaccuracies in the profileometry could account for the discrepancies between simulated and measured results. The closest fit to our data was for a thickness of $1.1a$ so for 440 nm instead of 400 nm. This result is plotted in Figure 4.65. alongside the experimental data. This simulation shares a few features with our results, most noticeably the peaks at 1550 nm.and 1650 nm bordering the measured band-gap like feature. It also has a shelf like feature close to 1400 nm and and dip at 1200 nm, both of which are visible in our data, particularly in Figure 4.56. Somewhat frustratingly in comparison to the other simulations,. and indeed the data it does not show a clear band-gap edge.

4.7 CONCLUSIONS AND FURTHER WORK

The aim of this project was to develop photonic crystal devices for biosensing applications. In this work I have optimised the processes of electron beam lithography, reactive ion etching and complementary clean-room techniques such as thermal oxidisation, HF etching, thin film deposition and resist spinning. I also developed customised programs to help assess fabrication process performance and reduce proximity effects. I successfully applied these to the fabrication of single etch step silicon on insulator air hole photonic crystal slab devices with a pitch of 400 nm with radii of 80–120 nm along with through-etch grating couplers and ridge waveguides. I have also developed a new technique for producing pillar devices, waveguides and grating couplers in a single step and made preliminary efforts to optimise this process. The next step in terms of fabrication is the optimisation of membrane structures, this will require an additional backside etching step.

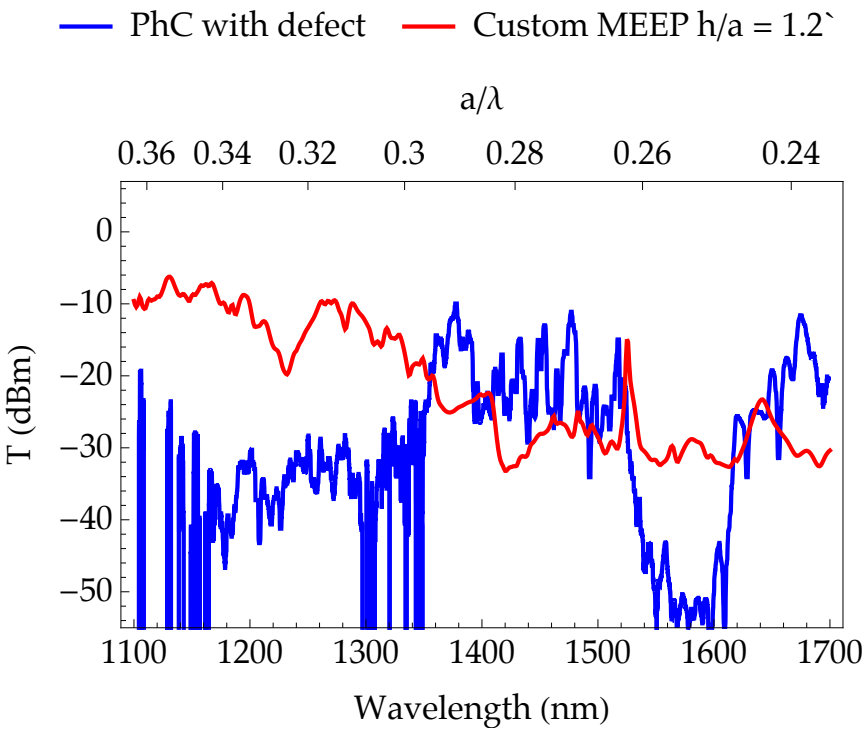

Figure 4.65: Comparison of simulated and experimental results for boxed PhC resonator and customised simulation structure.

I have developed a series of computational models that allow for the calculation of band structures, defect modes and transmission spectra for a variety of photonic band gap devices. These make use of freely available open source eigensolvers[31] and finite difference time domain techniques[30] and have been implemented to simulate two and three dimensional structures including defect cavities. I also made a novel bolt-on program for generating simulation geometries based on SEM images of actual devices. The simulations show the presence of defect resonances open to perturbation from outside agents such as biomolecule binding. These simulations have however shown the importance of achieving symmetry in the z-structure of devices suggesting the failure to implement membrane structures was a serious limitation of my experimental work.

Following the computational and fabrication efforts I carried out a thorough experimental examination of grating coupler performance. I experimentally studied the grating coupler performance over a wide range of coupling conditions and geometric parameters. This work demonstrates the fine control of the grating couplers optical performance is achievable though precise structural modifications. Furthermore I have measured the transmission of second order diffraction modes to realise multi-band transmission. This was also shown to be in close agreement with a dispersion modified version of the phase matching equation, which is as far as the author is aware a previously unstudied phenomenon.

I have measured numerous PhC resonator devices under a variety of coupling conditions. There are some clear band stop characteristics that hold some similarity to the simulation predictions, for example the measurements of the boxed devices shown in Figures 4.58 share a band edge at 1500 nm with the simulations. There are also a number of peaks and dips for which the data and simulations match as shown in Figure 4.65.

It is, however, impossible to say with great certainty that these are true band gaps. Possible causes of the difficulty in observing PhC effects could stem from a lack of uniformity in the device layer of the SOI employed or the lack of backside etch to create true membrane devices. While the control over feature size was heavily optimised the roughness was not scrutinised as thoroughly. Any roughness in optical devices will lead to scattering and the coupling of TM and TE modes leading to further losses so this may have been a further issue.

Finally due to the uniquely broad measurements we have performed the effects of dispersion at the lower wavelengths measured may have caused some deviation from the expected behaviour (as seen in the grating coupler case).

Returning to the literature discussed at the beginning of this chapter suggests some further mechanisms that could possibly have played a role. Krauss et al. were unable to observe a full TE band gap, they posited this was due an oxide layer forming on their devices and shifting the position of the gap out of the range of their source. Our source is sufficiently broad that we can see a band edge but it is possible that some of the features are shifted due to oxide growth. Another issue Krauss et al. found was the mismatch between their waveguide modes and the supported modes in the photonic crystal device. This meant that in regions where they were expecting to see transmission they did not. While we did measure devices with a range of waveguide sizes this may still have played a role if the symmetry of the modes simply did not match.

More positively, we do see significant stop bands with similar attenuation to that published by Krauss et al. and Yablonovitch. Furthermore we have been able to measure over much broader wavelength ranges and as such have demonstrated that these stop bands are indeed the exception rather than the norm.

Broadband measurements of photonic crystal devices such as those reported here are seriously lacking in the literature for optical wavelengths. The work presented here is a significant step in this direction and will hopefully provide a motivation for further studies into the fundamental behaviour of slab photonic crystal structures. It is only through these thorough, 'warts and all' studies that the true limitations and scope of the applications of these devices can be determined.

5

CONCLUSIONS AND FURTHER WORK

This thesis has been about the creation of materials and devices which, through patterning on the micro and nano scale, are able to intentionally modify the local electromagnetic environment and response to outside stimuli. This has been investigated on three different scales, each requiring a specific tool kit of computational, fabrication and measurement techniques. I will now summarise the work performed, the achievements and potential for future development.

Chapter 2: Radio frequency characterisation of microparticles

Through the use of micro-patterned electrodes, radio frequency fields have been shaped such that micro particles can be manipulated and characterised on-chip. I developed a simple, yet novel, supervisor-free real-time method to florescence quantification, as well as fabricating and measuring microfluidic devices. The synergy of micro-fluidic sample handling, electro-kinetic manipulation and rapid image quantification leads to many exciting applications.

Chapter 3: Terahertz Metamaterials

Metamaterials are materials whose interaction with electromagnetic radiation is a function of their microscopic geometric form rather than their constituent atoms. This fundamental shift in the way materials are understood, made and used is exciting both from a scientific and technological point of view. I have, in collaboration with Yongzhen Wen of Peking University, developed a series of novel metamaterial devices. The design of these devices required using commercial finite difference simulation tools. The fabrication of these devices used photolithographic clean room processes. Their measurement required advanced Fourier transform spectroscopy techniques. These devices provide new mechanisms for manipulating the dielectric response of materials such as the nesting of asymmetric resonators and varying the conductivity of the ground plane. The devices have been realised to achieve absorption in the critical THz band. This is of great use

for the development of THz detectors and filters, and key for the advancement of THz science and technology.

Chapter 4: Photonic Crystal Devices for Biosensing

Photonic crystals, periodically structured dielectrics, provide a powerful method to manipulate and confine light on the micrometer scale. This capability makes them exciting and versatile tools for many on-chip applications. I have used both commercial and open source computational packages to design devices including grating couplers, photonic crystals and resonators. I have also created my own complimentary software to customize these packages for device specific simulations based on scanning electron microscope images. I used advanced nano fabrication techniques such as electron beam lithography and reactive ion etching to realise silicon on insulator photonic crystal devices for near infrared wavelengths, finding new methods for fabricating incompatible features such as grating couplers, waveguides and pillar photonic crystals. To measure these devices I built an automated measurement system using motorised optomechanical components, fiber coupling, image processing and LabVIEW instrumentation control along with a cutting edge super continuum laser source. Using these techniques I undertook a broad experimental study of grating coupler performance, reporting their broadband spectral behaviour and their dependence on device geometry. I have also measured a variety of photonic crystal resonator devices, recording some of the first broad band spectral investigations of slab photonic crystal devices. While there are some strong indications of band gap like properties the failure to firmly tie these nor the fine structure of the measured spectra to numerical simulations limits the reliability and understanding of these results.

The ultimate aim of the work with photonic crystals was to develop devices for biosensing applications. Although unable to reach this point, going forward, one of the most exciting applications of photonic crystals to biosensing comes from the implementation of on-chip lasing capabilities. Photonic crystal cavity lasers have been previously developed, using both optical and electrical pumping[140,141]. By tailoring the optical modes accessible to the gain medium photonic crystal cavities can seriously reduce spontaneous emission into unwanted non-lasing modes[142]. Furthermore through suitable design extremely high Q single mode cavities can be fabricated with modal volumes

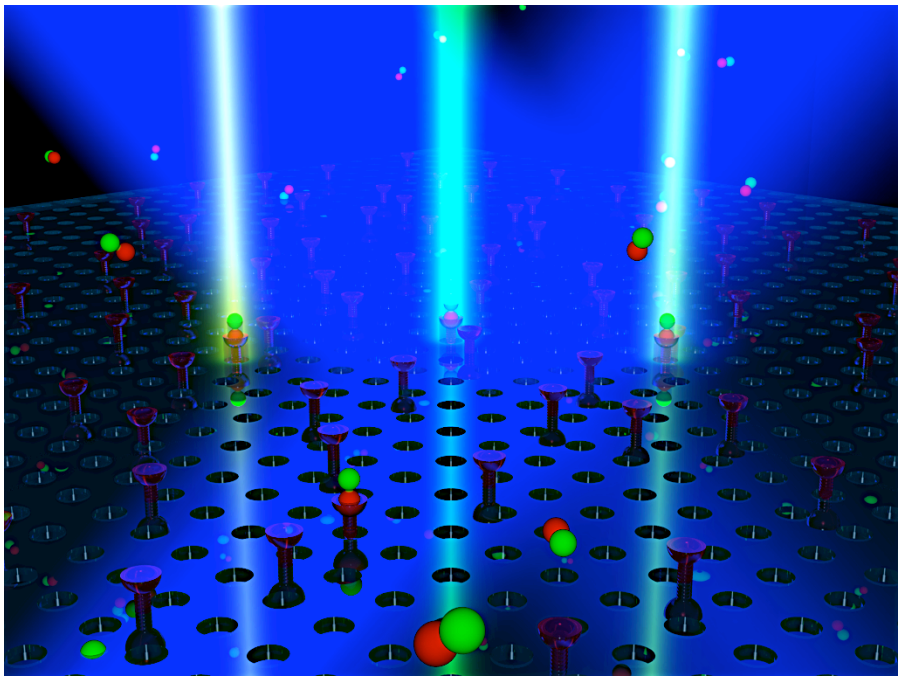

Figure 5.1: Illustration of proposed photonic crystal cavity laser biosensor

V on the order of a cubic wavelength. For such cavities the emission coupled to the lasing mode can be increased by a factor of (Q/V), the Purcell factor[143]. Using the non-linearity of a lasing system for biosensing applications could boost sensitivity greatly, providing unambiguous signals. Furthermore narrow band signals could lead to the borrowing of telecoms techniques for signal processing, e.g. the multiplexing of signals from different reporters.

While the work performed up to this date leaves us in a strong position to press forward with this idea, there are challenges to be addressed. Firstly most photonic crystal cavity lasers use embedded gain mediums, this is well suited to a photonic crystal cavity as regular cavities concentrate their field energy in the dielectric regions[144]. For the biosensing laser system we must design a cavity such that the energy is concentrated in the space occupied by a gain medium which is open to perturbation . To design such a cavity while not sacrificing other desirable features such as the Q factor will require care. Initial steps have been made to pursue this work in collaboration with Dr John Hales who has developed lasing biomarkers that are ideal for this application.[145].

Conclusion

To conclude, nanotechnology is by its very nature interdisciplinary, not only between the traditional branches of science, physics chemistry and biology, but also between science, technology and engineering. This thesis is very much a product of this interdisciplinarity. I believe the work contained here demonstrates both the benefits of versatility and creativity in finding solutions to multifaceted problems, but also the risk that without focussed and detailed attention to a specific field progress can be challenging. Ultimately it showcases the development of novel and advanced engineering solutions to address a number of challenges from the fields of nanofabrication, optics and microfluidics and presents the discovery of a series of novel techniques, mechanisms and applications across these fields.

A

PUBLICATIONS

Here I include a list of publications for which work was undertaken during the time of my PhD. Many ideas and figures included in this thesis have appeared previously in these publications, a fuller disclosure of my own and my collaborators contribution to the work is given in the relevant sections.

ACCEPTED PUBLICATIONS

Real-time dielectrophoretic signalling and image quantification methods for evaluating electrokinetic properties of nanoparticles

David J. Bakewell, *Joe Bailey* and David Holmes. All authors contributed equally. (2015). Elecectrophoresis, 36 (13)

Broadband Terahertz Metamaterial Absorber Based on Asymmetric Resonators With Perfect Absorption

Yongzheng Wen, Wei Ma, *Joe Bailey*, Guy Matmon & Xiaomei Yu. (2015). IEEE Transactions on Terahertz Science and Technology, 5 (3)

Absorption modulation of terahertz metamaterial by varying the conductivity of ground plane.

Yongzheng Wen, Wei Ma, *Joe Bailey*, Guy Matmon, Gabriel Aeppli and Xiaomei Yu. (2014) . Applied Physics Letters, 105(14),

Separation of blood cells with differing deformability using deterministic lateral displacement

Holmes, D., Whyte, G., *Bailey, J.*, Vergara-Irigaray, N., Ekpenyong, A., Guck, J., & Duke, T. (2014). Interface Focus, 4(6),

Planar broadband and high absorption metamaterial using single nested resonator at terahertz frequencies.

Y. Wen, W. Ma, *J. Bailey*, G. Matmon, X. Yu, & G. Aeppli (2014). Optics Letters, Vol. 39, pp. 1589-1592

Advancing image quantification methods and tools for analysis of nanoparticle electrokinetics

Bakewell, D. *J., Bailey*, J., & Holmes, D. (2013). AIP Advances, 3(10)

Direct and alignment-insensitive measurement of cantilever curvature

Hermans, R. I., *Bailey, J. M.*, & Aeppli, G. (2013). Applied Physics Letters, 103(3)

Polarization-independent dual-band terahertz metamaterial absorbers based on gold/parylene-C/silicide structure

Wen, Y., Ma, W., *Bailey, J.*, Matmon, G., Yu, X., & Aeppli, G. (2013). Applied Optics, 52(19)

Bistable collective behavior of polymers tethered in a nanopore

Osmanovic, D., *Bailey, J.*, Harker, A. H., Fassati, A., Hoogenboom, B. W., & Ford, I. J. (2012). Physical Review E, 85(6)

SUBMITTED PUBLICATIONS

Surface-catalyzed dimerization of drugs unravels a new mode of action for killing multidrug resistant microbes

Joseph W. Ndieyira, Joe Bailey, Alejandra Donoso-Barrera, Manuel Vögtli, Matthew Cooper, Chris Abell, Rachel McKendry and Gabriel Aeppli. Submitted to Nature Scientific Reports

PUBLICATIONS IN PREPARATION

Experimental observation of broadband grating coupler performance as a function of design and fabrication parameters.

Joe Bailey and Gabriel Aeppli.

Experimental study of the behaviour of slab photonic crystal devices with broadband super-continuum laser sources

Joe Bailey and Gabriel Aeppli.

ACKNOWLEDGEMENTS

Creativity unleashed

Grey, F. (2015). Nature Nanotechnology, 10(5), 480480.

Nanoscale stiffness topography reveals structure and mechanics of the transport barrier in intact nuclear pore complexes.

Bestembayeva, A., Kramer, A., Labokha, A. A., Osmanovic, D., Liashkovich, I., Orlova, E. V., et al. (2014). Nature Nanotechnology, 10(1), 6064.

Dual-cycle dielectrophoretic collection rates for probing the dielectric properties of nanoparticles

Bakewell, D. J., & Holmes, D. (2013). Electrophoresis, 34(7), 987999.

Cell cell signalling in sexual chemotaxis: a basis for gametic differentiation, mating types and sexes

Zena Hadjivasiliou, Yoh Iwasa, Andrew Pomiankowski (2015). J. R. Soc. Interface 12 (109), 1742-5689

B

LEGO2NANO

While in Beijing working on the THz metamaterial project I became involved in a project to design, build and test low-cost opensource scientific hardware for use in Chinese schools. This project has grown into an annual event, bringing students from UCL, MIT, and other top universities to China for a hands on PhD summer school and we are now attempting to spinout a low cost open source atomic force microscope.

The project is founded in the coming together of two ideas, that of citizen science and that of open hardware. By building scientific tools students learn about engineering, technology and open source hardware, empowering them to reclaim ownership over the everyday technology that surrounds us all. By having access to scientific tools students can learn about science and in particular nanotechnology by participating in scientific research. In this chapter I will discuss some of the key principles behind Lego2Nano, the achievements so far and outline its future including it's commercial potential.

Lego2Nano is a project that has involved numerous people, at UCL, Peking University, Tsinghua University, and the Shenzhen Open Innovation Lab. Francois Grey initiated the project. My own contribution has been as a technical coordinator for the three PhD summer school events, along with the development of the spin out proposal. Some portions of this section are edited extracts from publications.[146,147] Much of the time spent on this project was funded by the UCL Advances Enterprise Scholarship.

B.0.1 *The maker movement and open hardware*

In the last 10-15 years there has been an explosive growth in interest in building low cost hardware, making use of inexpensive electronics and rapid prototyping tools such as laser cutters and 3D printers. DIY and craft activities have always been a popular pastime, giving people the opportunity to express themselves, solve problems they experience in day to day life and save money, there are however three important aspects that distinguish the maker movements from these traditional activities. Firstly, the maker movements framing in the digital age, where people can share designs and ideas across large distances connecting people who may in the past have remain isolated. Secondly the increased access to cheap digital prototyping tools mean designs can be easily replicated with no physical contact between enthusiasts. Furthermore what was once dominated by woodwork, needlework, pottery and the like has been complemented with electronics and

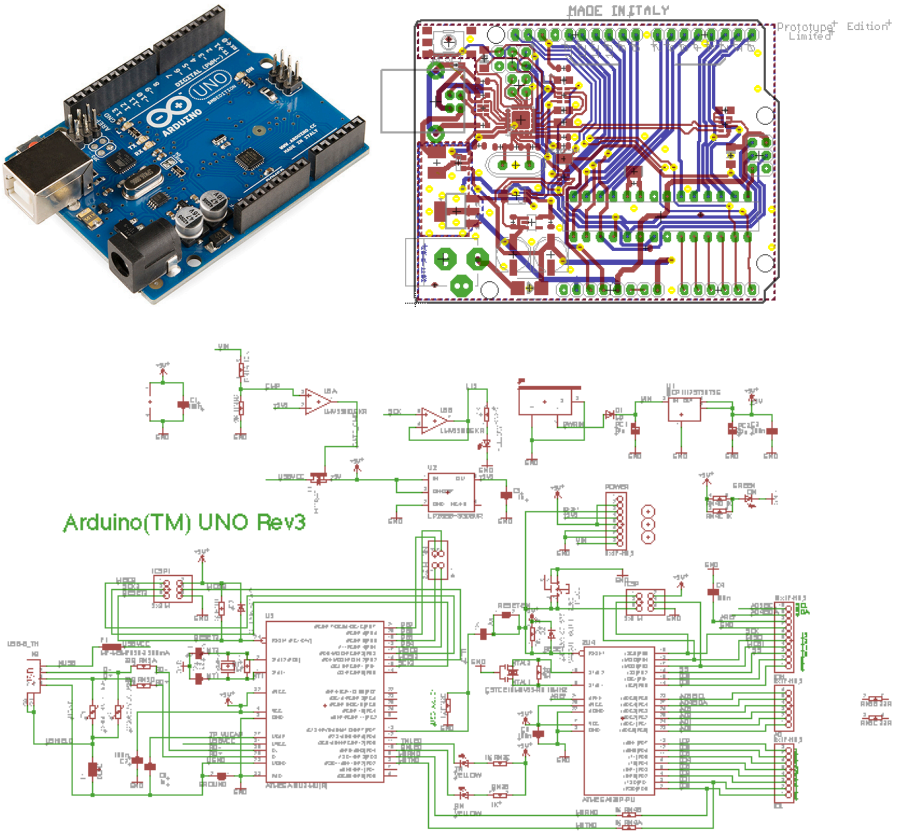

Figure B.1: Ardunio board and schematics. Ardunio board is branded and sold, with the Ardunio name protected. The schematics and design are freely available though[149].

computing. Low cost sensors and components spilling out from the mobile phone and consumer electronics markets have equipped inventors with ever more powerful tools, and the production of physical computing interfaces such as Arduino (see Figure B.1) have allowed people to make their inventions 'smart' and web connected[148].

One of the most inspiring aspects of the maker movement is the way it is empowering people to reclaim the technology that surrounds them. In the last 50 years the growing sophistication of technology, and its omnipresence in our day to day life has lead to a significant dissonance. Whereas 50 years ago it may have been rare to encounter an object that one could not make a reasonable attempt at explaining the mechanism by which it operates, today many people would struggle to explain even the vague principles of operation of objects that we spend significant parts of our lives using, computers, phones etc. One could argue that this incongruity, such heavy dependence on

alien objects and the companies that produce them is a harmful or at least unstable situation. People involved in the maker movement have taken ownership of such technology, empowering themselves to reshape the world around them as they want, inventing new products that meet their needs.

Not all but a significant portion of makers and maker communities have close links with the open source movement. This is unsurprising considering the pivotal role opensource software and hardware in establishing the movement. Many of the first low cost 3D printers were open source, Arduino the most successful physical computing interface that is the brain in many maker inventions is open source. The spirit of open source, that products should be open to tinkering and improvement by users is of course closely aligned with the maker approach.

One should not confuse opensource with free, unsurprisingly such unfettered invention has resulted in new products and new markets. Although many of the products are niche, the nature of the global market, the low cost of manufacture, sales and distribution means that products no longer necessarily need to dominate a market to be successful, the so called long tail economic model sees a significant market share made up by such niche products, for example the Etsy online maker market place saw $0.5billion worth of transactions in 2011[150]. There are also larger markets emerging in unexpected areas, the rapidly growing interest in unmanned aerial vehicles, UAV or drones being a good example, with open source projects such as DIY-drones.com and OpenPilot being integral to this, the former leading to 3DRobotics a commercial drone company with over $30 million of investment[151]. There are open source products such as Arduino that have been incredibly successful, with sales of approx $20 million in 2011, despite, and in fact largely due, to its hardware designs, software and documentation being freely released with an open source license, allowing users to adapt it to their needs and build products to interface with it, leading to a huge on-line community behind it.

Lego2Nano is rooted in the maker and openhardware movements in a number of ways. Primarily we believe making and building is the best way to learn, particularly when it comes to technology. Furthermore we believe that making things open increases the likelihood of a product being successful, even the most innovative company can rarely compete with a network of enthusiasts freed to manipulate and

adjust a product to their own needs. Finally we think these concepts are particularly relevant when it comes to science. Scientific inquiry is in its very nature creative, and requires an adaptable and diverse toolset. We believe many tools that are currently restricted to the research environment fall in this category and are ripe for open source development, some examples of previous efforts range from scanning tunnelling microscopes[152] to oscilloscopes[153], and are not restricted to the physical science, including polymerase chain reaction (PCR) machines[154].

B.0.2 *Citizen science*

Citizen science is defined in the Oxford English dictionary as being *scientific work undertaken by members of the general public, often in collaboration with or under the direction of professional scientists and scientific institutions*. Historically citizen science has described a large variety of styles of projects with a variety of aims and goals. At one end of the spectrum are projects that require very little volunteer engagement such as SETI@ home which makes use of a distributed network of volunteers computers to process data. One of the most successful citizen science projects, Galaxy Zoo expanded upon this idea. Instead of harnessing volunteers computer power, Galaxy Zoo, which is also directed by professional scientists, harnesses volunteers brain power to help classify images of distant galaxies. After the release of the first Galaxy Zoo more than 40 million classifications were made in approximately 175 days by more than 100,000 volunteers[155]. An unforeseen and interesting consequence that reinforces the power of the citizen science concept was the enthusiasm of the volunteers who did not stop at classifying the images in the way instructed, instead discussing their findings in on-line forums and ultimately suggesting further anomalies, some of which turned out to be genuinely new astronomical entities[156].

Other projects have pushed this approach further actively engaging the creativity of the users. Foldit is a web based game that scores users ability to fold a protein into a low energy configuration, users jiggle, stretch and twist proteins in ways that are predefined by the scientists behind the game to be physically realistic (Figure B.2). Similarly to Galxy Zoo, Foldit volunteers surprised the original developers and started forming teams to pursue different folding strategies, essentially

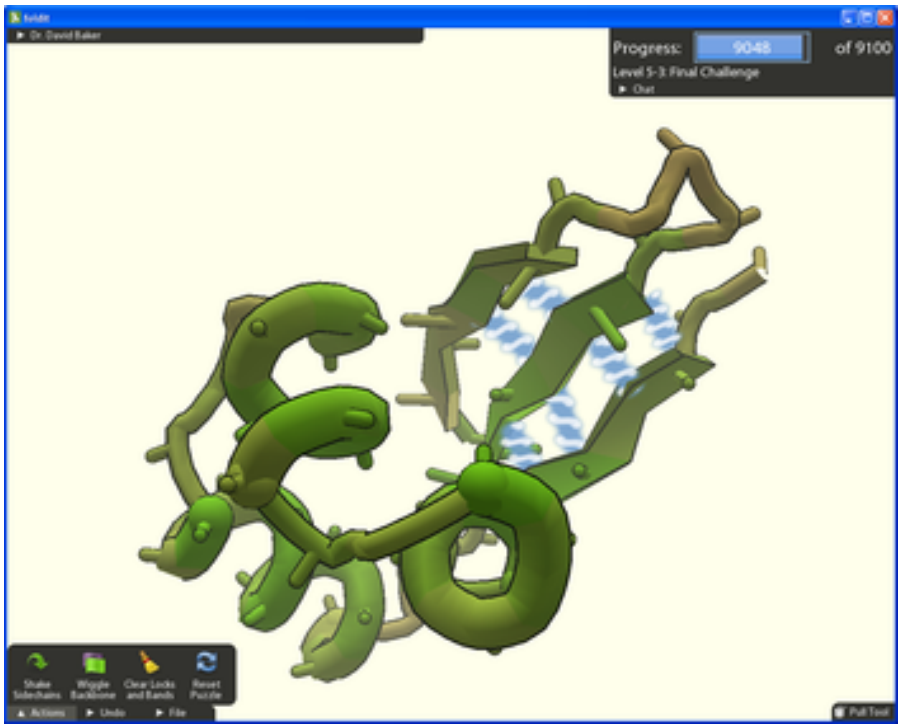

Figure B.2: Screen shot from Foldit on-line game. Users must compete to find the lowest energy configuration of the protein using a set of operations that have been preselected by scientists to replicate physically realistic processes[157]. The structures found by users have been published in Nature Biotechnology[158]

initiating their own research programs leading to improved protein design[159,158], and successfully deciphering the structure of a protein that had eluded scientists for 15 years in a matter of weeks[160]. Reaching the other end of the spectrum there are projects started and run by non-professional scientists. Radiation Watch[161] and SafeCast[162] were started after the Fukushima disaster by a citizen frustrated with the lack of transparency in government studies. He developed a small device that allows Japanese smart-phone users to monitor and upload radiation levels to a public map. Public Lab[163] was set up following the deepwater horizon oil spill, it is an on-line community sharing information on low cost environmental monitoring techniques, and distributing the data collected by members. The maps of the oil spill made by members using home built helium balloons were used by local residents and international news agencies alike.

Lego2Nano shares many aspects of these different approaches to citizen science, we hope to build an on-line community of students and individual enthusiasts and professional scientists with AFM's, who can share data and define their own projects and scientific questions.

B.1 LEGO2NANO 2013-PRESENT

Somewhat ironically given western countries often nostalgically admiring perspective of the traditional values common to Chinese education China is in the midst of a widespread re-evaluation of its education system. Rote-learning for exams is out of favour, and even the role of the notorious Gaokao college entrance exam is being reconsidered, as top leaders search for ways to nurture the sort of innovative talent and creativity that can match China's future economic needs.

Chinese children primarily learn science from textbooks, as do their teachers. Even for undergraduate science students, the majority of hands-on experience comes from lab exercises that are highly constrained in order to support textbook learning, and do not reflect the open-ended nature of real scientific enquiry. Lego2Nano proposes the pursuit of an emerging technological opportunity that can enable Chinese schoolchildren to gather, share and analyse real scientific data, even for schools on a very limited budget. This technological opportunity builds on the methods of crowdsourcing and citizen cyberscience to gather and share data online, and a trend called frugal science,

which focuses on lowering the cost of scientific equipment to make it more accessible to people in developing regions.

To explore this opportunity, we organized an international summer school at Tsinghua University in September 2013, where students from a range of disciplines (design, science, engineering...) ages (high school, undergraduate, postgraduate...) and nationalities (China, UK, Singapore...) collaborated on a challenge called Lego2Nano, which involved designing and building a low-cost atomic force microscope and associated on-line tools for sharing and analysing data.

An important feature of this summer school was its focus on collaborative learning between schoolchildren and university students. The rationale for this approach is that when designing interactive science for children, we should involve those children actively in the process, and be inspired by their vision for what they could learn this way. In the future, we plan to extend this "learning cascade", which starts with the students of Tsinghua University - an icon of the Chinese education system - so that it emanates through local high schools and regional middle schools to primary schools across the country. We also want to amplify this process by creating a virtual laboratory where tools, methods and data are shared online.

The Lego2Nano challenge was to develop, build and exploit an atomic force microscope (AFM) at a price below 1000 RMB (about $160), affordable for a Chinese middle school. To put this challenge in perspective, a laboratory-grade AFM costs around $100,000, and even so-called educational models are typically priced at $20,000. AFMs, in contrast to optical and electron microscopes, do not require expensive focusing lens components. Rather, they rely on sensing the direct action between a probe and a sample surface. The principle of the AFM is closely analogous to that of a vinyl record player. Nevertheless, AFMs have costly components, for example, the piezoelectric actuators that move the sample relative to the probe with nanometric precision, and the readout system used to detect the motion of the probe. The teams were encouraged to find low-cost alternatives to these and other AFM components. Kits containing useful materials and components were prepared in advance of the event, including stocks of LEGO, Makeblock, an Arduino, piezo buzzers, USB optical microscopes and micro-manipulators. The teams were also encouraged to use available tools such as 3D printers, as well as components from local consumer electronics markets in Beijing, to supplement their toolkit. It is worth

Figure B.3: Photos from previous Lego2Nano events. Clockwise from top left: Children Tsinghua high school discuss their lego model AFM. Prototyping control electronics for the openAFM. The top of the scanning stage with DVD head readout system on a prototype openAFM. A working prototype low cost AFM developed by En-Te Hwu. Visit of Danish PM, Lego CEO, LegoFoundation Director and Chinese deputy minister for education

noting that the students were under no compunction to use LEGO or any other specific component.

The unusual nature of the Lego2Nano event resulted in considerable press attention in China and subsequently worldwide. As a result, other research groups working on similar low-cost DIY efforts contacted us to share their experiences and learn more about ours. One of these groups had developed a fully functional AFM that ingeniously uses the cheap piezoelectric buzzers from electronic watches and the readout head from a standard DVD player to replace two of the expensive components of an AFM[164]. While the associated control electronics is still too expensive for schools, this model allowed us to explore what happens when middle schools students build and operate a DIY AFM by themselves. In this second event, held in January 2014, a team of middle school students assembled a DIY AFM and used it to scan objects successfully with nanometre-scale precision in less than a day. The students imaged microscopic dust particles on a DVD grating, typical of pollution in Beijing. This experiment made

visible the sort of particles that PM2.5 pollution detectors are sensitive to, while revealing a much broader spectrum of particle sizes.

Since this first summer school, two more have been held with the expansion of the event to include students from MIT and spend time in Shenzhen, hosted by the Shenzhen Open Innovation Laboratory.

B.2 OPENAFM SPINOUT

Following the success of these events the opportunity to spin out the project from the summer school events into a full time social enterprise was apparent. As I approach the end of my thesis I have decided, along with a number of the past participants of the summer school to pursue this opportunity. We are in the process of founding a social enterprise with the focus of delivering low cost scientific instrumentation to makers and schools. By gaining funding and exposure through these efforts we would also explore the possibility of applying our low cost approaches to more commercial applications. The next section is a reformatted version of our business proposal, currently being pitched to a number of investors and accelerator funding bodies.

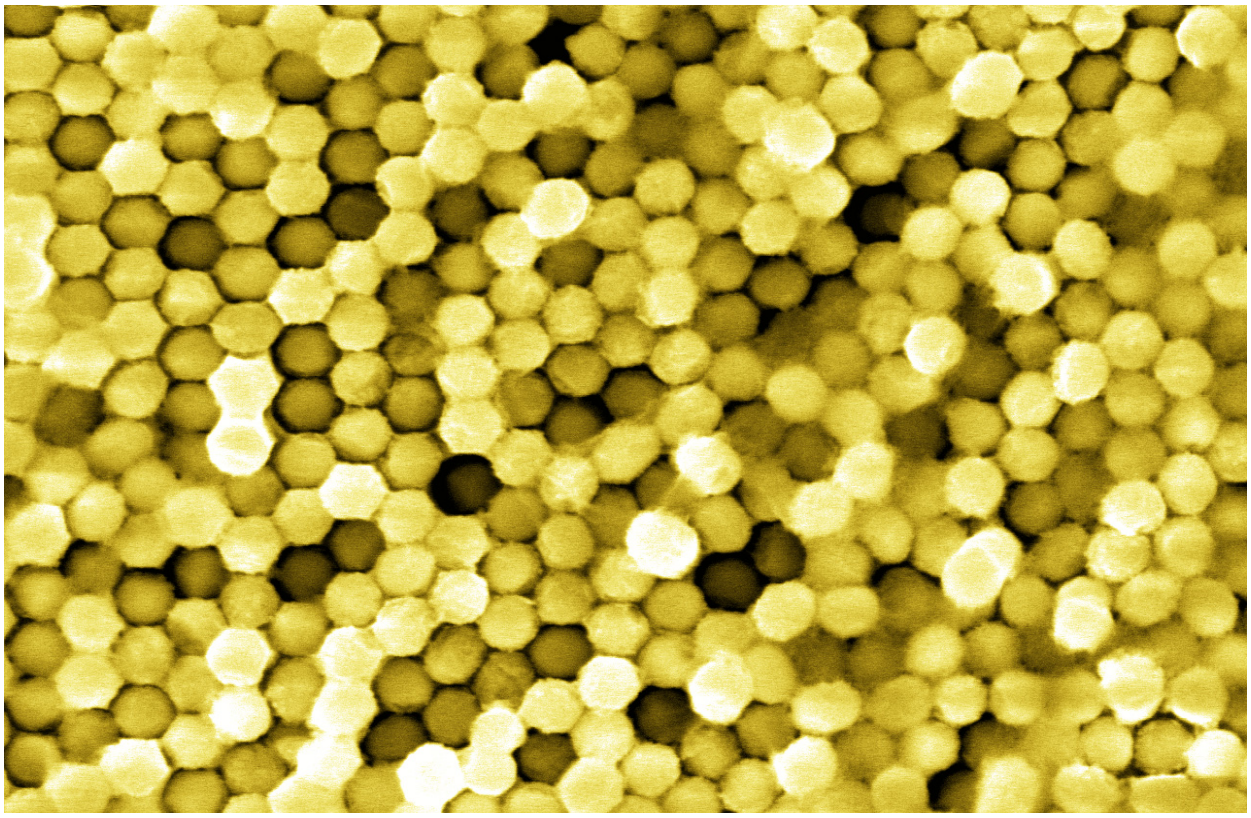

OpenAFM

December 2015

Executive Summary

Overview

Nanotechnology is one of the fastest growing technology sectors and research areas, it is also an area of science that captivates the imagination. Nanoscale materials continue to make their way into everyday products and enable advances in other fields like computing, optics and energy, developing low cost tools to measure and manipulate matter on this scale is essential to continued growth in this area.

A foundational technology in nanotechnology is the atomic force microscope (AFM), a microscope that maps the topography of matter on the atomic scale. It is an incredibly powerful technique not only due to its precision but also its versatility.

OpenAFM will provide low cost maker style kits and complementary educational and online resources to give schools, enthusiasts and budget restricted research groups access to this world initially through the use of low cost atomic force microscopes, but also by complementary instruments such as nano engravers, nano laser cutters and nanolithography tools.

Product

We have developed an atomic force microscope, that costs 500-1000 times cheaper than existing products. This microscope allows you to image and manipulate matter on the nanometer and even atomic scale. Our first product will be a maker style kit based on this prototype. We will follow up this product with hardware add-ons that add further functionality such as nanoengraving, nanoprinting. While also improving the sophistication of our product to access high end markets such as tech innovators and R&D.

Market

Initially, our product will be targeted at educators, makers and enthusiasts. We have seen enormous excitement about our product among these groups, both in China and during a recent showcase at Mozilla Festival. In order to break into these markets, we will use our existing connections with educational establishments and makespaces in the UK and China, such as Tsinghua University and SZOIL.

Beyond this, we intend to create a product which will be marketed at tech innovators working with nanotechnology and research and development facilities. This will require greater development costs to create a product with a higher specification but will in turn provide greater profit margins.

There are not currently any companies who would directly compete with us in this low cost market, although there are a number of large scientific instrument businesses producing products at a much higher price point.

Business

Our business will initially be focussed on developing our OpenAFM product into a maker style kit and developing the online community hubs and resources to compliment it. We will use our partnerships with education institutes and makespaces in Shenzhen to rapidly iterate our initial prototypes and increase our profile.

The long term plan for the company is to establish ourselves as front runner in the low cost, non specialist market, using our experiences to refine the product, using the exposure and credibility of a large low cost user base to leverage entry into the harder to penetrate but potentially more profitable market of established commercial and academic R&D users.

Team

The team is self-contained and has the required skills and expertise to achieve our goals during the short time frame of the programme. Our prototype is in its second iteration and the tasks to develop it into a fully functional product are achievable by the team. We also have a network of advisors and mentors that will provide guidance and feedback into the development.

Overview

Nanoscience is one of the fastest growing technology sectors - new insights into the physical, chemical and biological process that occur on this scale are driving the development of some of the most innovative new technologies, enabling huge progress in the fields of electronics, computing, optics, energy storage, environmental monitoring, drug development and healthcare.

Nanoscience and nanotechnology is also an area of science that captivates the imagination, with enthusiasts, makers and educators all becoming increasingly aware of its untapped potential.

The scanning probe microscope, of which AFM is a prominent example, arguably founded the field of nanotechnology when it's invention won Binnig and Rohrer the Nobel prize in 1986. The reason AFM and scanning probe techniques have been so successful is due to their versatility - once you have the ability to position matter with an atomic accuracy, the possibilities are endless. You can of course image a sample through mapping it's height, you can also push a sample to measure its stiffness, if your tip is conducting you can map the electrical conductivity. Furthermore if you push hard enough you can engrave, or if your tip is covered in chemicals you can paint molecules on a surface, all of these with nanometre accuracy. These features have made AFM a go-to tool in fields as diverse as material characterisation, drug development, device characterisation and environmental monitoring.

From a sophisticated device that launched the field of nanotechnology

Binnig and Rohrer
1986 Nobel Prize for Scanning Probe Microscope

To an affordable DIY project for children and makers around the world

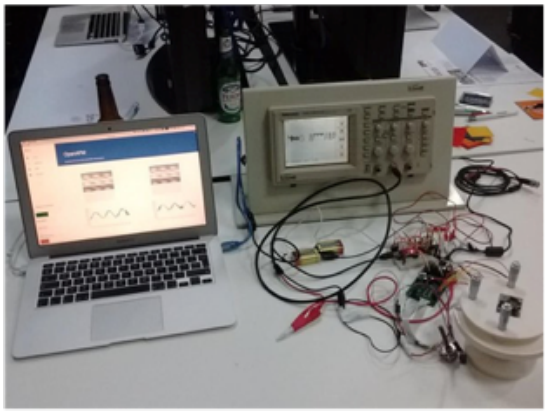

openAFM prototype
Mozfest 2015

We believe that there is a huge untapped potential for opening up a market for low cost, easy to use tools in the field of nanotechnology. Makers are increasingly interested in the cutting edge of science, while educators, students, and nanotechnology startups strive to gain access and exposure to research grade instrumentation and techniques. Furthermore

the proliferation of nanotechnology into everyday items means more and more startups and tech innovators need access to these types of tools.

We plan to establish ourselves as front runners in this currently unexploited market through the rapid delivery of a low cost open source atomic force microscope in a maker kit package. Our current prototype cost less than $100 in parts, for comparison a standard atomic force microscope being used in laboratories around the world ships for anything from US$ 50,000 – $USD 500,000 with more sophisticated models costing even more.

We will enhance the impact of our product by developing a complementary online community of enthusiasts, makers and educators around our product, harnessing the enthusiasm and diversification often seen for open source hardware. We will also develop education materials and online courses working with our network of educators and researchers to establish a collaboration framework around the device, increasing its profile and the adding to the establishment of an online community.

Following the launch of our brand via the OpenAFM product we will develop complementary hardware and software packages to expand the capabilities of the device and promote new applications.

Product

We have developed an atomic force microscope (AFM) that costs 500-5000 times less than similarly capable devices currently on the market. An AFM is a microscope that works by using cantilever probe to measure the height of a sample as a high precision stage moves the sample beneath it. By correlating the height readout from the cantilever with the position of the stage a topographical image of a sample is made, such images can have atomic resolution.

Our company takes this powerful technology and make it accessible to makers, educators and small companies and other tech start ups.

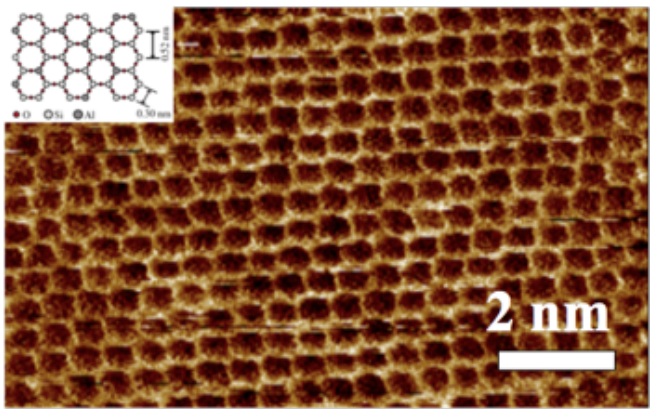

Hoogenboom *et al.*, Appl. Phys. Lett. (2006)
Kahn *et al.*, Rev. Sci. Instrum. (2010)

Our huge reduction in price is down to three factors. Firstly we have replaced the complex customised optical readout system with a DVD optical pickup unit, an incredibly engineered but low cost and commonplace component. Secondly we have replaced the expensive and high voltage piezo stacks used to move the sample with a lever design that uses low cost, low voltage piezo buzzers, another off the shelf electrical component. Finally, and partly due to the use of low voltage piezos we have managed to greatly simplify the control electronics making use of low cost PCI units like Arduino. We will turn this prototype into a maker style kit suitable for use by non specialists.

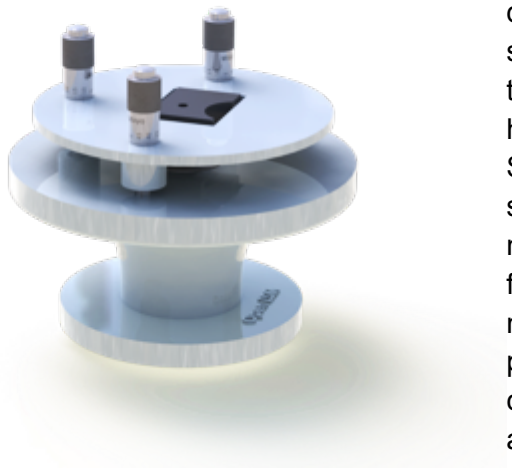

After developing a suitable product for educators and enthusiast we can move on to a complementary trajectory for further product development. Firstly we will increase the sophistication of our product, pushing into the high-tech and R&D environments currently dominated by high-end models and a handful of brands. Secondly, we will develop add-on products and software, for instance, nanofabrication tools such as nano engravers, nanolithography, nano bio-functionalisation tools along with other scanning modalities and probe types. Alongside our physical products we will produce learning resources, online courses and collaboration tools and also sample and probes subscription services. These will be developed hand in hand with the Lifelong Learning Laboratory a collaboration between the Lego Foundation and Tsinghua University, for which our Non-Executive Director Prof Francois Grey will be a co-director.

Market

The primary markets for our current product will be makers and educators. We have already established a network of educators and enthusiast that want to adopt this technology and make it accessible to students.

Educators and Makers

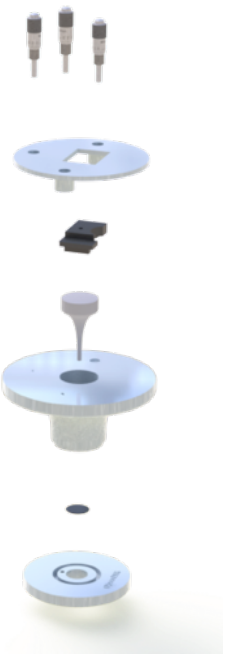

Through our previous work at the Lego2Nano programmes and in collaboration with Tsinghua University we have developed channels into the Chinese education system and gathered support from influential academics.

Similarly, schools and academies in the UK have shown significant interest in it. We participated in MozFest 2015 where we showcased our prototype to education and technology enthusiasts. We had very positive feedback and follow up communication to bring a more reliable product into schools.

Educators see numerous areas of educational potential in the product, from allowing children to explore the nano-world to teaching practical aspects of technology, data collection and making skills. Increasingly there are movements, both in China and the UK, away from traditional forms of education and towards more activity driven approaches.

"There are many new opportunities for deploying re-configurable lab equipment in China or around the world"
- 顾学雍 Prof Benjamin Koo (Department of Industrial Engineering Tsinghua Universty)

"Providing tools that operate on the nanoscale to makers could be a huge revolution in the maker community. I am really excited to see what openAFM can bring to the table and look forward to working with them in the future"
- 李大维 David Li (Founder SZOIL and XinCheJian, China's first makespace)

"When I told my students that they can build an AFM to detect pollution, for example, PM 2.5, they were very excited. It's a wonderful opportunity for us"
-邱楠 Qiu Nan (Teacher at Tsinghua High School)

We also plan to develop lessons tied to curriculum objectives and collaboration between schools and research institutions to promote engagement an increased use of the AFM.

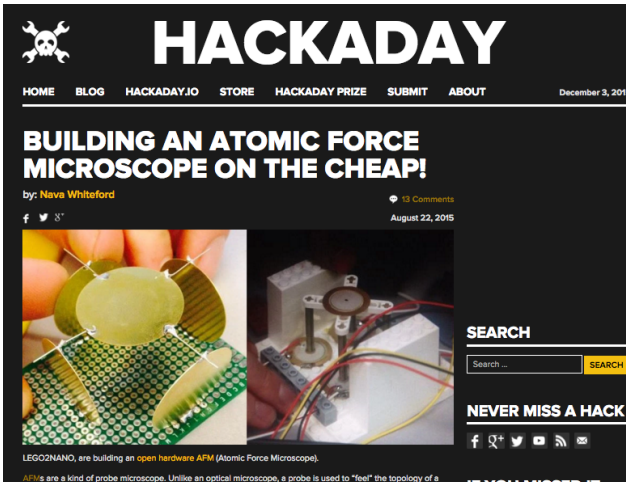

In the UK, there are roughly 25,000 schools. Despite highly constrained budgets, they already spend a significant portion of their science budget on optical microscopes which are greatly inferior to our product at imaging but even more so in their educational potential.

A comparable technology and sales approach is the current low cost 3D printer market. These are sold to individual enthusiasts, makespaces, schools and universities, with a predicted shipment of ~500,000 units this year which gives an upper band to sales in these areas.

We are scheduled to participate in GOSH! 2016, an open hardware gathering and open Assembly, an event being organised by Tsinghua University and CRI Paris being held in Shenzhen Aug 2016. We plan to use these events, along with others, to develop our links to the scientific community paving the way to place our product in higher-education institutions, R&D facilities and other startups.

NanoTech Startups and R&D

As we establish ourselves in that market and continue to develop our product we will move into high-tech industry segment and R&D facilities. This market will require slightly higher specifications and additional product development investment but will yield significantly larger margins.

Based on our research and online figures, there are currently several hundred nanotechnology startups operating in what is a rapidly expanding field.

Further sales to research institutions in Asia and South America is the second main market and could provide considerable revenue from technical support. There are over 2000 universities in China, 700 in India , 1300 in South America and over 1000 in South East Asia.

Competition

Although there are no existing companies that target a broad market through low-cost products there are companies that specialize in the provision of atomic force microscopes to research groups.

1) Bruker, field leaders in AFM provision, along with other scientific instruments ($393m revenues last quarter of 2015). https://www.bruker.com

2) JPK. Scientific instrumentation specialized in AFM for the life sciences. http://www.jpk.com/

3) Nanosurf, specializes in more compact and lower cost atomic force microscopes. Although Nanosurf would be a closer competitor than Bruker or JPK due to their lower priced device, their existing offering is still beyond the reach of the general public. https://www.nanosurf.com

Business

Our business will initially be focussed on developing our prototype into a maker style kit and developing the online community hubs and resources to compliment it. This will be achieved by integrating 3 development paths.

Firstly in house development will focus on fine-tuning performance, DFM and establishing supply chains. We will also establish beta-product user groups at hack spaces in Shenzhen and Shanghai.

We will collaborate with the Lifelong Learning Laboratory at Tsinghua University to set up our education trial users at Tsinghua High School and Tsinghua Experimental School in Shenzhen. These trials will help us establish a fast iteration and user feedback loop accelerating the products suitability for the target markets of makers and educators. As well as fine tuning this initial product we will develop complementary technologies and prototype hardware add-ons, these should be released soon after the launch of our initial product.

In school test users

Tsinghua High School

Shenzhen Experimental School

Product development

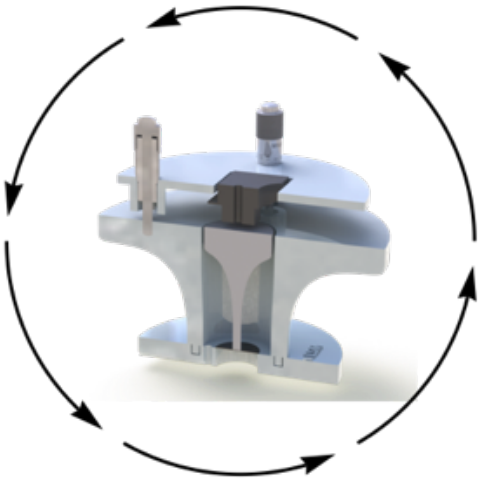

Hack space test users

新车间
[XINCHE]IAN
Hackerspace in Shanghai

As a first educational project we will establish a partnership between schools sharing data on PM2.5 particles imaged by their AFM's, this could create a big data repository of pollution information. This project has already been trialled in the lego2nano hacking events and was a great success with teachers and students.

The long term plan for the company is to establish ourselves as front runner in the low cost, non specialist market, using our experiences to refine the product, using the exposure and credibility of a large low cost user base to leverage entry into the harder to penetrate but potentially more profitable market of established commercial and academic R&D users.

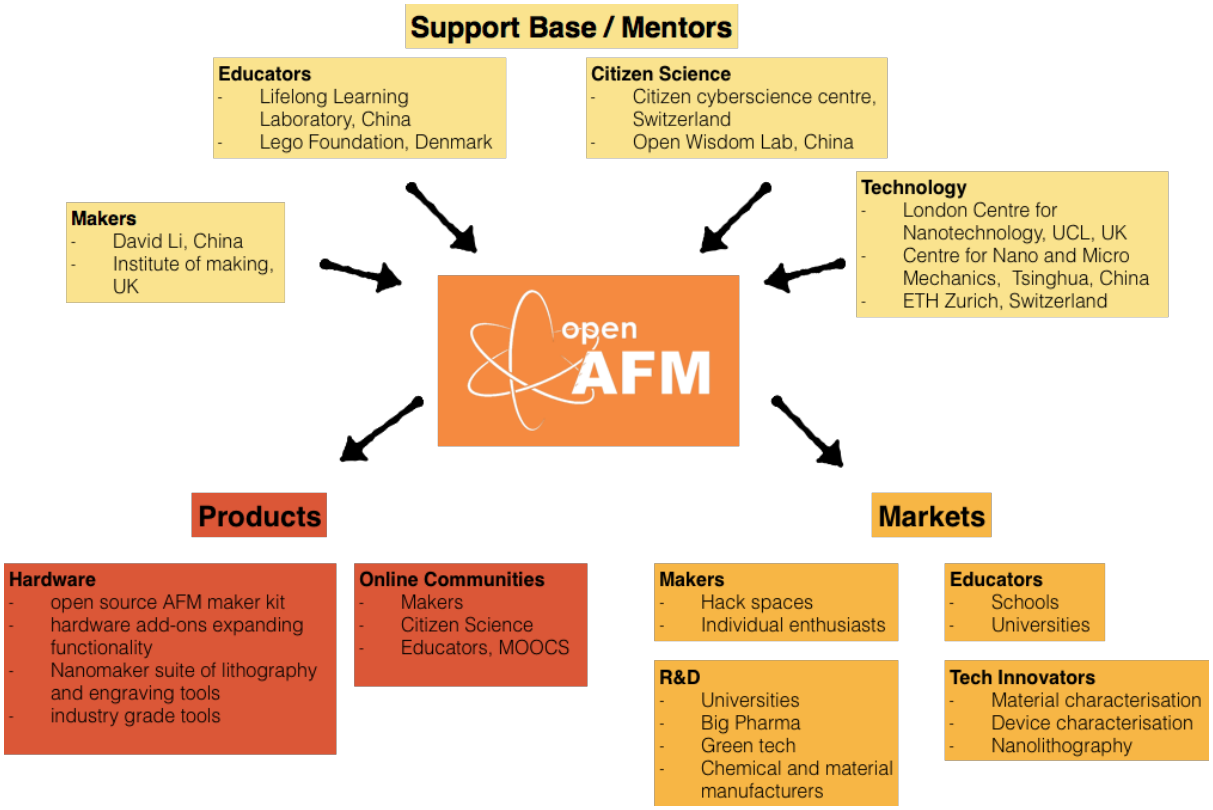
Support Base / Mentors
Educators
- Lifelong Learning Laboratory, China
- Lego Foundation, Denmark
Citizen Science
- Citizen cyberscience centre, Switzerland
- Open Wisdom Lab, China
Makers
- David Li, China
- Institute of making, UK
Technology
- London Centre for Nanotechnology, UCL, UK
- Centre for Nano and Micro Mechanics, Tsinghua, China
- ETH Zurich, Switzerland
open AFM
Products
Markets
Hardware
- open source AFM maker kit
- hardware add-ons expanding functionality
- Nanomaker suite of lithography and engraving tools
- industry grade tools
Online Communities
- Makers
- Citizen Science
- Educators, MOOCS
Makers
- Hack spaces
- Individual enthusiasts
Educators
- Schools
- Universities
R&D
- Universities
- Big Pharma
- Green tech
- Chemical and material manufacturers
Tech Innovators
- Material characterisation
- Device characterisation
- Nanolithography

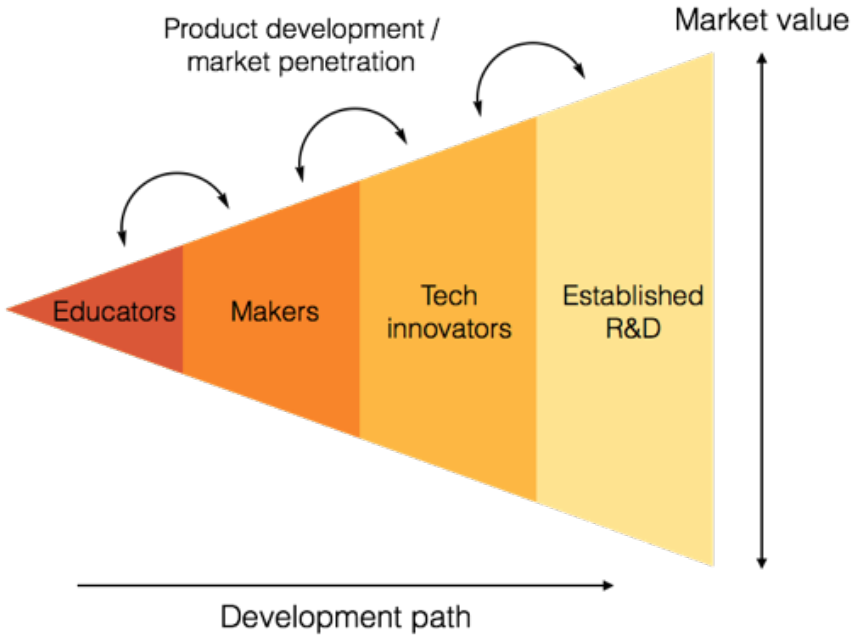
Product development / market penetration
Market value
Educators
Makers
Tech innovators
Established R&D
Development path

During our time at HAX we will aim to have fully functionally and easy to operate AFM. We will be focusing in the following task.

Mechanics

- Stage design
- Cantilever and probe mount
- Sample holder design

Firmware

- Improved control of the stage.
- Auto calibration and noise reduction.
- Sampling rates and modalities.
- Focus automation.

Interface

- Improved image tracing.
- Usability improvements.
- Firmware interaction development.

QA

- Calibration procedure.
- Sample staging

Business

- Kickstarter campaign
- Products and customer growth
- Community engagement

Team

Our team is self-contained and brings together a wide range of experiences, skills and access to networks.

Joe Bailey

Joe Bailey has studied physics and is completing a PhD in nanotechnology at the London Centre for Nanotechnology, part of UCL. He has experience of working with AFM's and designing instrumentation. He has also been a key member of the lego2nano organising team which has run hacking events in China the last 3 summers. Non-academic experiences include engineering consultancy work, and the design and construction of a geodesic dome filled with lasers, which has been used as a venue at numerous festivals in the UK

Role

Responsible for hardware development and CAD, and managing the beta-product testing groups in makespaces and schools.

Angus Whitehead

Whilst completing a BSc in Architectural Interdisciplinary Studies at UCL, Angus honed product design and making skills but increasingly found a better outlet for these in a newly discovered passion: technology. Initially as a self taught programmer, he has experience with many different languages and technologies, having completed projects spanning the Internet of Things and embedded systems, machine learning, wearable devices and the design of numerous user interfaces. He is currently undertaking an intensive bootcamp in web development to increase his skills in this fundamental area.

Role

Responsible for user interface and user experience, website development and management, community management and engagement.

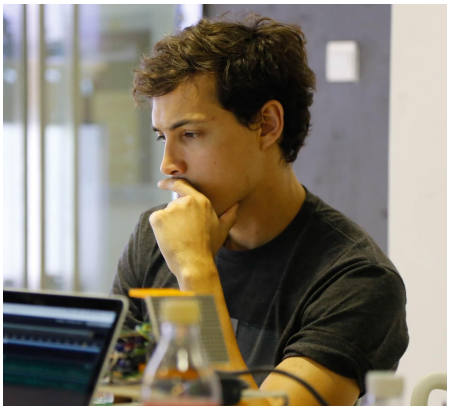

Jose Michel

Jose is a passionate developer with a BSc. in Computer Systems Engineering and currently studying a MSc. in Technology Entrepreneurship at UCL.
He has several years of experience as a professional software engineer in corporations large and small. He has a strong passion for building things and new technologies and is an advocate for lifelong learning activities that expand his understanding of everything around him. He joined the Lego2Nano programme where he developed his knowledge of firmware development.

Role

Software engineering and electronic interfacing, business and customer development.

Prof. Francois Grey

Francois Grey is a physicist by training, with a background in nanotechnology and a passion for citizen science. Since September 2014, he is Invited Professor at the University of Geneva and Manager of the Citizen Cyberscience Centre, a partnership between CERN, the United Nations Institute for Training and Research and the University of Geneva. From 2013-2014 Francois was Head of Citizen Science at NYU's Center for Urban Science and Progress, where he launched the Science and the City hackathons in collaboration with ITP, NYU's Interactive Telecommunications Program and Science Hack Day NYC in collaboration with the World Science Festival. Francois was based in Beijing from 2008-2013, where he helped establish the Open Wisdom Lab at Tsinghua University, China's MIT, to promote concepts of open and participatory science. He also helped establish Tsinghua's Lifelong Learning Lab, which extends concepts of participatory science to children of all ages. He has also been a visiting Senior International Expert with the Chinese Academy of Sciences, where he initiated online citizen science in China through a project called CAS@home. Francois received a prestigious Fellowship from the South-Africa-based Shuttleworth Foundation in 2010-11, for his efforts to promote citizen science in the developing world.

Role

Non-executive director and advisor

Prof. Gabriel Aeppli FRS

Gabriel Aeppli is professor of physics at ETH Zürich and EPF Lausanne, and head of the Synchrotron and Nanotechnology department of the Paul Scherrer Institute, also in Switzerland.

After taking his B.Sc., M.Sc. and PhD in Electrical Engineering from MIT, he spent the majority of his career in industry (NEC, AT&T and IBM) where he worked on problems ranging from liquid crystals to magnetic data storage. He was subsequently co-founder and director of the London Centre for Nanotechnology, Quain Professor at University College London, and cofounder of the Bio-Nano Consulting. He is a frequent advisor to numerous private and public entities worldwide (including China, Australia, Europe and the US) engaged in the funding, evaluation and management of technology. A member of the American Academy of Arts and Sciences and Fellow of the Royal Society (London), he was a recipient of the Mott Prize of the Institute of Physics(London), the Oliver Buckley prize of the American Physical Society and the Neel Medal/International Magnetism Prize.

Role

Non-executive director and advisor

Appendix A - Revenue Flow

Date			Jan-16	Feb-16	Mar-16	Apr-16	May-16	Jun-16	Jul-16	Aug-16	Sep-16	Oct-16	Nov-16
Operating Expenses													
Salary		1400	3080	3080	4200	4200	4200	4200	5600	5600	5600	5600	5600
Hardware Devlopment			1000	1000	1000	1000	1000	1000	2000	2000	2000	2000	2000
Marketing						700	700	700	700	700	700	700	700
Travel/Outreach			500		500		500	500	500	500	500	500	500
Total Operarating Expenses			**4580**	**4080**	**5700**	**5900**	**6400**	**6400**	**8800**	**8800**	**8800**	**8800**	**8800**
Sales													
openAFM	units sold		4	0	4	0	0	50	200	200	200	200	250
	cost to user per unit		0	0	0	0	0	100	100	100	100	100	100
	cost to company per unit		100	0	100	0	0	25	25	25	25	25	25
Cantilever Probes	units sold		0	0	0	0	0	0	25	50	90	130	170
	cost to user per unit		0	0	0	0	0	0	25	25	25	25	25
	cost to company per unit		0	0	0	0	0	0	10	10	10	10	10
Nano lasercutter	units sold		0	0	0	0	0	4	4	0	0	0	50
	cost to user per unit		0	0	0	0	0	0	0	0	0	0	100
	cost to company per unit		0	0	0	0	0	100	100	0	0	0	25
Conducing Tip AFM add on	units sold		0	0	0	0	0	0	0	0	0	0	0
	cost to user per unit		0	0	0	0	0	0	0	0	0	0	0
	cost to company per unit		0	0	0	0	0	0	0	0	0	0	0
Online Technical Support/ Ser	units sold		0	0	0	0	0	0	0	8	8	8	8
	cost to user per unit		0	0	0	0	0	0	0	50	50	50	50
	cost to company per unit		0	0	0	0	0	0	0	0	0	0	0
In person technical Support/ S	units sold		0	0	0	0	0	0	0	1	1	1	1
	cost to user per unit		0	0	0	0	0	0	0	500	500	500	500
	cost to company per unit		0	0	0	0	0	0	0	200	200	200	200
Gross Margin			**-400**	**0**	**-400**	**0**	**0**	**3350**	**14975**	**16450**	**17050**	**17650**	**25750**
Total													
Accumalated Balance		66500	61520	57440	51340	45440	39040	35990	42165	49815	58065	66915	83865
Operating Profit per month			-4980	-4080	-6100	-5900	-6400	-3050	6175	7650	8250	8850	16950

Dec-16	Jan-17	Feb-17	Mar-17	Apr-17	May-17	Jun-17	Jul-17	Aug-17	Sep-17	Oct-17	Nov-17	Dec-17	Jan-18
5600	10000	10000	10000	10000	10000	10000	10000	10000	10000	10000	10000	10000	10000
2000	2000	2000	2000	2000	2000	2000	2000	2000	2000	2000	2000	2000	2000
700	700	700	700	700	700	700	700	700	700	700	700	700	700
500	500	500	500	500	500	500	500	500	500	500	500	500	500
8800	**13200**	**13200**	**13200**	**13200**	**13200**	**13200**	**13200**	**13200**	**13200**	**13200**	**13200**	**13200**	**13200**
200	200	100	50	50	50	50	50	50	50	50	50	50	50
100	100	100	100	100	100	100	100	100	100	100	100	100	100
25	25	25	25	25	25	25	25	25	25	25	25	25	25
220	260	300	320	330	340	350	360	370	380	390	400	410	420
25	25	25	25	25	25	25	25	25	25	25	25	25	25
10	10	10	10	10	10	10	10	10	10	10	10	10	10
100	100	200	200	300	300	300	200	200	100	100	100	100	100
100	100	100	100	100	100	100	100	100	100	100	100	100	100
25	25	25	25	25	25	25	25	25	25	25	25	25	25
0	0	0	0	0	0	0	50	50	100	100	100	150	150
0	0	0	0	0	0	0	200	200	200	200	200	200	200
0	0	0	0	0	0	0	50	50	50	50	50	50	50
8	8	8	8	8	8	8	8	8	8	8	8	8	8
50	50	50	50	50	50	50	50	50	50	50	50	50	50
0	0	0	0	0	0	0	50	50	50	50	50	50	50
1	1	1	1	1	1	1	1	1	1	1	1	1	1
500	500	500	500	500	500	500	500	500	500	500	500	500	500
200	200	200	200	200	200	200	200	200	200	200	200	200	200
26500	**27100**	**27700**	**24250**	**31900**	**32050**	**32200**	**31950**	**32100**	**32250**	**32400**	**32550**	**40200**	**40350**
101565	115465	129965	141015	159715	178565	197565	216315	235215	254265	273465	292815	319815	346965
17700	13900	14500	11050	18700	18850	19000	18750	18900	19050	19200	19350	27000	27150

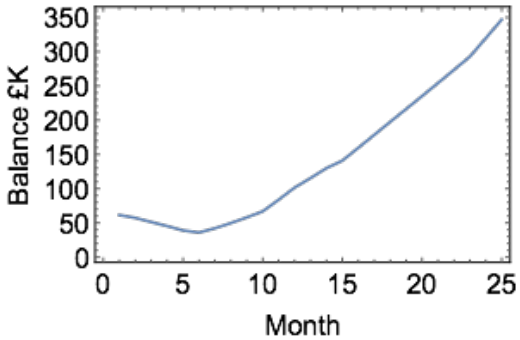

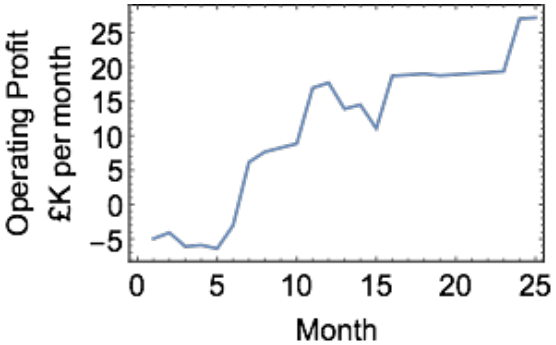

Appendix B - Press Coverage

人民网 people.cn

人民网 >> 教育 >> 滚动新闻

大学生自制显微镜 最低花费仅为五六百元

2013年09月07日09:50 来源：京华时报 手机看新闻

打印 网摘 纠错 商城 分享 推荐 人民微博 关注 字号

原标题：学生自制显微镜

昨天，清华大学国际暑期学校举行挑战学习项目《从乐高到纳米显微镜》的成果展示会。5天内，来自美国、英国、新加坡、罗马尼亚及中国等国家和地区的30多名博士、

新闻热搜词 来源： 百度新闻

梁洛施 禁拍性感戏 大黄鸭亮相园博园 网络舆情师
6颗螺丝2800元 邓文迪被指为间谍 英国禁售中成药
赵红霞 改名 菲召回驻华大使 村干部变黑老大
教师节 孔子生日 雷政富 二审 李开复患淋巴癌

精彩热图 | 人民电视

3分钟为您解密公务员面试的真谛

红领暑假班 盛大开启

People.cn

WIRED.CO.UK TECHNOLOGY ARDUINOS MAKERS MICROSCOPES

UCL students build low-cost, Arduino-powered, Lego atomic force microscope

TECHNOLOGY / 18 SEPTEMBER 13 / by KADHIM SHUBBER

851 shares
3 comments

When Alice Pyne starts talking about giving "crystallised virus structures" to school children, my heart skips a beat. Surely we've screwed up the next generation enough already without giving them the means to wage biological warfare.

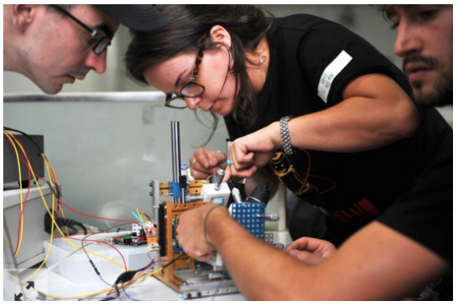

The virus in question, the tobacco mosaic virus, "cannot infect animals," she reassures me later. Her point is that instead of relying on 2D images in textbooks, we should be giving school children something real. Moreover, she

in the classroom

Creativity unleashed

Hands-on challenges such as building a low-cost atomic force microscope for schools can teach more than standard lessons, says François Grey.

When I arrived as a visiting professor at Tsinghua University in 2008, one of my first tasks was to set up an international summer school that would expose foreign students to the many exciting advances being made in China in the field of nanotechnology, and to encourage them to collaborate with their Chinese counterparts on practical projects. This summer school became an annual fixture, thanks to an ongoing collaboration between the London Centre for Nanotechnology at University College London (UCL), the Centre for Nano and Micro Mechanics at Tsinghua University and the Institute of Micro/Nanoelectronics at Peking University. By experimenting with the format over the years, I realized that hands-on projects, rather than lectures by experts, worked best for this interdisciplinary subject and international mix of students.

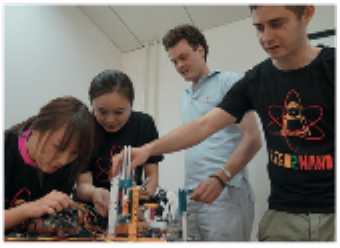

non-traditional themes, including thought-provoking introductions to the rapidly emerging maker movement in China, and the global hive of low-cost hardware production in Shenzhen.

In just five days (and several nights for some), the teams came up with a series of clever innovations, which tackled many of

prompted discussions about the relative health risks of different size particles, and their possible origins.

At the second LEGO2NANO summer school, held in September last year, new student teams went beyond the hardware design to look at how to bring down the cost of the associated electronics and software for operating the AFM. They even explored possibilities of crowdfunding the production of such devices, and crowdsourcing the analysis of the data that schoolchildren could gather with them.

The extension of LEGO2NANO to broader online public participation, or 'citizen cyberscience' is particularly important, if the project is to scale beyond a few select schools, and have a wider effect on the ongoing reforms to the education system in China. These reforms seek to wean schools off rote learning and an obsession

Article in Nature Nanotechnology

LEGO CEO, Danish PM and Chinese Deputy Minister for Education visiting Lego2Nano

C

CANTILEVER BIOSENSORS

My PhD started in the context of the 'Grand Challenge in Healthcare Diagnostics: Multi-marker Nanosensors for HIV' project, a multidisciplinary effort to develop low cost point of care diagnostic tools for HIV monitoring. This project brought together specialist in optics, virology, nanofabrication, microfluidics, and chemistry. Cantilever biosensors were to form the core sensing platform of the device and as such were a topic I worked on for a significant period of my PhD.

C.1 INTRODUCTION

Forces and mechanics play an incredibly important, and often under appreciated, role in biology. Forces and force transduction are often key to cell signalling, effecting the way cells grow, move, stay put, divide and die[165], they also effect the way molecules are transported and bind[166]. The forces and masses involved in biological process are, however, minute[167]. Modern silicon machining techniques have, however, allowed us to make equally minute structures, with properties such as mass sensitivity and mechanical compliance scaling accordingly. One of the most widespread examples of this is the field of microcantilever sensing, an approach that originated from the field of atomic force microscopy (AFM). Such cantilever devices have led to an ability to measure mass on the scale of nano and even zeptograms[168] and forces with a resolution of pico-newtons.

AFM was first developed as a technique in 1980s[171], since that time it has been adapted to work in many different modes and environments[172,173]. The first use of an AFM as a biosensor saw the tip itself functionalised[174] and used to probe single molecule interactions, after this success it was realised that by using the entire cantilever surface a more versatile sensing platform was available[175,176]. The fundamental principle is that the cantilevers are prepared with a specific antibody or binding site (see Figure C.3), then in the presence of a target biomolecule the cantilever coating will interact and consequently change their mechanical properties. The most common responses

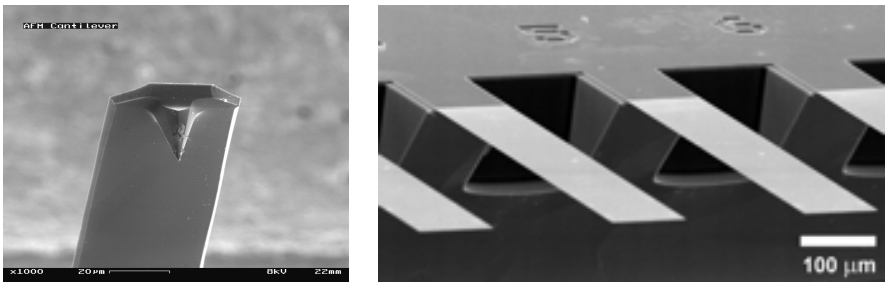

(a) (b)

Figure C.1: Cantilever biosensing is an offspring from atomic force microscopy. The cantilever probes of AFM (a) SEM image of AFM cantilever and tip taken from[169]) have been modified and made into tipless arrays (b) an SEM image of cantilever biosensor array taken from[170]).

utilised are a static deflection of the cantilever due to differential surface stress, or alternatively a change in resonant frequency due to adsorbed mass (see Figure C.2). Using nano-mechanical changes to detect biological species is of particular interest to due to its non-reliance on labels (e.g. fluorescent tags), allowing real-time unperturbed processes to be measured[177], furthermore it gives access to bimolecular forces and interactions at the resolution they are experienced in vivo.

The static response mode has been used widely to detect and measure the properties of many biological agents and events[178]. One of the major advantages of the stress mode of operation is the ease with which it works in the liquid environment. When using static mode it is important to use differential measurements due to the fact that single cantilever or absolute measurements can be distorted by non-specific reactions such as changes in temperature, changes in refractive index and uncontrolled reactions on the cantilever underside[179].

When a target species is adsorbed onto a cantilever there will be a change in the configuration of the receptor and the molecules surrounding it. These changes in configuration can lead to a redistribution of surface charge and steric interactions that generate a stress in the surface of the cantilever[180]. For cantilevers with a single active surface this stress in turn results in the bending of the cantilever, and a displacement of the free end. Normally stress is assumed to be

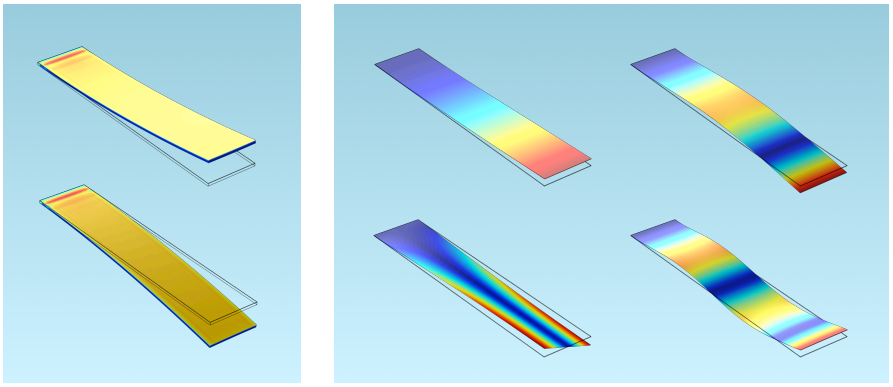

(a) (b)

Figure C.2: a) shows static mode deflection with tensile (bottom) and compressive stress (top) in the sensing layer with color equating to von Mises tress. The opposite notation is sometimes used if one considers the silicon structure itself. b) shows dynamic mode, first four resonant modes with colour equating to displacement

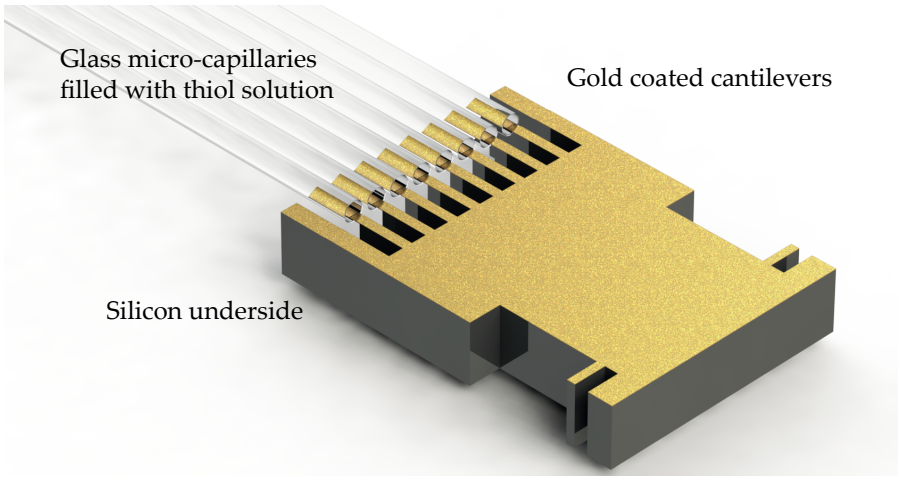

Figure C.3: Traditional method to functionalise cantilevers ready for biosensing experiments. By addressing each of the cantilevers with a separate capillary they can be functionalised with different sensing of reference layers. The drawback with this method is it is incredibly time consuming, requiring a high skill level to perform, both of which will only increase with the number of cantilevers..

uniform across the cantilever, allowing it to be determined from the deflection of the free end using Stoney's equation[181,182]:

$$\Delta\sigma = \frac{1}{3}\left(\frac{t}{L}\right)^2 \frac{E}{1-\nu}\Delta z_{abs} \tag{C.1}$$

where $\Delta\sigma$ is the differential stress, t and L are the thickness and length of the cantilever, E is the Young's modulus, ν is the Poisson ratio (the ratio of transverse expansion to its axial compression) of the cantilever and finally Δz_{abs} is the deflection of the free end of the cantilever. Rearranging in terms of the measurable, the deflection, gives:

$$\Delta z_{abs} = 3\left(\frac{L}{t}\right)^2 \frac{1-\nu}{E}\Delta\sigma \tag{C.2}$$

or alternatively in terms of the radius of curvature R:

$$\frac{1}{R} = 6\frac{1-\nu}{Et^2}\Delta\sigma \tag{C.3}$$

This is the standard method of equating the measurable (deflection or curvature) with the property of interest (the differential) stress due to bimolecular adsorption. Although the deflection of the free end is normally taken to be the measurable, in an optical lever readout mechanism in reality what is measured is a convolution between the tilt and displacement of the cantilever at the point where the laser beam meets it. More sophisticated measurement techniques can measure the profile of bending along the cantilever, either using scanning laser beams[183], astigmatic lenses[184] or diffraction based techniques[185]. These can give information on the curvature directly taking into account local variations which can arise due to inhomogeneities in surface coverage.

In this section we examine the role of macroscopic geometric effects on cantilever performance, studying the size and shape of the sensor and the sample delivery system. We discuss what physical principles about the way stress is generated on the cantilever can be deduced from these observations and is it possible to improve the sensitivity of cantilevers based on this further understanding.

Following this I discuss a study in which microscopic geometric effects dictate the mode of action of the Vancomycin family of drugs. In this section I will discuss the experiments carried out, and the models I developed to help interpret the data.

C.2.1 *Size and shape of sensor*

The most basic alteration to a cantilever sensor is to alter it's geometry. Stoney's equation suggests that the most significant parameter is the thickness of the cantilever and if the optical deflection read out mechanism is being used, the length of the cantilever. Increasing the length of the cantilever however, obviously increases the size of the sensing area, and thus the absolute number of molecules required for a signal. The guiding principle, for static made cantilevers, is to make cantilevers as 'soft' as possible such that any stress generated in the sensing layer is transduced into a large curvature or deflection. Stoney's equation does hinge on a number of assumptions that may not always be true. Firstly it neglects the width of the cantilever, something our group has modified and secondly it does not account for inhomogeneous stress. To test the validity of these assumptions and allow for enquiries involving them a finite element model of the cantilever system was developed using commercially available software (COMSOL).

Finite element analysis (FEA) has a number of advantages to analytical or even experimental studies, it allows us to rapidly model relatively complex geometries, different materials, different physical processes. It does not necessitate some of the assumptions required to make ground analytically, namely the response of the system is emergent from the local events, and of course is much cheaper, and quicker than experimental studies. Of course there are also serious limitations with FEA methods, and in particular the relatively 'black box' style software packages such as COMSOL and ANSYS, where one must be mindful of the underlying physical equations and the assumptions inherent within them, nevertheless FEA simulations are certainly a good starting point for studies of this type where the physics involved is relatively straight forward and the complexity is only a result of the geometry.

A model was constructed that simulates the response of the cantilever to thermal stress. This is a good proxy for the sensor's response to biochemical stress, and in fact is often used to test alignment prior to a sensing experiment, with a typical cantilever deflection of 100 nm

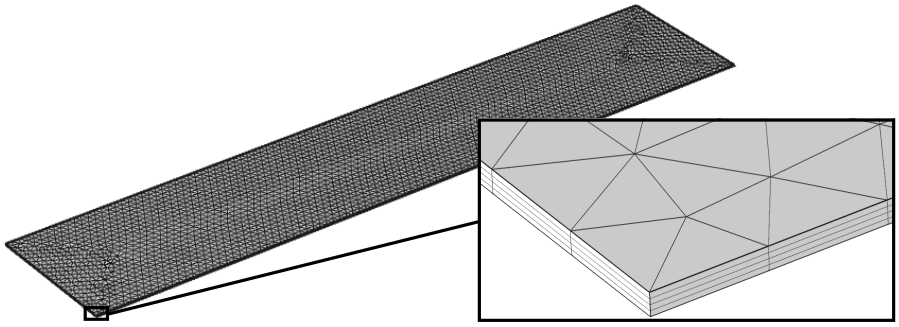

Figure C.4: One of the challenges of using finite element analysis methods to simulate cantilever systems is the high aspect ratio of the device geometries. To overcome this a swept mesh is employed. The mesh, and close-up show that a normal triangular mesh is created on the surface of the cantilever, this is then swept through the cantilever body and split into a predefined number of layers. This permits the creation of mesh elements that has a similar aspect ratio to the cantilever and prevents an unmanageable number of mesh elements being formed.

for a 1 °C change for 'standard size' (500 µm long 100 µm wide and 1 µm thick) cantilevers.

The model consists of a silicon cantilever beam w µm wide, L µm long and t µm thick with a 21 nm thick gold layer. This thickness has been found optimal in our research group[186,187], and is essentially approaching the thinnest layer of gold possible where full coverage is guaranteed. Silicon has a Young's modulus E of 131×10^9 Pa, a Poisson ratio ν, of 0.27, a coefficient of thermal expansion of $4.15 \times 10^{-6}\,\mathrm{K}^{-1}$. Gold has a Young's modulus E of 70×10^9 Pa, a Poisson ratio ν, of 0.44, coefficient of thermal expansion of $1.42 \times 10^{-6}\,\mathrm{K}^{-1}$. The boundary conditions consist of a fixed boundary for one end of the cantilever and a temperature difference above ambient for all boundaries, this temperature difference is applied in a time dependant manner, ramped from zero to of 1 °C over the course of 10 s. Deflection was measured by averaging the displacement of the top edge of the free end of the cantilever.

One of the challenges of using finite element analysis methods to simulate cantilever systems is the high aspect ratio of the device geometries. To overcome this a swept mesh is employed. Figure C.4 show that a normal triangular mesh is created on the surface of the cantilever, this is then swept through the cantilever body and split into a predefined number of layers. This permits the creation of mesh elements that has a similar aspect ratio to the cantilever and prevents

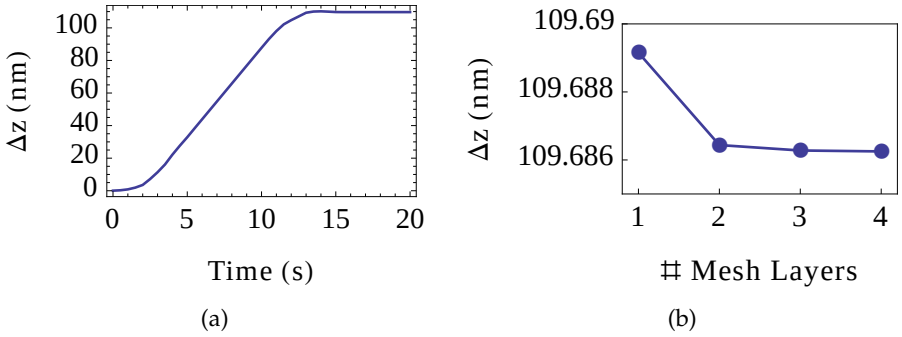

Figure C.5: a) The deflection of the cantilever as a function of time. b) The final deflection of the cantilevers (at $t = 20s$) as a function of mesh layers. Both plots are for the 'standard' size of 500 µmx100 µmx1 µm

an unmanageable number of mesh elements being formed. The convergence on the number of layers in the swept mesh is tested and was found not to have a large effect on the model's performance (see FigureC.5), with 2 layers per material (4 in total) being determined sufficient. The model was used to test the accuracy of Stoney's equations, as such the length and thickness of the cantilever were expected to result in a square and inverse square effect on deflection. The width of the cantilever was also varied, with no effect on the deflection predicted by Stoney's equation.

The length of the cantilever, L, was varied from 50–1000 µm with the width and thickness kept at 100 µm and 1 µm respectively. As can be seen in Figure C.6 the deflection changes with the square dependence predicted by Stoney's equation. The deflection at L =500 µm is equal to 111.9 nm, in good agreement with experiments. The thickness of the cantilever, t, was varied from 0.25–5 µm with the length and thickness kept constant at 500 µm and 1 µm respectively. As can be seen in Figure C.7 the deflection does show the inverse square dependence predicted by Stoney's equation. The radius of curvature varies along the length of the cantilever, with the highest values by the hinge region, this is due to the clamping of the cantilever at this point.

Varying the width of the cantilever does have a small effect but this is less than 1% of the deflection.

FEA modelling can provide an effective method to test simple geometrical alterations to cantilever structure and material as results for uniform stress match closely with Stoney's equation. Under these uniform stress conditions improving cantilever sensitivity can be achieved

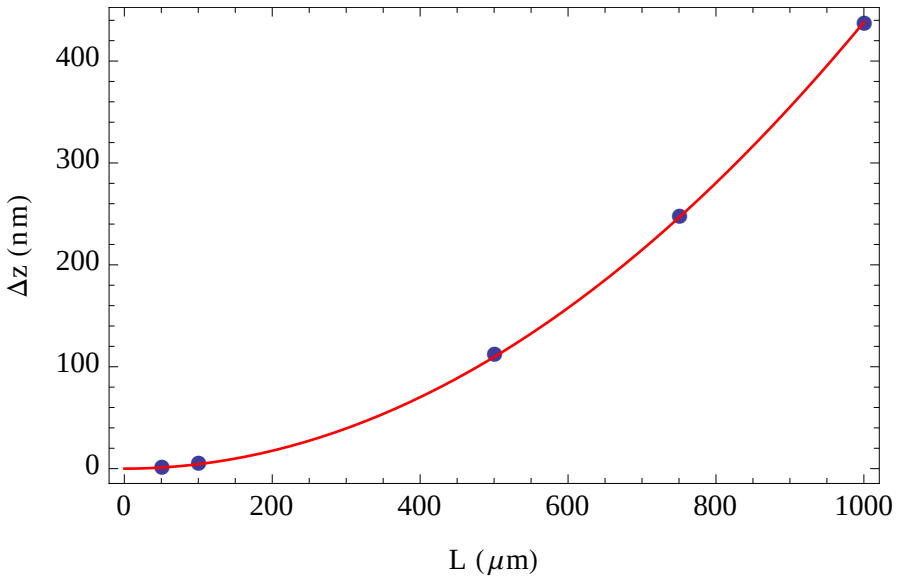

Figure C.6: Results from simulations varying the length of the cantilever. The blue dots show the simulation results for different length of cantilevers. The red line shows a fit of the length dependence in Stoney's equation (L^2). All deflections are at 20 sec and other parameters are for the 'standard size' cantilevers as defined previously.

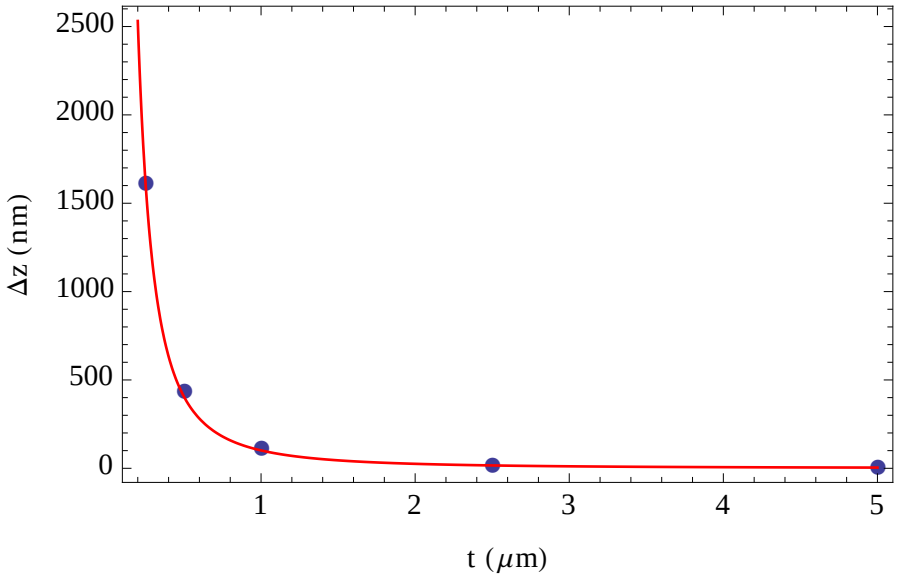

Figure C.7: Results from simulations varying the thickness of the cantilever. The blue dots show the simulation results for different length of cantilevers. The red line shows a fit of the thickness dependence in Stoney's equation ($\frac{1}{t^2}$). All deflections are at 20 sec and other parameters are for the 'standard size' cantilevers as defined previously.

by making thinner or longer cantilevers but it may come at the cost of reproducibility of results, difficulties in handling and alignment. Another approach to improving cantilever sensitivity is to investigate the possibility of non-uniform stress. This may be unintentional or intentionally, through the use of patterning.

C.2.2 *Size and shape of sensing layer*

Aside from altering the geometry of the cantilever itself, the size and shape of the sensing layer can also be altered. In this section I examine what the effects of these changes are and what information about the mechanism of stress transduction can be deduced.

We investigated the effect of changing the size and shape of the sensing layer using FEA simulations. We have examined four types of pattern as shown in figure C.8. We have also added a further parameter to our simulations that accounts for the possibility that reducing the receptive surface area may increase the density of bound molecules and therefore the local stress. Our model accounts for this effect through the introduction of an parameter P (see Figure C.9). We simulate adsorption generated stress by a change in temperature, as such if we want to simulate a higher or lower stress we adjust the temperature difference accordingly. The parameter P describes the coupling of the local stress to the surface area of the pattern. When P is equal to zero there is no dependency and the temperature change is kept constant at 1 °C, irrespective of pattern surface area. If P is equal to 1 then there is a strong dependency and the temperature change is decreased for the larger surface area patterns.

For this first iteration the results show what we would have intuitively guessed, namely that for the case where P equals zero the largest signal is for 100% coverage, we also see that as P is increased this optimum coverage decreases for all the patterns except for the free end (see Figure C.9). This is strong evidence that under certain conditions we may optimise cantilever sensitivity through patterning, specifically the results suggest that patterning the edges of the cantilevers will be most effective. This is an intuitive result as it is this geometry that maximises stress along the long axis of the cantilever (increasing total deflection) while minimising the stress along the torsional axis, the deformation of which will results in a more rigid profile. This model demonstrates the potential consequences not only

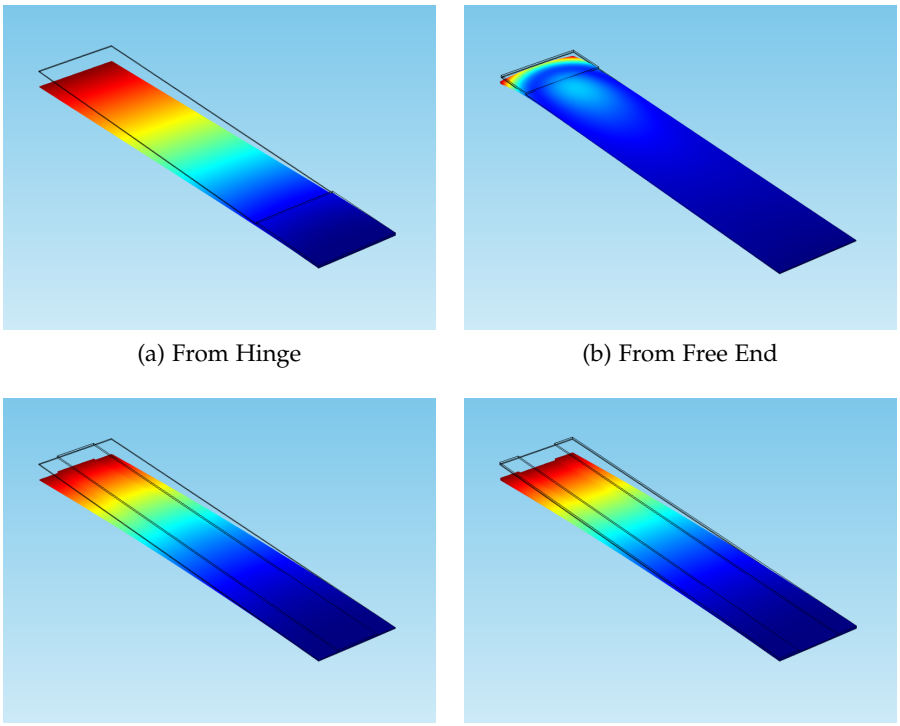

(a) From Hinge

(b) From Free End

(c) From Centre

(d) From Edge

Figure C.8: The four different types of patterning we simulate. Surface coverage is described as a fraction of the cantilever surface in four different ways. a) The whole width of the cantilever with coverage increasing from the hinge, or fixed end of the cantilever. b) The whole width of the cantilever with coverage increasing from the free end of the cantilever. c) The whole length of the cantilever with the coverage increasing from the centre of the cantilever. d) The whole length of the cantilever with the coverage increasing from the side edges of the cantilever

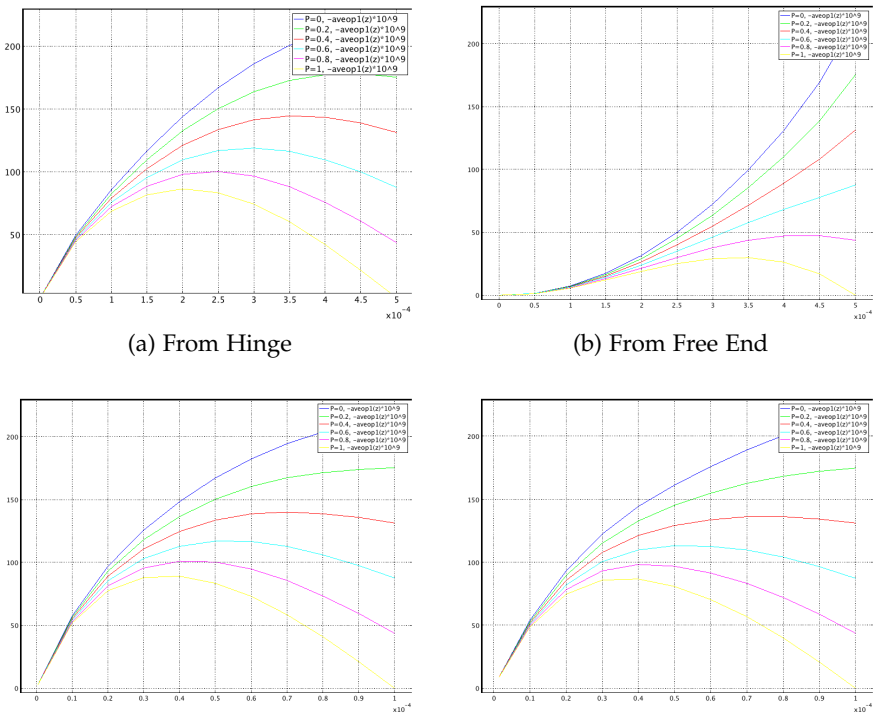

(a) From Hinge

(b) From Free End

(c) From Centre

(d) From Edge

Figure C.9: Plots show the deflection of the free end as a function of pattern size (left hand of x-axis is minimal pattern size, right side is maximal) for varying values of P the surface coverage to concentration factor. The different patterns correlate to the coverage shown in C.8.

of patterning, but also naturally occurring variations in sample adsorption across a sensing layer. To enhance this model and to remove the somewhat crude parameter P we have to include sample delivery in our model.

C.2.3 *Importance of edge effects*

In the previous section the intentional manipulation of the sensing layer was investigated, in this section I will discuss the naturally occurring variations in surface coverage and the way these inherent properties can be harnessed with alterations to sensor geometry to boost sensitivity.

Naturally occurring variations in surface coverage can occur at the molecular level, or at the macroscopic level. This second case most usually follows from the interaction between the detection surface, in this case the top side of the cantilever, and the sample delivery mechanism, most commonly a flow cell or microfluidic device. Flow conditions in and around surface based sensors have a large impact on their performance[14]. A fast flow rate will result in fast sample throughput but may result in advection forcing the sample past the sensing surface without having time to diffuse onto and bind to it, alternatively diffusion driven transport may require unrealistic sample processing time. These two cases are known as diffusion limited or convection limited cases. There are a number of factors and process to consider if we are to include the transport and adsorption of the sample into our model:

- Fluid flow and fluid cell geometry
- Convection and diffusion of sample
- The chemical binding reaction

Our FEA implementation reflects this having 3 coupled models. Firstly the steady state velocity field for a given fluid cell and flow rate is calculated. Secondly this velocity field is input into a mass transport model which incorporates diffusion. Finally this is coupled to a surface reaction model for adsorption and desorption of the species as a function of available sites and local concentrations.

C.2.3.1 *Fluid Flow*

The first component to include is the fluid flow, FEA simulations can be used to determine the velocity field for a given fluid cell geometry and flow rate. The fluid flow is laminar and given by the Navier-Stokes equations:

$$\begin{aligned} \rho \boldsymbol{u} \cdot \nabla \boldsymbol{u} &= \nabla \cdot \left[-p\boldsymbol{I} + \eta(\nabla \boldsymbol{u} + (\nabla \boldsymbol{u})^T) - (2\eta/3)(\nabla \cdot \boldsymbol{u})I \right] \\ \nabla \cdot (\rho \boldsymbol{u}) &= 0 \end{aligned} \tag{C.4}$$

where $\mathbf{u}$ is the fluid velocity field, ρ is the density, η is the viscosity and p is the pressure. The boundary conditions are such that $\mathbf{u}$=0 at the walls, the fluid velocity at the inlet is determined such that the total flow rate is 30 µl/ min and the outlet is at atmospheric pressure.

C.2.3.2 *Sample Transport*

The mass transport in the system is governed by the equation:

$$\frac{\partial c}{\partial t} + \nabla \cdot (-D\nabla c + c\boldsymbol{u}) = 0 \tag{C.5}$$

In which c mol m^{-3} is the concentration in solution, D m^2 s^{-1}, is the diffusion constant u m s^{-1} is the velocity vector.

C.2.3.3 *Surface Reaction*

The sample can adsorb and desorb from the cantilever surface following the reaction:

$$\mathrm{A} + \mathrm{R} \underset{\mathrm{k_{des}}}{\overset{\mathrm{k_{ads}}}{\rightleftharpoons}} \mathrm{AR} \tag{C.6}$$

where k_{ads} and k_{des} are the adsorption and desorption rates in units of m^3 mol^{-1} s^{-1} and s^{-1} respectively. The rate of adsorption is:

$$R_{ads} = k_{ads} c(\Gamma_s - c_s) \tag{C.7}$$

where c is the concentration of the sample in solution at the interface, Γ_s is the concentration of sites on the surface and c_s is the concentration of the sample on the surface. The rate of desorption is given by:

$$R_{des} = k_{des} c_s \tag{C.8}$$

These two terms are combined to give the total reaction rate:

$$R_{tot} = k_{ads} * c_r * (c\theta_{free} - K_d * \theta_{occ}) \tag{C.9}$$

Where θ_{free} and θ_{occ} are the fraction of sites free and occupied and K_d is the disassociation constant given by k_{des}/k_{ads}. The inclusion of the θ terms ensures there are never non-physical concentrations on the surface. The boundary condition for the sample in solution at the reacting interface is then given by:

$$\boldsymbol{n} \cdot (-D\nabla c + c\boldsymbol{u}) = -k_{ads} * c_r * (c\theta_{free} + K_d * \theta_{occ}) \tag{C.10}$$

C.2.3.4 *Simulation Details*

The fluid cell is a replication of a fluid cell currently being used by a VEECO cantilever system. It is approximately 107 µl in volume with the flow cell lid approx 0.9 mm above the cantilever. The cantilever chip is based on an IBM produced chip currently in use. The default cantilever size is 100 µm wide and 500 µm long, although the width is varied in the simulation. The thickness of the cantilever is 1 µm although in the simulations a thickness of 5 µm as such a fine edge can be problematic for meshing. The dynamic viscosity and density of the fluid is set to that of water at 273 15K. The sample is modelled as IgG with a diffusion constant of $5 \times 10^{-11}\,\mathrm{m^2\,s^{-1}}$, k_{ads} of $2.5\,\mathrm{Mol^{-1}\,s^{-1}}$ and a k_{des} of $3 \times 10^{10}\,\mathrm{s^{-1}}$ [188,189]. The surface concentration of receptors Γ_s is taken to be $1\,\mathrm{mol\,m^{-2}}$ [190], which equates to a footprint of 10x10 nm. The initial concentration in solution and on the surface is taken to be zero. The sample concentration at the inlet is increased by a rectangular pulse initiated at 1 min and terminated at 75 min. There is a smooth transition such that both the on and off switch takes 2 min, the absolute value while in the on mode is 10 nM. In reality this switching occurs quicker but having a longer period reduces the computational demand by reducing the temporal resolution requirements. The entire simulation is ran for 80 min.

C.2.4 *Results*

The sample delivery is found to be convection limited, as can be seen by the depletion zones in Figure C.10 which extend approximately 100 µm from the cantilever surface. The cantilever surface, as shown

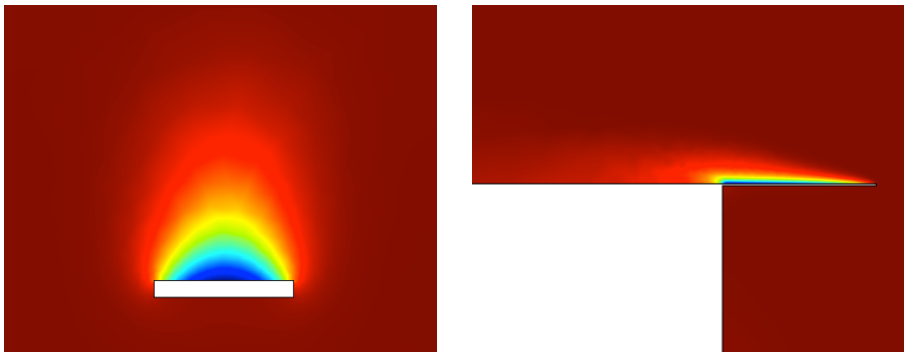

(a) (b)

Figure C.10: Solution sample concentration in the vicinity of the cantilever (Red is maximum concentration, blue is minimum). a) The concentration profile across the width of the cantilever (cut plane halfway along length of cantilever). b) shows the concentration profile along the length of the cantilever (cut plane midway through width of central cantilever), showing the depletion of the sample from the flow along the cantilever.

in the inset of Figure C.11, is shown to have a higher concentration at the cantilever edges. This is due to the higher level of access to the sample, if we imagine the sample sensing all molecules within a certain distance, defined by the diffusion rate and fluid velocity, the edges and in particular the corners have access to a greater volume of sample. The relatively greater perimeter of the thinner cantilevers leads to a faster adsorption of the sample, as is shown in Figure C.12 where the average surface concentration increases faster for thinner cantilevers.

The presence of these edge effects leads to the possibility that thinner cantilevers can indeed be more sensitive.

C.3 CONCLUSIONS

The FEA analysis work was carried out to partly to help explain recent extraordinary experimental results from narrow cantilevers (currently unpublished and not presented here due to the wishes of the lead author). These results showed sensitivities so great that there was concern the spacing between molecules on the cantilever surface would prevent any conventional explanation for stress production. These simulations suggest a mechanism that may explain these results, that is physically intuitive but not previously discussed in the literature.

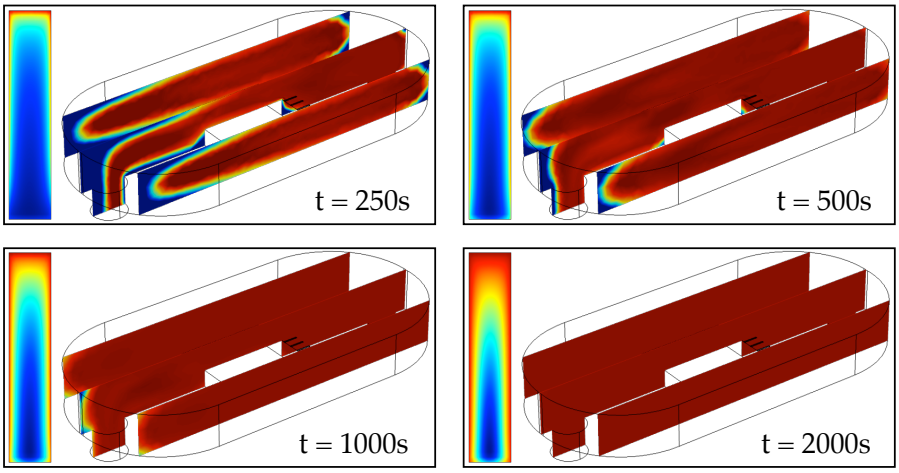

Figure C.11: Time series showing the transport of sample within the fluid cell and the concentration of sample on the cantilever surface. In both main and inset plots red denotes maximum concentration, blue minimum. As the simulation progresses the sample fills the fluidic chamber and is adsorbed onto the cantilever surface, starting with the cantilever edges then spreading to its centre.

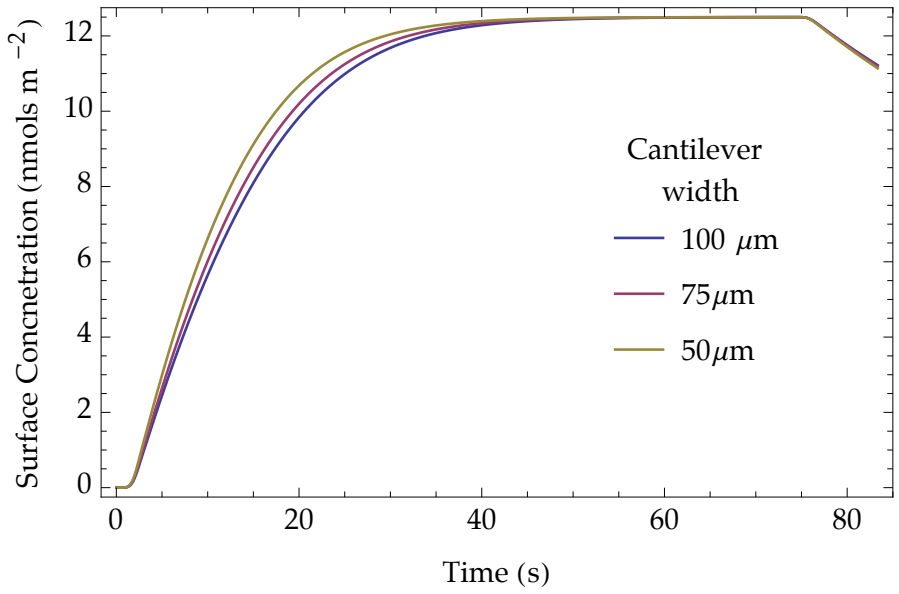

Figure C.12: Surface concentration as a function of time for different width cantilevers.

When working at low concentrations the ability of the edges to access a greater volume of sample, means that in fact there is not homogeneous surface coverage, but regions of high concentration around the edges. This means the molecules can indeed form dense enough networks to create mechanical stress despite being so few in total. Experimental work is needed to verify these findings but the literature does suggest it may indeed be accurate[191], as can be seen in figure C.13. As a further consequence of this effect thin cantilevers are expected to be more sensitive, as the width is reduced the proportion of the cantilever for which there is very low occupancy and therefore low stress also decreases. Furthermore as the stress is confined to the edges the contribution of the lateral torsion, and the corresponding stiffening of the cantilevers is reduced.

C.4 Cantilever study of importance of dimerzation in explaining oritavancin mode of action.

Dimerization plays an important role in the functionality of biomolecules, particularly the clinically relevant vancomycin family of antibiotics. In spite of common acceptance, this phenomenon has not been fully quantified to test the hypothesis that surface dimerization can enhance antibiotic activity. Here we show how different surface receptors, analogous to drug resistant and susceptible bacterial cell wall targets, respond to drugs with solution dimerization constants spanning four orders of magnitude. We quantify surface catalyzed dimerization and find an important mechanism in play, where the actions of drugs that are more powerful against resistant *Enterococcal* infections are controlled by surface dimerization mediated by the target itself. To analyse our data, we derive analytical formulae for drug-target binding which explicitly include solvent and surface dimerization. The experimental evidence presented here shows the need for a surface dimerization channel to explain enhanced efficacy of drugs against resistant infections.

The remarkable ability of biomolecules to self-assemble into multimeric structures, in particular on membranes, is an emerging theme of modern bio-inspired medicine and also lies at the heart of functional complexity in living systems. The simplest of these units, the dimer, formed by the union of two structurally similar molecules via weak

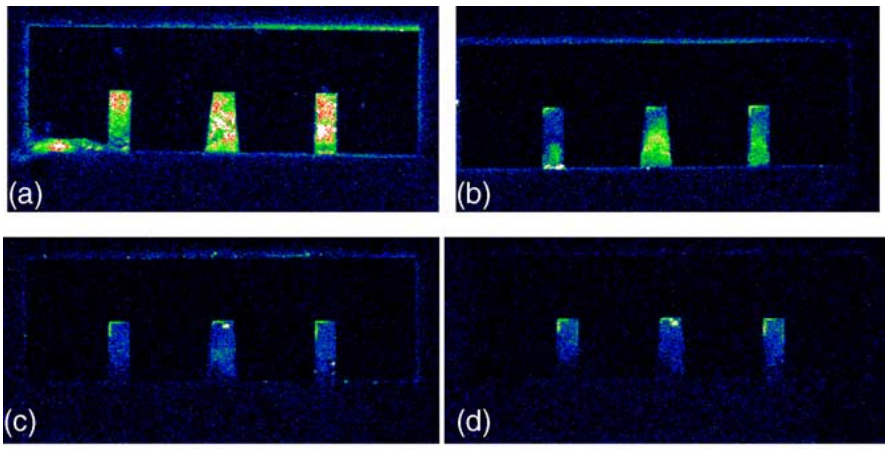

(a)

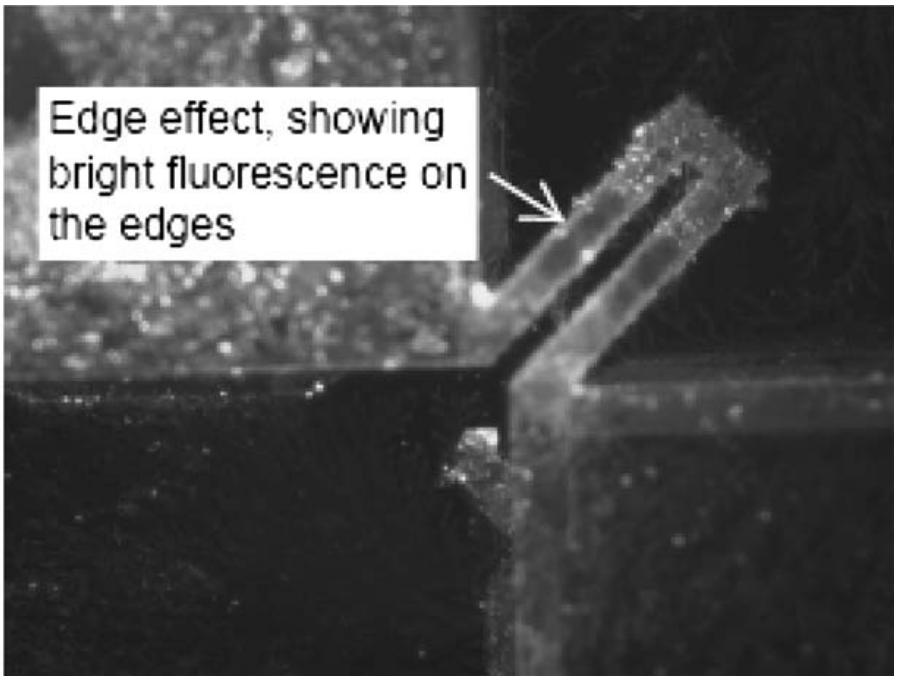

(b)

Figure C.13: Experimental images of cantilevers showing the surface distribution of adsorbed molecules. a) Is taken from Lee et al.[191]. b) Is taken from Joshi et al.[192], with their own annotations drawing attention to edge effects, although in their case they were concerned about the uncertainty due to inhomogeneous coverage. Both figures reveal a clear increase in molecule adsorption at the edges of the cantilevers, as suggested should be the case by our simulations.

DRUG	SOLUTION DIMERISATION DISASSOCIATION CONSTANT
Van	20 407 µM[196]
Rist	3333 µM[197]
CE	116.3 µM[196]
Ori	1.6 µM[196]

Table C.1: Solution dimerisation disassociation constants

non-covalent bonds, can gain stability, and in some cases specificity, by simultaneous binding to multiple receptors.

The lock-and-key theory of enzyme specificity implicit in molecular recognition implies that a molecular-scale match between a host and guest partner is a prerequisite for ligand-receptor interactions. This doctrine underpins molecular biology and has helped to answer many questions concerning the biochemical basis of immune and therapeutic efficacy of drugs. For example, the antimicrobial activity of vancomycin (Van) and related antibiotics is due to stereospecific recognition of polypeptide components in bacterial cell walls[194]. Van exemplifies the success of this theory by specifically targeting the peptidoglycan cell wall, a conserved structural feature of bacteria that is fundamental for their mechanical integrity. The specific interactions impose stress on the overall cell, causing death by inhibiting peptidoglycan biosynthesis. Resistance to vancomycin in methicillin-resistant *Staphylococcus aureus* (VRSA) and vancomycin-resistant *Enterococci* (VRE) is conferred by a molecular-scale structural change at the surface of bacterium cells. The changes in VRSA induce cell wall thickening while in VRE, it leads to a loss of just one hydrogen bond from the drug's binding pocket (Figure C.14), differentiating between vancomycin-susceptible and vancomycin-resistant bacteria[195].

Oritavancin (Ori), ristomycin (Rist) and chloroeremomycin (CE) are structurally related to vancomycin (Figure C.14) in that they share the same core peptide backbone and differ merely in the additional groups remote from the identical binding pocket. The variations in the distinct residues away from the binding pocket contribute to the variations in solution dimerisation constant observed for each of the drugs (shown in Table C.1).

The antibiotics work was undertaken in collaboration with a number of other people, most significantly Joseph Ndieyira who performed the experimental work, my own contribution was assisting with the analysis of experimental data, the formulation and implementation of the thermodynamic models. This work is currently under review with Nature Nanotechnology, some of the figures and text in this section are edited extracts from the submitted manuscript[193]

Despite having identical binding pockets to Van, Ori and CE have shown remarkable activity against VRE, Streptococcus pneumoniae, and the biofilms of Staphylococcus aureus. In contrast to the slow bactericidal properties of Van, typically between 6-24 h, Ori, in development for the treatment of acute bacterial skin and skin structure infections caused by susceptible gram-positive bacteria, including methicillin-resistant Staphylococcus aureus (MRSA) displays a rapid bactericidal activity within 15 min-2 h[198]. This paradox, representing a strong violation of the lock-and-key mechanism, has led to alternative theories, of its action such as a dual mechanism or direct interactions with proteins without binding to cell wall targets[199,200]. The question of whether the remarkable activity of Ori and its related antibiotics can be described by lock-and-key hypothesis remains to be answered. Determining ligand-receptor binding activity is of fundamental importance and would be essential to understand how proteins or cells interact with one another and with the membrane bound receptors in a natural or model experimental system.

C.4.1 *Experimental Methods*

The experiments measured the stress imparted directly by two-dimensional (2-D) membrane bound receptors on silicon cantilever sensor arrays (Figure C.15). We used the cantilever method because of its multiple advantages over conventional small molecule screening methods; among them are label-free detection and the screening of multiplexed ligand-receptor interactions in parallel under identical conditions without prior sample tagging. This ability allows detailed analysis of diverse ligands and biochemical interactions ranging from bacteria, yeast, fungal spores, and the detection of antibacterial resistance. Moreover, nanomechanical sensing is a fast and accurate, and could become an effective method that would provide a shorter route to understanding how antibiotics kill pathogens.

C.4.1.1 *Cantilever measurements*

A functionalised cantilever sensor array chip was manually positioned in a sealed liquid chamber with a volume of approximately 100 µL. The liquid cell and drug solutions were placed into the temperature-controlled cabinet so that experimental measurements could be undertaken. The liquid flow rate was 180 ± 30 µL min^{-1} and the temperature

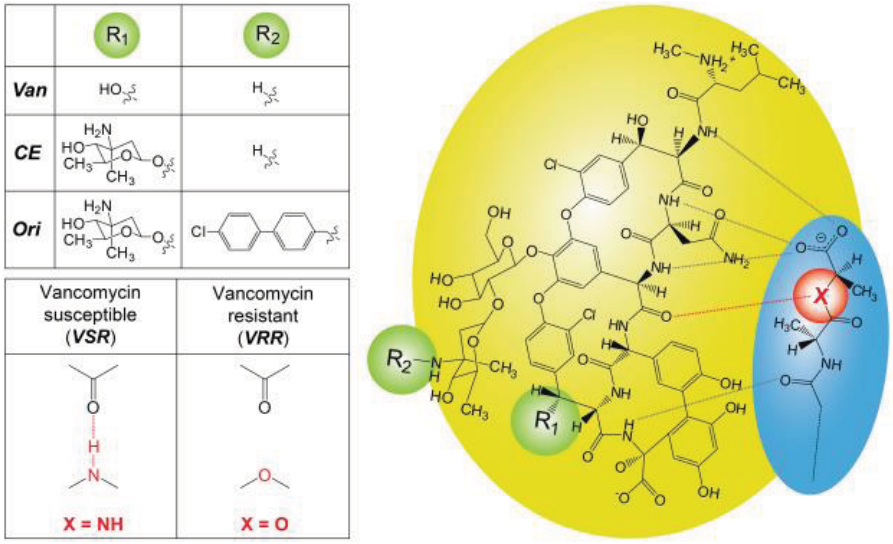

Figure C.14: Schematic representation of Van family of drugs binding to cell wall peptides at the surface of a bacterium and a cantilever sensor:(a) Chemical structure of the drug binding to cell wall peptides, where R groups distinguish the structures of Van, CE, Rist and Ori. The dotted lines in the antibiotic-peptide complex represent the 5 hydrogen bonds formed upon binding to drug susceptible peptide analogues. The X group on the peptide corresponds to the mutation of an amide to an ester in resistant phenotypes, VRR, whereby a single hydrogen bond is deleted from the drug binding pocket. b) Illustration of Van mode of action on a bacterium. In the absence of the drugs, the peptide precursors are cross-linked to form a rigid network, which is vital for the bacteria's mechanical strength. Van binds to cell wall peptide precursors tethered to the extracellular cytoplasmic membrane of a bacterium, thereby inhibiting cell wall crosslinking. c) Schematic representation of Van binding to a cell wall peptide analogue tethered to one side of a cantilever surface via gold-thiol linker chemistry

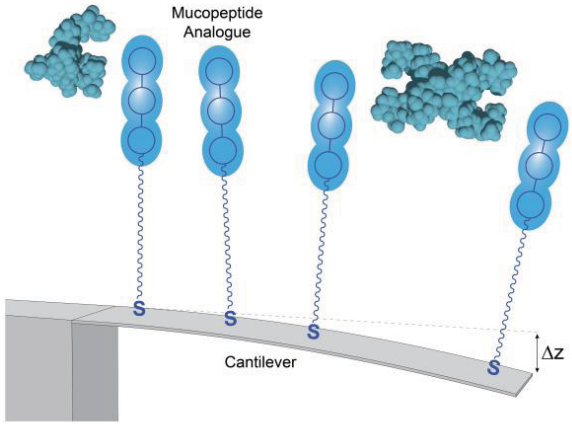

Figure C.15: Cantilever measurement of antibiotic binding

was maintained at 22±0.2 °C. The differential bending signals were acquired in the following sequence, (i) injection of phosphate buffer/serum buffered solution to establish the baseline for approximately 5 mins; (ii) injection of drugs in phosphate buffer/serum solution for approximately 30-60 mins; (iii) injection of 10 mM HCl to regenerate surface for approximately 30 mins and (iv) injection of phosphate buffer to restore the baseline for approximately 10 mins. The absolute bending signals from cantilevers can be susceptible to artefacts that accompany their exposure to liquids including changes in temperature, refractive index, non-specific binding to underlying surfaces, and reactions occurring on the bare silicon native oxide underside of the cantilevers. Artefacts that produce non-specific signals were overcome by carrying out differential measurements. In situ PEG-coated cantilevers act as references, their deflection, which is due to the non-specific effects such as temperature fluctuations, changes in refractive index and non-specific binding can be averaged and subtracted from the VSR/VRR coated cantilever signals.

To determine the uniformity of surface coverage of the receptor molecules, we used X-ray photoelectron spectroscopy (XPS), the results of which are shown in Table C.2

C.4.2 *Experimental Results*

Figure C.16 demonstrates the utility of the cantilever technology for screening novel drugs in buffer and human serum . The data reveal that upon injection of 3 µM Van, the VSR peptide coated cantilevers

COATING	NORMALISED S/AU RATIO	MOLECULAR FOOTPRINT
PEG	1.0±0.16	27 Å
VSR	0.61±0.1	44 ± 0.6 Å^2
VRR	0.66±0.1	41 ± 0.6 Å^2

Table C.2: XPS Spectroscopy of cantilever coating

rapidly (<10 min) bend downwards yielding a stable equilibrium differential compressive bending signal of 90 nm, while for resistant VRR surface targets, no signals are observed, in good agreement with bacterial resistance to vancomycin. Van was subsequently rinsed off via a buffer washing step, after which the signal converged back towards the baseline. In contrast, a 3 µM injection of Ori, was shown for the first time to bind with enhanced bending signals of 184 and 120 nm for both VSR and VRR respectively, again in agreement with Ori's effective therapy against vancomycin susceptible and resistant phenotypes.

To quantify the thermodynamic equilibrium dissociation constants of drug-target interactions, K_{surf}, we performed a titration of antibiotic concentration for all 4 antibitoics, Van, Rist, Ce and Ori. Each concentration of drug was introduced and the saturation stress for the VRR VSR and PEG cantilevers was recorded (See Figure C.17). To determine K_{surf} and the effects of cooperativity. The data was fitted to the standard Hill equation:

$$\sigma_{eq} = \frac{\sigma_{max}\,[N_s]^n}{K_{surf}^n + [N_s]^n} \tag{C.11}$$

where σ_{max} is the maximum surface strain induced when all accessible peptide binding sites are occupied and n is the Hill coefficient, a measure of cooperativity in binding reactions. Setting $n = 1$ yields the Langmuir isotherm where the reactions occur independently. $n > 1$ corresponds to positive co-operative interactions and $n < 1$ indicates negative cooperativity. Figure C.18 shows the fit to the data, where σ_{max} was determined independently (for the VRR cases where saturation is not reached for Van, Rist and CE it is fixed at the Ori value) with the shaded regions showing the 10% uncertainty regions. The Hill

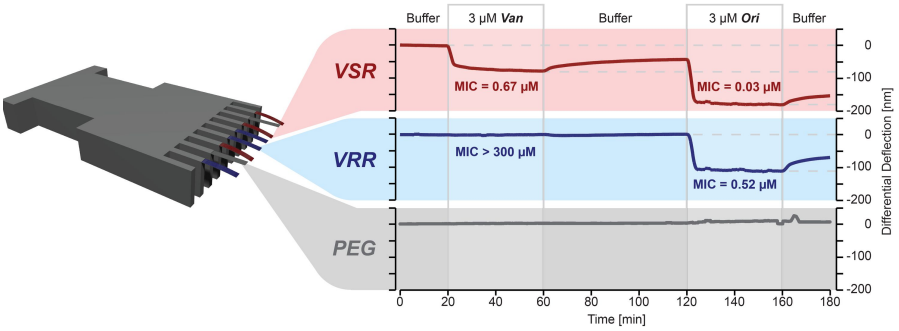

Figure C.16: Vancomycin and Oritivancin binding to VSR and VRR coated cantilevers. Investigating the mechanics of drug-target interactions for Van and Ori on multiple cantilever arrays. We show the injection of Van and Ori only, though similar measurements were performed for Rist and CE: A schematic of an array of eight rectangular silicon cantilevers, each measuring 500 µm long, 100 µm wide and 1 µm thick with a spring constant of 8 mN m^{-1}. The bending of all cantilevers is monitored in parallel using time-multiplexed optical beam detection on a single photodetector. The downward bending signal corresponds to a compressive (repulsive) surface stress. The differential bending signal in buffer of VSR (red), VRR (blue) and PEG (dark grey) is shown upon injection of (i) buffer; (ii) 3 µM Van; (iii) buffer washing step; (iv) 3 µM Ori (v) buffer washing step. (B) Differential VSR signals for 0.1, 10, 50, 100 and 500 nM Ori. The differential PEG reference signal (PEG1-PEG2) is shown in black.

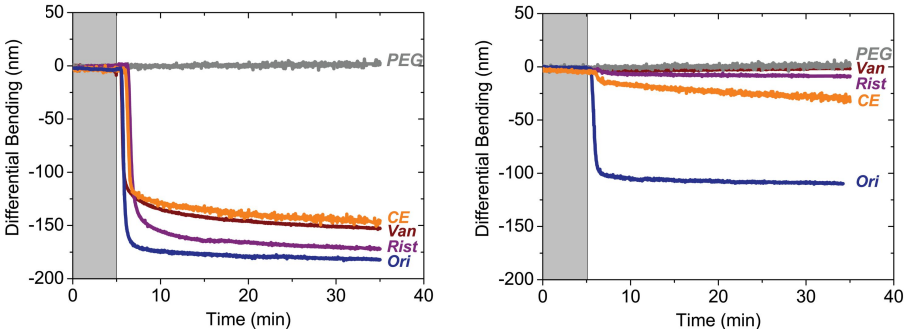

(a) VSR (b) VRR

Figure C.17: Deflection of VSR and VRR coated cantilevers to the four different antibitoics. a) The VSR coasted cantilevers exhibit a significant response all the antibiotics (Ori, CE,Rist and Van all at 10 µmol dm^{-3}), reaching a saturation deflection of around 125–175 nm. b) The VSR coated cantilevers however, show a wide range of responses to the different drugs. The deflection is negligible for all the drugs except for Ori, for which it reaches a saturation deflection of around 100 nm.

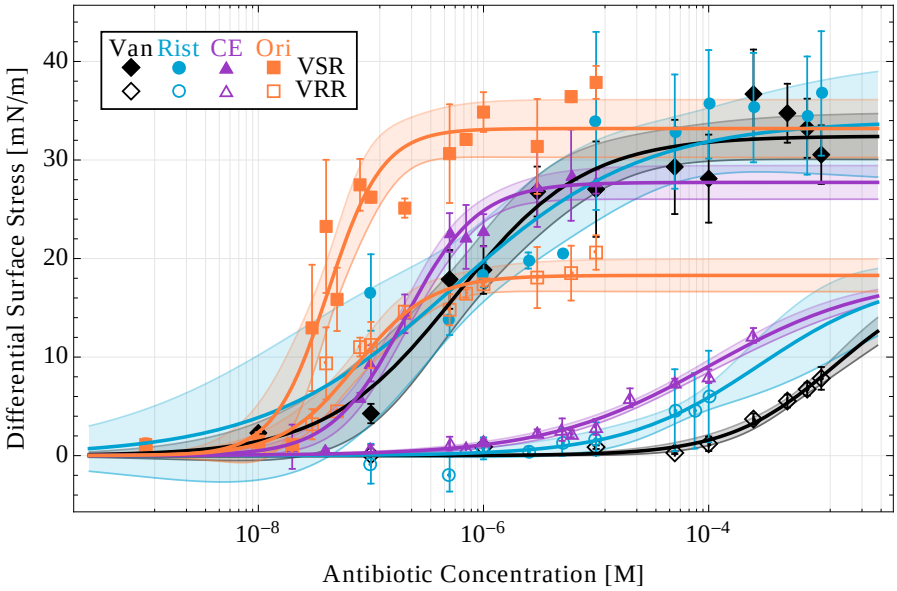

Figure C.18: Hill equation fits to full vancomycin family of drugs. For each drug (Ori, CE, Rist and Van) and for each coating (VSR, VRR) a titration in drug concentration was performed. For each drug concentration - surface combination the saturation stress was recorded. The results of the survey are plotted here. Furthermore for each drug-surface combination a hill equation was fitted to estimate the equilibrium surface dissociation constant, K_surf and cooperativity factor n. The shaded regions indicate the 10% uncertainty region.

equation provides a good description of the data and quantified the cooperativity needed for surface binding, revealing that CE and Ori molecules exhibited the largest n values as can be seen for the fitted parameter values shown in Figure C.19

C.4.3 *Quantitative correlation between nanomechanical stress and microbiological assays*

For a new technique to be useful in well-established fields such as bacteriology, it must bear a strong quantitative relation to conventional assays. To define the relationship between the drugs' ability to bind extracellular surface targets with their ability to inhibit intact bacterial cell growth, we correlated the cantilever drug-target binding affinity, K_{surf} and the MIC values for clinically problematic bacteria. The logarithmic plots for K_{surf} versus MICs (Figure C.20) reveal a linear correlation over a remarkable four decades between biomechanical

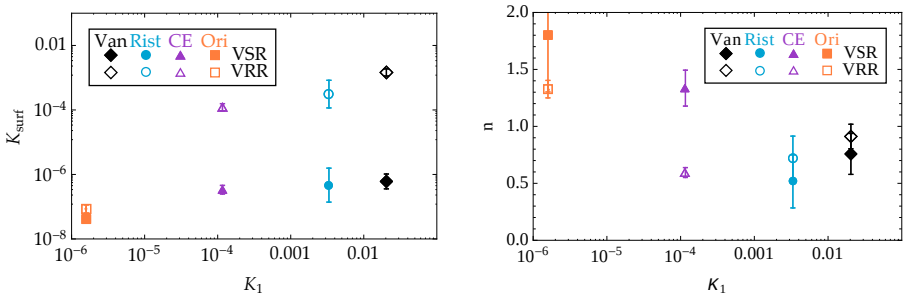

(a) K_{surf} (b) n

Figure C.19: Parameter values and their errors for the Hill fits. Here the found parameters in the Hill equation for each drug-surface combination are plotted along with their errors. The x-axis is K_1 the measure solution dimerisation constant for the drugs. The reason for plotting on this scale x-axis is, as will be shown later, its importance to drug performance.

responses of extracellular targets and MIC values determined from intact bacterial cells as measured by microbiologists. This demonstrates the correlation between the in vitro action of the drugs against VSR and VRR coated cantilevers and the live bacteria, strong evidence for the cantilever platforms efficacy as a drug screening tool. This strong correlation of the cantilever bound surface targets with the in vivo performance implies that theories suggesting an alternative mode of action are incorrect and it is indeed the binding of the drugs to the surface peptides that leads to bacterial death. This finding reinforces, however, the paradoxical nature of the variation in drug efficacy and surface receptor binding despite the identical binding pockets.

C.4.4 *The importance of the surface*

To help identify the process responsible for the variation in efficacy of drugs against resistant bacterial targets we compared the correlation of antibiotic binding against freely floating receptors in solution and with the same receptors fixed to a surface (see Figure C.21). That is to say we measured the dissociation constants of each drug to both the VRR and VSR receptors, for the purpose of comparing the case of the receptors being in solution to that when they are on a surface. In solution, we find weak mM binding interactions across all antibiotics against VRR receptors and a strong relatively uniform µm affinity for

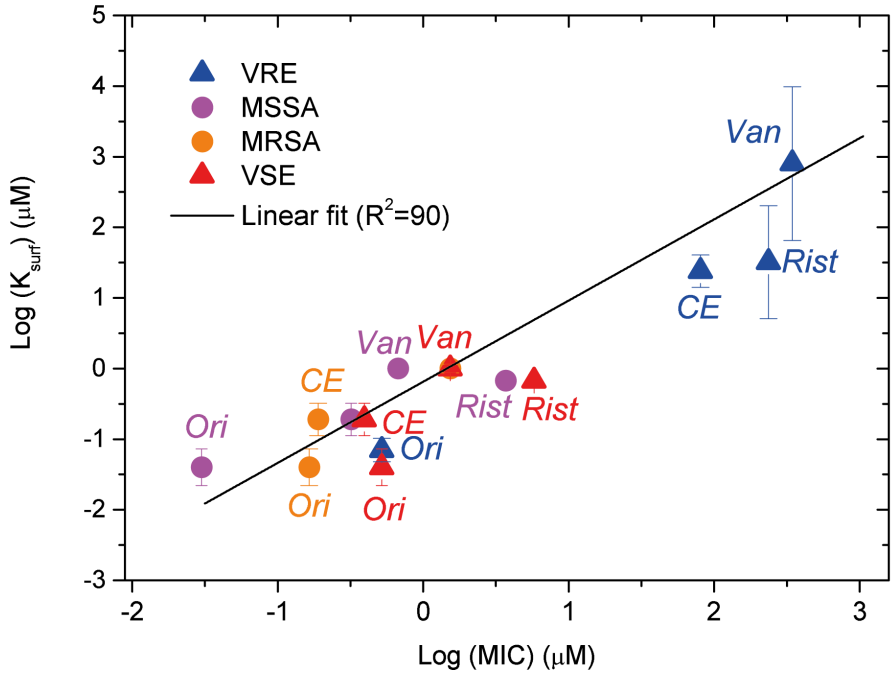

Figure C.20: Minimum inhibitory concentrations vs K_{surf} . Here we show the correlation over 5 orders of magnitude between the in-vivo physiological gold standard MIC measurements with, K_{surf} , the antibiotic performance as measured by cantilevers coated with the peptide analogue receptors, this shows that the cantilever - peptide analogue system proved a useful and instructive method for both the screening and study of drug action

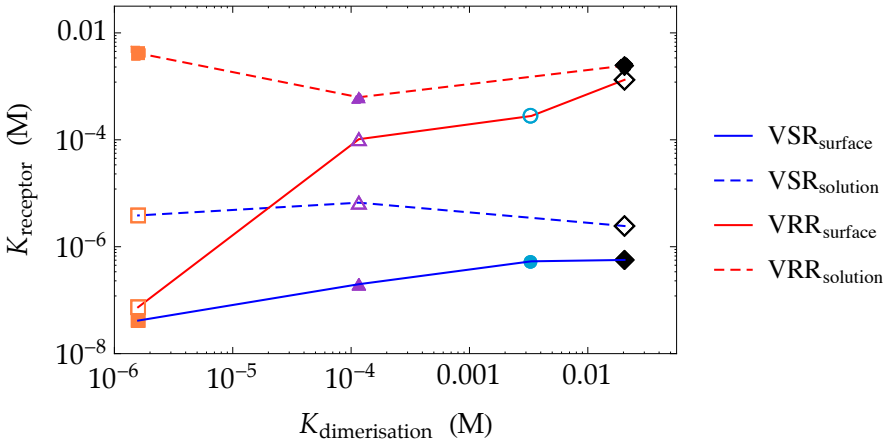

Figure C.21: Solution (dashed) and surface (solid) binding affinity for the VSR (blue line) and VRR (red line) receptors. The different color and shape markers denote the different drugs, Ori (orange), CE (purple), Rist (cyan) and Van (black). The first thing to notice from these results is that in all drug-receptor combinations the surface bound receptors bind to the drugs more strongly. The second thing to note is the extent of this effect seems to correlate with the drugs solution dimerisation constant K_1. Finally one should note that this effect is most pronounced for the VRR receptors where in the case of Ori we see the binding strength, as characterised by the disassociation constant, to be increased by 5 orders of magnitude.

the VSR targets, in good agreement with the lock-and-key hypothesis. However in the surface bound receptors we see a clear variation across the drugs for both VSR and in particular the VRR receptors which are heavily dependant on the drugs' rate of solution dimerisation. This finding highlights two areas that may help explain the performance of the drugs, firstly the surface is effecting the drugs behaviour, secondly the degree to which this effect takes place seems to depend on the propensity of the drugs to dimerise.

C.4.5 *Simple Model*

We have developed a simple model incorporating solution dimerisation, monomer and dimer binding, as shown in Figure C.22. We know the drugs have varying solution dimerisation constants (see Tab. C.1), and we want to see if this is enough to explain the variation in binding affinity observed between the drugs and for the different surfaces. As

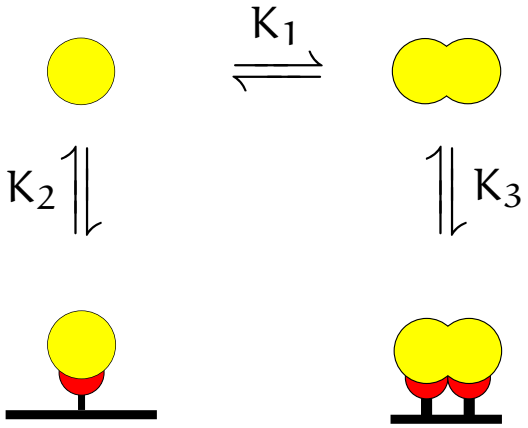

Figure C.22: Simplified model of drug - receptor interaction. This model has a single equilibrium dissociation constant that pertains to the dimerisation process, K_1, which is determined experimentally. It then has two pathways for binding to tthe surface, one for monomeric drugs, described by K_2 and one for dimers, K_3. This model is the simplest model that allows us to separate the drug performances dependence on its binding pocket (K_2,K_3 and kept constant between drugs) and its dimerisation (K_3 and varying between the drugs).

such we fix K_2 and K_3, the monomer and dimer binding coefficients for all the drugs on a particular surface.

C.4.5.1 *Tiling vs Binding*

There are geometrical constraints due to the size of the drugs and receptors. We know the footprint of the receptors is equal to 44 ± 0.6 Å^2 and 41 ± 0.6 Å^2 for the VSR and VRR surface respectively. Published work also estimates the radius of gyration for Vancomycin monomers and dimers to be 8 and 9.4 Å for the monomer and dimer case[201]. This leads us to two conclusions, firstly that the footprint of a bound molecule is significantly larger than that of a receptor (Figure C.23, and meaning that the problem of adsorption, the restriction of finding a site is one one of tiling rather than availability of receptors. Secondly that the footprint of a monomer and dimer can be considered equivalent which will effect the mathematical formulation of the model, as noted below.

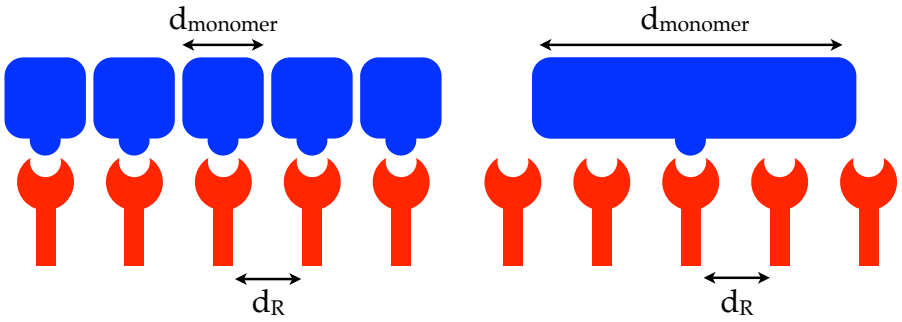

(a) Monomer of comparable size top receptor binding

(b) monomer with much larger footprint than receptor binding

Figure C.23: Monomer tiling. a) shows the system when the target and receptor are of comparable size. In this case the probability of finding a receptor is prtoportional to the number of free receptors on the surface. b) shows the system when the target is significantly larger than the receptor. In this case the probability of binding is instead proportional to the available space on the surface.

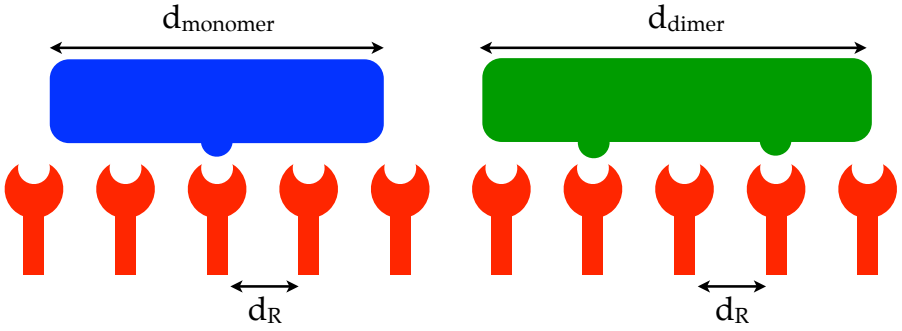

(a)

(b)

Figure C.24: Monomer and dimer tiling when monomers and dimers are of similar size. In this case the probability of either a dimer or a monomer finding a free site is a tiling issue, it is proportional to the amount of available space rather than the receptors themselves (assuming uniform dense coverage).

C.4.5.2 *Ligand interactions at equilibrium*

The guiding equations, for a general reaction involving x subunits of A combining with y subunits of B to form a multimeric structure A_xB_y, i.e.

$$\mathrm{xA} + \mathrm{yB} \underset{\mathrm{k_{off}}}{\overset{\mathrm{k_{on}}}{\rightleftharpoons}} \mathrm{A}_x\mathrm{B}_\mathrm{y} \tag{C.12}$$

we can write the reaction rate as:

$$\frac{d[A_xB_y]}{dt} = k_{on}[A]^x[B]^y - k_{off}[A_xB_y] \tag{C.13}$$

which for the steady state condition of $\frac{d[A_xB_y]}{dt} = 0$ gives:

$$k_{off}[A_xB_y] = k_{on}[A]^x[B]^y \tag{C.14}$$

leading to:

$$\frac{k_{on}}{k_{off}} = \frac{[A_xB_y]}{[A]^x[B]^y} \tag{C.15}$$

or equivalently:

$$K_a = \frac{[A_xB_y]}{[A]^x[B]^y} = \frac{1}{K_d} \tag{C.16}$$

Where K_d is the disassociation constant and for first order equations (x and y = 1) has the units of concentration and K_a is the association constant.

C.4.6 *Derivation of model*

We derive analytically the theromdynamic equilibrium where all reaction rates are equal to zero.

C.4.6.1 *Solution dimerisation*

To determine the number of monomers and dimers in solution,N_{ms} and N_{ds} respectively, we can consider the dimerisation process, governed by the association constant K_1:

$$\mathrm{N_{ms}} + \mathrm{N_{ms}} \underset{\mathrm{k_{1off}}}{\overset{\mathrm{k_{1on}}}{\rightleftharpoons}} \mathrm{N_{ds}}$$

Which for the steady state is equal to:

$$K_1 = \frac{[N_{ds}]}{[N_{ms}]^2} \tag{C.17}$$

C.4.6.2 *Monomer in solution binding to surface*

Aside from solution dimerisation monomers in solution, N_{ms}, may bind to the surface to become bound monomers, N_{mf} monomers binding to the surface are governed by the association constant K_2:

$$\mathrm{N_{ms}} + \mathrm{R_{free}} \underset{\mathrm{k_{2off}}}{\overset{\mathrm{k_{2on}}}{\rightleftharpoons}} \mathrm{N_{ds}}$$

Leading to:

$$K_2 = \frac{[N_{mf}]}{[N_{ms}][R_{free}]} \tag{C.18}$$

where R_{free} is the number of free sites.

C.4.6.3 *Dimer in solution binding to surface*

A dimer in solution, N_{ds}, may bind one of its constituent drug molecules to the surface to become a singly bound dimer, N_{df}. This reaction is governed by K_3:

$$\mathrm{N_{ds}} + \mathrm{R_{free}} \underset{\mathrm{k_{3off}}}{\overset{\mathrm{k_{3on}}}{\rightleftharpoons}} \mathrm{N_{df}}$$

Leading to:

$$K_3 = \frac{[N_{df}]}{[N_{ds}][R_{free}]} \tag{C.19}$$

where R_{free} is the number of free sites. Due to the tiling considerations the sites considered here are equal to the sites in the monomer case, alternatively we could use an R_{free}^2 term to indicate the need for two sites, or as will be discussed more below more complex functions that consider the geometrical constraints posed on finding a 'second' site.

C.4.6.4 *Further equations*

We also use the following equations:

$$N_s = N_{ms} + 2N_{ds} \tag{C.20}$$

Which relates the number of molecules in solution (or concentration) to the number of monomers (N_{ms}) and dimers (N_{ds}) in solution. On the surface we also have the following relations:

$$\theta = \frac{N_{mf} + N_{df}}{N_{mf} + N_{df} + R_{free}} \tag{C.21}$$

where θ is the fraction of occupied sites, N_{mf} is the number of monomers on the surface, N_{df} is the number of dimers on the surface and R_{free} is the number of unoccupied sites.

C.4.6.5 *Derivation of fitted equation for simple model*

We begin by expressing N_{ms} and N_{ds} in terms of N_s, the total number of molecules in solution, given by:

$$N_s = N_{ms} + 2N_{ds} \tag{C.22}$$

To get N_{ms} as a function of K_1 and N_s we rearrange equation C.17 to get:

$$N_{ds} = N_{ms}^2 K_1 \tag{C.23}$$

inserting this into equation C.22 gives us:

$$N_s = N_{ms} + 2N_{ms}^2 K_1 \tag{C.24}$$

Which we can solve for N_{ms} to get the solutions:

$$N_{ms} = -\frac{1}{4K_1} \pm \frac{1}{4}\sqrt{\frac{1 + 8K_1 N_s}{K_1^2}} \tag{C.25}$$

Because all our values remain real and positive we can discard the negative solution leaving us:

$$\boxed{N_{ms} = -\frac{1}{4K_1} + \frac{1}{4}\sqrt{\frac{1 + 8K_1 N_s}{K_1^2}}} \tag{C.26}$$

If we repeat this process, instead rearranging equation C.17 to get N_{ds}, before inserting into C.22 we solve to get:

$$N_{ds} = \frac{1 + 4K_1 N_s}{8K_1} \pm \frac{1}{8}\sqrt{\frac{1 + 8K_1 N_s}{K_1^2}} \tag{C.27}$$

We know that as $N_s \to 0$ then N_{ds} must do so too, irrespective of the value of K_1. This means we select the negative sqrt solution that obeys this rule, so that:

$$\boxed{N_{ds} = \frac{1 + 4K_1 N_s}{8K_1} - \frac{1}{8}\sqrt{\frac{1 + 8K_1 N_s}{K_1^2}}} \tag{C.28}$$

To find the stress we begin with:

$$\sigma = \sigma_{max}\theta = \sigma_{max}\frac{N_{mf} + N_{df}}{N_{mf} + N_{df} + R_{free}} \tag{C.29}$$

We use C.19 to replace N_{df} to get:

$$\sigma = \sigma_{max}\frac{N_{mf} + K_3 N_{ds} R_{free}}{N_{mf} + K_3 N_{ds} R_{free} + R_{free}} \tag{C.30}$$

Then using eq:C.18 we replace N_{mf}:

$$\sigma = \sigma_{max}\frac{K_2 N_{ms} R_{free} + K_3 N_{ds} R_{free}}{K_2 N_{ms} R_{free} + K_3 N_{ds} R_{free} + R_{free}} \tag{C.31}$$

and divide each term by R_{free}

$$\boxed{\sigma = \sigma_{max}\frac{K_2 N_{ms} + K_3 N_{ds}}{K_2 N_{ms} + K_3 N_{ds} + 1}} \tag{C.32}$$

This equation along with equations C.26 and C.28 gives us the stress a s a function of σ_{max}, K_1, K_2, K_3 and N_s, or concentration.

c.4.6.6 *Fit of simple model*

To test the hypothesis that it is the variation in the solution dimerisation along with the coopertavity of dimer bding with receptor binding that explains the differences in drug efficacy we fit the simple model with σ_{max}, K_2 and K_3 fixed for the drugs. This gives us the 6 parameters: $\sigma_{max-VSR}$, $\sigma_{max-VRR}$, K_{2-VSR}, K_{2-VRR}, K_{3-VSR} and K_{3-VRR} to fit the 8 data sets (4 drugs on two surfaces each).

c.4.6.7 *Fitting to data*

The fit, shown in Figure C.25, is good for the VSR case but fails drastically for the VRR case. The simplest addition to this model we

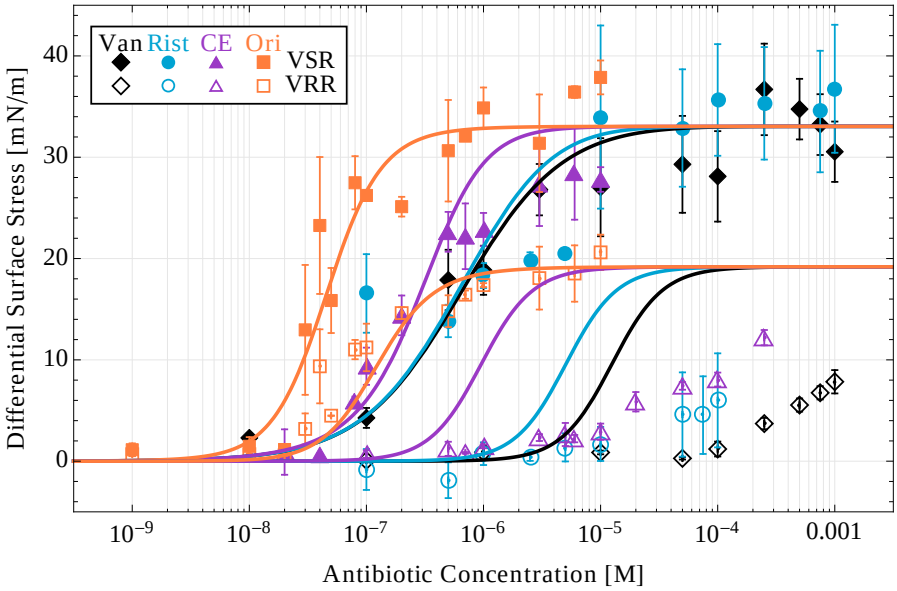

Figure C.25: Simplified model case 0 fit to full vancomycin family of drugs on both VSR and VRR surfaces

tested was allowing the stress contributions for monomers and dimers to be different.

C.4.6.8 *Simple model with varying stress contributions*

Working through a similar derivation as above we arrive at the following formula for the total stress:

$$\boxed{\sigma = \frac{\sigma_m K_2 N_{ms} + \sigma_d K_3 N_{ds}}{K_2 N_{ms} + K_3 N_{ds} + 1}} \tag{C.33}$$

where σ_m and σ_d are the monomer and dimer stress contributions, as before these are fixed for the different drugs, leading to 8 fitted parameters σ_{m-VSR}, σ_{m-VRR}, σ_{d-VSR}, σ_{d-VRR}, K_{2-VSR}, K_{2-VRR}, K_{3-VSR} and K_{3-VRR} to fit the 8 data sets (4 drugs on two surfaces each). This fit appears to be significantly improved but closer examination of the parameter values renders this fit non-physical. For the VRR case the larger spread in the drug efficacy is explained due to the reduction of the monomers impact, in fact the monomer stress contribution is found to be zero. While this could well be physical, indeed the lower affinity of the monomers could reduce the stress due to monomers more than the stress due to a dimer, the full dimer coverage requires

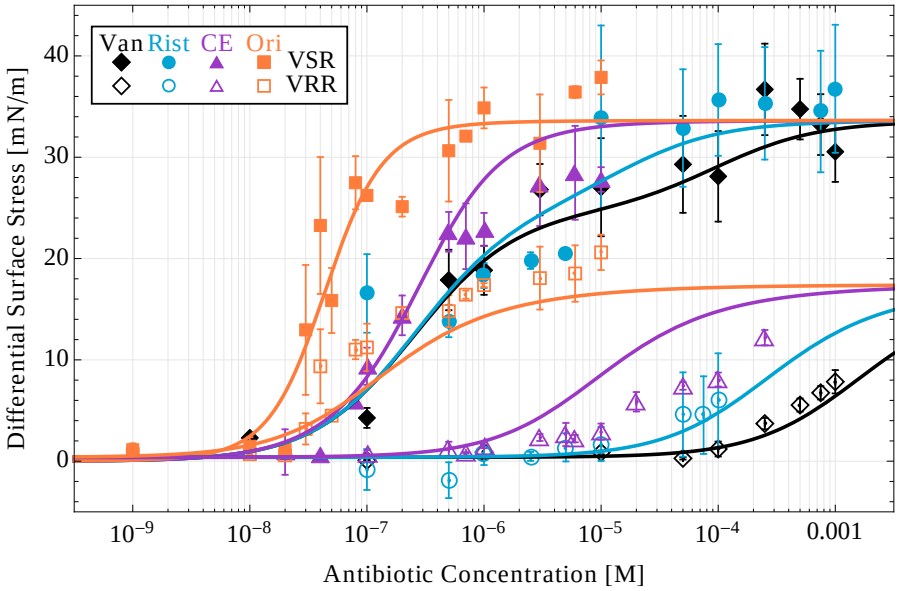

Figure C.26: Simplified model case 1 fit to full vancomycin family of drugs on both VSR and VRR surfaces

monomer binding at a lower concentration for the VRR case than the VSR case. This can be seen from the Bayesian analysis shown in FigureC.27. The Bayesian analysis from 200×10^6 randomly chosen parameter sets the values for K_2 and K_3 which give acceptable fits (χ^2 scores normalised to drug data set of less than 11, equating to 0.00007% of parameter sets). This result shows although the model is able ot fit the data accurately it requires both the monomer and dimer affinity for VRR receptors to be higher than for the VSR case, something that is known not to be true, due to the loss of a NH bond in the VRR binding pocket.

C.4.7 *Complete Model*

Following the failure of the simple model to explain the data we developed a model including all the possible states for a two drug molecule system (the effects of introducing larger multimeric structures will be discussed later). Figure C.28 shows the different states we consider. There are monomers and dimers in solution, monomers bound to the surface and dimers bound to the surface with a single bond, and a double bond. Our aim in constructing this model is to explain why we see the variations in drug efficacy when the binding pocket is identical

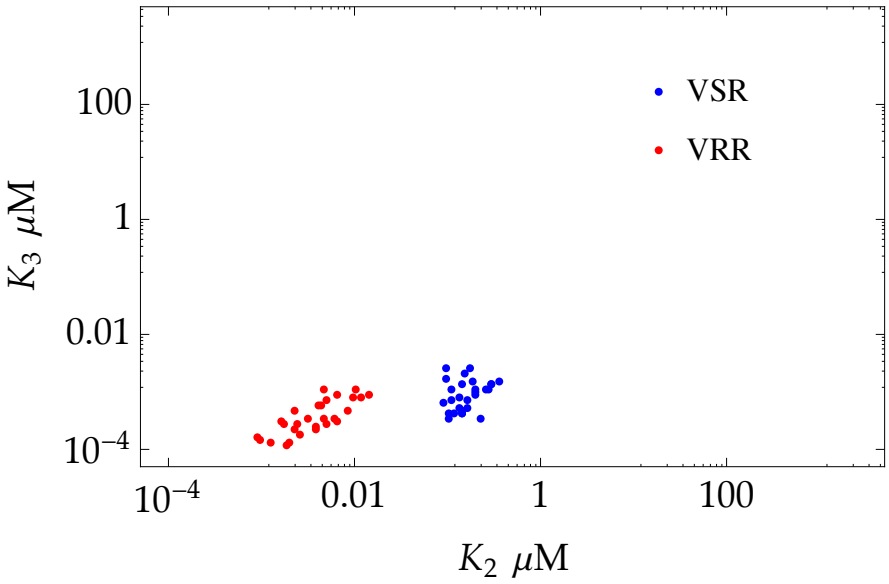

Figure C.27: Approximate Bayesian computation methods provide estimates of the parameter distributions for the simple model. K_2 and K_3 are found to be physically unrealistic, i.e. both the monomer and dimer - receptor binding is stronger for the VRR than the VSR case, something we know to be untrue. On the basis of this the simple model is ruled out as unable to explain the experimental data.

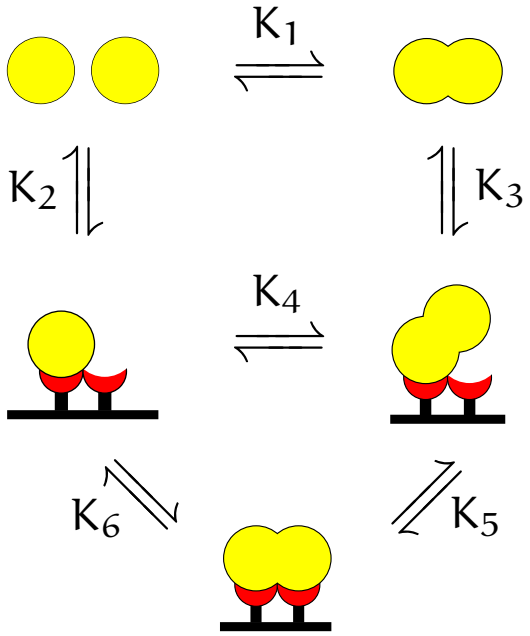

Figure C.28: Model of drug - receptor interaction. The parameters can be split into two groups. Those that quantify the dimerisation reaction in the various situations (K_1, K_4 and K_6) and those the quantify the drug-receptor binding in the different situations (K_2 and K_3 and K_5). The hypothesis is that due to the similarity in the binding pockets of the different drugs the variation in their performance can be explained solely using the variation in the former. To test this we fit this model to the data keeping the latter set fixed for the different drugs.

for the different drugs, in terms of the Figure C.28, are differences in K_1, K_4 and K_6 sufficient to explain the different drugs behaviour with K_2 and K_3 and K_5 being kept constant from drug to drug?

Due to the more complex surface interactions a number of numerical simulations were performed to verify the interactions described by the thermodynamic equilibrium equations, we tested the random sequential adsorption, and cooperative sequential adsorption[202,203,204] of monomers and dimers.

C.4.8 *Thermodynamic model*

As for the simple model, to find the equations describing the stress we begin by deriving analytically the thermodynamic equilibrium where all the reaction rates are equal to zero.

C.4.8.1 *Solution dimerisation*

To determine the number of monomers and dimers in solution,N_{ms} and N_{ds} respectively, we can consider the dimerisation process, governed by the association constant K_1:

$$\mathrm{N_{ms}} + \mathrm{N_{ms}} \underset{\mathrm{k_{1off}}}{\overset{\mathrm{k_{1on}}}{\rightleftharpoons}} \mathrm{N_{ds}}$$

Which for the steady state is equal to:

$$K_1 = \frac{[N_{ds}]}{[N_{ms}]^2} \tag{C.34}$$

C.4.8.2 *Monomer in solution binding to surface*

Aside from solution dimerisation monomers in solution, N_{ms}, may bind to the surface to become bound monomers, N_{mf} monomers binding to the surface are governed by the association constant K_2:

$$\mathrm{N_{ms}} + \mathrm{R_{free}} \underset{\mathrm{k_{2off}}}{\overset{\mathrm{k_{2on}}}{\rightleftharpoons}} \mathrm{N_{ds}}$$

Leading to:

$$K_2 = \frac{[N_{mf}]}{[N_{ms}][R_{free}]} \tag{C.35}$$

Where R_{free} is the number of free sites. This is verified in the numerical simulations of random sequential adsorption[205]. Simulations were performed for a square lattice, a hexagonal lattice and no lattice, where molecules are free to pick a point from continuous space. For the latter case the fraction of free sites is calculated based on the number of bound molecules in proportion to the maximum number of sites in the close packed or hexagonal configuration. For the square and hexagonal lattice the trivial solution of the probability of finding a free site being identical to the fraction of sites that are free. For the continuous space we see the effects of jamming reduce the probability of finding a free site. This final case is discarded as non-physical for the case of drug binding as our model deals with thermodynamic equilibrium steady state which would require the reactions to be entirely non-reversible, any deviation from this will result in a drift to the closely packed case[206].

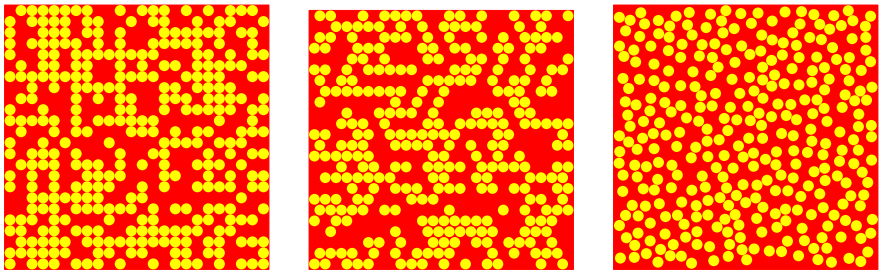

Figure C.29: Adsorption of monomer onto surface for square lattice, hexagonal lattice and continuous space.

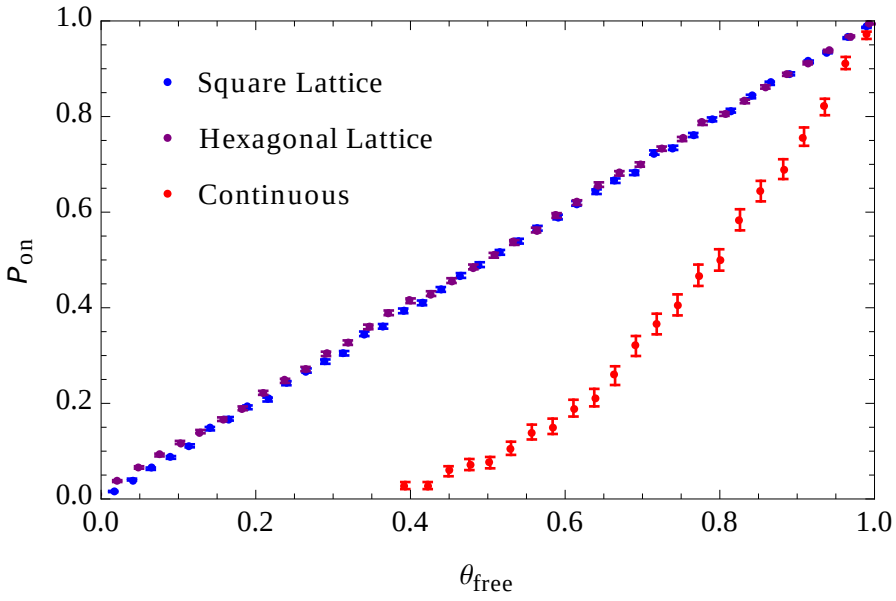

Figure C.30: Probability of finding free site vs occupancy

C.4.8.3 *Dimer in solution binding to surface*

A dimer in solution, N_{ds}, may bind one of its constituent drug molecules to the surface to become a singly bound dimer, N_{df1}. This reaction is governed by K_3:

$$\mathrm{N_{ds}} + \mathrm{R_{free}} \underset{\mathrm{k_{3off}}}{\overset{\mathrm{k_{3on}}}{\rightleftharpoons}} \mathrm{N_{df1}}$$

Leading to:

$$K_3 = \frac{[N_{df1}]}{[N_{ds}][R_{free}]} \tag{C.36}$$

C.4.8.4 *Monomer in solution binding to a monomer bound to surface to form a singly bound dimer*

A monomer in solution,N_{ms}, may bind to a monomer bound to the surface to become a singly bound dimer, N_{df1}. This reaction is governed by K_4:

$$\mathrm{N_{ms}} + \mathrm{N_{mf}} \underset{\mathrm{k_{4off}}}{\overset{\mathrm{k_{4on}}}{\rightleftharpoons}} \mathrm{N_{df1}}$$

Leading to:

$$K_4 = \frac{[N_{df1}]}{[N_{ms}][N_{mf}]} \tag{C.37}$$

C.4.8.5 *A singly bound dimer binding to the surface to form a doubly bound dimer*

A singly bound dimer's, N_{df1}, free drug molecule may bind to the surface to form a doubly bound dimer, N_{df2}.This reaction is governed by K_5:

$$\mathrm{N_{df1}} + \mathrm{R_{free}} \underset{\mathrm{k_{5off}}}{\overset{\mathrm{k_{5on}}}{\rightleftharpoons}} \mathrm{N_{df2}}$$

The ability of it to do this is however effected by its restricted motion. As it no longer has access to all the sites on the surface the likelihood of finding a site is given by the fraction of neighbouring sites that are free i.e for n sites:

$$\sum_{i}^{n} R_{free} = nR_{free} \tag{C.38}$$

Leading to:

$$K_5 = \frac{[N_{df2}]}{[N_{df1}]n[R_{free}]} \tag{C.39}$$

However the tiling considerations outlined above considerations lead us to reassess equation C.39, removing the nR_s term such that:

$$K_5 = \frac{[N_{df1}]}{[N_{df2}]} \tag{C.40}$$

The process governed by K_5 in Figure C.28 involves a single bound dimer finding a free receptor in an adjacent site. The likelihood of finding one in this restricted space is proportional to the number of empty neighbouring sites:

$$\sum_{i}^{n} R_{free} = nR_{free} \tag{C.41}$$

where n is the number of adjacent sites. This is identical to the below case, except being proportional to the fraction of free sites instead of those occupied by a monomer.

C.4.8.6 *Two bound monomers may dimerise to form a doubly bound dimer*

Two bound dimers, N_{dmf} may dimirise to form a doubly bound dimer, N_{df2}. This reaction is governed by K_6:

$$\mathrm{N_{mf}} + \mathrm{N_{mf}} \underset{\mathrm{k_{6off}}}{\overset{\mathrm{k_{6on}}}{\rightleftharpoons}} \mathrm{N_{df2}}$$

The likelihood of this is however effected by the restricted motion. As it no longer has access to all the sites on the surface the likelihood of finding bound monomer on in an adjacent site is given by the fraction of neighbouring sites that are occupied by monomers i.e for n sites:

$$\sum_{i}^{n} N_{mf} = nN_{mf} \tag{C.42}$$

Leading to:

$$K_6 = \frac{[N_{df2}]}{n[N_{mf}]^2} \tag{C.43}$$

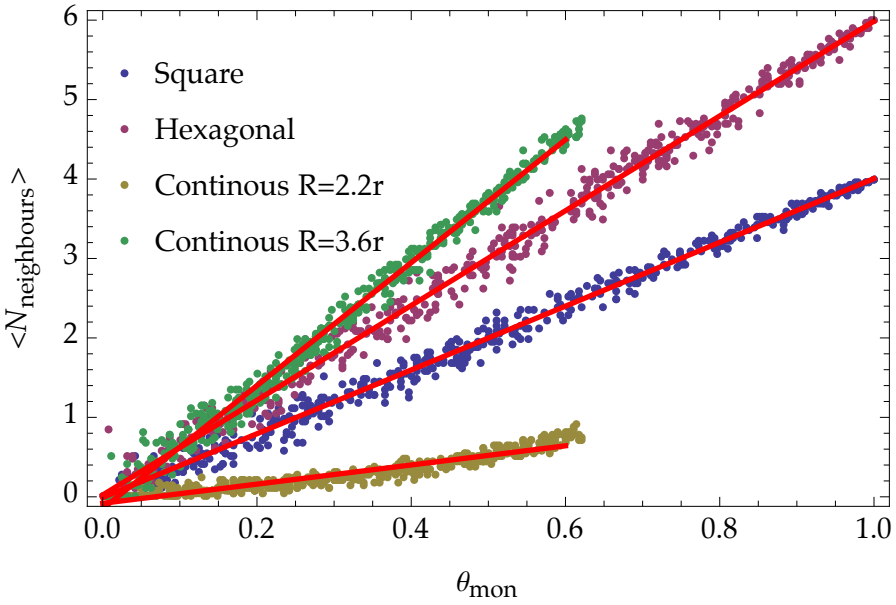

Figure C.31: Mean number of neighbours vs fraction of sites occupied with monomers. The number slope of the line corresponds to the number of neighbours, i.e. 4 for the square lattice 6 for the hexagonal lattice. For the continuous space model as there are no strict sites, neighbours must be defined as those within a certain distance R, given in terms of r the radius of the monomers.

The process governed by K_6 in Figure C.28 involves two bound monomers binding to form a dimer. In this case the relative spaces available for any given monomer to search is heavily restricted by its attachment to the surface. The probability of a surface bound monomer finding another to bind to is proportional to the number of bound monomers in adjacent sites:

$$\sum_{i}^{n} N_{mf} = nN_{mf} \tag{C.44}$$

where N_{mf} is the probability that a site is occupied by a bound monomer.

C.4.8.7 *Further Equations*

Further to the thermodynamic equilibria we can say certain things about the populations of different states that are useful to our analysis:

The total number of molecules in solution, that is the concentration is equal to:

$$N_s = N_{ms} + 2N_{ds} \tag{C.45}$$

The total number of sites on the cantilever is equal to:

$$R_{tot} = R_{occ} + R_{free} \tag{C.46}$$

The total number of occupied sites is equal to:

$$R_{occ} = N_{mf} + N_{df1} + N_{df2} \tag{C.47}$$

Where the lack of factor of twos for the N_{df1} and N_{df2} terms indicate their equivalence to N_{mf} in terms of site occupancy, as deduced from the tiling considerations.. The stress is equal to the fraction of occupied sites, given by:

$$\sigma = \sigma_{max}\theta = \sigma_{max}\frac{R_{occ}}{R_{tot}} \tag{C.48}$$

C.4.9 *Derivation of model*

C.4.9.1 *Derivation of monomers and dimers in solution*

We begin by expressing N_{ms} and N_{ds} in terms of N_s, the total number of molecules in solution, given by:

$$N_s = N_{ms} + 2N_{ds} \tag{C.49}$$

To get N_{ms} as a function of K_1 and N_s we rearrange equation C.34 to get:

$$N_{ds} = N_{ms}^2 K_1 \tag{C.50}$$

inserting this into equation C.49 gives us:

$$N_s = N_{ms} + 2N_{ms}^2 K_1 \tag{C.51}$$

Which we can solve for N_{ms} to get the solutions:

$$N_{ms} = -\frac{1}{4K_1} \pm \frac{1}{4}\sqrt{\frac{1 + 8K_1 N_s}{K_1^2}} \tag{C.52}$$

Because all our values remain real and positive we can discard the negative solution leaving us:

$$\boxed{N_{ms} = -\frac{1}{4K_1} + \frac{1}{4}\sqrt{\frac{1+8K_1N_s}{K_1^2}}} \tag{C.53}$$

If we repeat this process, instead rearranging equation C.34 to get N_{ds}, before inserting into C.49 we solve to get:

$$N_{ds} = \frac{1+4K_1N_s}{8K_1} \pm \frac{1}{8}\sqrt{\frac{1+8K_1N_s}{K_1^2}} \tag{C.54}$$

We know that as $N_s \to 0$ then N_{ds} must do so too, irrespective of the value of K_1. This means we select the negative sqrt solution that obeys this rule, so that:

$$\boxed{N_{ds} = \frac{1+4K_1N_s}{8K_1} - \frac{1}{8}\sqrt{\frac{1+8K_1N_s}{K_1^2}}} \tag{C.55}$$

C.4.9.2 *Derivation of K's interrelation*

By rearranging the equations for K_1, K_2 and K_4 we get:

$$\begin{aligned} N_{ds} &= K_1N_{ms}^2 \\ R_{free} &= \frac{N_{mf}}{N_{ms}K2} \\ N_{df1} &= N_{mf}N_{ms}K_4 \end{aligned} \tag{C.56}$$

If substitute these into the equation for K_3 we get the following:

$$\boxed{K_3 = \frac{K_4K_2}{K_1}} \tag{C.57}$$

This relationship is a consequence of the fact that the K's simply describe the relative populations of molecules in the different state, in a loop like structure these must have an interdependence. Using:

$$\begin{aligned} K_5 &= \frac{N_{df2}}{6N_{mf}^2} \\ K_6 &= \frac{N_{df2}}{N_{df1}} \end{aligned} \tag{C.58}$$

We can also equate K_5 to K_6:

$$K_6 = \frac{K_5 N_{mf}^2}{N_{df1}} \tag{C.59}$$

C.4.9.3 *Derivation of stress*

To get σ the stress in terms of the K parameters, N_{ms} and N_{ds} we begin by replacing R_{occ} and R_{tot} terms in:

$$\sigma = \sigma_{max} \frac{R_{occ}}{R_{tot}} \tag{C.60}$$

using $R_{occ} = N_{mf} + N_{df1} + N_{df2}$ and $R_{tot} = R_{free} + R_{occ}$ we get:

$$\sigma = \sigma_{max} \frac{N_{df1} + N_{df2} + N_{mf}}{N_{df1} + N_{df2} + N_{mf} + R_{free}} \tag{C.61}$$

Using:

$$K_6 = \frac{n[N_{mf}]^2}{[N_{df2}]} \tag{C.62}$$

to replace N_{df2} we get:

$$\sigma = \sigma_{max} \frac{N_{df1} + 6K_6 N_{mf}^2 + N_{mf}}{N_{df1} + 6K_6 N_{mf}^2 + N_{mf} + R_{free}} \tag{C.63}$$

Using equation C.59 we can substitute K_6 to get:

$$\sigma = \sigma_{max} \frac{N_{df1} + K_5 N_{df1} + N_{mf}}{N_{df1} + K_5 N_{df1} + N_{mf} + R_{free}} \tag{C.64}$$

Using the equation for K_4 we can remove N_{df1}:

$$\sigma = \sigma_{max} \frac{K_4 N_{mf} N_{ms} + K_5 K_4 N_{mf} N_{ms} + N_{mf}}{K_4 N_{mf} N_{ms} + K_5 K_4 N_{mf} N_{ms} + N_{mf} + R_{free}} \tag{C.65}$$

Then using the equation for K_2 we can remove R_{free} and cancel N_{mf} from each term:

$$\sigma = \sigma_{max} \frac{K_2 N_{ms} + K_2 K_4 N_{ms}^2 + K_2 K_4 K_5 N_{ms}^2}{1 + K_2 N_{ms} + K_2 K_4 N_{ms}^2 + K_2 K_4 K_5 N_{ms}^2} \tag{C.66}$$

Using the equation for K_1 we can replace N_{ms}^2 with N_{ds} to get:

$$\sigma = \sigma_{max} \frac{K_2 N_{ms} + \frac{K_2 K_4}{K1} N_{ds} + K_5 \frac{K_2 K_4}{K1} N_{ds}}{1 + K_2 N_{ms} + \frac{K_2 K_4}{K1} N_{ds} + K_5 \frac{K_2 K_4}{K1} N_{ds}} \tag{C.67}$$

Which using eq C.57 is equal to:

$$\boxed{\sigma = \sigma_{max} \frac{K_2 N_{ms} + K_3 N_{ds} + K_5 K_3 N_{ds}}{1 + K_2 N_{ms} + K_3 N_{ds} + K_5 K_3 N_{ds}}} \tag{C.68}$$

This gives us an equation for the stress observed based on the values of the K parameters and the concentration. To fit such a model in a useful manner we must make some assumptions about the relation between the different K values for the different drugs and surfaces.

C.4.10 *Fitting to data*

As previously mentioned, there are a number of physical constraints to this model that we need to impose on the various parameters and their relation to one another. Firstly concerning the parameters describing drug-receptor interactions, K_2, K_3 and K_5 we expect them to be constant for the different drugs, but different for the VSR and VRR case. This reflects the fact that the drugs share the same binding pocket, but that one bond in this pocket is removed for the VRR case. Secondly for the drug-drug reactions, governed by K_1, K_4 and K_6 we expect them to vary between the drugs as is shown by the experimentally determined solution dimerisation constants K_1 (see Tab. C.1), however these may not necessarily vary for the VSR and VRR surfaces.

Cooperativity, the property by which an alteration to one binding site on a ligand effects the performance of another should also be considered. This can occur in two ways, firstly for receptor coopertaivty we may say that the ability of the drugs to dimerize is enhanced or effected by the presence of a bound receptor to one or both of the drug molecules. Secondly for dimer coopertivity we may say that the ability for the drugs to bind to a receptor is effected or enhanced by the presence of dimer bound drug molecule. Both our own findings from the Hill fits and published work does indeed show that dimersation and receptor binding are cooperative in the vancomycin family of

drugs, such that we would expect K_3 and K_5 to be greater than $K_2$and K_4 and K_6 to be greater than K_1.[207,208,209,210]

As our model contains a large number of parameters and we have limited direct empirical information of the processes occurring on the cantilever surface to determine which of these processes are necessary to explain the observed variations in drug binding we gradually introduce these assumptions, finding the minimal set of assumptions for which this model will explain the data. To further simplify the fitting the saturation stress values are kept constant across the drugs such that all the VSR reactions are fixed to saturate at the mean saturation determined from the VSR hill fits, for the VRR case it is fixed to the Ori - VRR case as this is the only VRR data set that reaches saturation.

C.4.10.1 *Case 0 - No cooperativty between dimerisation or receptor binding*

This, the absolute simplest case, the lack of cooperativty for either dimers or receptors means we can use eq. C.68 with K_3 and K_5 set to be equal to K_2. This means the fits are controlled by the experimentally determined solution dimerisation K_1, the previously fitted saturation stress $\sigma_{max-VSR}$ and $\sigma_{max-VRR}$ and two fitted parameters K_{2-VSR} and K_{2-VRR}. As expected this fit does not perform well failing for both the VSR and VRR case as shown in Figure C.32.

C.4.10.2 *Case 1 - Cooperativty for dimers but not for receptor binding*

In this case we allow for the fact that a dimer may have a different propensity to bind to the receptor than a monomer, but we have this enhancement fixed for the different drugs, such that K_3 and K_5 both equal $K_2^{x_2}$. We give a power law relation as a general form of dependence and allow this to vary from the VSR surface to the VRR as we imagine the degree to which this coopertivity occurs may depend on the receptor. This means the fits are controlled by the experimentally determined solution dimerisation K_1, the previously fitted saturation stress $\sigma_{max-VSR}$ and $\sigma_{max-VRR}$ and four fitted parameters K_{2-VSR}, K_{2-VRR}, x_{2-VSR} and x_{2-VRR} which is common to both surfaces. This fit performs well for the VSR case but not for the VRR case as shown in Figure C.33.

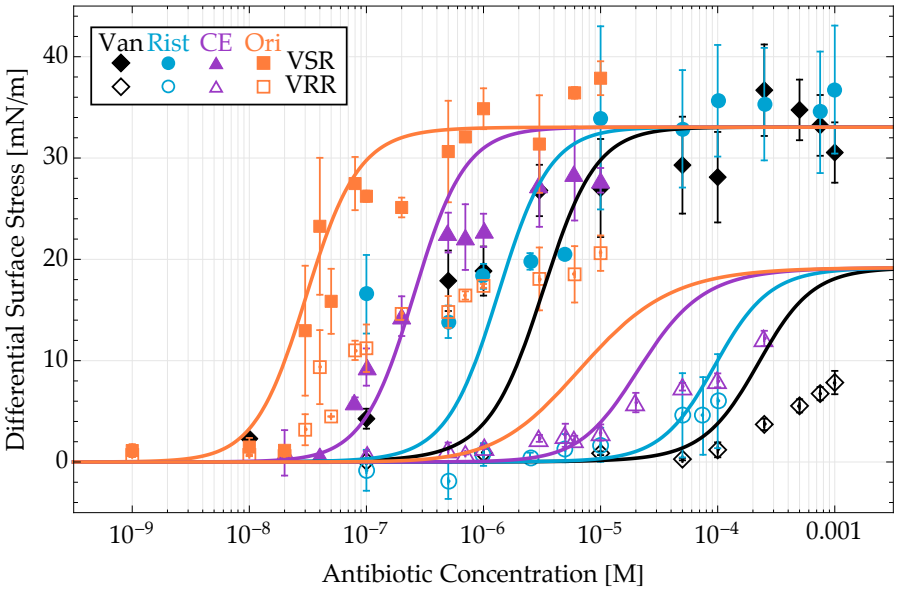

Figure C.32: Case 0 fit to full vancomycin family of drugs on both VSR and VRR surfaces

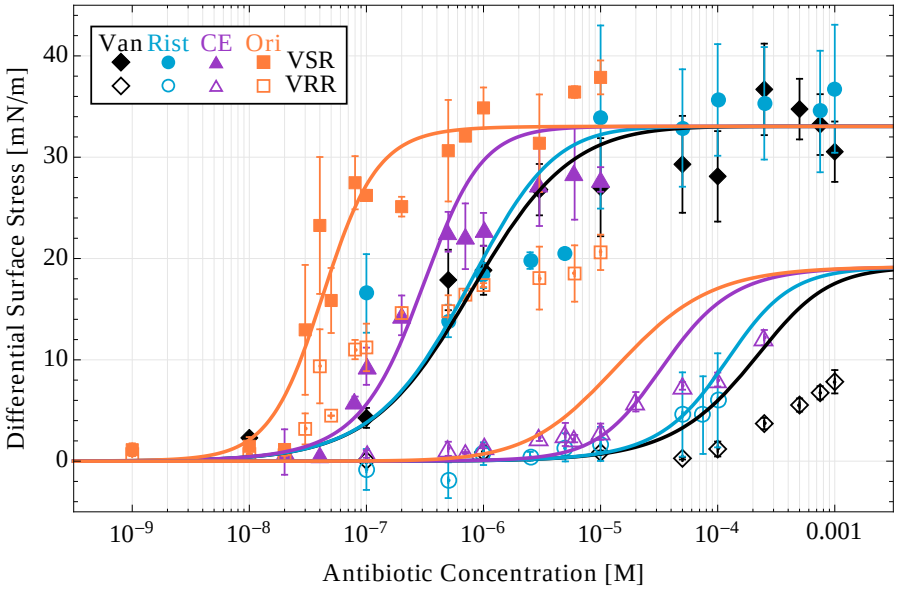

Figure C.33: Case 1 fit to full vancomycin family of drugs on both VSR and VRR surfaces

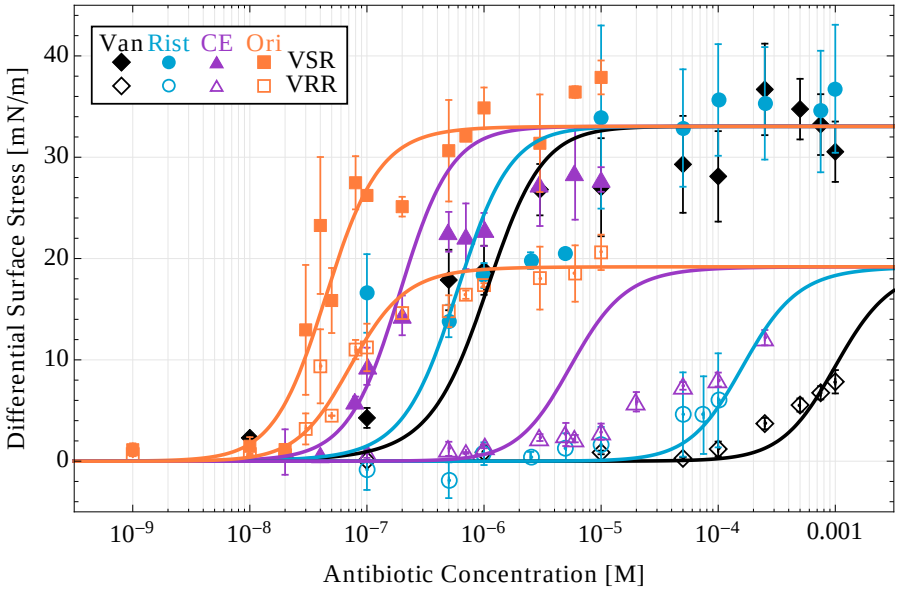

Figure C.34: Case 2 fit to full vancomycin family of drugs on both VSR and VRR surfaces

C.4.10.3 *Case 2 - Cooperativty for receptors but not for dimers*

In this case we test the opposite of case 1, neglecting dimer coopertaivity but allowing for the fact that the presence of a bound receptor may effect a drugs ability to dimerise, such that K_3 is again set equal to K_2 but K_4 is equal to $K_1^{x_1}$. We give a power law relation as a general form of dependence and allow this to vary from the VSR surface to the VRR as we imagine the degree to which this coopertivity occurs may depend on the receptor. To include K_4 in the model explicitly we must use the substitution from eq:C.40 to replace K_5. This means the fits are controlled by the experimentally determined solution dimerisation K_1, the previously fitted saturation stress $\sigma_{max-VSR}$ and $\sigma_{max-VRR}$ and four fitted parameters K_{2-VSR}, K_{2-VRR}, x_{1-VSR} and x_{1-VRR} which is common to both surfaces. This fit performs well for the VRR case, and ok,but not as well as case 1, for the VSR surface as shown in Figure C.34.

C.4.10.4 *Case 3 - Cooperativty for both receptors and for dimers*

Finally in this case we test coopertaivity both for dimers and receptors. K_3 is again set equal to $K_2^{x_2}$ and K_4 is equal to $K_1^{x_1}$ we also again use the substitution from eq:C.39 to replace K_5. This means the fits are

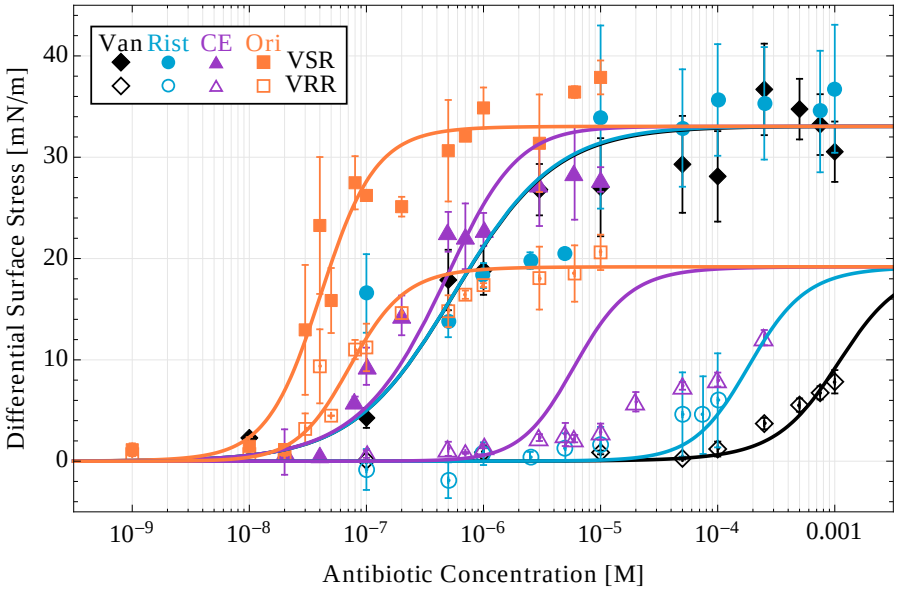

Figure C.35: Case 3 fit to full vancomycin family of drugs on both VSR and VRR surfaces

controlled by the experimentally determined solution dimerisation K_1, the previously fitted saturation stress $\sigma_{max-VSR}$ and $\sigma_{max-VRR}$ and 6 fitted parameters K_{2-VSR}, K_{2-VRR}, x_{1-VSR}, x_{1-VRR}, K_{2-VRR}, x_{2-VSR} and x_{2-VRR} which is common to both surfaces. The fit resulting from this is shown in Figure C.35.

This fit is far from perfect, the VRR Rist trace in particular is off by some distance, however given the extent of the data (6 orders of magnitude in concentration) and the relative paucity of fitting parameters, 8 as opposed to the 24 that would be required to fit individual Hill equation fits to every trace it is notably accurate.

C.4.11 *Ignoring tiling effects*

As a further test of our findings we repeat the above process but ignoring the tiling considerations. This is to say that instead of assuming doubly bound dimers occupy an identical site to a monomer we work with a 1:1 drug to receptor binding relationship such that a double bound dimer occupies two sites to a bound monomers single site. This leads to a slightly different algebraic form of the model, most notably

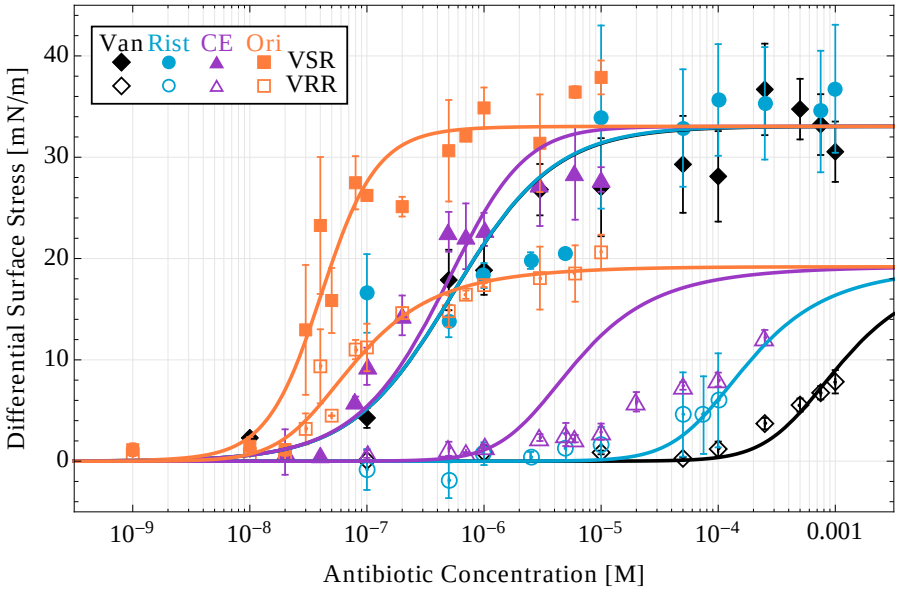

Figure C.36: Case 3b fit to full vancomycin family of drugs on both VSR and VRR surfaces

we arrive at the following relationship for K_5 in terms of K_6 which in the former case cancels out of our final equations:

$$K_5 = \frac{K_2 K_6}{K_4} \tag{C.69}$$

We also are unable to cancel the R_{free} term, giving us an extra parameter related to the sites on the surface. This can be rearranged such that the extra fitting parameter is R_{tot}, a factor that represents the concentration of the sites on the cantilever and can be fixed for all drugs and both surfaces (both VSR and VRR have similar footprints). If we go through the same procedure of gradually introducing assumptions regarding cooperativity as for the tiled case we achieve simila results. As for the tiling case we find coopertivity for the dimers leads to a good fit for the VSR with cooperttivty for the receptors also being needed to fit both VSR and VRR

Once again testing coopertaivity both for dimers and receptors. K_3 is again set equal to $K_2^{x_2}$ and K_4 is equal to $K_1^{x_1}$ we also again use the substitution from eq:C.40 to replace K_5, but not the substitution for K_5. This means the fits are controlled by the experimentally determined solution dimerisation K_1, the previously fitted saturation stress $\sigma_{max-VSR}$ and $\sigma_{max-VRR}$ and 6 fitted parameters K_{2-VSR}, K_{2-VRR},

x_{1-VSR}, x_{1-VRR},K_{2-VRR}, x_{2-VSR} and x_{2-VRR}. The fit resulting from this is shown in Figure C.36.

C.4.12 *Modelling Results*

We observe two key findings in both the tiling and non tiling case

- Having receptor coopertivity is key to getting good fit on Dala i.e. $K_3 = K_2^{x2}$
- Having dimerisation cooperativity that depends on surface is key to achieving spread in drugs i.e. $K_4 = K_1^{x1dala/dlac}$

We can see from the values for the *K's* deduced from the fitted parameters (see Figure C.37) that K_2 is significantly lower for the VSR case, as would be expected due to the greater affinity for the VSR targets. K_3 is also lower for the VSR case, although its dependence on K_1 means that this difference is lower for the more strongly dimerising drugs, we also observe K_3 to be lower than K_2, in line with common acceptance that dimers bind more strongly. K_5 is found to be very weak for both the VRR and VSR case, but is stronger for the VRR case.

We also observe from the fitted parameters is that K_4 is enhanced with respect to K_1 demonstrating a positive cooperativty on dimerisation for when a ligand is bound. This is of particular note for the VRR case where enhancement reaches a million for the Ori drug. For K_6 we see and enhancement for the VRR case but not for the VSR case, but similarly to the K_4 case the degree to which it is enhanced depends on the K_1. The extent of this enhancement is much greater than the figures normally observed in solution and, as suggested by the experimental findings in Figure C.21 is likely to be due to the presence of the surface which reduces the dimensionality and entropic costs in dimerising.

Furthermore we can define the coverage due to sub-populations on the surface with:

$$\begin{aligned} \theta_{mf} &= \frac{\theta_{mf}}{R_{occ}} \\ \theta_{df1} &= \frac{\theta_{df1}}{R_{occ}} \\ \theta_{df2} &= \frac{\theta_{df2}}{R_{occ}} \end{aligned} \tag{C.70}$$

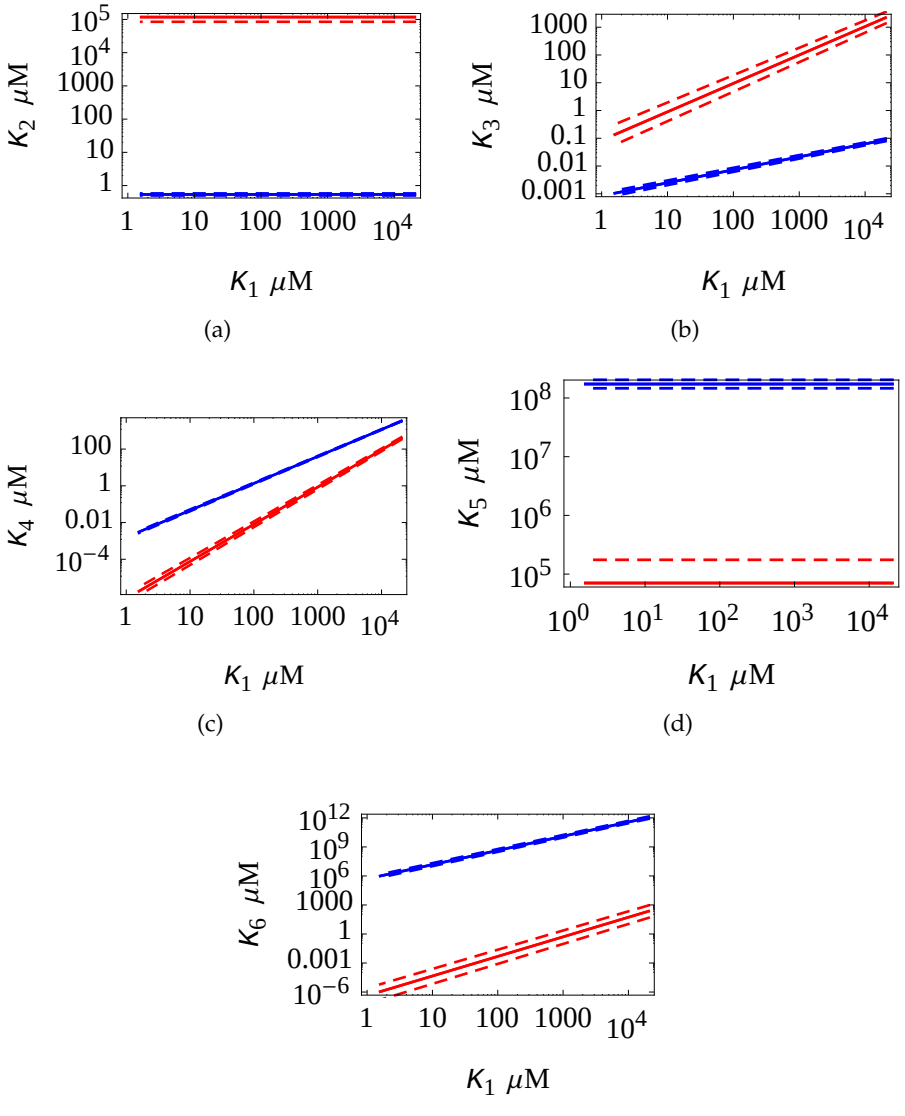

Figure C.37: Complete model K values from fit to data for case 3b

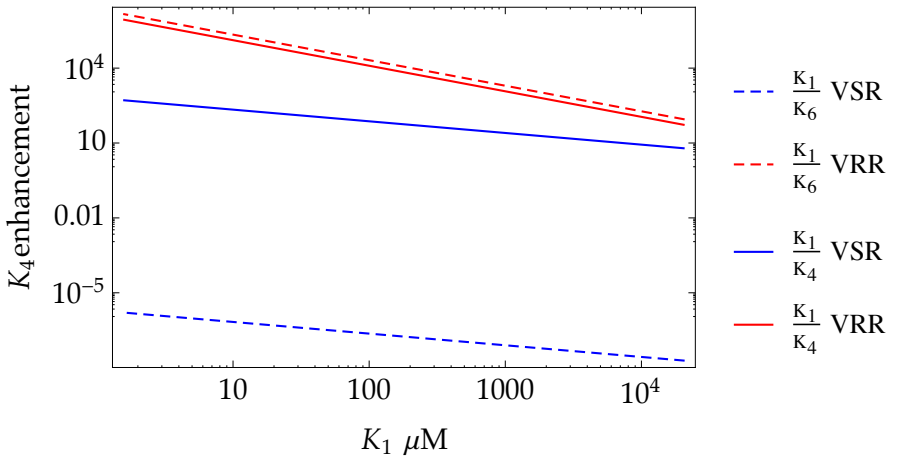

Figure C.38: Case 3b K_4 and K_6 enhancement

Plotting these sub-populations (see Figure C.39 gives an intuitive picture of the cantilever surface. Namely that the populations transition through monomer coverage to doubly bound dimer to singly bound dimer coverage at the highest concentrations. We also see on both VSR and VRR the role of monomers is diminished for the more strongly dimerising drugs.

C.5 CONCLUSIONS

Our research shows the utility of the cantilever D-Ala and D-Lac receptor system for screening vancomycin related antibiotics, our system tracks the MIC values over four decades. We have also shown that the mechanism of action is the binding to the surface peptides D-Ala and D-Lac and not likely to be significantly due to any secondary action. We have shown that despite this reliance on a lock and key binding process Ori's lower target affinity is overcome due to the catalysing effect of the surface VRR. We have investigated quantitatively how surface dynamics are important for tuning and controlling molecular binding events for antibiotics against vancomycin-susceptible and vancomycin-resistant targets. The findings demonstrate that while the single binding site lock- and-key mechanism dominates the behaviour of susceptible targets, it fails dramatically for the drug-resistant target. To explain the large variation in drug efficacy on the VRR targets we

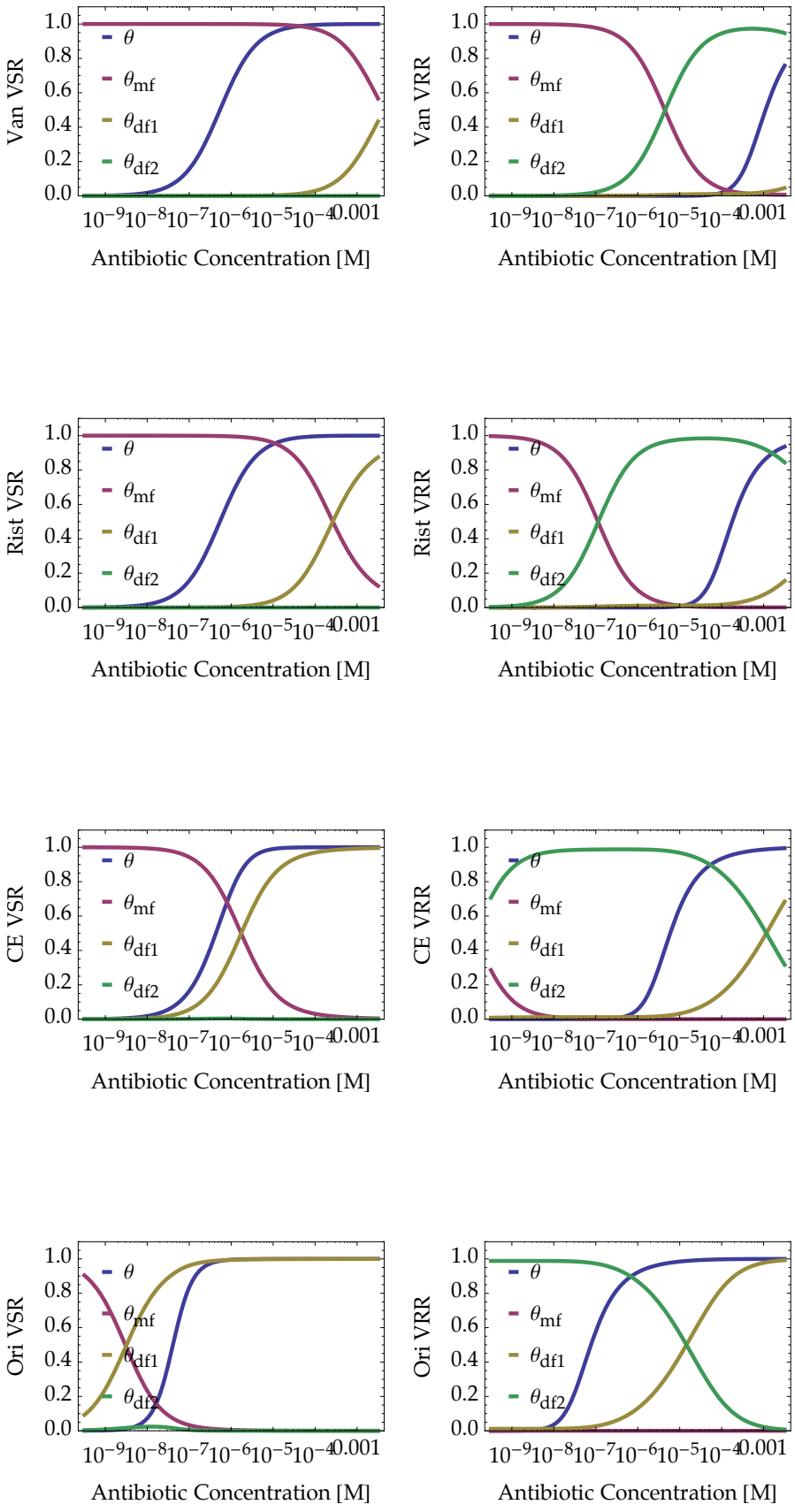

Figure C.39: Sub populations on surface

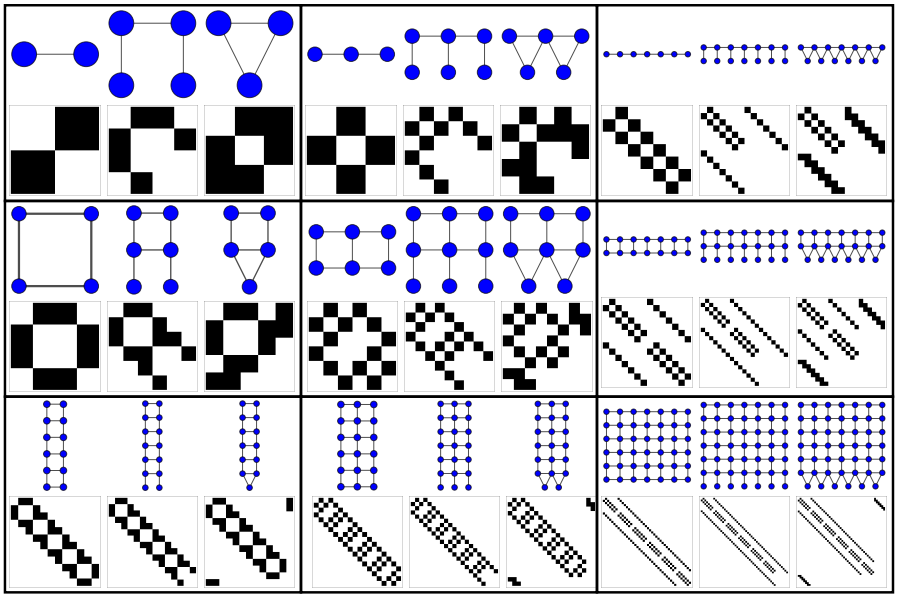

Figure C.40: Graphs and adjacency matrices for different models

must consider the surface modes of dimerisation, namely the K_4 and K_6 channels.

We have been deliberately cautious in the complexity and assumptions introduced as we have limited data at present regarding the molecules on the surface, and are largely relying on Ocam's razor to select the simplest model that explains the data further examination of the model either through further experiments or molecular dynamics simulations are needed.

Further extensions of this work could be to examine broader structural patterns in dimer and multimeric binding pathways. Figure C.40 shows 3 models with different terminations, that is to say the eventual surface binding pathways a flat, pointed (as in our complete model) and protruded (as in our simple model) the addition of extra layers, or larger multimeric structures will obviously lead to repeated motifs, the possibility of saying more fundamental limitations of such different networks may be of great use.

BIBLIOGRAPHY

[1] C Vieu, F Carcenac, A Pépin, Y Chen, M Mejias, A Lebib, L Manin-Ferlazzo, L Couraud, and H Launois. Electron beam lithography: resolution limits and applications. *Applied Surface Science*, 164(1-4):111–117, September 2000. (Cited on page 13.)

[2] Paul W K Rothemund. Folding DNA to create nanoscale shapes and patterns. *Nature*, 440(7082):297–302, March 2006. (Cited on page 13.)

[3] M D LaHaye, Olivier Buu, Benedetta Camarota, and K C Schwab. Approaching the quantum limit of a nanomechanical resonator. *Science*, 304(5667):74–77, 2004. (Cited on page 13.)

[4] Lei Liao, Yung-Chen Lin, Mingqiang Bao, Rui Cheng, Jingwei Bai, Yuan Liu, Yongquan Qu, Kang L Wang, Yu Huang, and Xiangfeng Duan. High-speed graphene transistors with a self-aligned nanowire gate. *Nature*, 467(7313):305–308, September 2010. (Cited on page 13.)

[5] Kin Wong, Stefan Johansson, and Bengt Kasemo. Nanofabricated model catalysts. Manufacturing and model studies. *Faraday Discussions*, 105:237–246, 1996. (Cited on page 13.)

[6] Alexandra Boltasseva and Vladimir M Shalaev. Fabrication of optical negative-index metamaterials: Recent advances and outlook. *Metamaterials*, 2(1):1–17, 2008. (Cited on page 13.)

[7] Bahram Jalali and Sasan Fathpour. Silicon Photonics. *Lightwave Technology, Journal of*, 24(12):4600–4615, December 2006. (Cited on page 13.)

[8] Efstratios Kehayas, Dimitris Tsiokos, Paraskevas Bakopoulos, Dimitris Apostolopoulos, Dimitrios Petrantonakis, Leontios Stampoulidis, Alistair Poustie, Rob McDougall, Graeme Maxwell, Yong Liu, Shaoxian Zhang, Harmen J S Dorren, Jorge Seoane, Pablo Van Holm-Nielsen, Palle Jeppesen, and Hercules Avramopoulos. 40-Gb/s All-Optical Processing Systems Using

Hybrid Photonic Integration Technology. *Lightwave Technology, Journal of*, 24(12):4903–4911. (Cited on page 13.)

[9] A V Krishnamoorthy, Ron Ho, Xuezhe Zheng, H Schwetman, Jon Lexau, P Koka, GuoLiang Li, I Shubin, and J E Cunningham. Computer Systems Based on Silicon Photonic Interconnects. *Proceedings of the IEEE*, 97(7):1337–1361, July 2009. (Cited on page 13.)

[10] Adam L. Washburn, Matthew S Luchansky, Adrienne L Bowman, and Ryan C Bailey. Quantitative, Label-Free Detection of Five Protein Biomarkers Using Multiplexed Arrays of Silicon Photonic Microring Resonators. *Analytical Chemistry*, 82(1): 69–72, January 2010. (Cited on page 13.)

[11] Kewal K Jain. Nanotechnology in clinical laboratory diagnostics. *Clinica Chimica Acta*, 358(1-2):37–54, August 2005. (Cited on page 13.)

[12] Daniel V Lim, Joyce M Simpson, Elizabeth A Kearns, and Marianne F Kramer. Current and developing technologies for monitoring agents of bioterrorism and biowarfare. *Clinical Microbiology Reviews*, 18(4):583–607, 2005. (Cited on page 13.)

[13] Peter B Luppa, Lori J Sokoll, and Daniel W Chan. Immunosensors—principles and applications to clinical chemistry. *Clinica Chimica Acta*, 314(1-2):1–26, December 2001. (Cited on page 13.)

[14] T.M. Squires, R.J. Messinger, and S R Manalis. Making it stick: convection, reaction and diffusion in surface-based biosensors. *Nature biotechnology*, 26(4):417–426, 2008. (Cited on pages 15 and 216.)

[15] Xudong Fan and Ian M White. Optofluidic microsystems for chemical and biological analysis. *Nature Photonics*, 5(10):591–597, September 2011. (Cited on page 15.)

[16] X Fan, I M White, S I Shopova, H Zhu, J D Suter, and Y Sun. Sensitive optical biosensors for unlabeled targets: a review. *analytica chimica acta*, 620(1):8–26, 2008. (Cited on pages 15 and 89.)

[17] Adam L. Washburn and Ryan C Bailey. Photonics-on-a-chip: recent advances in integrated waveguides as enabling detection

elements for real-world, lab-on-a-chip biosensing applications. *The Analyst*, 136(2):227–236, 2011. (Cited on pages 15 and 91.)

[18] John David Jackson. *Classical Electrodynamics*. Wiley, August 1998. (Cited on pages 16 and 17.)

[19] David J Griffiths. Introduction to electrodynamics. 2013. (Cited on pages 16 and 17.)

[20] Shadowitz. *The Electromagnetic field*. Dover Publications, 1975. (Cited on page 16.)

[21] S Anantha Ramakrishna and Tomasz M Grzegorczyk. *Physics and applications of negative refractive index materials*. CRC, 2009. (Cited on page 28.)

[22] J B Pendry, A J Holden, D J Robbins, and W J Stewart. Low frequency plasmons in thin-wire structures. *Journal of Physics: Condensed Matter*, 10(22):4785–4809, January 1999. (Cited on pages 28 and 31.)

[23] K Busch, S Lölkes, R B Wehrspohn, and H Föll. *Photonic Crystals: Advances in Design, Fabrication, and Characterization*. Wiley-VCH, January 2004. (Cited on page 32.)

[24] J Lourtioz, H Benisty, V Berger, J Gerard, D Maystre, and A Tchelnokov. Photonic Crystals: Towards Nanoscale Photonic Devices, 2005. (Cited on page 32.)

[25] Andrew R Parker and Natalia Martini. Structural colour in animals—simple to complex optics. *Optics & Laser Technology*, 38(4-6):315–322, June 2006. (Cited on pages 32 and 33.)

[26] L. Rayleigh. Studies of Iridescent Colour and the Structure Producing it. III. The Colours of Labrador Felspar. *Proceedings of the Royal Society of London. Series A*, 103(720):34–45, 1923. (Cited on page 32.)

[27] E Yablonovitch. Inhibited Spontaneous Emission in Solid-State Physics and Electronics. *Physical Review Letters*, 58(20):2059–2062, 1987. (Cited on page 32.)

[28] S John. Strong localization of photons in certain disordered dielectric superlattices. 58(23):2486–2489, 1987. (Cited on page 32.)

[29] J D Joannopoulos, S G Johnson, J.N. Winn, and R.D. Meade. *Photonic Crystals: Molding the Flow of Light (Second Edition)*. Princeton University Press, 2011. (Cited on pages 32, 37, 92, and 99.)

[30] Ardavan F Oskooi, David Roundy, Mihai Ibanescu, Peter Bermel, J D Joannopoulos, and Steven G Johnson. Meep: A flexible free-software package for electromagnetic simulations by the FDTD method. *Computer Physics Communications*, 181(3):687–702, March 2010. (Cited on pages 37, 38, 39, 101, and 167.)

[31] Steven Johnson and John Joannopoulos. Block-iterative frequency-domain methods for Maxwell's equations in a planewave basis. *Optics Express*, 8(3):173, 2001. (Cited on pages 37, 102, and 167.)

[32] SL McCall, PM Platzman, R. Dalichaouch, D. Smith, and S Schultz. Microwave propagation in two-dimensional dielectric lattices. 67(15):2017–2020, 1991. (Cited on page 37.)

[33] B.S. Song, S. Noda, T. Asano, and Y. Akahane. Ultra-high-Q photonic double-heterostructure nanocavity. *Nature Materials*, 4 (3):207–210, 2005. (Cited on page 39.)

[34] Jon Olav Grepstad, Peter Kaspar, Olav Solgaard, Ib-Rune Johansen, and Aasmund S Sudbø. Photonic-crystal membranes for optical detection of single nano-particles, designed for biosensor application. *Optics Express*, 20(7):7954–7965, 2012. (Cited on pages 39 and 91.)

[35] M G Scullion, A Di Falco, and T F Krauss. Slotted photonic crystal cavities with integrated microfluidics for biosensing applications. *Biosensors and Bioelectronics*, 27(1):101–105, September 2011. (Cited on page 39.)

[36] N. Skivesen, A.Ú. Tŕtu, M. Kristensen, J. Kjems, L.H. Frandsen, and P.I. Borel. Photonic-crystal waveguide biosensor. *Optics Express*, 15(6):3169–3176, 2007. (Cited on page 39.)

[37] Charles J Choi, Ian D Block, Brian Bole, David Dralle, and Brian T Cunningham. Label-Free Photonic Crystal Biosensor Integrated Microfluidic Chip for Determination of Kinetic Reaction Rate Constants. *IEEE Sensors Journal*, 9(12):1697–1704. (Cited on page 39.)

[38] Herbert Ackland Pohl. Dielectrophoresis, 1978. (Cited on pages 41 and 46.)

[39] David J Bakewell, Joe Bailey, and David Holmes. Real-time dielectrophoretic signaling and image quantification methods for evaluating electrokinetic properties of nanoparticles. *Under review with Electrophoresis*, pages 1–23, October 2014. (Cited on page 41.)

[40] D J Bakewell, J Bailey, and D Holmes. Advancing image quantification methods and tools for analysis of nanoparticle electrokinetics. *AIP Advances*, 3(10):102101–102101–21, October 2013. (Cited on page 41.)

[41] David J Bakewell, Joe Bailey, and David Holmes. Real-time dielectrophoretic signaling and image quantification methods for evaluating electrokinetic properties of nanoparticles. *ELECTROPHORESIS*, pages n/a–n/a, April 2015. (Cited on page 41.)

[42] T B Jones. Basic theory of dielectrophoresis and electrorotation. *Ieee Engineering in Medicine and Biology Magazine*, 22(6):33–42, 2003. (Cited on pages 41 and 42.)

[43] H Morgan, M P Hughes, and N G Green. Separation of submicron bioparticles by dielectrophoresis. *Biophysical Journal*, 77(1): 516–525, July 1999. (Cited on pages 43 and 46.)

[44] D J Bakewell and H Morgan. Measuring the frequency dependent polarizability of colloidal particles from dielectrophoretic collection data. *IEEE Transactions on Dielectrics and Electrical Insulation*, 8(3):566–571, June 2001. (Cited on pages 43 and 44.)

[45] Blanca H Lapizco-Encinas and Marco Rito-Palomares. Dielectrophoresis for the manipulation of nanobioparticles. *ELECTROPHORESIS*, 28(24):4521–4538, December 2007. (Cited on page 43.)

[46] Ronald Pethig. Review Article—Dielectrophoresis: Status of the theory, technology, and applications. 4:022811, 2010. (Cited on page 43.)

[47] David J Bakewell and David Holmes. Dual-cycle dielectrophoretic collection rates for probing the dielectric properties

of nanoparticles. *ELECTROPHORESIS*, 34(7):987–999, March 2013. (Cited on pages 43, 46, and 54.)

[48] Todd A Duncombe, Augusto M Tentori, and Amy E Herr. Microfluidics: reframing biological enquiry. *Nature Reviews Molecular Cell Biology*, 16(9):554–567, September 2015. (Cited on pages 43 and 45.)

[49] P R C Gascoyne, J Noshari, F F Becker, and R Pethig. Use of dielectrophoretic collection spectra for characterizing differences between normal and cancerous cells. *IEEE Transactions on Industry Applications*, 30(4):829–834, 1994. (Cited on pages 43, 44, 46, and 47.)

[50] Hong-Yuan Huang, Yu-Hsuan Huang, Wei-Lun Kao, and Da-Jeng Yao. Embryo formation from low sperm concentration by using dielectrophoretic force. *Biomicrofluidics*, 9(2):022404, March 2015. (Cited on page 43.)

[51] Jean-Christophe Baret, Oliver J Miller, Valerie Taly, Michaël Ryckelynck, Abdeslam El-Harrak, Lucas Frenz, Christian Rick, Michael L Samuels, J Brian Hutchison, Jeremy J Agresti, Darren R Link, David A Weitz, and Andrew D Griffiths. Fluorescence-activated droplet sorting (FADS): efficient microfluidic cell sorting based on enzymatic activity. *Lab on a Chip*, 9(13): 1850–1858, 2009. (Cited on page 43.)

[52] Rainer Pepperkok and Jan Ellenberg. High-throughput fluorescence microscopy for systems biology. *Nature Reviews Molecular Cell Biology*, 7(9):690–696, September 2006. (Cited on page 43.)

[53] Avery Sonnenberg, Jennifer Y Marciniak, James McCanna, Rajaram Krishnan, Laura Rassenti, Thomas J Kipps, and Michael J Heller. Dielectrophoretic isolation and detection of cfc-DNA nanoparticulate biomarkers and virus from blood. *ELECTROPHORESIS*, 34(7):1076–1084, April 2013. (Cited on page 44.)

[54] Charles L Asbury and Ger van den Engh. Trapping of DNA in Nonuniform Oscillating Electric Fields. *Biophysical Journal*, 74 (2):1024–1030, February 1998. (Cited on page 44.)

[55] Michael Pycraft Hughes. AC electrokinetics: applications for nanotechnology. *Nanotechnology*, 11(2):124–132, June 2000. (Cited on page 44.)

[56] Irina Ermolina, Joel Milner, and Hywel Morgan. Dielectrophoretic investigation of plant virus particles: Cow Pea Mosaic Virus and Tobacco Mosaic Virus. *ELECTROPHORESIS*, 27 (20):3939–3948, October 2006. (Cited on page 44.)

[57] Yongzheng Wen, Wei Ma, Joe Bailey, Guy Matmon, Gabriel Aeppli, and Xiaomei Yu. Absorption modulation of terahertz metamaterial by varying the conductivity of ground plane. *Applied Physics Letters*, 105(14):141111, October 2014. (Cited on page 57.)

[58] Yongzheng Wen, Wei Ma, Joe Bailey, Guy Matmon, and Xiaomei Yu. Broadband Terahertz Metamaterial Absorber Based on Asymmetric Resonators With Perfect Absorption. *IEEE Transactions on Terahertz Science and Technology*, pages 1–6. (Cited on page 57.)

[59] Yongzheng Wen, Wei Ma, Joe Bailey, Guy Matmon, Xiaomei Yu, and Gabriel Aeppli. Planar broadband and high absorption metamaterial using single nested resonator at terahertz frequencies. 2014. (Cited on page 57.)

[60] Yongzheng Wen, Wei Ma, Joe Bailey, Guy Matmon, Xiaomei Yu, and Gabriel Aeppli. Polarization-independent dual-band terahertz metamaterial absorbers based on gold/parylene-C/silicide structure. *Applied Optics*, 52(19):4536–4540, 2013. (Cited on page 57.)

[61] Masayoshi Tonouchi. Cutting-edge terahertz technology. *Nature Photonics*, 1(2):97–105, February 2007. (Cited on pages 57 and 59.)

[62] Yun-Shik Lee. *Principles of Terahertz Science and Technology*. Springer Science & Business Media, March 2009. (Cited on page 57.)

[63] Lyubov V Titova, Ayesheshim K Ayesheshim, Andrey Golubov, Dawson Fogen, Rocio Rodriguez-Juarez, Frank A Hegmann, and Olga Kovalchuk. Intense THz pulses cause H2AX phosphorylation and activate DNA damage response in human skin tissue. *Biomedical Optics Express*, 4(4):559, 2013. (Cited on page 57.)

[64] Peter H Siegel. Terahertz technology in biology and medicine. *Microwave Theory and Techniques, IEEE Transactions on*, 52(10): 2438–2447, 2004. (Cited on pages 57 and 58.)

[65] Roger Appleby and H Bruce Wallace. Standoff Detection of Weapons and Contraband in the 100 GHz to 1 THz Region. *IEEE Transactions on Antennas and Propagation*, 55(11):2944–2956, November 2007. (Cited on page 58.)

[66] John F Federici, Dale Gary, Robert Barat, and David Zimdars. THz standoff detection and imaging of explosives and weapons (Invited Paper). In Theodore T Saito, editor, *Defense and Security*, pages 75–84. SPIE, May 2005. (Cited on page 58.)

[67] Y Miura, A Kamataki, M Uzuki, and T Sasaki. Terahertz-Wave Spectroscopy for Precise Histopathological Imaging of Tumor and Non-tumor Lesions in Paraffin Sections. *The Tohoku Journal of . . .*, 2011. (Cited on page 58.)

[68] P Haring Bolivar, M Nagel, F Richter, M Brucherseifer, H Kurz, A Bosserhoff, and R Buttner. Label-free THz sensing of genetic sequences: towards 'THz biochips'. *Philosophical Transactions of the Royal Society A: Mathematical, Physical and Engineering Sciences*, 362(1815):323–335, February 2004. (Cited on page 59.)

[69] M Nagel, F Richter, P Haring Bolivar, and H Kurz. A functionalized THz sensor for marker-free DNA analysis. *Physics in Medicine and Biology*, 48(22):3625, November 2003. (Cited on page 59.)

[70] Samuel P Mickan, Abdellah Menikh, Haibo Liu, Carmen A Mannella, Robert MacColl, Derek Abbott, Jesper Munch, and X-C Zhang. Label-free bioaffinity detection using terahertz technology. *Physics in Medicine and Biology*, 47(21):3789–3795, October 2002. (Cited on page 59.)

[71] N Oda, H Yoneyama, and T Sasaki. SPIE | Proceeding | Detection of terahertz radiation from quantum cascade laser using vanadium oxide microbolometer focal plane arrays. *SPIE Defense . . .*, 2008. (Cited on page 59.)

[72] Fabio Alves, Dragoslav Grbovic, Brian Kearney, and Gamani Karunasiri. Microelectromechanical systems bimaterial terahertz sensor with integrated metamaterial absorber. *Optics letters*, 37 (11):1886–1888, June 2012. (Cited on page 59.)

[73] Xiaomei Yu, Yuliang Yi, Shenglin Ma, Ming Liu, Xiaohua Liu, Liquan Dong, and Yuejin Zhao. Design and fabrication of a high

sensitivity focal plane array for uncooled IR imaging. *Journal of Micromechanics and Microengineering*, 18(5):057001, 2008. (Cited on page 60.)

[74] D R Smith, J B Pendry, and MCK Wiltshire. Metamaterials and Negative Refractive Index. *Science*, 2004. (Cited on page 60.)

[75] Impact of resonator geometry and its coupling with ground plane on ultrathin metamaterial perfect absorbers | Browse - Applied Physics Letters, . URL http://apl.aip.org/resource/1/applab/v101/i10/p101102_s1. (Cited on page 61.)

[76] Hu Tao, C Bingham, A Strikwerda, D Pilon, D Shrekenhamer, N Landy, K Fan, X. Zhang, W Padilla, and R Averitt. Highly flexible wide angle of incidence terahertz metamaterial absorber: Design, fabrication, and characterization. *Physical Review B*, 78 (24):241103, December 2008. (Cited on pages 62 and 70.)

[77] Xiaopeng Shen, Tie Jun Cui, Junming Zhao, Hui Feng Ma, Wei Xiang Jiang, and Hui Li. Polarization-independent wide-angle triple-band metamaterial absorber. *Optics Express*, 19(10):9401–9407, May 2011. (Cited on page 62.)

[78] Yu Qian Ye, Yi Jin, and Sailing He. Omnidirectional, polarization-insensitive and broadband thin absorber in the terahertz regime. *JOSA B*, 27(3):498–504, 2010. (Cited on page 62.)

[79] Nan Zhang, Peiheng Zhou, Dengmu Cheng, Xiaolong Weng, Jianliang Xie, and Longjiang Deng. Dual-band absorption of mid-infrared metamaterial absorber based on distinct dielectric spacing layers. *Optics letters*, 38(7):1125–1127, April 2013. (Cited on page 62.)

[80] Jin Woo Park, Pham Van Tuong, Joo Yull Rhee, Ki Won Kim, Won Ho Jang, Eun Ha Choi, Liang Yao Chen, and YoungPak Lee. Multi-band metamaterial absorber based on the arrangement of donut-type resonators. *Optics Express*, 21(8):9691–9702, April 2013. (Cited on page 62.)

[81] James Grant, Yong Ma, Shimul Saha, Ata Khalid, and David R S Cumming. Polarization insensitive, broadband terahertz metamaterial absorber. *Optics letters*, 36(17):3476–3478, September 2011. (Cited on pages 62 and 86.)

[82] N Landy, S Sajuyigbe, J Mock, D. Smith, and W Padilla. Perfect Metamaterial Absorber. *Physical Review Letters*, 100(20):207402, May 2008. (Cited on page 65.)

[83] Shuomin Zhong and Sailing He. Ultrathin and lightweight microwave absorbers made of mu-near-zero metamaterials. *Scientific reports*, 3:–, June 2013. (Cited on page 65.)

[84] Yong Ma, Qin Chen, James Grant, Shimul C Saha, A Khalid, and David RS Cumming. A terahertz polarization insensitive dual band metamaterial absorber. *Optics letters*, 36(6):945–947, 2011. (Cited on pages 66 and 78.)

[85] V Fedotov, M Rose, S Prosvirnin, N Papasimakis, and N Zheludev. Sharp Trapped-Mode Resonances in Planar Metamaterials with a Broken Structural Symmetry. *Physical Review Letters*, 99 (14):147401, October 2007. (Cited on page 70.)

[86] Karen Maex. Silicides for integrated circuits: TiSi2 CoSi2. *Materials Science and Engineering: R: Reports*, 11(2-3):vii–153, November 1993. (Cited on page 74.)

[87] Hu Tao, C M Bingham, D Pilon, Kebin Fan, A C Strikwerda, D Shrekenhamer, W J Padilla, Xin Zhang, and R D Averitt. A dual band terahertz metamaterial absorber. *Journal of Physics D-Applied Physics*, 43(22):225102, June 2010. (Cited on page 78.)

[88] Na Liu and Annemarie Pucci. Plasmonic biosensors: Know your molecules. *Nature*, 11(1):9–10, December 2011. (Cited on page 89.)

[89] Jiří Homola. Surface Plasmon Resonance Sensors for Detection of Chemical and Biological Species. *Chemical Reviews*, 108(2): 462–493, February 2008. (Cited on page 89.)

[90] Saurabh Mani Tripathi, Arun Kumar, Emmanuel Marin, and Jean-Pierre Meunier. Bragg grating based biochemical sensor using submicron Si/SiO_2 waveguides for lab-on-a-chip applications: a novel design. *Applied Optics*, 48(23):4562, 2009. (Cited on page 89.)

[91] Lina He, Şahin Kaya Özdemir, Jiangang Zhu, Woosung Kim, and Lan Yang. Detecting single viruses and nanoparticles using

whispering gallery microlasers. *Nature Nanotechnology*, 6(7):428–432, June 2011. (Cited on page 90.)

[92] Séverine Maguis, Guillaume Laffont, Pierre Ferdinand, Benjamin Carbonnier, Khémara Kham, Tahar Mekhalif, and Marie-Claude Millot. Biofunctionalized tilted Fiber Bragg Gratings for label-free immunosensing. *Optics Express*, 16(23):19049–19062, November 2008. (Cited on page 90.)

[93] Brian T Cunningham. Photonic Crystal Surfaces as a General Purpose Platform for Label-Free and Fluorescent Assays. *Journal of the Association for Laboratory Automation*, 15(2):120–135, April 2010. (Cited on page 90.)

[94] Yumei Hu, Xiaomei Jiang, Laiying Zhang, Jiao Fan, and Weitai Wu. Construction of near-infrared photonic crystal glucose-sensing materials for ratiometric sensing of glucose in tears. *Biosensors and Bioelectronics*, 48:94–99, October 2013. (Cited on page 90.)

[95] Sudeshna Pal, Amrita R Yadav, Mark A Lifson, James E Baker, Philippe M Fauchet, and Benjamin L Miller. Selective virus detection in complex sample matrices with photonic crystal optical cavities. *Biosensors and Bioelectronics*, 44:229–234, June 2013. (Cited on page 90.)

[96] Daphné Duval, Ana Belén González-Guerrero, Stefania Dante, Johann Osmond, Rosa Monge, Luis Fernández, Kirill Zinoviev, Carlos Domínguez, and Laura Lechuga. Nanophotonic lab-on-a-chip platforms including novel bimodal interferometers, microfluidics and grating couplers. *Lab on a Chip*, 2012. (Cited on page 91.)

[97] Yi Zou, Swapnajit Chakravarty, Wei-Cheng Lai, Che-Yun Lin, and Ray T Chen. Methods to array photonic crystal microcavities for high throughput high sensitivity biosensing on a silicon-chip based platform. *Lab on a Chip*, 12(13):2309, 2012. (Cited on page 91.)

[98] J B Pendry, A J Holden, D J Robbins, and W J Stewart. Magnetism from Conductors and Enhanced Nonlinear Phenomena. *IEEE Transactions on Microwave Theory and Techniques*, 47(11):1–10, October 1999. (Cited on pages 92 and 94.)

[99] Manfred Fiebig. Revival of the magnetoelectric effect. *Journal of Physics D-Applied Physics*, 38(8):R123–R152, April 2005. (Cited on pages 92 and 94.)

[100] J C Knight, T A Birks, P St J Russell, and D M Atkin. All-silica single-mode optical fiber with photonic crystal cladding. *Optics letters*, 21(19):1–3, September 1996. (Cited on pages 92 and 95.)

[101] Phillip Russell. Photonic Crystal Fibers. *Frontiers in Optics*, pages 1–6, January 2003. (Cited on page 92.)

[102] T A Birks, J C Knight, and P St J Russell. Endlessly single-mode photonic crystal fiber. *Optics letters*, 22(13):1–3, June 1997. (Cited on page 92.)

[103] F Caruso. Nanoengineering of particle surfaces. *Advanced Materials*, 2001. (Cited on page 92.)

[104] J D Joannopoulos, P.R. Villeneuve, and S. Fan. Photonic crystals: putting a new twist on light. *Nature*, 1997. (Cited on page 92.)

[105] John M Dudley, Goëry Genty, and Stephane Coen. Supercontinuum generation in photonic crystal fiber. *Rev.Mod.Phys.*, 78(4): 1135–1184, October 2006. (Cited on pages 92 and 95.)

[106] Y S Kivshar and G Agrawal. Optical solitons: from fibers to photonic crystals, 2003. (Cited on page 92.)

[107] O Painter, R K Lee, A Scherer, A Yariv, J D O'Brien, P D Dapkus, and I Kim. Two-Dimensional Photonic Band-Gap Defect Mode Laser. *Science*, 284(5421):1819–1821, June 1999. (Cited on page 93.)

[108] Yoshihiro Akahane, Takashi Asano, Bong-Shik Song, and Susumu Noda. High-Q photonic nanocavity in a two-dimensional photonic crystal. *Nature*, 425(6961):944–947, October 2003. (Cited on pages 93, 95, and 98.)

[109] Y. Xia, B Gates, Y Yin, and Y Lu. Monodispersed Colloidal Spheres: Old Materials with New Applications. *Advanced Materials*, 12(10):693–713, May 2000. (Cited on page 93.)

[110] J E Wijnhoven. Preparation of Photonic Crystals Made of Air Spheres in Titania. *Science*, 281(5378):1–4, August 1998. (Cited on page 93.)

[111] Lincoln J Lauhon, Mark S Gudiksen, Deli Wang, and Charles M Lieber. Epitaxial core–shell and core– multishell nanowire heterostructures. *Nature*, 420(6911):1–5, October 2002. (Cited on pages 93 and 94.)

[112] Uwe H F Bunz. Poly(aryleneethynylene)s: Syntheses, Properties, Structures, and Applications. *Chemical Reviews*, 100(4):1605–1644, April 2000. (Cited on page 93.)

[113] A. Mekis, JC Chen, I. Kurland, S. Fan, PR Villeneuve, and JD Joannopoulos. High Transmission through Sharp Bends in Photonic Crystal Waveguides. *Physical Review Letters*, 77(18): 3787–3790, October 1996. (Cited on page 93.)

[114] T Yoshie, A Scherer, J Hendrickson, and G Khitrova. Vacuum Rabi splitting with a single quantum dot in a photonic crystal nanocavity. *Nature*, 2004. (Cited on pages 93 and 95.)

[115] M Campbell, D N Sharp, M T Harrison, and R G Denning. Fabrication of photonic crystals for the visible spectrum by holographic lithography. *Nature*, 2000. (Cited on page 93.)

[116] R F Cregan. Single-Mode Photonic Band Gap Guidance of Light in Air. *Science*, 285(5433):1–4, August 1999. (Cited on page 93.)

[117] A. Blanco, E. Chomski, S. Grabtchak, M. Ibisate, and S John. Large-scale synthesis of a silicon photonic crystal with a complete three-dimensional bandgap near 1.5 micrometres. *Nature*, 2000. (Cited on page 94.)

[118] Y A Vlasov, X Z Bo, J C Sturm, and D J Norris. On-chip natural assembly of silicon photonic bandgap crystals. *Nature*, 414(6861): 289–293, November 2001. (Cited on pages 94, 95, and 96.)

[119] E Yablonovitch. Photonic band-gap structures. *JOSA B*, 1993. (Cited on pages 94 and 168.)

[120] Steven Johnson, Shanhui Fan, Pierre Villeneuve, J Joannopoulos, and L Kolodziejski. Guided modes in photonic crystal slabs. *Physical Review B*, 60(8):5751–5758, August 1999. (Cited on page 94.)

[121] T F Krauss, M Richard, and S. Brand. Two-dimensional photonic-bandgap structures operating at near-infrared wavelengths. *Nature*, 1996. (Cited on pages 94, 95, 98, and 168.)

[122] S Lin. Experimental Demonstration of Guiding and Bending of Electromagnetic Waves in a Photonic Crystal. *Science*, 282(5387): 1–4, October 1998. (Cited on page 94.)

[123] O Painter, J Vuckovic, and A Scherer. Defect modes of a two-dimensional photonic crystal in an optically thin dielectric slab. *Journal of the Optical Society of America B-Optical Physics*, 16(2): 1–11, January 1999. (Cited on page 94.)

[124] Peter Lodahl, A Floris van Driel, Ivan S Nikolaev, Arie Irman, Karin Overgaag, Daniël Vanmaekelbergh, and Willem L Vos. Controlling the dynamics of spontaneous emission from quantum dots by photonic crystals. *Nature*, 430(7000):654–657, August 2004. (Cited on page 95.)

[125] E Yablonovitch. Photonic Band-Gap Structures. *Journal of the Optical Society of America B-Optical Physics*, 10(2):283–295, 1993. (Cited on pages 95 and 96.)

[126] S. Fan, J D Joannopoulos, J.N. Winn, and A Devenyi. Guided and defect modes in periodic dielectric waveguides. *JOSA B*, 1995. (Cited on page 97.)

[127] M.R. Lee and P.M. Fauchet. Nanoscale microcavity sensor for single particle detection. *Optics letters*, 32(22):3284–3286, 2007. (Cited on page 102.)

[128] Masao Miyake, Ying Chieh Chen, Paul V Braun, and Pierre Wiltzius. Fabrication of Three-Dimensional Photonic Crystals Using Multibeam Interference Lithography and Electrodeposition. *Advanced Materials*, 21(29):3012–3015, 2009. (Cited on page 114.)

[129] Juan F Galisteo-López, Marta Ibisate, Riccardo Sapienza, Luis S Froufe-Pérez, Álvaro Blanco, and Cefe López. Self-Assembled Photonic Structures. *Advanced Materials*, 23(1):30–69, September 2010. (Cited on page 114.)

[130] Huigao Duan, Donald Winston, Joel K W Yang, Bryan M Cord, Vitor R Manfrinato, and Karl K Berggren. Sub-10-nm half-pitch electron-beam lithography by using poly(methyl methacrylate) as a negative resist. *Journal of Vacuum Science & Technology B: Microelectronics and Nanometer Structures*, 28(6):C6C58, 2010. (Cited on page 122.)

[131] I Zailer, J E F Frost, V Chabasseur-Molyneux, C J B Ford, and M Pepper. Crosslinked PMMA as a high-resolution negative resist for electron beam lithography and applications for physics of low-dimensional structures. *Semiconductor Science and Technology*, 11(8):1235–1238, January 1999. (Cited on page 122.)

[132] K M Hilligsøe, T Andersen, H Paulsen, and C Nielsen. Supercontinuum generation in a photonic crystal fiber with two zero dispersion wavelengths. *Optics . . .*, 2004. (Cited on page 135.)

[133] R Alfano and S Shapiro. Observation of Self-Phase Modulation and Small-Scale Filaments in Crystals and Glasses. *Physical Review Letters*, 24(11):592–594, March 1970. (Cited on page 135.)

[134] R Alfano and S Shapiro. Emission in the Region 4000 to 7000 Å Via Four-Photon Coupling in Glass. *Physical Review Letters*, 24 (11):584–587, March 1970. (Cited on page 135.)

[135] John M Dudley and Goëry Genty. Supercontinuum light. *scitation.aip.org*, pages 29–34, June 2013. (Cited on page 135.)

[136] Dirk Taillaert, Frederik Van Laere, Melanie Ayre, Wim Bogaerts, Dries Van Thourhout, Peter Bienstman, and Roel Baets. Grating couplers for coupling between optical fibers and nanophotonic waveguides. 45(8A):6071–6077, 2006. (Cited on page 136.)

[137] Xia Chen and Hon K Tsang. Polarization-independent grating couplers for silicon-on-insulator nanophotonic waveguides. *Optics letters*, 36(6):796, 2011. (Cited on page 137.)

[138] R. Halir, I. Molina-Fernandez, P. Cheben, JH Schmid, R. Ma, S. Janz, D.X. Xu, A. Densmore, and J.M. Fedeli. Single etch fibre-to-chip grating couplers for high-volume production in SOI. *Information Photonics (IP), 2011 ICO International Conference on*, pages 1–2, 2011. (Cited on page 139.)

[139] Liu Liu, Minhao Pu, Kresten Yvind, and Jorn M Hvam. High-efficiency, large-bandwidth silicon-on-insulator grating coupler based on a fully-etched photonic crystal structure. *Applied Physics Letters*, 96(5):051126, 2010. (Cited on page 139.)

[140] O Painter. Two-Dimensional Photonic Band-Gap Defect Mode Laser. *Science*, 284(5421):1819–1821, June 1999. (Cited on page 170.)

[141] Bryan Ellis, Marie A Mayer, Gary Shambat, Tomas Sarmiento, James Harris, Eugene E Haller, and Jelena Vučković. Ultralow-threshold electrically pumped quantum-dot photonic-crystal nanocavity laser. *Nature Photonics*, 5(5):297–300, April 2011. (Cited on page 170.)

[142] M Fujita. Simultaneous Inhibition and Redistribution of Spontaneous Light Emission in Photonic Crystals. *Science*, 308(5726): 1296–1298, May 2005. (Cited on page 170.)

[143] Hatice Altug, Dirk Englund, and Jelena Vučković. Ultrafast photonic crystal nanocavity laser. *Nature Physics*, 2(7):484–488, July 2006. (Cited on page 171.)

[144] B Zhen, S L Chua, and J Lee. Enabling enhanced emission and low-threshold lasing of organic molecules using special Fano resonances of macroscopic photonic crystals. In *Proceedings of the National Academy of Sciences*, 2013. (Cited on page 171.)

[145] Hales JE. *Implementing the synthetic biology design cycle to fabricate laser dyes*. PhD thesis, University College London. (Cited on page 171.)

[146] Francois Grey, En-Te Hwu, Bradley Camburn, kun Jia, Benjamin Koo, Zhi-Cong Lu, Yun-Zi Qian, Gabriel Aeppli, Joe M Bailey, Ellie Doney, James Lawrence, Alice Pyne, Valerian Turbe, Wei Ma, and Xiaomei Yu. LEGO2NANO: Designing interactive science for children in China. URL `http://idc2014.org/wp-content/uploads/2014/09/idc20140_submission_203.pdf`. (Cited on page 177.)

[147] Francois Grey. Creativity unleashed. *Nature Nanotechnology*, 10 (5):480–480, May 2015. (Cited on page 177.)

[148] Chris Anderson. *Makers*. The New Industrial Revolution. Random House, September 2012. (Cited on page 178.)

[149] SparkFun Electronics. Arduino Uno - R3 Licensed under Creative Commons Attribution 2.0 via Wikimedia Commons . (Cited on page 178.)

[150] Chris Anderson. *The Long Tail*. Why the Future of Business Is Selling Less of More. Harper Collins, July 2006. (Cited on page 179.)

[151] Philip Ross. Chris Anderson's Expanding Drone Empire. URL http://spectrum.ieee.org/aerospace/aviation/chris-andersons-expanding-drone-empire. (Cited on page 179.)

[152] Rahmenlayout Schüler STM Homepage, . URL http://sxm4.uni-muenster.de/stm-en/. (Cited on page 180.)

[153] OsciPrime - An Open Source Android Oscilloscope, . URL http://www.osciprime.com/. (Cited on page 180.)

[154] OpenPCR, . URL http://openpcr.org/. (Cited on page 180.)

[155] Chris Lintott, Kevin Schawinski, Steven Bamford, Anže Slosar, Kate Land, Daniel Thomas, Edd Edmondson, Karen Masters, Robert C Nichol, M Jordan Raddick, Alex Szalay, Dan Andreescu, Phil Murray, and Jan Vandenberg. Galaxy Zoo 1: data release of morphological classifications for nearly 900 000 galaxies. *Monthly Notices of the Royal Astronomical Society*, 410(1):166–178, November 2010. (Cited on page 180.)

[156] D Clery. Galaxy Zoo Volunteers Share Pain and Glory of Research. *Science*, 333(6039):173–175, July 2011. (Cited on page 180.)

[157] Foldit Screenshot. (Cited on page 181.)

[158] Christopher B Eiben, Justin B Siegel, Jacob B Bale, Seth Cooper, Firas Khatib, Betty W Shen, Foldit Players, Barry L Stoddard, Zoran Popovic, and David Baker. Increased Diels-Alderase activity through backbone remodeling guided by Foldit players. *Nature biotechnology*, 30(2):190–192, January 2012. (Cited on pages 181 and 182.)

[159] Chiara Franzoni and Henry Sauermann. Crowd Science: The Organization of Scientific Research in Open Collaborative Projects. *SSRN Electronic Journal*, 2012. (Cited on page 182.)

[160] Firas Khatib, Frank DiMaio, Seth Cooper, Maciej Kazmierczyk, Miroslaw Gilski, Szymon Krzywda, Helena Zabranska, Iva Pichova, James Thompson, Zoran Popovic, Mariusz Jaskolski, and David Baker. Crystal structure of a monomeric retroviral protease solved by protein folding game players. *Nature Structural & Molecular Biology*, 18(10):1175–1177, September 2011. (Cited on page 182.)

[161] Radiation Watch, . URL http://www.radiation-watch.org/p/english.html. (Cited on page 182.)

[162] Safecast, . (Cited on page 182.)

[163] Public Lab: a DIY environmental science community, . URL http://publiclab.org/. (Cited on page 182.)

[164] E T Hwu, H Illers, L Jusko, and H-U Danzebrink. A hybrid scanning probe microscope (SPM) module based on a DVD optical head. *Measurement Science and Technology*, 20(8):084005, June 2009. (Cited on page 184.)

[165] Viola Vogel and Michael Sheetz. Local force and geometry sensing regulate cell functions. *Nature Reviews Molecular Cell Biology*, 7(4):265–275, April 2006. (Cited on page 205.)

[166] Deborah Leckband and Jacob Israelachvili. Intermolecular forces in biology. *Quarterly Reviews of Biophysics*, 34(02):105, December 2001. (Cited on page 205.)

[167] J L Arlett, E B Myers, and M L Roukes. Comparative advantages of mechanical biosensors. *Nature Nanotechnology*, 6(4):203–215, March 2011. (Cited on page 205.)

[168] Thomas Braun, Viola Barwich, Murali Ghatkesar, Adriaan Bredekamp, Christoph Gerber, Martin Hegner, and Hans Lang. Micromechanical mass sensors for biomolecular detection in a physiological environment. *Physical Review E*, 72(3), September 2005. (Cited on page 205.)

[169] Cantilever - Wikipedia, the free encyclopedia, . URL http://en.wikipedia.org/wiki/Cantilever. (Cited on page 206.)

[170] J Fritz. Translating Biomolecular Recognition into Nanomechanics. *Science*, 288(5464):316–318, April 2000. (Cited on page 206.)

[171] Gerd Binnig, C.F. Quate, and C Gerber. Atomic force microscope. *Physical Review Letters*, 56(9):930–933, 1986. (Cited on page 205.)

[172] P K Hansma, J P Cleveland, M Radamacher, D A Walters, P E Hillner, M Bezanilla, M Fritz, D Vie, H G Hansma, and C B Prater. Tapping mode atomic force microscopy in liquids. *Applied Physics Letters*, 64(13):1738–1740, 1994. (Cited on page 205.)

[173] Seonghwan Kim, Kenneth D Kihm, and Thomas Thundat. Fluidic applications for atomic force microscopy (AFM) with microcantilever sensors. *Experiments in Fluids*, 48(5):721–736, February 2010. (Cited on page 205.)

[174] E L Florin, V T Moy, and H E Gaub. Adhesion forces between individual ligand-receptor pairs. *Science*, 264(5157):415–417, 1994. (Cited on page 205.)

[175] A M Moulin, S J O'Shea, and M E Welland. Microcantilever-based biosensors. *Ultramicroscopy*, 82(1-4):23–31, 2000. (Cited on page 205.)

[176] R Raiteri, G Nelles, H J Butt, W Knoll, and P Skladal. Sensing of biological substances based on the bending of microfabricated cantilevers. *Sensors & Actuators: B. Chemical*, 61(1):213–217, 1999. (Cited on page 205.)

[177] Kyo Seon Hwang, Sang-Myung Lee, Sang Kyung Kim, Jeong Hoon Lee, and Tae Song Kim. Micro- and Nanocantilever Devices and Systems for Biomolecule Detection. *Annual Review of Analytical Chemistry*, 2(1):77–98, July 2009. (Cited on page 206.)

[178] F Huber, H P Lang, N Backmann, D Rimoldi, and Ch Gerber. Direct detection of a BRAF mutation in total RNA from melanoma cells using cantilever arrays. *Nature Nanotechnology*, 8(2):125–129, February 2013. (Cited on page 206.)

[179] Moyu Watari, Jane Galbraith, Hans-Peter Lang, Marilyne Sousa, Martin Hegner, Christoph Gerber, Mike A Horton, and Rachel A McKendry. Investigating the Molecular Mechanisms of In-Plane Mechanochemistry on Cantilever Arrays. *Journal of the American Chemical Society*, 129(3):601–609, January 2007. (Cited on page 206.)

[180] Michel Godin, Vincent Tabard-Cossa, Yoichi Miyahara, Tanya Monga, P J Williams, L Y Beaulieu, R Bruce Lennox, and Peter Grutter. Cantilever-based sensing: the origin of surface stress and optimization strategies. *Nanotechnology*, 21(7):075501, January 2010. (Cited on page 206.)

[181] Karen M Goeders, Jonathan S Colton, and Lawrence A Bottomley. Microcantilevers: Sensing Chemical Interactions via Mechanical

Motion. *Chemical Reviews*, 108(2):522–542, February 2008. (Cited on page 208.)

[182] Christiane Ziegler. Cantilever-based biosensors. *Analytical and Bioanalytical Chemistry*, 379(7-8), July 2004. (Cited on page 208.)

[183] J Mertens, M Álvarez, and J Tamayo. Real-time profile of microcantilevers for sensing applications. *Applied Physics Letters*, 87 (23):234102, November 2005. (Cited on page 208.)

[184] En-Te Hwu, Shao-Kang Hung, Chih-Wen Yang, Kuang-Yuh Huang, and Ing-Shouh Hwang. Real-time detection of linear and angular displacements with a modified DVD optical head. *Nanotechnology*, 19(11):115501, February 2008. (Cited on page 208.)

[185] Rodolfo I Hermans, Joe M Bailey, and Gabriel Aeppli. Direct and alignment-insensitive measurement of cantilever curvature. *Applied Physics Letters*, 103(3):034103–034103–5, 2013. (Cited on page 208.)

[186] Moyu Watari. In-plane Mechanochemistry at Model Biological Interfaces. pages 1–176, October 2007. (Cited on page 210.)

[187] Maria L Sushko, John H Harding, Alexander L Shluger, Rachel A McKendry, and Moyu Watari. Physics of Nanomechanical Biosensing on Cantilever Arrays. *Advanced Materials*, 20(20): 3848–3853, October 2008. (Cited on page 210.)

[188] Leo Tom Varghese, Rajeev K Sinha, and Joseph Irudayaraj. Study of binding and denaturation dynamics of IgG and anti-IgG using dual color fluorescence correlation spectroscopy. *analytica chimica acta*, 625(1):103–109, September 2008. (Cited on page 218.)

[189] Nafisa Islam, Fei Shen, Patrick V Gurgel, Orlando J Rojas, and Ruben G Carbonell. Dynamic and equilibrium performance of sensors based on short peptide ligands for affinity adsorption of human IgG using surface plasmon resonance. *Biosensors and Bioelectronics*, 58:380–387, 2014. (Cited on page 218.)

[190] E Behravesh, V I Sikavitsas, and A G Mikos. Quantification of ligand surface concentration of bulk-modified biomimetic hydrogels. *Biomaterials*, 24(24):4365–4374, November 2003. (Cited on page 218.)

[191] J H Lee, K S Hwang, J Park, K H Yoon, and D S Yoon. Immunoassay of prostate-specific antigen (PSA) using resonant frequency shift of piezoelectric nanomechanical microcantilever. *Biosensors and . . .*, 2005. (Cited on pages 221 and 222.)

[192] Manoj Joshi, Prasanna S Gandhi, Rakesh Lal, V Ramgopal Rao, and Soumyo Mukherji. Modeling, Simulation, and Design Guidelines for Piezoresistive Affinity Cantilevers. *Journal of Microelectromechanical Systems*, 20(3):774–784, June 2011. (Cited on page 222.)

[193] Joseph Wafula Ndieyira, Joe Bailey, Alejandra Donoso-Barrera, Manuel Vogtli, Matthew Cooper, Chris Abell, Rachel McKendry, and Gabriel Aeppli. Surface-catalyzed dimerization of drugs unravels a new mode of action for killing multidrug resistant microbes. *Submitted to Nature Nanotechnology*. (Cited on page 223.)

[194] Daohui Li, Uma Sreenivasan, Nenad Juranic, Slobodan Macura, Francisco J Puga, Paul M Frohnert, and Paul H Axelsen. Simulated dipeptide recognition by vancomycin. *Journal of Molecular Recognition*, 10(2):73–87, March 1997. (Cited on page 223.)

[195] C T Walsh, S L Fisher, I S Park, M Prahalad, and Z Wu. Bacterial resistance to vancomycin: Five genes and one missing hydrogen bond tell the story. *Chemistry & Biology*, 3(1):21–28, January 1996. (Cited on page 223.)

[196] Norris E Allen and Thalia I Nicas. Mechanism of action of oritavancin and related glycopeptide antibiotics. *FEMS Microbiology Reviews*, 26(5):511–532, January 2003. (Cited on page 223.)

[197] M A Cooper and D H Williams. Binding of glycopeptide antibiotics to a model of a vancomycin-resistant bacterium. *Chemistry & Biology*, 6(12):891–899, December 1999. (Cited on page 223.)

[198] Geoffrey A McKay, Sylvain Beaulieu, Francis F Arhin, Adam Belley, Ingrid Sarmiento, Thomas Jr Parr, and Gregory Moeck. Time-kill kinetics of oritavancin and comparator agents against Staphylococcus aureus, Enterococcus faecalis and Enterococcus faecium. *Journal of Antimicrobial Chemotherapy*, 63(6):1191–1199, June 2009. (Cited on page 224.)

[199] M Ge. Vancomycin Derivatives That Inhibit Peptidoglycan Biosynthesis Without Binding D-Ala-D-Ala. *Science*, 284(5413): 507–511, April 1999. (Cited on page 224.)

[200] Sung Joon Kim, Lynette Cegelski, Dirk Stueber, Manmilan Singh, Evelyne Dietrich, Kelly SE Tanaka, Thomas R Parr Jr, Adel Rafai Far, and Jacob Schaefer. Oritavancin Exhibits Dual Mode of Action to Inhibit Cell-Wall Biosynthesis in Staphylococcus aureus. *Journal of Molecular Biology*, 377(1):281–293, 2008. (Cited on page 224.)

[201] Patrick J Loll, Ariss Derhovanessian, Maxim V Shapovalov, Jeffrey Kaplan, Lin Yang, and Paul H Axelsen. Vancomycin Forms Ligand-Mediated Supramolecular Complexes. *Journal of Molecular Biology*, 385(1):200–211, January 2009. (Cited on page 233.)

[202] Federica Rampf and Ezequiel Albano. Interplay between jamming and percolation upon random sequential adsorption of competing dimers and monomers. *Physical Review E*, 66(6): 061106, December 2002. (Cited on page 242.)

[203] M Hassan, Jürgen Schmidt, Bernd Blasius, and Jürgen Kurths. Jamming coverage in competitive random sequential adsorption of a binary mixture. *Physical Review E*, 65(4):045103, April 2002. (Cited on page 242.)

[204] Brian C Barnes, Daniel W Siderius, and Lev D Gelb. Structure, Thermodynamics, and Solubility in Tetromino Fluids. 25(12): 6702–6716, June 2009. (Cited on page 242.)

[205] J Evans. Random and cooperative sequential adsorption. *Rev.Mod.Phys.*, 65(4):1281–1329, October 1993. (Cited on page 243.)

[206] J Talbot, G Tarjus, P R Van Tassel, and P Viot. From car parking to protein adsorption: an overview of sequential adsorption processes. *Colloids and Surfaces A: Physicochemical and Engineering Aspects*, 165(1-3):287–324, May 2000. (Cited on page 243.)

[207] D H Williams. An Analysis of the Origins of a Cooperative Binding Energy of Dimerization. 280(5364):711–714, May 1998. (Cited on page 252.)

[208] Dudley H Williams and Ben Bardsley. The vancomycin group of antibiotics and the fight against resistant bacteria. *Angewandte Chemie International Edition*, 38(9):1172–1193, 1999. (Cited on page 252.)

[209] Joel P Mackay, Ute Gerhard, Daniel A Beauregard, Rachael A Maplestone, and Dudley H Williams. Dissection of the contributions toward dimerization of glycopeptide antibiotics. 116(11): 4573–4580, 1994. (Cited on page 252.)

[210] Joel P Mackay, Ute Gerhard, Daniel A Beauregard, Dudley H Williams, Martin S Westwell, and Mark S Searle. Glycopeptide antibiotic activity and the possible role of dimerization: a model for biological signaling. *Journal of the American Chemical Society*, 116(11):4581–4590, 1994. (Cited on page 252.)